# THREE-DIMENSIONAL BOUNDARY INTEGRAL EQUATION STRESS ANALYSIS OF CRACKED COMPONENTS

by

Tan Choon Lai, B.Sc.(Eng.), A.C.G.I.

A thesis submitted for the degree of

Doctor of Philosophy

of the

Faculty of Engineering, University of London,

and for the

Diploma of Imperial College

July 1979

Department of Mechanical Engineering,
Imperial College of Science & Technology,
University of London.

# THREE-DIMENSIONAL BOUNDARY INTEGRAL EQUATION STRESS ANALYSIS OF CRACKED COMPONENTS

by

Tan Choon Lai

## ABSTRACT

This thesis presents the application of an efficient numerical tool, namely, the Boundary Integral Equation (BIE) method, to the three-dimensional stress analysis of cracked components which, for the present study, is limited to elastostatics of elastically homogeneous and isotropic bodies.

The basic concepts of linear elastic fracture mechanics are reviewed, and, from the governing partial differential equations of elasticity, the boundary integral equations are derived. To solve these equations, the boundary surface of the solution domain is discretized into eight-node quadrilateral elements, over each of which the distributions of surface geometry, and unknown displacements and tractions, are expressed in terms of quadratic shape functions of the intrinsic coordinates. A three-dimensional boundary integral equation computer program was developed, as was a plotting program with which the mesh discretization data could be visually checked in terms of element topology and nodal coordinates before use.

Different procedures for determining fracture mechanics parameters, in particular, the stress intensity factor, for three-dimensional crack problems by means of the BIE method are discussed and the results of several test problems are presented. An attempt to elucidate the strength of the stress singularity near the point where the crack front intersects the free surface of the body is also presented. The numerical results show qualitative agreement with the semi-analytical results in the literature, with the singularity at this point being generally lower than at points remote from the free surface. The BIE method is further used for the stress analysis of an internally pressurised thick-walled cylinder with a semi-elliptical surface crack. The fracture mechanics analysis includes the numerical fatigue analysis of the propagating surface crack in a cylinder. Results of the stress analysis, where possible, are compared with those obtained experimentally. The problem of an internally pressurised cylinder with a radial cross-bore is also investigated, both for the case where there are no cracks, and for several sizes of the cracks at the cross-bore.

*To my mother*

## ACKNOWLEDGEMENTS

The author wishes to express his sincere appreciation and gratitude to Dr R.T. Fenner for his valuable guidance and encouragement throughout the course of this study. Special thanks are also due to Dr J.O. Watson for his valuable advice and fruitful discussions on the numerical implementation of the boundary integral equation method, and to Mr P.S.J. Crofton for making available the experimental data used in the present work.

The helpful assistance of the departmental librarians, Miss E.M. Archer, Mrs S.D. Boote and Miss A. Gelder, in obtaining reference material is deeply appreciated. The author is also indebted to Mrs E.A. Hall for the considerable care and exactness shown in typing the manuscript.

This work was made possible with the generous financial support of Ato-Chemie, Dutch State Mines, Mannesman, USI and Dart Incorporated, to whom the author is grateful.

CONTENTS


| | | Page |
|---|---|---|
| Title Page | | 1 |
| Abstract | | 2 |
| Acknowledgements | | 4 |
| Contents | | 5 |
| Nomenclature | | 9 |
| CHAPTER 1: | INTRODUCTION | 18 |
| CHAPTER 2: | BASIC PRINCIPLES OF FRACTURE MECHANICS | 23 |
| 2.1 | General Remarks | 23 |
| 2.2 | Theories of Fracture | 25 |
| 2.2.1 | The Griffith theory | 26 |
| 2.2.2 | Modified Griffith theory | 27 |
| 2.2.3 | Irwin's theory - the stress intensity factor approach | 28 |
| 2.2.4 | Sih's theory - the strain energy density factor approach | 32 |
| 2.3 | Fracture Mechanics Approach to Fatigue | 35 |
| 2.3.1 | Paris' crack-propagation law | 36 |
| 2.3.2 | Alternative crack-growth formulae | 37 |
| 2.4 | Limitations of LEFM | 39 |
| 2.5 | Final Remarks | 41 |
| CHAPTER 3: | FORMULATION OF THE BOUNDARY INTEGRAL EQUATIONS | 46 |
| 3.1 | Review of the Governing Equations of Elasticity | 46 |
| 3.2 | Derivation of the Integral Equations | 48 |

| | | Page |
|---|---|---|
| 3.2.1 | The fundamental solution | 48 |
| 3.2.2 | Betti's reciprocal work theorem | 54 |
| 3.2.3 | Integral equations for displacements and stresses at interior points | 55 |
| 3.2.4 | The boundary integral equation | 59 |
| 3.3 | Final Remarks | 60 |
| CHAPTER 4: | THE NUMERICAL SOLUTION OF THE INTEGRAL EQUATIONS | 64 |
| 4.1 | Review of Various Numerical Formulation | 64 |
| 4.2 | Parametric Representation of Geometry and Functions | 69 |
| 4.3 | Numerical Formulation of the Boundary Integral Equation | 71 |
| 4.3.1 | Evaluation of equation coefficients | 72 |
| 4.3.2 | Further notes on the formation of the coefficient matrix of the equations | 75 |
| 4.4 | Solution of the System of Equations | 77 |
| 4.5 | Evaluation of the Surface Stress Tensor | 79 |
| 4.6 | Evaluation of Stresses and Displacements at Interior Points | 81 |
| 4.7 | Final Remarks | 81 |
| CHAPTER 5: | APPLICATION OF THE BOUNDARY INTEGRAL EQUATION METHOD TO LINEAR ELASTIC FRACTURE MECHANICS | 87 |
| 5.1 | Numerical Evaluation of the Stress Intensity Factor | 88 |
| 5.1.1 | The displacement method | 88 |
| 5.1.2 | The stress method | 89 |
| 5.1.3 | The indirect method | 90 |

| | | Page |
|---|---|---|
| 5.2 | The Singularity Element | 95 |
| 5.3 | Further Notes on the Evaluation of Stress Intensity Factors | 97 |
| 5.4 | Numerical Analysis of Fatigue Crack Growth | 99 |
| 5.5 | Test Problems | 101 |
| 5.5.1 | Compact tension specimen | 102 |
| 5.5.2 | Embedded penny-shaped crack in a square prism | 105 |
| 5.5.3 | Corner quadrant crack in a long square prism | 106 |
| 5.5.4 | Semi-circular surface crack in a long rectangular prism | 107 |
| 5.6 | Singularity Analysis | 109 |
| 5.6.1 | Centre-crack tension (CCT) specimen | 112 |
| 5.6.2 | Semi-circular surface crack in a long rectangular prism | 115 |
| 5.6.3 | Further discussion | 116 |
| CHAPTER 6: | ON THE SURFACE FLAW PROBLEM IN INTERNALLY PRESSURIZED THICK-WALLED CYLINDERS | 147 |
| 6.1 | Introduction to the Problem | 147 |
| 6.2 | Review of Previous Work | 150 |
| 6.3 | Present Numerical Investigation | 154 |
| 6.4 | Overall Response | 155 |
| 6.4.1 | Stress distributions | 155 |
| 6.4.2 | Hoop strains | 159 |
| 6.4.3 | Stress intensity factors | 162 |

| | | Page |
|---|---|---|
| 6.5 | Further Numerical Investigation | 164 |
| 6.6 | Crack Propagation Analysis | 167 |
| | 6.6.1 Evaluation of stress intensity factors | 168 |
| | 6.6.2 Prediction of crack growth | 173 |
| CHAPTER 7: | ON INTERNALLY PRESSURIZED THICK-WALLED CYLINDERS WITH CROSS-BORES | 217 |
| 7.1 | Review of the Problem and Scope of the Present Investigation | 217 |
| 7.2 | Hoop Stress Distributions in the Absence of Cracks | 221 |
| 7.3 | Analysis of the Cracked Component | 225 |
| | 7.3.1 Stress intensity factors | 226 |
| | 7.3.2 Hoop strains | 228 |
| | 7.3.3 Hoop stress distributions | 230 |
| CHAPTER 8: | CONCLUSIONS | 255 |
| APPENDIX A: | DERIVATION OF $U_{ij}(p,q)$ AND $T_{ij}(p,q)$ | 260 |
| APPENDIX B: | THE VALUE OF $C_{ij}(P)$ WHEN THE TANGENT PLANE AT $P(x)$ IS SMOOTH | 264 |
| APPENDIX C: | TANGENTIAL STRAINS AT THE SURFACE IN THE LOCAL COORDINATE SYSTEM OF ELEMENT | 267 |
| APPENDIX D: | APPROXIMATE SOLUTION FOR THE STRESS CONCENTRATION FACTOR FOR A PRESSURIZED CYLINDER WITH A SMALL CIRCULAR CROSS-BORE | 269 |
| References | | 273 |

## NOMENCLATURE

The notation used in the main text and Appendices are briefly defined in alphabetical order in the following list. Symbols whose use is confined to only a specific analysis are omitted here and are defined at the appropriate point in the text. Where there are more than one definition for the same symbol, the relevant section or chapter is indicated in parentheses; otherwise, the definition applies everywhere other than for the alternative definitions. Where appropriate, the number of the equation in which the symbol first appears is given.

| Symbol | | Definition | Equation |
|---|---|---|---|
| $a$ | : | Major semi-axis of an ellipse representing a notch in a body (Section 2.2) | (2.1) |
| $a$ | : | Major semi-axis of a semi-ellipse representing a surface crack in a body | |
| $A$ | : | Surface area of the crack in a body | (5.5) |
| $b$ | : | Minor semi-axis of an ellipse representing a notch in a body (Section 2.2) | (2.1) |
| $b$ | : | Minor semi-axis of a semi-ellipse representing a surface crack in a body | |
| $c$ | : | Measure of crack length | (2.4) |
| $C$ | : | Material constant in Paris' Law of fatigue crack propagation (Section 2.3.1) | (2.29) |
| $C_{ij}$ | : | The limiting value of the surface integral of $T_{ij}(P,Q)$; $i = 1,3$ , $j = 1,3$ (Section 3.2.4) | (3.55) |

| Symbol | | Definition | Equation |
|---|---|---|---|
| $d(b,c)$ | : | $c$th node of the $b$th surface element; $c = 1,8$ , $b = 1,M$ | (4.12) |
| $D_{kij}(p,Q)$ | : | Third order tensor for obtaining stresses at $p(\underset{\sim}{x})$; $i = 1,3$ , $j = 1,3$ , $k = 1,3$ | (3.48) |
| $e_i$ | : | Base vector; $i = 1,3$ | (3.14) |
| $e_{ij}$ | : | Strain tensor; $i = 1,3$ , $j = 1,3$ | (3.2) |
| $\bar{e}_{ij}$ | : | Strain tensor in the orthogonal local coordinate system defined by $\mu_{ij}$; $i = 1,3$ , $j = 1,3$ | (4.20) |
| $E$ | : | Young's modulus | (2.6) |
| $g$ | : | Total number of distinct nodal points on the surface of solution domain (Section 4.3) | |
| $g_i(\underset{\sim}{x})$ | : | Prescribed boundary displacement function; $i = 1,3$ | (3.6) |
| $G$ | : | Strain energy release rate | |
| $G_c$ | : | Critical strain energy release rate, at incipient fracture | (2.9) |
| $G_i$ | : | Galerkin vector; $i = 1,3$ (Section 3.2.1) | (3.12) |
| $G_I, G_{II}, G_{III}$ | : | Strain energy release rate corresponding to Modes I, II and III, respectively | (2.18) |
| $h_i(\underset{\sim}{x})$ | : | Prescribed boundary traction function; $i = 1,3$ | (3.7) |
| $H$ | : | Measure of length of cracked specimen | |
| $H'$ | : | Material stiffness $= \begin{cases} E & \text{, for plane stress} \\ E/(1-\nu^2) & \text{, for plane strain} \end{cases}$ | (2.6) |

| Symbol | | Definition | Equation |
|---|---|---|---|
| $J(\xi)$ | : | Jacobian of transformation from global Cartesian coordinates to intrinsic coordinates of element | (4.8) |
| $k_h$ | : | Hoop stress concentration factor | (7.1) |
| $K_I, K_{II}, K_{III}$ | : | Stress intensity factor corresponding to Modes I, II and III, respectively | (2.10) |
| $K_{Ic}, K_{IIc}, K_{IIIc}$ | : | Critical stress intensity factor corresponding to Modes I, II and III, respectively (fracture toughness) | |
| $\overline{K}_I$ | : | Root-mean-square value of $K_I$ | (5.7) |
| $\Delta K_I$ | : | Stress intensity factor range | (2.30) |
| $\ell$ | : | Characteristic measure of crack size (Section 2.3) | (2.28) |
| $\ell_o$ | : | Greatest physical dimension of solution domain (Section 4.3.2) | |
| $L^m(\eta)$ | : | Linear shape functions in intrisic coordinates, $\eta$; $m = 1,4$ | (4.16) |
| $m$ | : | Material constant in Paris' Law of fatigue crack propagation (Section 2.3.1) | (2.29) |
| $m_{\beta j}$ | : | Unit vectors in the local coordinate directions, $\xi_\beta$; $\beta = 1,2$ , $j = 1,3$ (Section 4.5) | |
| $m_{3j}$ | : | Direction cosines of the unit outward normal ($\equiv n_j$); $j = 1,3$ (Section 4.5) | |
| $M$ | : | Total number of surface elements | (4.2) |
| $\overline{n}$ | : | Stress (strain) singularity index (Section 5.6) | (5.28) |

| Symbol | | Definition | Equation |
|---|---|---|---|
| $n_j$ | : | Unit outward normal vector to the surface of the elastic body; $j$ = 1,3 | (3.7) |
| $N$ | : | Number of load cycles | (2.28) |
| $N^c(\xi)$ | : | Quadratic shape-function corresponding to the $c$th-node of the element; $c$ = 1,8 | (4.4) |
| $p(x)$ | : | Load point within the elastic domain $R$ (Chapters 3 and 4) | |
| $P(x)$ | : | Load point at the surface of the elastic domain $R$ (Chapters 3 and 4) | |
| $P_n$ | : | $n$th-node at the surface of solution domain; $n$ = 1,$g$ | (4.1) |
| $P$ | : | Internal pressure in a cylinder | (6.2) |
| $q(x)$ | : | Field point within the elastic domain $R$ (Chapters 3 and 4) | |
| $Q(x)$ | : | Field point at the surface of elastic domain $R$ (Chapters 3 and 4) | |
| $r$ | : | Distance of point from the crack front | (2.10) |
| $r$ | : | Distance between field and load points (Chapters 3 and 4) | (3.4) |
| $R$ | : | Elastic domain | |
| $R_\varepsilon$ | : | Spherical region of exclusion in elastic domain, $R$ | |
| $R_1$ | : | Internal radius of cylinder | (6.2) |
| $R_2$ | : | External radius of cylinder | (6.2) |
| $R_s$ | : | Radius of circular cross-bore in a cylinder | |
| $s$ | : | Linear distance along the crack front | (5.7) |

| Symbol | | Definition | Equation |
|---|---|---|---|
| $s_{i\beta}$ | : | Vectors tangent to intrinsic coordinate lines, $\xi_\beta$, of element; $\beta = 1,2$ , $i = 1,3$ | (4.6) |
| $S$ | : | Strain energy density factor (Section 2.2.4) | (2.21) |
| $S$ | : | Surface or boundary of elastic domain, $R$ | |
| $S_b$ | : | $b$th-element of the discretized surface; $b = 1,M$ | (4.12) |
| $S_{cr}$ | : | Critical value of strain energy density factor, at incipient fracture (Section (Section 2.2.4) | (2.26) |
| $S_{min}$ | : | Minimum value of strain energy density factor (Section 2.2.4) | |
| $S_t$ | : | The part of the surface of the elastic domain where tractions are prescribed | (3.7) |
| $S_u$ | : | The part of the surface of the elastic domain where displacements are prescribed | (3.6) |
| $S_\epsilon$ | : | Surface of the region of exclusion, $R_\epsilon$ | (3.36) |
| $S_{kij}(p,Q)$ | : | Third order tensor for obtaining stresses at $p(x)$; $i = 1,3$ , $j = 1,3$ , $k = 1,3$ | (3.48) |
| $\Delta S_m$ | : | $m$th-triangular surface element | (4.1) |
| $t_i$ | : | Traction vector; $i = 1,3$ | (3.7) |
| $\bar{t}_i$ | : | Traction vector in the orthogonal local coordinate system defined by $\mu_{ij}$; $i = 1,3$ , $j = 1,3$ | (4.21) |
| $T$ | : | Measure of thickness of cracked specimen | |
| $T_{ij}(p,q)$ | : | The $i$th-component of the traction vector at point $q(x)$ due to a unit point load in the $j$th-direction at $p(x)$; $i = 1,3$ , $j = 1,3$ | (3.30) |

| Symbol | | Definition | Equation |
|---|---|---|---|
| $u_i$ | : | Displacement vector; $i$ = 1,3 | (2.11) |
| $\bar{u}_\alpha$ | : | Displacements in the local orthogonal tangential directions defined by $\mu_{ij}$; $\alpha$ = 1,2 | (4.19) |
| $U$ | : | Strain energy of the body | (5.5) |
| $U_{ij}(p,q)$ | : | The $i$th-component of the displacement vector at point $q(\underset{\sim}{x})$ due to a unit point load in the $j$th-direction at $p(\underset{\sim}{x})$; $i$ = 1,3 , $j$ = 1,3 | (3.29) |
| $v$ | : | Crack-face displacements | (5.2) |
| $V$ | : | Volume of elastic domain, $R$ | (3.9) |
| $W$ | : | Strain energy density (Section 2.2.4) | (2.22) |
| $W$ | : | Measure of width of cracked specimen (Sections 5.5 and 5.6) | |
| $W$ | : | Wall thickness of cylinder (Chapters 6 and 7) | |
| $W_s$ | : | Total surface energy of a crack | (2.3) |
| $W_T$ | : | Total potential energy of a body | (2.3) |
| $x_i$ | : | Rectangular Cartesian coordinates; $i$ = 1,3 | |
| $x_i^e$ | : | Cartesian coordinates of the $e$th-node of element; $e$ = 1,8 , $i$ = 1,3 | (4.4) |
| $X_i$ | : | Body force vector; $i$ = 1,3 | (3.1) |
| $\alpha_c$ | : | Lateral constraint parameter | (5.25) |
| $\alpha_s$ | : | Shape factor (Section 6.2) | (6.1) |
| $\gamma$ | : | Specific surface energy (Section 2.2.1) | (2.5) |

| Symbol | | Definition | Equation |
|---|---|---|---|
| $\gamma_p$ | : | Energy dissipation due to plastic flow (Section 2.2.1) | (2.8) |
| $\delta_{ij}$ | : | Kronecker delta $= \begin{cases} 0 \text{ , when } i \neq j \\ 1 \text{ , when } i = j \end{cases}$ | (3.4) |
| $\varepsilon$ | : | Radius of spherical region of exclusion $R_\varepsilon$ | |
| $\varepsilon_h$ | : | Hoop strain in a cylinder | |
| $\varepsilon_h^*$ | : | Lamé solution hoop strain in a cylinder | |
| $\zeta_i$ | : | Coordinates of load point; $i = 1,3$ | (3.10) |
| $\eta_\alpha$ | : | Intrinsic coordinates of triangular sub-element; $\alpha = 1,2$ | (4.14) |
| $\kappa$ | : | Muskhelishvilli's constant $= \begin{cases} (3-4\nu) & \text{, for plane strain} \\ (3-\nu)/(1+\nu) & \text{, for plane stress} \end{cases}$ | (2.11) |
| $\lambda$ | : | Lamé's constant $= \frac{2\mu\nu}{1-2\nu}$ (Section 3.1) | |
| $\mu$ | : | Shear modulus | (2.11) |
| $\mu_{ij}$ | : | Direction cosines of the orthogonal local coordinate axes; $i = 1,3$ , $j = 1,3$ | (4.19) |
| $\nu$ | : | Poisson's ratio | (2.6) |
| $\xi_\alpha$ | : | Intrinsic coordinates of isoparametric quadrilateral element; $\alpha = 1,2$ | (4.4) |
| $\rho$ | : | Radius of curvature at the apex of the major semi-axis of an elliptical notch in a body | (2.1) |

| Symbol | | Definition | Equation |
|---|---|---|---|
| $\sigma_{ij}$ | : | Stress tensor; $i = 1,3$ , $j = 1,3$ | (2.10) |
| $\bar{\sigma}_{ij}$ | : | Stress tensor in the orthogonal local coordinate system defined by $\mu_{ij}$; $i = 1,3$ , $j = 1,3$ | (4.21) |
| $\sigma_{cr}$ | : | Critical stress required for crack extension | (2.7) |
| $\sigma_h$ | : | Hoop stress in a cylinder | |
| $\sigma_h^*$ | : | Lamé solution hoop stress in a cylinder | (6.2) |
| $(\sigma_h)_{max}$ | : | Maximum hoop stress in a cylinder | |
| $\sigma_m$ | : | Mean stress | (5.27) |
| $\sigma_o$ | : | Remote tensile stress applied to a cracked body in the direction perpendicular to the crack plane | (2.1) |
| $(\sigma_y)_{max}$ | : | Maximum stress at the apex of the major semi-axis of an elliptical notch in a body | (2.1) |
| $\sigma_{ys}$ | : | Yield stress | (2.35) |
| $\tau_o$ | : | Flow stress | (5.26) |
| $\chi$ | : | Order of Gaussian quadrature formula | (4.13) |

## LIST OF ABBREVIATIONS

| | | |
|---|---|---|
| ASME | : | American Society of Mechanical Engineers |
| ASTM | : | American Society for Testing and Materials |
| BIE | : | Boundary Integral Equation |
| BIESIF | : | Three-dimensional BIE computer program for linear elastostatics |
| CCT | : | Centre-Crack-Tension |
| CEGB | : | Central Electricity Generating Board |
| DOF | : | Degree(s)-Of-Freedom |
| DRAW | : | Computer program for checking mesh idealization data, using graphic facilities at ICCC |
| FEM | : | Finite Element Method |
| ICCC | : | Imperial College Computer Centre |
| LEFM | : | Linear Elastic Fracture Mechanics |
| SEC | : | Single-Edge-Crack |

# CHAPTER 1

# INTRODUCTION

One of the salient features in the development of engineering design methods in the past decade or so is the general trend to allow higher working stresses in engineering components and structures. This has been due in part to improved material properties, giving higher strength, and also to the greater degree of confidence in using experimentally or theoretically determined design stresses. In high pressure vessel technology, for example, these trends were spawned by the rapid scaling-up of chemical plants and accelerated by the advent of nuclear power. Because of the potential dangers involved if there is any failure of the components, new levels of functional reliability as well as safety requirements are called for.

As materials in service will always contain inclusions and flaws, the presence of these defects tends to give rise to growing cracks, especially under these elevated levels of operating stresses. In such circumstances, failure can occur in a dramatic and catastrophic manner by cleavage fracture at loads which are significantly lower than the ultimate strength of the material, or in the case of cyclic loading, after a relatively small number of load cycles. Such characteristics are difficult to explain in terms of traditional design concepts. In view of this, the need for a method by which the presence of cracks can be considered has become apparent and the discipline of "Fracture Mechanics" has emerged to fill this rôle. This discipline has led to the emergence of new design concepts which are increasingly being incorporated in standards and codes of practice.

In essence, fracture mechanics assumes the pre-existence of cracks or

flaws in a real structure and utilizes continuum mechanics principles to develop parameters which characterize the stress field in the vicinity of the crack front. When the material is linearly elastic, classical analyses show that stresses (strains) are singular in that region, being inversely proportional to the square root of the distance from the crack tip or front. The constant of proportionality, or stress intensity factor, defines the strength of this singularity, and is the most important of these fracture mechanics parameters. In the next chapter, the basic principles of this discipline is presented and how it can be applied is also discussed.

Although the classical solutions in stress analysis can be applied, with proper judgement, to many design details, the geometry and loading in a practical problem are often such that the problem cannot be solved analytically. This is particularly true of practical three-dimensional crack problems. In this respect, a key role in the development of the design and analysis procedures was played by the advent of high-speed digital computers and the subsequent developments in numerical analysis. They paved the way for detailed determinations of stresses and strain under the relevant boundary conditions.

One of the most successful of the numerical tools developed in recent years has been the finite element method. But despite its versatility, this method has some drawbacks, particularly when the problem concerned is three-dimensional and involves rapidly varying stress fields of the type encountered near stress concentrations and cracks. In such regions, very fine subdivision of the component or structure into elements is required if reasonably accurate distributions of stresses and displacements are to be obtained. Also, while the most commonly used finite element approach based on displacement can give good results for

displacements, it yields somewhat less accurate values for stresses which are generally of greater practical interest. Further, the system of linear equations which has to be solved is so large in three-dimensional problems that, even though the coefficient matrix is symmetric and banded in form, the computing costs are high. In some respects, the finite element method is wasteful in that it provides a great deal of information about internal nodal points and elements which is never used. Finally, even using the most sophisticated data generation and checking facilities, the cost of preparing mesh data can be high, particularly when solving three-dimensional problems.

The boundary integral equation (BIE) method offers an attractive alternative solution procedure by which many of the limitations associated with the finite element method can be overcome. Historically, the method is based on classical mathematical formulations in potential theory by early Italian and Russian elasticians, notably, Betti, Somigliana, Cerruti, Lamicella, Fredholm and, more recently, Mikhlin and Kupradze. The formulations lead to integral equations which relate the basic boundary data, hence the name of the method. In stress analysis, the boundary integral equation provides an integral constraint relating the boundary tractions and boundary displacements. Where tractions are prescribed on the boundary, the corresponding displacements are the unknowns for which the integral equation is to be solved, and vice versa. Once the boundary integral equation has been solved, the displacements, tractions and stress tensor are known everywhere on the boundary, and from these data the displacements and stresses at any specified interior points may be obtained.

Numerical solutions to the boundary integral equation are found by discretizing the boundary into elements and expressing the distribution of the unknowns over these elements in terms of suitable algebraic functions

involving values at certain nodal points associated with the elements. Whereas in, say, the finite element method, the entire solution domain has to be discretized, it is only necessary to discretize the boundary in the BIE method. An advantage of the latter approach is therefore clear: a three-dimensional volume problem becomes a numerically two-dimensional surface problem. This reduction in dimensionality by one results in significantly reduced numerical problem size, computer requirements and data preparation compared with the finite element method. The coefficient matrix associated with the much smaller set of linear equations obtained from the boundary integral equation is, however, both non-symmetric and fully populated. This need not be a serious disadvantage because the domain can be divided into sub-regions, for each of which an integral equation is established and a banded matrix is obtained. An additional benefit is that each sub-region can have different material properties.

A further advantage of the BIE method is that, because there is no internal discretization of the domain, no further approximations are imposed on the solution at interior points, hence there is generally a better resolution of stresses. Also, it is possible to concentrate on a particular region of interest, such as around the crack front in fracture mechanics analysis, to a greater extent than with the finite element method. The computing resources used to calculate unwanted information are therefore reduced.

The BIE method is the numerical tool used for the present study, which is limited to three-dimensional linear elastostatics involving cracks. In Chapter 3, the mathematical basis of the method is outlined and the key equations derived. This is followed, in Chapter 4, by a discussion of the numerical formulation adopted for the present work, based on which, a computer program was developed. In Chapter 5, it is shown how fracture

mechanics parameters, in particular, stress intensity factors, can be obtained using the BIE method. The results of several test problems are also presented for comparison with established solutions in the literature.

In three-dimensional crack problems, the crack front can often intersect the free surface of the body. At this point of intersection, the nature of the stress (strain) singularity may no longer be the classical inverse square root of the distance from the crack front. Although the elucidation of the nature of the singularity at such points has been considered analytically and semi-analytically to a very limited extent, a direct numerical approach, as far as is known, has not been carried out previously. In the final section of Chapter 5, an attempt to determine the order of this singularity by the BIE method will be presented.

Chapter 6 is devoted to the stress analysis of an internally pressurized thick-walled cylinder with a semi-elliptical surface crack. The results presented include stress intensity factor solutions. Also included in the chapter is the numerical analysis of crack propagation in a thick-walled cylinder which is subjected to cyclic pressure loading. Where possible, the numerical results are compared with available experimental data.

Finally, in Chapter 7, the problem of an internally pressurized thick-walled cylinder with a radial cross-bore is investigated. Stress analysis results are presented both for the case when there are no cracks and for several sizes of crack. In the latter case, stress intensity factor solutions are also obtained.

# CHAPTER 2

# BASIC PRINCIPLES OF FRACTURE MECHANICS

Serious inadequacies exist in conventional design concepts particularly where new levels of functional and structural integrity of engineering components and structures, such as pressure vessels and reactors, are called for. In this respect, the discipline of fracture mechanics has an increasingly important rôle to play. Although a relatively new field, it has advanced to the stage where its value to engineering design is generally no longer in question. In this chapter, the basic concepts involved will be presented.

## 2.1 GENERAL REMARKS

Conventional design philosophy is based mainly on the stress analysis of unflawed structures with ultimate strength, yield strength and buckling resistance being the basic criteria. Where uncertainty about the loading and material behaviour may arise, it is often allowed for by applying a factor of safety (or more appropriately, a factor of ignorance). However, the failure criteria based on this design philosophy cannot explain in any certain terms the kind of failure which occur at nominal stresses considerably lower than the ultimate strength of the material. Such failures of engineering components usually occur without warning in a catastrophic manner, a failure mode which is normally referred to as brittle fracture. These failures are not restricted to static loading systems; indeed, a great many of them occur in cyclic loading systems where brittle fracture occurs after relatively small numbers of loading cycles. Reports of many dramatic examples of these kinds of failure are well documented in the literature (see, for example, Shank (1954), Boyd

(1970), Lancaster (1973), Rich & Cartwright (1977)).

In view of the potential dangers associated with this mode of failure, such as in chemical or nuclear reactors, and that the severity has increased over the years due to the increasing use of higher strength materials for weight and cost saving reasons, special emphasis has been given to analytical method for determining the operating stresses and their influence on the different modes of failure. It has also become evident that it is necessary to assume the existence of flaws, voids or inclusions in materials which cause elevation of stresses in those regions. In these respects, the treatment of fracture can be viewed in at least two levels - a microscopic level and a macroscopic level.

At the micro or atomic level, studies relate to the mechanism of fracture; for a sufficiently high level of stress, atomic bonds may be broken and the flaw may grow until complete failure of the solid occurs. Analytical treatment at this level is, however, not generally straightforward; the alternative macroscopic level for which continuum mechanics theory can be applied seems a more satisfactory and practical approach to the engineer. The macroscopic approach relates to the mechanics of overall fracture of a component or structure as a function of the applied loads, geometry, etc., with the viewpoint that real structures will always contain cracks or flaws from fabrication or service loading (corrosion, fatigue, etc.). This macro-study, in the absence of gross plasticity or non-linear effects in the vicinity of the cracks, for a linear elastic material is referred to as Linear Elastic Fracture Mechanics (LEFM).

Although the term "brittle fracture" may imply the restriction of LEFM to brittle materials, such as glass or high strength alloys, this is not necessarily true. The terms "brittle" and "ductile" material are relative; the so-called "ductile" materials can behave in a brittle

fashion depending on the loading conditions and specimen size. Lowering the temperature, increasing the specimen size and the speed of loading can create situations where the same "ductile" materials can behave in a brittle manner. LEFM thus pertains not just to "brittle" materials, but rather to the general phenomenon of "brittle" behaviour.

## 2.2 THEORIES OF FRACTURE

Using the two-dimensional configuration of an elliptical hole in a plate subjected to a remote tensile stress, $\sigma_o$ (Figure 2.1), Inglis (1913) obtained an expression for the maximum stress, $(\sigma_y)_{max}$, at the apex of the major axis of the ellipse where the radius of curvature $\rho = b^2/a$ is minimum, viz:

$$(\sigma_y)_{max} = \sigma_o \left[1 + \frac{2a}{b}\right] \tag{2.1}$$

In (2.1), $a$ and $b$ are the major and minor semi-axes which coincide with the $x$- and $y$-coordinate axes, respectively. If the flaw is in the shape of a very narrow ellipse, i.e. $a >> b$, the maximum tensile stress which occurs at the end of the notch is given approximately by:

$$(\sigma_y)_{max} = 2\,\sigma_o \sqrt{\frac{a}{\rho}} \tag{2.2}$$

As $\rho$ is very small in comparison with $a$, it is argued that the stress $(\sigma_y)_{max}$ could be large enough to cause crack growth.

However, when the ellipse degenerates into a sharp crack, Inglis' solution leads to an infinite elastic stress at the crack-tip leading to the paradoxical conclusion that a cracked body cannot support any load. This paradox was resolved by Griffith (1921,1924) who proposed an explanation of the fracture phenomenon by appealing to the first law of thermodynamics.

### 2.2.1 The Griffith Theory

Griffith (1921,1924) postulated that for a crack to propagate under the action of external loads, the energy absorbed by the creation of a new fracture surface must be less than the elastic strain energy released by the increment of the crack growth. Let $W_T$ be the total stored energy of the body, $W_s$ the total surface energy of an existing crack, then, according to the Griffith theory, the crack will propagate if:

$$dW_T \geq dW_s \tag{2.3}$$

For a crack of length $2c$ contained within an infinite elastic plate subject to uniform remote tension, $\sigma_o$, Griffith obtained:

$$dW_T = \frac{2\pi\sigma_o^2 c}{H} dc \tag{2.4}$$

$$dW_s = 4\gamma\, dc \tag{2.5}$$

where $\gamma$ is the specific surface energy, and:

$$H' = \begin{cases} E/(1-\nu^2) & \text{for plane strain conditions} \\ E & \text{for plane stress conditions} \end{cases} \tag{2.6}$$

In (2.6), $E$ is the Young's modulus and $\nu$ is the Poisson's ratio. Substitution of (2.4) and (2.5) into (2.3) leads to the critical stress required for crack extension, viz:

$$\sigma_{cr}\sqrt{\pi c} = \sqrt{2\gamma H'} \tag{2.7}$$

Experiments performed by Griffith on hard glass showed very encouraging results; a constant value of $\sigma_{cr}\sqrt{\pi c}$ was obtained for a range of crack lengths, as is to be expected if (2.7) is valid.

However, (2.7) suffers some important deficiencies, such as the lack of parameters to account for the geometry of the body and the type of boundary conditions. Further, it is strictly applicable only to materials with linear response on the continuum scale prior to fracture, thus virtually ruling out considerations of many engineering situations. Much credit must, however, be given to Griffith for laying the theoretical foundations from a continuum mechanics point of view, for the study of fracture.

### 2.2.2 Modified-Griffith Theory

Almost thirty years after Griffith's contribution, Irwin (1948) and Orowan (1949) independently suggested a modification of Griffith's work to accommodate limited plastic deformation prior to failure. The modification was to replace the $2\gamma$ term in (2.7) by a term $\gamma_p$ which represented the energy dissipation due to plastic flow around the crack tip. The plastic energy term, $\gamma_p$, appeared to be independent of the initial crack length and further was, Orowan estimated, about three orders of magnitude greater than $\gamma$ which led him to rewrite (2.7) as:

$$\sigma_{cr}\sqrt{\pi c} = \sqrt{H' \gamma_p} \tag{2.8}$$

Orowan argued that this modified Griffith theory would only be valid if the amount of plastic flow at instability was very much smaller in extent than either the crack length of the width of the sheet. Irwin's approach was similar, but in his view a precise interpretation of the

plastic surface energy term was unnecessarily restrictive. He argued that if for different loadings and geometries the fracture process is essentially similar, then unstable propagation of the crack would occur if the strain energy release rate, $G$, reached a critical value, $G_c$. This critical value would be regarded as a material property and has to be determined from suitable fracture experiments. The value $G_c$ provides a convenient parameter to include all supplementary energy-dissipating terms (such as plastic flow, heat, etc.) in addition to the energy required to create new fracture surfaces. Irwin's modified-Griffith approach thus led to:

$$\sigma_{cr} \sqrt{\pi\, c} = \sqrt{H'\, G_c} \tag{2.9}$$

Because $G$ has the same dimensions as force, it is often also known as the "crack-extension force".

### 2.2.3 Irwin's Theory - The Stress Intensity Factor Approach

Irwin (1957a,1957b,1958) proposed that instead of considering the energy of the entire crack system, the stress field in the immediate vicinity of the crack tip ought to be examined. Cracks in solids may be regarded as surfaces of discontinuities of the displacement field and Irwin noted that there are three classes of independent movements of the upper and lower crack surfaces with respect to each other. These three basic modes of deformation are necessary and sufficient to describe all the possible modes of crack behaviour. Characteristically known as Mode I (opening mode), Mode II (in-plane shear or sliding mode) and Mode III (anti-plane shear or tearing mode), respectively, these three basic types of deformation are illustrated by Figure 2.2 for a crack lying in the $x_1 x_3$-plane.

Corresponding to each of these three modes of deformation, there exists a particular singular stress field in the immediate vicinity of the crack edge. By employing the method of Westergaard (1939), Irwin obtained, for an ideally plain, sharp-ended crack in an isotropic elastic body, the stresses in the vicinity of the crack tip for the opening mode, viz:

$$\begin{bmatrix} \sigma_{11} \\ \sigma_{22} \\ \sigma_{12} \end{bmatrix} = \frac{K_I \cos(\theta/2)}{\sqrt{2\pi r}} \begin{bmatrix} 1 - \sin\frac{\theta}{2}\sin\frac{3\theta}{2} \\ 1 + \sin\frac{\theta}{2}\sin\frac{3\theta}{2} \\ \sin\frac{\theta}{2}\cos\frac{3\theta}{2} \end{bmatrix} + \ldots . \qquad (2.10)$$

where $r$ and $\theta$ are the polar coordinates defined in Figure 2.3. The omitted terms involve increasing half powers of the ratio of $r$ to the crack length and hence are only important when the magnitude of this ratio is large.

The parameter $K_I$ is Irwin's "stress intensity factor" for Mode I and is a function only of loading and geometry of both the crack and the body. For a general three-dimensional crack, the stress intensity factor will vary with the position along the crack front. The associated displacement field for Mode I has been shown to be given by:

$$\begin{bmatrix} u_1 \\ u_2 \end{bmatrix} = \frac{K_I}{4\mu}\sqrt{\frac{2r}{\pi}} \begin{bmatrix} \cos\frac{\theta}{2}\left[\kappa - 1 + 2\sin^2\frac{\theta}{2}\right] \\ \sin\frac{\theta}{2}\left[\kappa + 1 - 2\cos^2\frac{\theta}{2}\right] \end{bmatrix} + \ldots . \qquad (2.11)$$

where $\mu$ is the shear modulus, and:

$$\kappa = \begin{cases} (3 - 4\nu) & \text{for plane strain} \\ (3 - \nu)/(1 + \nu) & \text{for plane stress} \end{cases} \qquad (2.12)$$

Similar expressions can be obtained for Mode II; the singular stress field being given by:

$$\begin{bmatrix} \sigma_{11} \\ \sigma_{22} \\ \sigma_{12} \end{bmatrix} = \frac{K_{II}}{\sqrt{2\pi r}} \begin{bmatrix} -\sin\frac{\theta}{2}\left[2 + \cos\frac{\theta}{2}\cos\frac{3\theta}{2}\right] \\ \sin\frac{\theta}{2}\cos\frac{\theta}{2}\cos\frac{3\theta}{2} \\ \cos\frac{\theta}{2}\left[1 - \sin\frac{\theta}{2}\sin\frac{3\theta}{2}\right] \end{bmatrix} + \ldots . \qquad (2.13)$$

where $K_{II}$ is the Mode II stress intensity factor. The corresponding displacement field is:

$$\begin{bmatrix} u_1 \\ u_2 \end{bmatrix} = \frac{K_{II}}{4\mu}\sqrt{\frac{2r}{\pi}} \begin{bmatrix} \sin\frac{\theta}{2}\left[\kappa + 1 + 2\cos^2\frac{\theta}{2}\right] \\ -\cos\frac{\theta}{2}\left[\kappa - 1 - 2\sin^2\frac{\theta}{2}\right] \end{bmatrix} + \ldots . \qquad (2.14)$$

The stress component $\sigma_{33}$ from the first two modes is given by:

$$\sigma_{33} = \begin{cases} \nu(\sigma_{11}+\sigma_{22}) & \text{for plane strain} \\ 0 & \text{for plane stress} \end{cases} \qquad (2.15)$$

The components $\sigma_{13}$ and $\sigma_{23}$ are non-singular for both these modes; in particular, they are zero for plane strain conditions.

For Mode III deformation, the only singular stresses are:

$$\begin{bmatrix} \sigma_{13} \\ \sigma_{23} \end{bmatrix} = \frac{K_{III}}{\sqrt{2\pi r}} \begin{bmatrix} -\sin\frac{\theta}{2} \\ \cos\frac{\theta}{2} \end{bmatrix} + \ldots . \qquad (2.16)$$

where $K_{III}$ is the Mode III stress intensity factor, and the only non-zero

displacement component is:

$$u_3 = \frac{K_{III}}{\mu}\sqrt{\frac{2r}{\pi}}\,sin\,\frac{\theta}{2} + .... \qquad (2.17)$$

It was shown by Irwin (1957a,1957b), by using virtual work arguments, that the concept of stress-intensity factor can be associated with the idea of strain energy release rate, $G$. Indeed, Irwin demonstrated that there exists this relationship:

$$G_I = \frac{\kappa+1}{8\mu} K_I^2 \qquad (2.18)$$

where the subscript in $G$ represents the basic mode.

This equivalence may be generalised to cover the other two basic modes, viz:

$$G_{II} = \frac{\kappa+1}{8\mu} K_{II}^2 \qquad (2.19)$$

$$G_{III} = \frac{1}{2\mu} K_{III}^2 \qquad (2.20)$$

The implication of the equations (2.18) to (2.20) is significant, for if fracture may be characterized by the attainment of a critical strain-energy release rate, then this is equivalent to characterizing fracture by the attainment of a critical stress environment. To the extent linear elasticity is appropriate, all crack tip stress fields are of identical functional form, as seen in (2.10) to (2.17); the loading conditions and geometry of the cracked body being sensed in the crack tip environment through the stress intensity factors. Fracture thus may be characterized by the attainment of critical values of the stress intensity factors ($K_{Ic}$, $K_{IIc}$ or $K_{IIIc}$ for the respective modes) which can be regarded

as material properties and determined experimentally.

### 2.2.4 Sih's Theory - The Strain Energy Density Factor Approach

The formal equivalences in (2.19) and (2.20) were obtained with the assumption that the crack extends in the plane of the original crack, as in Mode I. The physical meaning of Mode II and Mode III crack extension was in fact never really questioned and very few attempts have been made to study the direction of crack propagation in Modes II and III. Yet engineering components are often loaded in ways that produce three-dimensional stress states so that, if cracks are present, the three basic modes of deformation exist together. The direction of crack extension is no longer known *a priori* and the criterion of fracture will not be a simple matter of requiring any one of the basic mode stress intensity factor values reaching a critical value. A theory capable of describing non-coplanar crack extension is thus essential for a more general application of the fracture mechanics concept.

A fracture theory based on the field strength of the strain energy density in the vicinity of the crack front was recently proposed by Sih (1973,1975). This theory uses a direction-sensitive "strain energy density factor", $S$, as the characterizing parameter. The factor $S$ is defined as:

$$S = r\,W \tag{2.21}$$

where $r$ is the radius of a core region centred around a convenient reference point which is made to coincide with the crack front at which fracture initiates, and $W$ is the strain energy density defined in terms of the stress tensor as:

$$W = \frac{1+\nu}{E}\left[\sigma_{11}^2 + \sigma_{22}^2 + \sigma_{33}^2 - \frac{\nu}{1+\nu}(\sigma_{11}+\sigma_{22}+\sigma_{33})^2 + 2(\sigma_{12}^2 + \sigma_{23}^2 + \sigma_{31}^2)\right] \qquad (2.22)$$

With reference to spherical coordinates $(r, \theta, \omega)$, where $-\pi/2 < \omega < \pi/2$ and $-\pi < \theta < \pi$, as shown in Figure 2.4, the rectangular components of the local stresses defined in Figure 2.4, in the vicinity of the crack front may be written as (see, for example, Hartranft & Sih (1977)):

$$\begin{bmatrix} \sigma_{11} \\ \sigma_{22} \\ \sigma_{33} \\ \sigma_{12} \\ \sigma_{13} \\ \sigma_{23} \end{bmatrix} = \frac{K_I}{\sqrt{2\pi r \cos\omega}} \begin{bmatrix} \cos\frac{\theta}{2}\left(1 - \sin\frac{\theta}{2}\sin\frac{3\theta}{2}\right) \\ \cos\frac{\theta}{2}\left(1 + \sin\frac{\theta}{2}\sin\frac{3\theta}{2}\right) \\ 2\nu\cos\frac{\theta}{2} \\ \sin\frac{\theta}{2}\cos\frac{\theta}{2}\cos\frac{3\theta}{2} \\ 0 \\ 0 \end{bmatrix} +$$

$$\frac{K_{II}}{\sqrt{2\pi r \cos\omega}} \begin{bmatrix} -\sin\frac{\theta}{2}\left(2 + \cos\frac{\theta}{2}\cos\frac{3\theta}{2}\right) \\ \sin\frac{\theta}{2}\cos\frac{\theta}{2}\cos\frac{3\theta}{2} \\ -2\nu\sin\frac{\theta}{2} \\ \cos\frac{\theta}{2}\left(1 - \sin\frac{\theta}{2}\sin\frac{3\theta}{2}\right) \\ 0 \\ 0 \end{bmatrix} + \frac{K_{III}}{\sqrt{2\pi r \cos\omega}} \begin{bmatrix} 0 \\ 0 \\ 0 \\ 0 \\ -\sin\frac{\theta}{2} \\ \cos\frac{\theta}{2} \end{bmatrix} \qquad (2.23)$$

By combining these singular solutions for the stress components with the

strain energy density function (2.22), the strain energy density factor can be expressed as a quadratic form in the stress intensity factors $K_I$, $K_{II}$ and $K_{III}$:

$$S = a_{11} K_I^2 + 2 a_{12} K_I K_{II} + a_{22} K_{II}^2 + a_{33} K_{III}^2 \qquad (2.24)$$

where:

$$a_{11} = \frac{1}{16 \pi \mu} \frac{(3 - 4\nu - \cos \theta)(1 + \cos \theta)}{\cos \omega} \qquad (2.25a)$$

$$a_{12} = \frac{1}{16 \pi \mu} \frac{(2 \sin \theta)(\cos \theta - 1 + 2\nu)}{\cos \omega} \qquad (2.25b)$$

$$a_{22} = \frac{1}{16 \pi \mu} \frac{4(1 - \nu)(1 - \cos \theta) + (3 \cos \theta - 1)(1 + \cos \theta)}{\cos \omega} \qquad (2.25c)$$

$$a_{33} = \frac{1}{4 \pi \mu \cos \omega} \qquad (2.25d)$$

The fundamental hypotheses made in this theory may then be stated as:

1. Crack growth is directed along the line from the centre of the spherical core to the point on the spherical surface with the minimum strain energy density factor, $S_{min}$.
2. Crack extension occurs when $S_{min}$ reaches the maximum critical value $S_{cr}$ which the material can tolerate.

The values of $(\theta_o, \omega_o)$ corresponding to $S_{min}$ are obtained by taking:

$$\frac{\partial S}{\partial \theta} = 0 \quad ; \quad \frac{\partial S}{\partial \omega} = 0 \qquad (2.26)$$

with the second derivatives of $S$ satisfying the conditions:

$$\left(\frac{\partial^2 S}{\partial\theta\,\partial\omega}\right)^2 - \frac{\partial^2 S}{\partial\theta^2}\frac{\partial^2 S}{\partial\omega^2} < 0 \quad ; \quad \frac{\partial^2 S}{\partial\theta^2} > 0 \quad \text{and} \quad \frac{\partial^2 S}{\partial\omega^2} > 0 \qquad (2.27)$$

i.e. mathematical conditions for $S(\theta,\omega)$ to be a minimum.

The critical value of $S$ at incipient fracture, $S_{cr}$, may be regarded as a crack extension force which should be independent of loading conditions and crack configuration. It can be used, subject to experimental verification, as a material constant that serves as an indication of the fracture toughness of the material.

This strain energy density factor approach (or so-called $S$-theory) seems capable of predicting the critical load and direction of crack growth even under mixed-mode conditions. As a theory, it is still in its early days and a great deal more experiments have yet to be carried out to test the soundness of the hypotheses. The relatively few experimental results that are in the literature do, however, show good agreement with the theoretical predictions from this theory (see, for example, Sih (1973), Sih (1978), Barr et al (1978)).

The $S$-theory will not be considered further. In what follows, attention is confined only to the opening mode (Mode I) failure with the stress intensity factor approach being used throughout.

## 2.3 FRACTURE MECHANICS APPROACH TO FATIGUE

The fracture mechanics approach to fatigue analysis is concerned only with the crack growth stage, the presence of initial defects in the structural component being thus presumed. The primary task is to characterize the kinetics of fatigue crack growth in terms of an appropriate mechanical crack driving force, and the estimation of the

service life and/or inspection intervals under projected severe loading and environmental conditions. As crack extension is most likely to proceed from the highly stressed region at the crack front, it is therefore most appropriate to characterize the mechanical crack driving force in terms of the crack front stress-intensity factor $K_I$.

Fatigue crack growth can also be influenced by many other factors such as cyclic load frequency, load history, metallurgical variables and environment. Whilst it is ideally desirable to characterize the crack growth behaviour in terms of all these relevant variables, say, of the form:

$$\frac{dl}{dN} = F(K_I, \text{material}, \text{history}, \text{environment}, \text{etc.}) \qquad (2.28)$$

where $l$ is some characteristic measure of the crack size,

$N$ is the number of load cycles, and

$F$ is an empirically determined function.

such a complete characterization is not currently feasible. But insofar as the kinetic data are to be obtained for (2.28) under the restricted conditions, these conditions have to be consistent with the service loading and environment.

### 2.3.1 Paris' Crack-Propagation Law

Several fatigue crack propagation laws of the form of (2.28) have been proposed over the years, but perhaps that which is most widely used is the so-called Paris' Law (Paris et al (1961), Paris & Erdogan (1963)). Paris proposed the following power-law representation for the empirical data obtained for different materials, the material being characterized in terms of its crack growth rate as a function of the

cyclic change in the crack-front stress intensity factor:

$$\frac{dl}{dN} = C\ (\Delta K_I)^m \tag{2.29}$$

where $C$ and $m$ are empirically determined material constants, and:

$$\Delta K_I = K_{I_{max}} - K_{I_{min}} \tag{2.30}$$

In (2.30), $K_{I_{max}}$ and $K_{I_{min}}$ are the maximum and minimum crack-front stress intensity factors, respectively, in a load cycle.

A double-logarithmic plot of $dl/dN$ versus $\Delta K_I$ would be a straight line according to (2.29). But typical fatigue growth rate data in practice are generally in the form of sigmoidal curves (Figure 2.5). Thus, (2.29) is valid only within a certain range of $\Delta K_I$. At low values, crack propagation is extremely slow and experiments have shown that there exists a lower threshold value of $\Delta K_I$ below which the crack remains dormant. Also, when the value of $K_{I_{max}}$ approaches the critical value $K_{Ic}$, the crack growth rate predicted by (2.29) can be far too low.

Although Paris' Law implies that the rate of crack growth is independent of these and some other factors mentioned earlier, the simplicity of the formula does not invalidate its use in engineering design. In fact, despite its short-comings, this propagation formula has been very extensively applied to a wide range of practical problems with much success.

### 2.3.2 Alternative Crack-Growth Formulae

Various attempts have been made to obtain a generalised crack growth formula which incorporates the effects of all the possible

variables, but they have not been met with complete success. The experimental results on fatigue crack growth rates obtained by Broek & Schijve (1963) and Erdogan (1967) showed a dependence on the cyclic load ratio, $K_{I_{min}}/K_{I_{max}}$, which led them to write the following crack-growth formula:

$$\frac{dl}{dN} = C\ \Delta K_I\ K_{I_{max}}^2 \tag{2.31}$$

A more general equation was used by Walker (1970), viz:

$$\frac{dl}{dN} = C\ (\Delta K_I)^{m_1}\ K_{I_{max}}^{m_2} \tag{2.32}$$

where $m_1$ and $m_2$ are again material constants, to account for the effect of the load ratio, which he further modified and presented in the form of an "effective stress".

Forman et al (1967) argued that when $K_{I_{max}}$ reaches the value of $K_{Ic}$, $dl/dN$ should become infinite and they suggested:

$$\frac{dl}{dN} = \frac{C\ (\Delta K_I)^m}{[1 - K_{I_{min}}/K_{I_{max}}]\ K_{Ic} - \Delta K_I} \tag{2.33}$$

To account for the lower threshold value of the stress intensity factor range, $\Delta K_{It}$, Klesnil & Lucas (1972) proposed a simple modification of Paris' formula (2.29) when this threshold value is significant:

$$\frac{dl}{dN} = C\left[(\Delta K_I)^m - (\Delta K_{It})^m\right] \tag{2.34}$$

Other attempts to incorporate both the threshold and load ratio effects include those of Priddle (1976) and Branco (1976).

Even more sophisticated expressions for fatigue crack growth

which could take into account crack closure due to residual stresses (see, for example, Elbers (1971), Duggan (1977)), as well as other effects, have been suggested. A complete treatment of these and other more sophisticated formulae is beyond the scope of the present review. Suffice to note that none of the formulae presented here (or elsewhere) have a general applicability. Each of them may be found to be reasonably satisfactory in a limited region or for particular sets of data.

## 2.4 LIMITATIONS OF LEFM

According to the elastic field solutions discussed in Section 2.2.3, infinitely high stresses exist at the crack front. This, of course, is inconsistent with the behaviour of real materials (especially metals) which tend to exhibit a yield stress beyond which they deform plastically. There is thus always a region around the crack front in a metal where plastic flow occurs. This fact, however, does not invalidate the methods of LEFM provided the extent of plasticity is small compared with the characteristic geometric dimension of the crack. In practice, this is often true, for as the elastic field solutions predict, the high stresses decrease rapidly away from the crack border.

Modifications of the LEFM analysis have been suggested to account for the size of the small plastic zone and several procedures have been proposed. They basically involve the "repositioning" of the crack border. Irwin (1960) argued that the effect of the plastic zone is to make the crack behave as if it were longer than its physical size. He suggested the effective extra crack length (or the "notional" elastic crack length) being equal to the radius, $r_p$, of an idealized circular plastic zone ahead of the crack. For plane stress conditions, it was estimated that:

$$r_p = \frac{1}{2\pi} \left(\frac{K_I}{\sigma_{ys}}\right)^2 \tag{2.35}$$

where $\sigma_{ys}$ is the yield stress in uniaxial tension. For plane strain conditions, the correction factor becomes:

$$r_p = \frac{1}{6\pi} \left(\frac{K_I}{\sigma_{ys}}\right)^2 \tag{2.36}$$

Notable among the other plastic zone corrections proposed is the one by Dugdale (1960) in which the concept of the effective crack being larger than the physical crack is again considered. The spread of plasticity ahead of the crack, $d_y$, is, however, obtained by a different mathematical approach, and at relatively low applied stress levels, the estimated plastic zone size under plane stress conditions is:

$$d_y = \frac{\pi}{8} \left(\frac{K_I}{\sigma_{ys}}\right)^2 \tag{2.37}$$

This is almost identical to Irwin's approximation where $d_y = 2r_p$, but at high applied stress levels, Irwin's estimate of the plastic zone size differs significantly from that obtained by the Dugdale approach.

The application of these plastic zone corrections becomes questionable if the spread of plasticity is extensive relative to the crack size. An elasto-plastic analysis would have to be employed then, this being beyond the scope of the present study. The current testing standard for the determination of $K_{Ic}$ (ASTM E399-74) requires that the thickness and the uncracked ligament of the test specimen should both exceed 2.5 $(K_{Ic}/\sigma_{ys})^2$. This means that, with Irwin's approximation (2.36), the radius of the plastic zone, $r_p$, may not exceed 2% of the specimen thickness.

## 2.5 FINAL REMARKS

Fracture prevention criteria can thus be derived from fracture mechanics principles where traditional engineering design methods break down. To apply these principles successfully, information and data in three areas are required: material properties, nature of defects in the structure or component, and the stress state. In addition to the conventional mechanical properties, such as Young's modulus and Poisson's ratio, one of the fracture mechanics material parameters required is the fracture toughness of the material. This is expressed in terms of the critical value of the stress intensity factor, $K_{Ic}$, and, as mentioned in the last section, standard experimental methods for its determination have already been developed (ASTM E399-74). Where the problem involves cyclic loading, the appropriate information concerning the fatigue crack growth rate characteristics of the material (such as $C$ and $m$ in Paris' Law (2.29)) is also a prerequisite.

The detection, description and dimensional measurement of the defects is essential as the location, size, shape, orientation and distribution of these defects affect the stress state of the component. Such information is therefore vital to all considerations and computations of the critical or allowable stresses which can be applied to avoid fast fracture or for slow crack growth. To this end, non-destructive inspection techniques have been developed. They include ultrasonic and radiographic techniques as well as magnetic particle and dye penetrant methods.

In LEFM, the stress state in the vicinity of the crack is characterized in terms of the stress intensity factor. Indeed, the evaluation of the stress intensity factor for the crack problem under consideration is an essential part of the solution. A number of methods for the determination of the stress intensity factor are available. In

cases where the geometry is relatively simple, analytical tools such as complex analytical methods and integral transform methods may be used. Experimental methods are also feasible in some simple cases, but the value of the stress intensity factor has to be obtained indirectly through a measurable quantity such as strain or compliance. In practice, the physical geometry and the boundary conditions of crack problems are usually complicated, so numerical methods have to be employed. Stress intensity factor solutions have been obtained numerically by methods such as Boundary Collocation, Conformal Mapping, the Alternating Method, Finite Element Methods, and, not least of all, the Boundary Integral Equation method. Discussions on these numerical methods and the stress intensity factor solutions obtained therefrom are very well documented in the literature (see, for example, Sih (1973), Cartwright & Rooke (1975), Luxmore & Owen (1978)), except perhaps for the relatively new Boundary Integral Equation method. Indeed, the determination of stress intensity factors by this numerical method forms the major part of the present study.

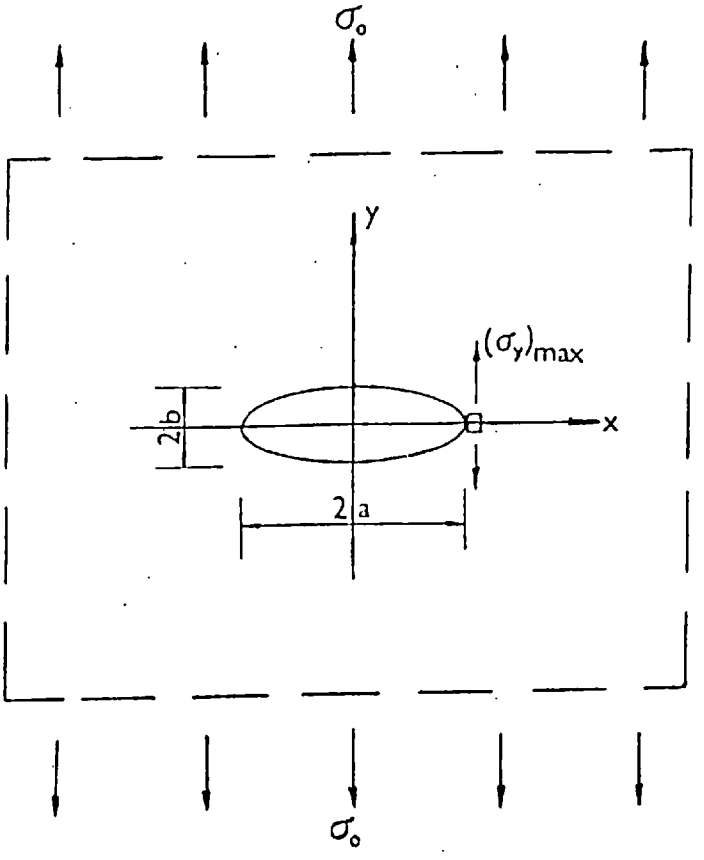
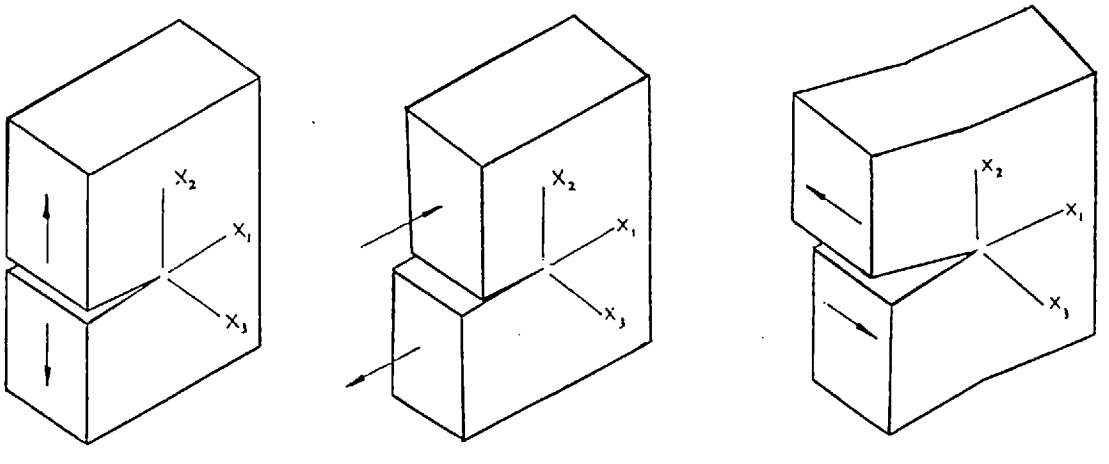



Figure 2.1: Plate with elliptical hole under uniform tension




Mode I Mode II Mode III

Figure 2.2: Basic modes of crack deformation

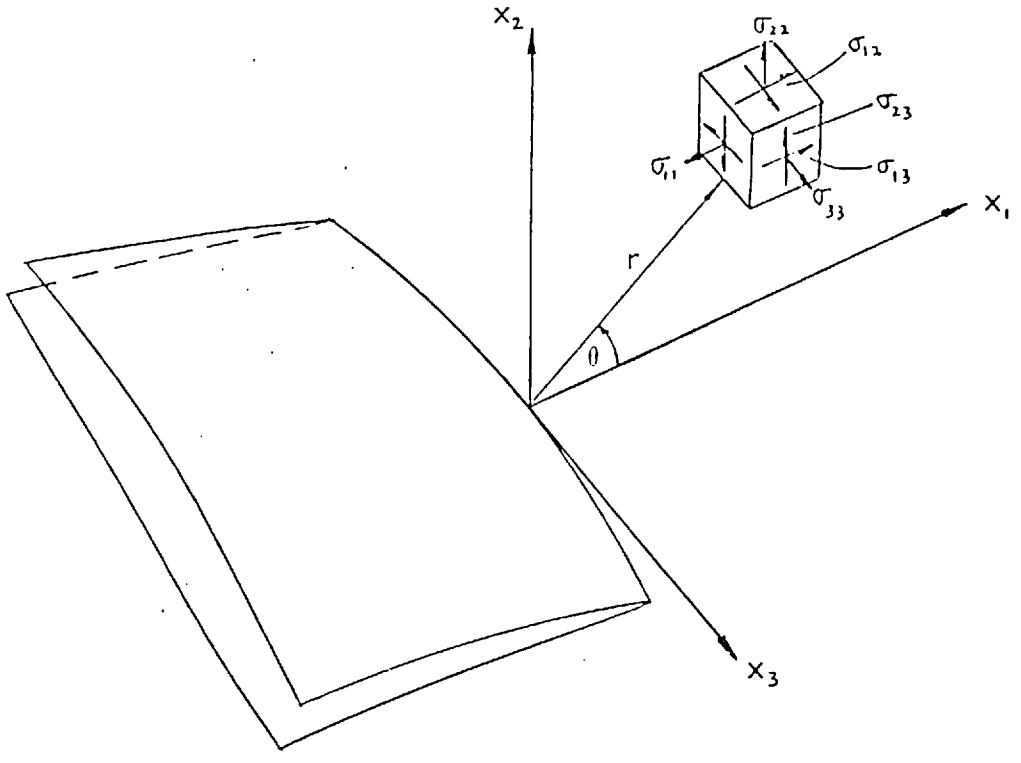



Figure 2.3: Coordinate system of crack-border stress components

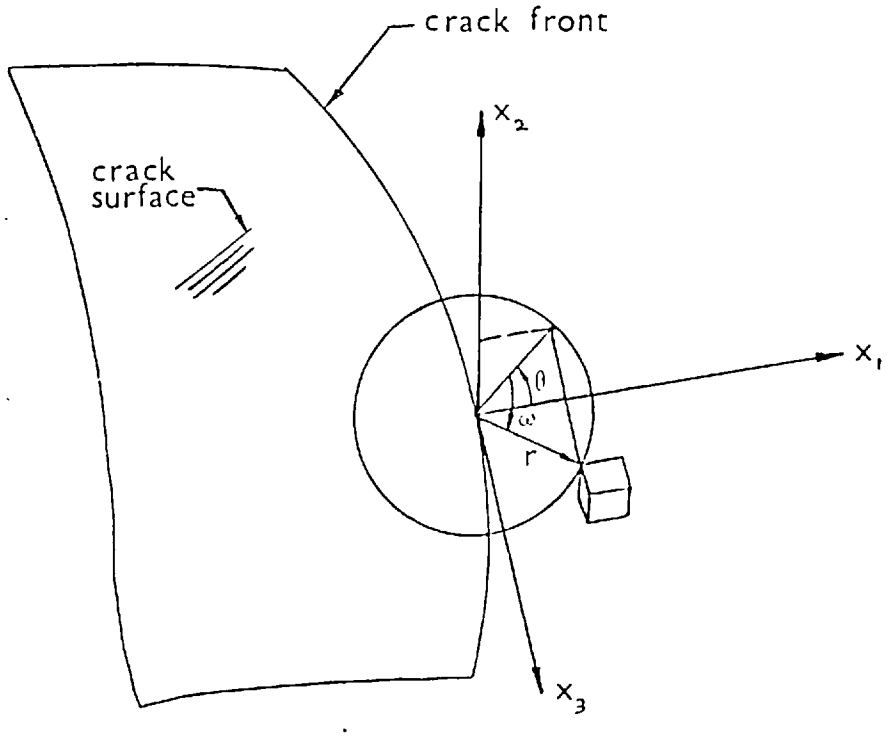



Figure 2.4: Local spherical coordinate system at crack front

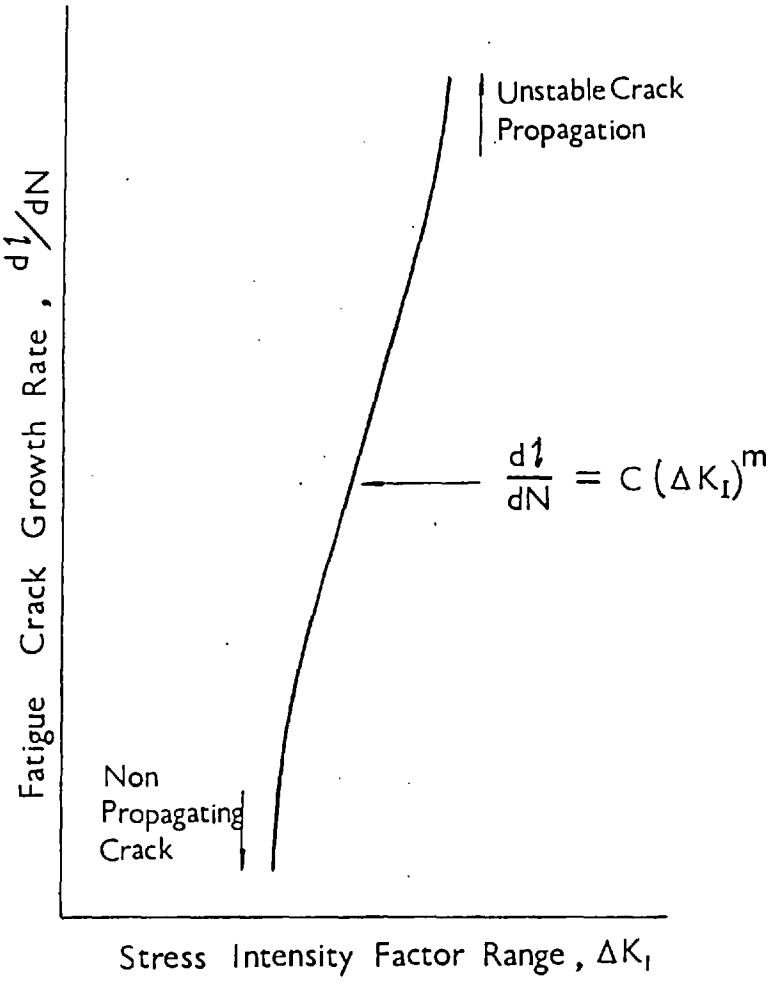



Figure 2.5: Log-log plot of fatigue crack growth rate versus stress intensity factor range

# CHAPTER 3

# FORMULATION OF THE BOUNDARY INTEGRAL EQUATION

Although, as an efficient numerical tool for stress analysis, the boundary integral equation method is relatively new, the mathematical basis is classical, and analogous to the methods developed in potential theory (see, for example, Jaswon & Symm (1977), Cruse (1977)). The analytical formulation involves the transformation of the governing field equations applicable to the whole domain into an integral equation over the boundary. Fundamental to this formulation is (a) the existence of a solution to the governing partial differential equations of elasticity for a point load, and (b) a reciprocal theorem relating two functions (such as displacements and tractions) which are continuous and possess continuous first derivatives. In elastostatics, the reciprocal theorem is provided by the well-known Betti's theorem. The requirements for the functions in (b) do not present difficulties as the governing partial differential equations in elastostatics are elliptic in nature, thus ensuring continuity of the displacements and tractions. In this chapter, a review of the governing equations in elastostatics will be presented and the fundamental solution of the three-dimensional problem will be obtained. This will be followed by the proof of the reciprocal theorem, before the integral equations are derived. For compactness, the usual Cartesian tensor notation is used, with implied summation on repeated indices and partial differentiation being denoted by the comma-index notation.

## 3.1 REVIEW OF THE GOVERNING EQUATIONS OF ELASTICITY

The equations of equilibrium for an elastic continuum, $R$, written in tensor notation is:

$$\sigma_{ij,j} + X_i = 0 \tag{3.1}$$

where $X_i$ is the body force vector.

In linear elastic theory, the strain-displacement relations are:

$$e_{ij} = \tfrac{1}{2} (u_{i,j} + u_{j,i}) \tag{3.2}$$

and Hooke's Law for a homogeneous isotropic material is:

$$\sigma_{ij} = \lambda\, e_{kk}\, \delta_{ij} + 2\,\mu\, e_{ij} \tag{3.3}$$

In (3.2) and (3.3), $e_{ij}$ is the strain tensor; $\lambda = (2\mu\nu)/(1-2\nu)$ is the Lamé constant; and $\delta_{ij}$ is the Kronecker Delta where:

$$\delta_{ij} = \begin{cases} 0 & i \neq j \\ 1 & i = j \end{cases} \tag{3.4}$$

Substitution of (3.3) into (3.1) and using (3.2) results in Navier's equations of equilibrium in terms of displacements:

$$\mu\, u_{i,jj} + (\lambda + \mu)\, u_{j,ji} = - X_i \tag{3.5}$$

The solution to (3.5) must satisfy the appropriate boundary conditions for the displacements and tractions on the surface $S$ (Figure 3.1), given respectively as:

$$u_i(x) = g_i(x) \qquad \text{on} \qquad S_u \tag{3.6}$$

and:

$$t_i(\underset{\sim}{x}) = \sigma_{ij}\, n_j = h_i(\underset{\sim}{x}) \qquad \text{on} \qquad S_t \tag{3.7}$$

where $g_i(\underset{\sim}{x})$ and $h_i(\underset{\sim}{x})$ are prescribed functions, and $n_j$ is the unit outward normal to the surface $S$.

Substitution of (3.2) and (3.3) into (3.7) results in:

$$[\lambda\, u_{k,k}\, \delta_{ij} + \mu\, (u_{i,j} + u_{j,i})]\, n_j = h_i(\underset{\sim}{x}) \tag{3.8}$$

The boundary conditions for a well-posed boundary value problem are, thus, that either $u_i$, or a combination of the first derivatives of $u_i$ are prescribed over $S$.

## 3.2 DERIVATION OF THE INTEGRAL EQUATIONS

### 3.2.1 The Fundamental Solution

The general solution of the non-homogeneous Navier's equation (3.5) can be obtained by adding a particular integral of (3.5) to the complementary function. By an extension of the method of singularities in the theory of Newtonian potentials, Lord Kelvin obtained a particular integral of (3.5) (see, for example, Love (1944)). The particular integral is:

$$u_i(\underset{\sim}{x}) = A \int_R \left\{ B\, \frac{X_i(\zeta)}{r} - (\bar{x}_j - \zeta_j)\, X_j(\zeta)\, \left(\frac{1}{r}\right)_{,i} \right\} dV \tag{3.9}$$

where: $$r = [(\bar{x}_i - \zeta_i)(\bar{x}_i - \zeta_i)]^{\frac{1}{2}} \tag{3.10}$$

$$A = \frac{\lambda + \mu}{8\, \pi\, \mu\, (\lambda + 2\mu)} \quad , \quad B = \frac{\lambda + 3\mu}{\lambda + \mu} \tag{3.11}$$

In (3.9), $r$ is the distance between the field point $q(\underset{\sim}{x})$, with coordinates

$\bar{x}_i$, to the variable point $p(\underset{\sim}{x})$ with coordinates $\zeta_i$. The functions $X_i(\zeta)$ are the components of the body force $X_i$ expressed in terms of the variables of integration $\zeta_i$.

If an idealized case is considered in which a small sphere, $R_\varepsilon$, is isolated in the body with its centre at the point $p(\underset{\sim}{x})$ in which the body force concentrates, the notion of a concentrated load $X_i^0$ acting at the point $p(\underset{\sim}{x})$ is conceived in the limit as $R_\varepsilon \to 0$. This provides the solution to the well-known problem, often referred to as the Kelvin solution, of a point load acting in the interior of an infinite body.

This fundamental solution can also be quite conveniently obtained by using displacement potential functions. It can be easily verified that (3.5) is satisfied when:

$$2\,\mu\,u_i = 2\,(1-\nu)\,G_{i,jj} - G_{j,ji} \tag{3.12}$$

if $G_i$ satisfies the equation:

$$G_{i,jjmm} = \frac{-X_i}{1-\nu} \tag{3.13}$$

The vector $G_i$ is commonly known as the Galerkin vector and the $G_i$ are biharmonic functions if $X_i = 0$. In order to solve a problem in static equilibrium, these functions have to be determined.

If the coordinate axes are chosen so that $X_i^0$ acts at the origin $\zeta_i = 0$ in the $x_i$-direction, the boundary conditions of the problem are thus:

(i) All stresses vanish at infinity;

(ii) The stress singularity is equivalent to a concentrated load of magnitude $|X_i^0|$ in the $x_i$-direction at the origin.

Since body forces are absent, the Galerkin functions for this problem must be biharmonic and their third derivatives should define stresses that vanish at infinity but are singular at the origin. A function which satisfies these conditions is:

$$G_i = B\, r\, e_i \tag{3.14}$$

where $B$ is a constant, and $e_i$ the base vector.

Because of the symmetry of the problem, it is convenient to work in the cylindrical coordinates system $(\overline{r}, \theta, z)$ in which the $z$th-direction and $x_i$-direction are coincident. Thus:

$$G_i = B\, r\, e_i = B\, (z^2 + \overline{r}^2)^{\frac{1}{2}} \tag{3.15}$$

from which:

$$\frac{\partial G_i}{\partial \overline{r}} = \frac{B\, \overline{r}}{r} \tag{3.16a}$$

$$\frac{\partial G_i}{\partial z} = \frac{B\, z}{r} \tag{3.16b}$$

$$\frac{\partial^2 G_i}{\partial \overline{r}^2} = B\, \left(\frac{1}{r} - \frac{\overline{r}^2}{r^3}\right) = B\, \frac{z^2}{r^3} \tag{3.16c}$$

$$\frac{\partial^2 G_i}{\partial z^2} = B\, \left(\frac{1}{r} - \frac{z^2}{r^3}\right) = B\, \frac{\overline{r}^2}{r^3} \tag{3.16d}$$

$$\nabla^2 G_i = \frac{2B}{r} \tag{3.16e}$$

where:

$$\nabla^2 \equiv \frac{\partial^2}{\partial \overline{r}^2} + \frac{1}{\overline{r}} \frac{\partial}{\partial \overline{r}} + \frac{1}{\overline{r}^2} \frac{\partial^2}{\partial \theta^2} + \frac{\partial^2}{\partial z^2}$$

Let $(W_{\overline{r}}, W_\theta, W_z)$ and $(\sigma_{\overline{r}\overline{r}}, \sigma_{\overline{r}\theta}$, etc.) be the physical components of displacements and stresses, respectively, in the cylindrical coordinate

system. Then:

$$W_{\bar{r}} = \frac{B\,\bar{r}\,z}{2\,\mu\,r^3} \tag{3.17a}$$

$$W_\theta = 0 \tag{3.17b}$$

$$W_z = \frac{B}{2\mu}\left[\frac{2\,(1-2\nu)}{r} + \frac{1}{r} + \frac{z^2}{r^3}\right] \tag{3.17c}$$

$$\sigma_{\bar{r}\bar{r}} = B\left[\frac{(1-2\nu)\,z}{r^3} - \frac{3\,r^2\,z}{r^5}\right] \tag{3.18a}$$

$$\sigma_{\theta\theta} = \frac{B\,(1-2\nu)\,z}{r^3} \tag{3.18b}$$

$$\sigma_{zz} = -B\left[\frac{(1-2\nu)\,z}{r^3} + \frac{3\,z^3}{r^5}\right] \tag{3.18c}$$

$$\sigma_{\bar{r}z} = -B\left[\frac{(1-2\nu)\,\bar{r}}{r^3} + \frac{3\,\bar{r}\,z^2}{r^5}\right] \tag{3.18d}$$

$$\sigma_{\bar{r}\theta} = \sigma_{z\theta} = 0 \tag{3.18e}$$

Since the stresses in (3.18) vanish at infinity and are singular at the origin with the correct symmetry, the stress singularity can only be equivalent to that due to a point load. A proper choice of the constant $B$ would thus ensure that (3.14) is indeed the desired solution.

The constant $B$ can be determined by considering a cylinder with a small cavity at its centre at the origin and with bases at $z = \pm a$ (Figure 3.2). The cylinder is in equilibrium, therefore:

$$|X_i^0| = \int_0^\infty 2\,\pi\,\bar{r}\,d\bar{r}\,(-\sigma_{zz})_{z=a} + \int_0^\infty 2\,\pi\,\bar{r}\,d\bar{r}\,(\sigma_{zz})_{z=-a}$$

$$+ \lim_{\bar{r}\to\infty} \int_{-a}^{a} 2\,\pi\,\bar{r}\,dz\,(\sigma_{\bar{r}z}) \tag{3.19}$$

The values of the first and second integrals of (3.19) are the same, and the third integral is zero in the limit. Since $\bar{r}\,d\bar{r} = r\,dr$:

$$|X_i^0| = 2 \int_0^\infty 2\pi r\,dr\,(-\sigma_{zz})_{z=a}$$

$$= 4\pi B \left[(1-2\nu)\,a \int_0^\infty \frac{r}{r^3}\,dr + 3a^3 \int_0^\infty \frac{r}{r^5}\,dr\right]$$

$$= 8\pi(1-\nu)B \tag{3.20}$$

If $|X_i^0|$ is unity, then:

$$B = \frac{1}{8\pi(1-\nu)} \tag{3.21}$$

The function: $$G_i = \frac{1}{8\pi(1-\nu)}\,r(p,q)\,e_i \tag{3.22}$$

is thus the particular Galerkin vector solution of (3.5).

The particular displacement solution is obtained by carrying out the indicated operations in (3.12), as shown in Appendix A. The results is:

$$u_i(p,q) = \frac{1}{16\pi\mu(1-\nu)} \left(\frac{1}{r}\right) [(3-4\nu)\,\delta_{ij} + r_{,i}\,r_{,j}]\,e_j \tag{3.23}$$

where the derivatives of $r(p,q)$ are with respect to the coordinates of the field point $q(x)$, i.e.

$$r_{,i} = \frac{\partial r}{\partial \bar{x}_i} = \frac{1}{r}(\bar{x}_i - \zeta_i) = -\frac{\partial r}{\partial \zeta_i} \tag{3.24}$$

The tractions on an arbitrary surface around the point $p(x)$

can be obtained by differentiation at $p(x)$, using (3.8), of the displacement solution (see Appendix A). The result is:

$$t_i(p,q) = -\frac{1}{8\pi(1-\nu)}\left(\frac{1}{r^2}\right)\left\{\frac{\partial r}{\partial n}\left[(1-2\nu)\,\delta_{ij} + 3\,r_{,i}\,r_{,j}\right]\right.$$

$$\left. -(1-2\nu)\,(n_j\,r_{,i} - n_i\,r_{,j})\right\}\,e_j \qquad (3.25)$$

where the normal is taken at $q(x)$ and:

$$\frac{\partial r}{\partial n} = \frac{\partial r}{\partial \bar{x}_i}\,n_i = \frac{1}{r}\,(\bar{x}_i - \zeta_i)\,n_i \qquad (3.26)$$

If $U_{ij}(p,q)$ and $T_{ij}(p,q)$ are the $i$th components of the displacement and traction vectors at point $q(x)$ corresponding to a unit point load in the $j$th-direction at $p(x)$, then, from (3.23) and (3.25):

$$u_i(p,q) = U_{ij}(p,q)\,e_j \qquad (3.27)$$

$$t_i(p,q) = T_{ij}(p,q)\,e_j \qquad (3.28)$$

and:

$$U_{ij}(p,q) = \frac{1}{16\pi\mu(1-\nu)}\left(\frac{1}{r}\right)\left[(3-4\nu)\,\delta_{ij} + r_{,i}\,r_{,j}\right] \qquad (3.29)$$

$$T_{ij}(p,q) = -\frac{1}{8\pi(1-\nu)}\left(\frac{1}{r^2}\right)\left\{\frac{\partial r}{\partial n}\left[(1-2\nu)\,\delta_{ij} + 3\,r_{,i}\,r_{,j}\right]\right.$$

$$\left. -(1-2\nu)\,(n_j\,r_{,i} - n_i\,r_{,j})\right\} \qquad (3.30)$$

### 3.2.2 Betti's Reciprocal Work Theorem

The boundary integral equation for the complementary function may be derived from the Divergence Theorem which may be stated as:

$$\int_R a_{i,i}\, dV = \int_S a_i\, n_i\, dS \tag{3.31}$$

where the vector field $a_i$ is continuously differentiable in $R$ and on its surface $S$.

Consider two equilibrium states of an elastic body: one with displacements $u_i$ due to the body forces $X_i$ and surface tractions $t_i$, and the other with displacements $u_i'$ due to body forces $X_i'$ and surface tractions $t_i'$. Using (3.2) and the Divergence Theorem (3.31), the work that would be done by the unprimed forces $X_i$, $t_i$, if they acted through the primed displacements $u_i'$ can be written as:

$$\begin{aligned}
&\int_S t_i\, u_i'\, dS + \int_R X_i\, u_i'\, dV \\
&= \int_S \sigma_{ij}\, n_j\, u_i'\, dS - \int_R \sigma_{ij,j}\, u_i'\, dV \\
&= \int_R (\sigma_{ij}\, u_i')_{,j}\, dV - \int_R \sigma_{ij,j}\, u_i'\, dV
\end{aligned} \tag{3.32}$$

Carrying out the indicated differentiation in (3.32), and using Hooke's Law (3.4):

$$\begin{aligned}
&\int_S t_i\, u_i'\, dS + \int_R X_i\, u_i'\, dV \\
&= \int_R \sigma_{ij}\, u_{i,j}'\, dV
\end{aligned}$$

$$= \int_R (\lambda\, \delta_{ij}\, e_{kk} + 2\,\mu\, e_{ij})\, u'_{i,j}\, dV$$

$$= \int_R [\lambda\, e_{kk}\, u'_{i,i} + \mu\, (u_{i,j} + u_{j,i})\, u'_{i,j}]\, dV$$

$$= \int_R [\lambda\, e_{kk}\, e'_{kk} + \mu\, u_{i,j}\, u'_{i,j} + \mu\, u_{j,i}\, u'_{i,j}]\, dV \qquad (3.33)$$

Since: $\mu\, u_{j,i}\, u'_{i,j} = \mu\, u_{i,j}\, u'_{j,i} = \mu\, u'_{j,i}\, u_{i,j}$

the integral (3.33) and hence the original expression is symmetric with respect to the primed and unprimed states. Thus:

$$\int_S t_i\, u'_i\, dS + \int_R X_i\, u'_i\, dV = \int_S t'_i\, u_i\, dS + \int_R X'_i\, u_i\, dV \qquad (3.34)$$

which, in the absence of body forces, becomes:

$$\int_S t_i\, u'_i\, dS = \int_S t'_i\, u_i\, dS \qquad (3.35)$$

This result is the well-known Betti's Reciprocal Theorem.

In what follows, only the case of zero body force will be treated.

### 3.2.3 Integral Equations for Displacements and Stresses at Interior Points

With no loss of generality, assume in (3.35) that one stress state is unknown and regular, and the other stress state corresponds to the fundamental solution to Navier's equation, (3.23) and (3.25). Consider the domain $(R - R_\varepsilon)$ where $R_\varepsilon$ is the part of $R$ with surface $S_\varepsilon$,

contained within a sphere with centre at $p(x)$ and radius $\varepsilon$ (Figure 3.3). Writing (3.35) for this region, viz:

$$\int_S t_i\, u_i^*\, dS + \int_{S_\varepsilon} t_i\, u_i^*\, dS = \int_S t_i^*\, u_i\, dS + \int_{S_\varepsilon} t_i^*\, u_i\, dS \qquad (3.36)$$

where $u_i^*$ and $t_i^*$ come from (3.23) and (3.25).

The reason $p(x) \in R$ has to be isolated is because of the singular nature of the fundamental solution at $p(x)$. The limits for (3.36) as $\varepsilon \to 0$ is now taken in the usual way as in potential theory. Since $u_i^*$ is singular, $1/r$, the integral $\int_{S_\varepsilon} t_i u_i^* dS$ can be written as $\int_{S_\varepsilon} (f(Q)/\varepsilon)\, dS(Q)$ where $f(Q)$ is continuous. Further, it may be written as:

$$\int_{S_\varepsilon} \frac{f(Q)}{\varepsilon}\, dS(Q) = \int_{S_\varepsilon} \frac{f(p)}{\varepsilon}\, dS + \int_{S_\varepsilon} \frac{f(Q) - f(p)}{\varepsilon}\, dS$$

$$= \quad I_1 \quad + \quad I_2 \qquad (3.37)$$

Since the area of the sphere is $4\pi\varepsilon^2$:

$$\lim_{\varepsilon\to 0} I_1 = \lim_{\varepsilon\to 0} \frac{f(p)}{\varepsilon}\, 4\pi\varepsilon^2 = 0 \qquad (3.38)$$

Also, since a surface integral does not exceed the area of the surface times the maximum value of the integral, we have:

$$|I_2| \leqslant 4\pi\varepsilon^2 \frac{\max |f(Q) - f(p)|}{\varepsilon} \leqslant 4\pi \max |f(Q) - f(p)| \qquad (3.39)$$

and since $f$ is continuous. $|I_2|$ tends to zero as $\varepsilon \to 0$, i.e.

$$\lim_{\varepsilon\to 0} \int_{S_\varepsilon} t_i\, u_i^*\, dS = 0 \qquad (3.40)$$

The integral $\int_{S_\varepsilon} t_i^* u_i \, dS$ may similarly be written as:

$$\int_{S_\varepsilon} u_i \, t_i^* \, dS = \int_{S_\varepsilon} [u_i(Q) - u_i(p)] \, t_i^* \, dS + u_i(p) \int_{S_\varepsilon} t_i^* \, dS$$

$$= J_1 + J_2 \tag{3.41}$$

Since displacements are continuous at $p(x)$, by similar arguments as in (3.39), $J_1$ vanishes as $\varepsilon \to 0$. But:

$$\lim_{\varepsilon \to 0} \int_{S_\varepsilon} t_i^* \, dS = \delta_{ij} \, e_j \tag{3.42}$$

Thus: $$\lim_{\varepsilon \to 0} \int_{S_\varepsilon} u_i \, t_i^* \, dS = u_i(p) \, \delta_{ij} \, e_j = u_j(p) \, e_j \tag{3.43}$$

Substituting these results into (3.36) and taking the limit as $\varepsilon \to 0$ results in:

$$\int_S t_i \, u_i^* \, dS = u_j(p) \, e_j + \int_S u_i \, t_i^* \, dS \tag{3.44}$$

Taking each of the $e_j$ terms as independent and making the substitutions $u_i^* = U_{ij} \, e_j$, $t_i^* = T_{ij} \, e_j$, the following integral equations are obtained:

$$u_i(p) = \int_S t_j(Q) \, U_{ij}(p,Q) \, dS(Q) - \int_S u_j(Q) \, T_{ij}(p,Q) \, dS(Q) \tag{3.45}$$

This result is known as Somigliana's identity for displacements and is a continuous representation for the displacements at any interior point $p(x)$ in $R$.

To obtain the stress state at interior points, Hooke's Law is again invoked following the differentiation of (3.45) with respect to the

coordinates at $p(x)$, viz:

$$\sigma_{ij}(p) = \lambda\, \delta_{ij}\, u_{k,k} + \mu\, (u_{i,j} + u_{j,i}) \tag{3.46}$$

Substituting (3.45) into (3.46) and operating (3.46) as indicated, thus:

$$\sigma_{ij}(p) = \int_S t_k\, [\lambda\, \delta_{ij}\, U_{mk,m} + \mu\, (U_{ik,j} + U_{jk,i})]\, dS$$

$$- \int_S u_k\, [\lambda\, \delta_{ij}\, T_{mk,m} + \mu\, (T_{ik,j} + T_{jk,i})]\, dS \tag{3.47}$$

which may be abbreviated to the form:

$$\sigma_{ij}(p) = \int_S t_k(Q)\, D_{kij}(p,Q)\, dS(Q) - \int_S u_k(Q)\, S_{kij}(p,Q)\, dS(Q) \tag{3.48}$$

The third order tensors $D_{kij}$ and $S_{kij}$ may be obtained by utilizing the identity (3.24) and following the operations under the parenthesis signs in (3.47):

$$D_{kij}(p,Q) = \frac{1-2\nu}{8\,\pi\,(1-\nu)} \left(\frac{1}{r^2}\right) [\delta_{ki}\, r_{,j} + \delta_{kj}\, r_{,i}$$

$$- \delta_{ij}\, r_{,k} + \frac{3}{(1-2\nu)}\, r_{,i}\, r_{,j}\, r_{,k}] \tag{3.49}$$

$$S_{kij}(p,Q) = \frac{\mu}{4\,\pi\,(1-\nu)} \left(\frac{1}{r^3}\right) \{3\, \frac{\partial r}{\partial n}\, [(1-2\nu)\, \delta_{ij}\, r_{,k}$$

$$+ \nu\, (\delta_{ki}\, r_{,j} + \delta_{kj}\, r_{,i}) - 5\, r_{,i}\, r_{,j}\, r_{,k}]$$

$$+ n_i\, [3\, \nu\, r_{,j}\, r_{,k} + (1-2\nu)\, \delta_{kj}]$$

$$+ n_j \left[3 \nu r_{,i} r_{,k} + (1-2\nu) \delta_{ki}\right]$$

$$+ n_k \left[3 (1-2\nu) r_{,i} r_{,j} - (1-4\nu) \delta_{ij}\right]\} \qquad (3.50)$$

In (3.49) and (3.50), all implied differentiation is again with respect to the coordinates at the field point $Q(\underset{\sim}{x})$ and the normal evaluated there too.

### 3.2.4 The Boundary Integral Equation

The boundary integral equation is obtained by taking the point $p(\underset{\sim}{x})$ to a boundary point $P(\underset{\sim}{x})$. Let $P(\underset{\sim}{x})$ be a point on a smooth surface, or at the intersection of several smooth surfaces, i.e. at an edge or corner, on the boundary $S$ of $R$ (Figure 3.4). $R_\varepsilon$ is again taken as the part of $R$ contained within a sphere of radius $\varepsilon$ centred at $P(\underset{\sim}{x})$ and Betti's theorem again written for the domain $(R - R_\varepsilon)$ as in Section 3.2.3, with the limit as $\varepsilon \to 0$ examined, i.e.

$$\lim_{\varepsilon \to 0} \int_{S-S_\varepsilon+S'_\varepsilon} \left\{t_j(Q)\, U_{ij}(P,Q)\, dS(Q) - u_j(Q)\, T_{ij}(P,Q)\right\} dS(Q) = 0 \qquad (3.51)$$

By the limiting procedures as described in Section 3.2.3, it can be easily seen that:

$$\lim_{\varepsilon \to 0} \int_{S-S_\varepsilon+S'_\varepsilon} t_j(Q)\, U_{ij}(P,Q)\, dS(Q) = \int_S t_j(Q)\, U_{ij}(P,Q)\, dS(Q) \qquad (3.52)$$

The second integral of (3.51) can be written as:

$$\int_{S-S_\varepsilon+S'_\varepsilon} u_j(Q)\, T_{ij}(P,Q)\, dS = \int_{S-S_\varepsilon+S'_\varepsilon} \left[u_j(Q) - u_j(P)\right] T_{ij}(P,Q)\, dS$$

$$+ \int_{S-S_\varepsilon+S'_\varepsilon} u_j(P)\, T_{ij}(P,Q)\, dS \qquad (3.53)$$

and provided that the surface at $P(x)$ or the surfaces that intersect at $P(x)$ are smooth, by the argument developed in (3.39):

$$\lim_{\varepsilon \to 0} \int_{S'_\varepsilon - S_\varepsilon} [u_j(Q) - u_j(P)]\, T_{ij}(P,Q)\, dS = 0 \tag{3.54}$$

Thus:
$$\lim_{\varepsilon \to 0} \int_{S'_\varepsilon - S_\varepsilon} u_j(P)\, T_{ij}(P,Q)\, dS = C_{ij}(P)\, u_j(P) \tag{3.55}$$

where:
$$C_{ij}(P) = \lim_{\varepsilon \to 0} \int_{S'_\varepsilon - S_\varepsilon} T_{ij}(P,Q)\, dS(Q) \tag{3.56}$$

The boundary integral equation is:

$$C_{ij}(P)\, u_j(P) + \int_S u_j(Q)\, T_{ij}(P,Q)\, dS = \int_S t_j(Q)\, U_{ij}(P,Q)\, dS \tag{3.57}$$

The integral on the left hand side of (3.57) only exists in the sense of the Cauchy principal value and is to be interpreted as such.

If the tangent plane at $P(x)$ is continuous, it can be shown (see Appendix B) that:

$$C_{ij}(P) = \tfrac{1}{2}\, \delta_{ij} \tag{3.58}$$

(3.57) is thus the boundary constraint equation relating surface tractions to surface displacements for an elastic body.

## 3.3 FINAL REMARKS

The boundary integral equation (3.57) has been formed in terms of the physical tractions and displacements on the boundary of the elastic domain. Where tractions are prescribed on the boundary, the corresponding displacements are the unknowns for which the integral equation is to be solved for, and vice versa. Once (3.57) has been solved, the displacements,

tractions and stress tensor will then be known everywhere on the boundary. From these data, the displacements and stresses at any specified interior points may be obtained from (3.45) and (3.48).

The formulation described above is often known as the direct formulation. Other methods of integral formulation do exist for two- and three-dimensional problems and they are broadly classified as the semi-direct and the indirect methods. In the semi-direct method, the integral equations are formed by using unknown functions which are related to the stress functions, from which the displacements and tractions are obtained on solution of the integral equations. In the indirect formulation, the integral equations are formed in terms of fictitious density functions which have no physical significance but once obtained will provide the values of stresses and displacements. Semi-direct methods have been developed and implemented by several authors such as Jaswon & Symm (1977) for elastic problems and by Mendelson (1973) for elastic as well as elasto-plastic problems. The indirect method was originally developed by Kupradze (1963) and has been simplified and applied to elastic problems by Banerjee (1976), Altiero & Sikarskie (1975) and Butterfield & Tomlin (1972), among others.

Finally, questions pertaining to the existence and uniqueness of solution for the boundary-value problem formulated in the manner described may arise. Equation (3.57) is strongly suggestive of the integral equations of the Fredholm-type, therefore the demonstration of existence and uniqueness of solution can be made to depend on the existence of the solution of the Fredholm-type equations. The kernels occurring in the equation are, however, strongly singular, but the equation may be transformed by regularization operators into equivalent weakly singular equations thereby allowing the Fredholm alternatives to be applicable (see, for example, Mikhlin (1965), Cruse (1977)).

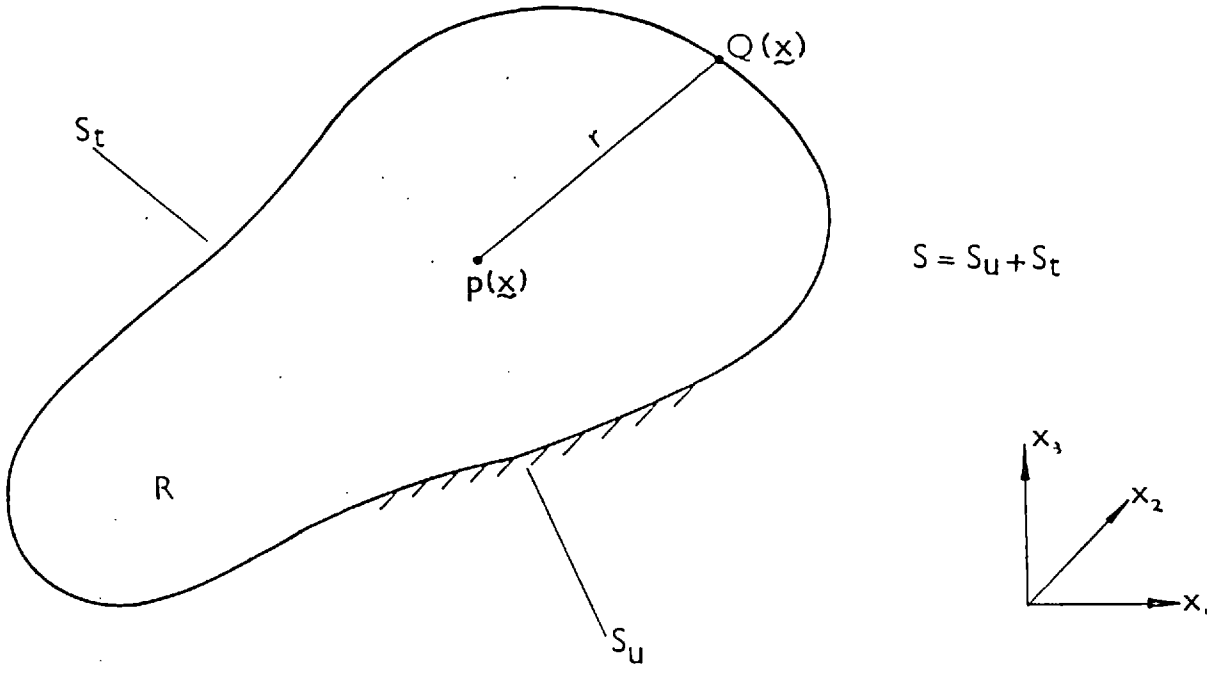



Figure 3.1: The physical domain of a mixed boundary-value problem

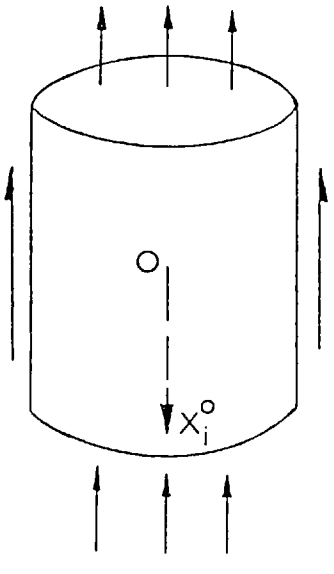



Figure 3.2: Cylindrical boundary used for evaluating the constant $B$ for Kelvin's problem (equation (3.14))

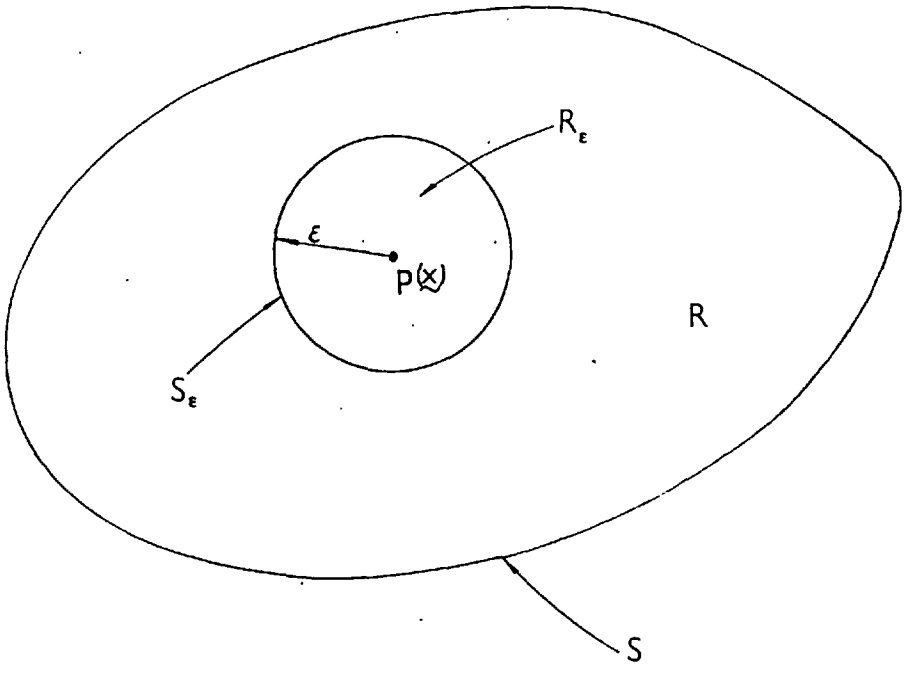



Figure 3.3: The domain $R_\varepsilon$ isolating $p(x)$

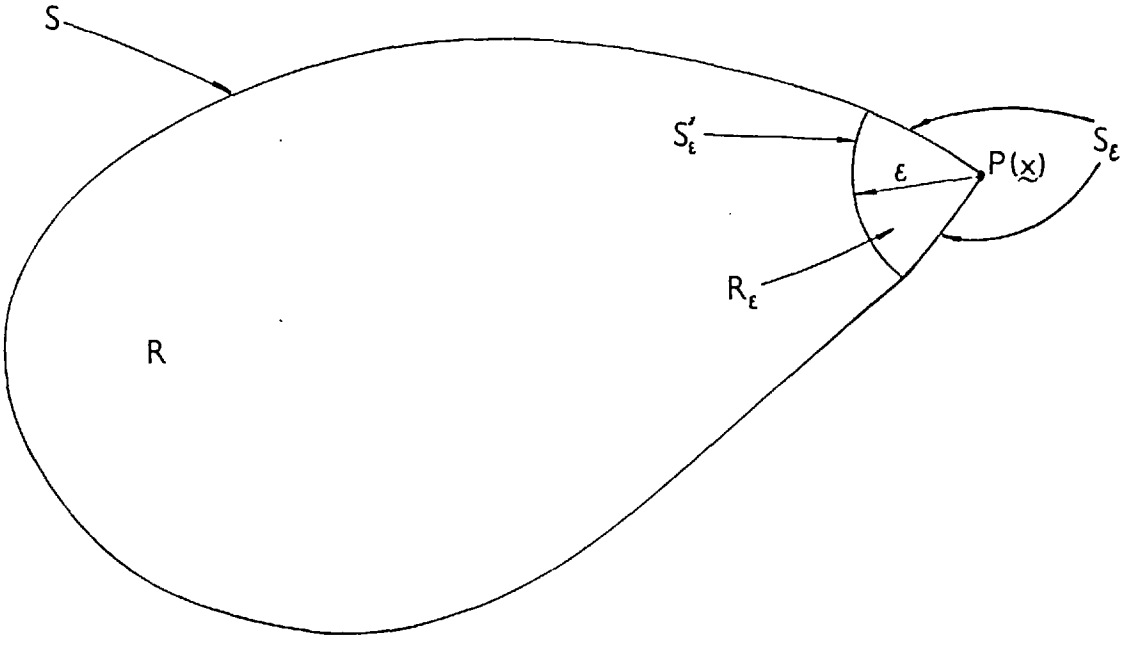



Figure 3.4: The domain $R_\varepsilon$ isolating $P(x)$

# CHAPTER 4

# THE NUMERICAL SOLUTION OF THE INTEGRAL EQUATIONS

To solve analytically the integral equations obtained in the previous chapter is, in general, quite difficult, if not impossible. The advent of high speed electronic digital computers has, however, facilitated the solution of these equations by numerical means. Since Rizzo (1967) first presented the numerical solutions for some plane problems in elastostatics, the advances in the numerical implementation for both two- and three-dimensional problems have enabled the boundary integral equation method to become a worthy alternative to other numerical methods, such as the finite element and finite difference methods, in stress analysis. In this chapter, the various numerical formulations for the direct method will be reviewed and the particular solution strategy adopted for the present work will then be discussed in greater detail.

## 4.1 REVIEW OF VARIOUS NUMERICAL FORMULATIONS

The numerical solutions to the integral equations obtained in the previous chapter are found by discretizating the surface $S$ of the domain into elements. Unlike many other numerical methods in stress analysis, the interior of the domain is not discretized; this being unnecessary because of the integrals appearing in the equations are surface integrals. The main difference between the various numerical formulations to be described here then is the manner in which the surface $S$ is represented by the elements and the assumptions made as regards the variation of the tractions and displacements over these surface elements.

The formulation by Rizzo (1967) for plane elastostatics follows very closely to that by Jaswon (1963) and Symm (1963) for potential theory,

where some simple boundary value problems were solved using the boundary integral equation method. The boundary in this case is represented by segments, each of which is a straight line joined at points on the surface, and over each of which the unknown functions are assumed to be constant; the constant value being associated with the mid-point of each segment.

The extension to three-dimensional elastostatics by Cruse (1969) follows very similar lines except now the surface of the body is represented by plane triangles over each of which both the displacement and traction vectors are assumed constant. The boundary integral equation is written for the centroid of each of these elements so that the load point $P(x)$ is never located at an edge or a corner. With this form of discretization, the boundary integral equation (3.57) reduces to a set of algebraic equations, viz:

$$\tfrac{1}{2}\, u_j(P_n) + \sum_{m=1}^{M} u_i(Q_m) \int_{\Delta S_m} T_{ji}(P_n, Q)\, dS(Q)$$

$$= \sum_{m=1}^{M} t_i(Q_m) \int_{\Delta S_m} U_{ji}(P_m, Q)\, dS(Q) \qquad (4.1)$$

for each centroidal point $n = 1, M$ where $M$ is the total number of surface elements $\Delta S$.

The integrals in (4.1) may each be evaluated analytically which was done by Cruse, knowing the size, orientation and location of each of the surface elements, and the material properties. Because the coefficients of $u_i(Q_m)$ and $t_i(Q_m)$ are, in general, not of the same order of magnitude, Cruse scales the coefficient of $u_i(Q_m)$ by the shear modulus to ensure proper conditioning of the system of equations, which are then solved by standard Gaussian elimination. Once these equations are solved, all the boundary data are known and may be used to obtain the solution for the

displacements and stresses at any specific points by direct integration of the identities (3.45) and (3.48). Substitution of the discretized boundary solution into (3.45) and (3.48) yields:

$$u_j(p) = \sum_{m=1}^{M} t_i(Q_m) \int_{\Delta S_m} U_{ij}(p,Q)\, dS(Q) - \sum_{m=1}^{M} u_i(Q_m) \int_{\Delta S_m} T_{ij}(p,Q)\, dS(Q) \qquad (4.2)$$

$$\sigma_{ij}(p) = \sum_{m=1}^{M} t_k(Q_m) \int_{\Delta S_m} D_{kij}(p,Q)\, dS(Q) - \sum_{m=1}^{M} u_k(Q_m) \int_{\Delta S_m} S_{kij}(p,Q)\, dS(Q) \qquad (4.3)$$

Again, the integrals in (4.2) and (4.3) may be obtained in closed form.

With this boundary discretization, Cruse (1969,1973) obtained very high numerical resolution of the solution, a feature quite unlike finite element and finite difference methods. But for the solution of practical problems, a large number of surface elements is often needed so the advantages over, say, the finite element method, is not often clear.

Ricardella (1973) and Cruse (1974) later improved on this numerical formulation by allowing displacements and tractions to vary linearly over each boundary element. In the three-dimensional improved formulation by Cruse (1974), most of what has been described remains basically the same but the unknowns are now associated with the three nodes at the vertex of each triangular planar surface element. Writing the integral equations at these nodes results in a system of equations as before. Again, the integrations necessary to obtain the matrix coefficients may be obtained analytically, but the coefficient of the free term of the integral equation may not be $\frac{1}{2}\delta_{ij}$, this being the case when $P(x)$ is at a corner or an edge.

The coefficient of this free term is, however, calculated implicitly by considering rigid body translation corresponding to which the stress field is zero. Suffice to say here that the results and run statistics presented for the problems solved showed this formulation to be more efficient than the previous one. However, the number of surface elements required to model practical problems is still fairly large and the advantages over other numerical methods, in terms of efficiency, are again not often very evident.

In this respect, the most significant advances in elastostatics applications were made by Lachat (1975) and Lachat & Watson (1975,1976, 1977). In their formulation, parametric representations of geometry and functions are used. The surface elements are allowed to be curved, the geometry of each being defined by quadratic shape functions of intrinsic coordinates similar to those used in finite element analysis for plane problems (see, for example, Zienkiewicz (1977)). The variations of displacement and tractions, on the other hand, are defined by either linear, quadratic or cubic shape functions. Gaussian quadrature formulae are used to evaluate the integrals for the coefficient matrix, as they are extremely difficult to obtain analytically, especially for curved elements. The coefficient of the free term of the integral equation and the Cauchy principal value of the integrals are calculated implicitly by, again, considering rigid body translation. Further, suitable transformation of the intrinsic coordinates ensures accuracy to be maintained even when integrating over regions where the functions vary very rapidly. In their formulation, a variable integration scheme was adopted; the quadrature formula for each element of integration being chosen according to the size of the element and its distance from the singularity of the kernels. Sub-division of the finite body can also be done, and the integral equation is

then written for each sub-region. This would result in a banded system of equations which are then solved by Gaussian elimination block solution techniques.

The numerical formulation used in the present work is almost identical to that proposed by Lachat (1975) and Lachat & Watson (1975,1976, 1977) and hence will not be presented in this review, but instead be discussed in greater detail in subsequent sections of this chapter. Based broadly on this numerical formulation, Rizzo & Shippy (1977) have also presented an analysis, with numerical results, for three-dimensional linear, homogeneous, isotropic steady-state thermo-elasticity. With this isoparametric formulation, it has been shown (see, for example, Lachat (1975), Lachat & Watson (1975,1976), Tan & Fenner (1978), Cruse & Wilson (1978)) that the accuracy and resolution of solutions are greatly improved, and for most practical cases, it is more economical than the finite element method.

More recently, Watson (1978) extended the isoparametric formulation to the analysis of infinite bodies consisting of several sub-regions, by the introduction of "infinite elements". The limiting state of stress at infinity is assumed to be known in this formulation. Except for some minor modifications pertaining to the integration over the infinite elements, and an important modification of the implicit calculation of the Cauchy principal values of certain integrals and the coefficient of the free term, the rest remains basically the same as in the finite body formulation above. In the same reference, Watson also presented an alternative formulation - the Galerkin formulation - in which surface integrals are matched. The surface is still discretized into isoparametric elements as before, but collocation is at the Gauss integration points for the integration over each element, unlike the earlier formulation which is at the nodes of the

element. But, by using the shape functions corresponding to the nodes, the construction of the system of equations is in terms of nodal values of displacements and tractions as before. There are some inherent computational difficulties in this formulation. Although not insurmountable, they cause considerable computational effort which led Watson (1978) to conclude that this method involves about the same amount of computation, if not more, than the nodal collocation formulation.

In the subsequent sections, the isoparametric nodal collocation formulation adopted for the present work will be described and discussed. For three-dimensional analyses, it has been found that the isoparametric quadratic variation is usually the most efficient (see Lachat (1975), Lachat & Watson (1975,1976)), hence only this form of geometric and functional variation is implemented in the present work.

## 4.2 PARAMETRIC REPRESENTATION OF GEOMETRY AND FUNCTIONS

The surface of the body is divided into quadrilateral elements (Figure 4.1), each of which has eight nodes. The elements are generally curved and the geometry of the surface is defined in terms of the quadratic shape functions of intrinsic coordinates of the elements. Thus, the Cartesian coordinates $x_i(\xi)$ of any point of an element are defined in terms of the nodal coordinates $x_i^c$ by:

$$x_i(\xi) = N^c(\xi)\, x_i^c \quad , \quad c = 1,8 \tag{4.4}$$

where:
$$N^1(\xi) = -\frac{1}{4}(1-\xi_1)(1-\xi_2)(1+\xi_1+\xi_2) \tag{4.5a}$$

$$N^2(\xi) = \frac{1}{2}(1-\xi_1^2)(1-\xi_2) \tag{4.5b}$$

$$N^3(\xi) = -\frac{1}{4}(1+\xi_1)(1-\xi_2)(1+\xi_2-\xi_1) \tag{4.5c}$$

$$N^4(\xi) = \frac{1}{2}(1+\xi_1)(1-\xi_2^2) \tag{4.5d}$$

$$N^5(\xi) = -\frac{1}{4}(1+\xi_1)(1+\xi_2)(1-\xi_1-\xi_2) \tag{4.5e}$$

$$N^6(\xi) = \frac{1}{2}(1+\xi_2)(1-\xi_1^2) \tag{4.5f}$$

$$N^7(\xi) = -\frac{1}{4}(1-\xi_1)(1+\xi_2)(1+\xi_1-\xi_2) \tag{4.5g}$$

$$N^8(\xi) = \frac{1}{2}(1-\xi_1)(1-\xi_2^2) \tag{4.5h}$$

Differentiating with respect to the intrinsic coordinates, the vectors tangent to the local coordinate lines are:

$$s_{i\beta} = \frac{\partial x_i}{\partial \xi_\beta} = \frac{\partial N^c(\xi)}{\partial \xi_\beta} x_i^c \quad , \quad \begin{matrix} i = 1,3 \\ \beta = 1,2 \end{matrix} \tag{4.6}$$

The vector normal to the element is thus the vector product of the two vectors defined by (4.6), i.e.

$$s_{i1} \wedge s_{i2} = \begin{vmatrix} \underset{\sim}{e}_1 & \underset{\sim}{e}_2 & \underset{\sim}{e}_3 \\ \frac{\partial x_1}{\partial \xi_1} & \frac{\partial x_2}{\partial \xi_1} & \frac{\partial x_3}{\partial \xi_1} \\ \frac{\partial x_1}{\partial \xi_2} & \frac{\partial x_2}{\partial \xi_2} & \frac{\partial x_3}{\partial \xi_2} \end{vmatrix}$$

$$= J_1 \underset{\sim}{e}_1 + J_2 \underset{\sim}{e}_2 + J_3 \underset{\sim}{e}_3 \tag{4.7}$$

The Jacobian of transformation is then the modulus of (4.7), i.e.

$$|J(\xi)| = (J_1^2 + J_2^2 + J_3^2)^{\frac{1}{2}} \tag{4.8}$$

and the unit outward normal components are then given by:

$$n_i = \frac{J_i}{|J(\xi)|} \quad , \quad i = 1,3 \tag{4.9}$$

Similarly, the displacements, $u_i(\xi)$, and tractions, $t_i(\xi)$, at any arbitrary point of an element are defined in terms of the nodal values and the same shape functions (4.5), viz:

$$u_i(\xi) = N^c(\xi)\, u_i^c \tag{4.10}$$

$$t_i(\xi) = N^c(\xi)\, t_i^c \tag{4.11}$$

## 4.3 NUMERICAL FORMULATION OF THE BOUNDARY INTEGRAL EQUATION

Let there be a total of $g$ distinct nodes and $d(b,c)$ represent the $c$th node of the $b$th element, $c = 1,8$, $b = 1,M$. Substitution of the parametric representation of $u_i$ and $t_i$ into (3.57) for each of the $g$ functional nodes results in the following set of simultaneous equations:

$$C_{ij}(P_n)\, u_j(P_n) + \sum_{b=1}^{M} \sum_{c=1}^{8} u_j(P_{d(b,c)}) \int_{S_b} T_{ij}(P_n, Q(\xi))\, N^c(\xi)\, |J(\xi)|\, d\xi$$

$$= \sum_{b=1}^{M} \sum_{c=1}^{8} t_j(P_{d(b,c)}) \int_{S_b} U_{ij}(P_n, Q(\xi))\, N^c(\xi)\, |J(\xi)|\, d\xi \tag{4.12}$$

Equation (4.12) represents a set of $3g$ equations in $6g$ nodal values

of displacement and traction, half of which are known. These equations are equations of nodal collocation, for they assure, subject to the approximations made in representing the surface $S$ and the functions $u_i$ and $t_i$, satisfaction of the integral equation at the $g$ nodal points. The coefficients of these equations are the values of the free term of the integral equation at functional nodes and the integrals of the kernel-shape function products over the surface elements. How these coefficients are evaluated will now be discussed.

### 4.3.1 Evaluation of Equation Coefficients

Provided that due precautions are taken when the integrand tends to infinity, the integrals appearing in (4.12) may be accurately evaluated by Gaussian quadrature formulae. To do this, it is necessary to consider both the case in which the node $P_n$ is one of the nodes of the element to be integrated over, $S_b$, and the case when it is not.

Where $P_n$ is not a node of $S_b$, the integrand varies smoothly over the region of integration and hence may reasonably be approximated by a polynomial. The integrals may thus be evaluated by the following Gaussian quadrature formula:

$$\int_{-1}^{+1}\int_{-1}^{+1} f(\xi_1,\xi_2)\, d\xi_1\, d\xi_2 = \sum_{l=1}^{\chi}\sum_{m=1}^{\chi} w_l\, w_m\, f(\phi_m,\psi_l) \qquad (4.13)$$

where $w_l$ are the weighting coefficients, $f(\phi_m,\psi_l)$ the value of the integrand at specified points $(\phi_m,\psi_l)$, and $\chi$ the number of Gauss points in each coordinate direction used. It is implied in (4.13) that the order of the integration formula is invariant for all $S_b$ and all $P_n$, which is the scheme used in the present work. Although an invariant integration scheme can be wasteful of computing resources, this inefficiency may be

largely offset by a good choice of boundary discretization, which admittedly can only be made in the light of experience. The order of integration formula is therefore fixed for a given problem and it is found that a reasonable value for $\chi$ is 4.

Where $P_n$ is a node of $S_b$, the integrand varies very rapidly and a somewhat different integration scheme has to be adopted. The quadrilateral element is divided into either two or three triangular sub-elements (Figure 4.3), depending on whether $P_n$ is a corner or mid-side node of the quadrilateral element. In each triangular sub-element, $P_n$ is located at the vertex and the base opposite $P_n$ is a side of the quadrilateral element.

For each triangular sub-element, a local system of coordinates $(\eta_1,\eta_2)$ may be defined (Figure 4.4). The coordinates $\eta_\alpha$ are defined in terms of $\xi_\alpha$ by the relations:

$$\xi_\alpha(\eta) = L^m(\eta)\ \xi_\alpha^{(m)} \quad , \quad m = 1,4 \tag{4.14}$$

where $L^m(\eta)$ are the linear shape functions defined in:

$$L^m(\eta) = \frac{1}{4}\ (1 + \eta_1\ \eta_1^m)\ (1 + \eta_2\ \eta_2^m) \tag{4.15}$$

In (4.15), $\eta_\alpha^m$ are the intrinsic (triangular) coordinates of the $m$th node of the sub-element. Also, in (4.14), $\xi_\alpha^{(m)}$ are the intrinsic coordinates of the vertices of the triangle and at the vertex where $P_n$ is located, $\xi_\alpha^{(1)} = \xi_\alpha^{(2)}$.

The Jacobian of transformation from the $\eta_\alpha$-system of coordinates to the $\xi_\alpha$-system is thus given by:

$$\bar{J}(\eta) = \begin{vmatrix} \frac{\partial L^m(\eta)}{\partial \eta_1} \xi_1^m & \frac{\partial L^m(\eta)}{\partial \eta_1} \xi_2^m \\ \frac{\partial L^m(\eta)}{\partial \eta_2} \xi_1^m & \frac{\partial L^m(\eta)}{\partial \eta_2} \xi_2^m \end{vmatrix} \tag{4.16}$$

and the Jacobian for integration over each of the sub-elements is then:

$$J(\eta) = J(\xi)\, \bar{J}(\eta) \tag{4.17}$$

Since the lines $\eta_1 = +1$ and $\eta_1 = -1$ converge to a point at $P_n$, the Jacobian $J(\eta)$ is $O(r)$. Where $P_n \neq P_{d(b,c)}$, the shape function $N^c(\xi)$ is also $O(r)$, so although $U_{ij}$ is $O(1/r)$ and $T_{ij}$ is $O(1/r^2)$, the kernel-shape function products tend to a finite limit as $P_n$ is approached. Where $P_n = P_{d(b,c)}$, the shape function $N^c(\xi)$ at $P_n$ equals unity; the product $U_{ij}(P_n,Q)\, N^c(\xi)\, J(\eta)$ thus still tends to a finite limit as $P^a$ is approached. Gaussian quadrature formula (4.13) may therefore be used for all these cases.

This leaves the integrals of $T_{ij}(P_n,Q)\, N^c(\xi)\, J(\eta)$ for the case when $P_n = P_{d(b,c)}$. They exist only in the sense of the Cauchy principal value and there is no suitable quadrature rule for obtaining these values. However, there is no need to evaluate separately either this integral or the coefficient $C_{ij}(P_n)$ of the free term both of which contribute to the same leading diagonal $(3 \times 3)$ sub-matrix of the coefficients of equations (4.12). This leading diagonal term is evaluated indirectly using the fact that the stress field corresponding to rigid body translation is zero. Writing the integral equation in global coordinates for this case where $t_j(P) = 0$ everywhere, thus:

$$C_{ij}(P_n) + \sum_{b=1}^{M} \sum_{c=1}^{8} \delta_{nd} \int_{S_b} T_{ij}(P_n, Q(\xi))\, N^c(\xi)\, |J(\xi)|\, d\xi$$

$$= - \sum_{b=1}^{M} \sum_{c=1}^{8} (1 - \delta_{nd}) \int_{S_b} T_{ij}(P_n, Q(\xi))\, N^c(\xi)\, |J(\xi)|\, d\xi \qquad (4.18)$$

### 4.3.2 Further Notes on the Formation of the Coefficient Matrix of the Equations

For each node $P_n$, a set of three equations corresponding to the three degrees of freedom are calculated simultaneously. The integrals in (4.12) when $P_n \neq P_{d(b,c)}$ are calculated directly and placed in the matrix and second member. Where $u_j(P_d)$ is the unknown, the integral of $T_{ij}\, N^c$ is placed in the matrix, while the integral of $U_{ij}\, N^c$ is multiplied by the known function $t_j(P_d)$ and placed in the second member. Where $u_j(P_d)$ is known, then it is multiplied by the integral of $T_{ij}\, N^c$, sign reversed, and placed in the second member, while the integral of $U_{ij}\, N^c$, sign reversed, is placed in the matrix. The values of the coefficients of the leading diagonal sub-matrix are meanwhile summed according to (4.18) and if $u_j(P_d)$ is the unknown, the corresponding coefficient is placed in the matrix. Conversely, if $t_j(P_d)$ is unknown, the corresponding coefficient of $u_j(P_d)$ is multiplied by $u_j(P_d)$, sign reversed, and placed in the second member.

Thus, as expressed in (4.12), there is a contribution both to the matrix and the second member for every term of the double sum. But consider the case where there are two adjoining elements, one fixed in the $i$th direction, while the other free in that direction (Figure 4.5) and $P_{d(b,c)}$ is a common node. The unknown in the $i$th direction is then $t_i(P_d)$ so the integral over $S_b'$ (the free element) of the product $T_{ij}\, N^c$ must be multiplied by the known $u_i(P_d)$ and placed in the second member. But,

although the traction $t_i(P_d)$ is the unknown, the limiting value of the traction on $S_b'$ as $P_d$ is approached is known. The integral over $S_b'$ of the product $U_{ij}\ N^c$ should therefore be multiplied by the known limiting value of the traction and also placed in the second member. The same is true for the other shared nodes. Thus, in this case, there are terms in the double sum of (4.12) for which both of the integrals of the kernel products should be placed in the second member. The matrix coefficients of $t_i$ of the shared nodes should consist of the integrals over the fixed element only.

Now, although physically point or line constraints and loading are impossible (being mathematical conceptions), it is often useful to have such boundary conditions in practice. However, if the procedure described above is applied to these cases, there would result a system of equations of traction/displacement unknowns to which there correspond zero surface areas. For these cases, Lachat (1975) spread the point/line displacements or loads over the elements sharing these isolated nodes or common sides by means of the shape functions. Local errors are therefore to be expected, although away from these points, the error in the solution would probably be relatively insignificant. Except for a special case, these point or line constraints and loading are not treated in the present work.

The special case of point constraint will now be considered. Often, even though tractions are to be solved for where displacements are prescribed, the values of these tractions can be obtained, even before the equations are solved, from physical arguments. In this case, isolated point or line displacement constraints can be treated without causing any significant local errors. For each such constrained node, the whole row and column of the matrix corresponding to that node is made equal to zero, with the exception of the diagonal coefficient which is set equal to unity.

The corresponding second member of the matrix is then replaced by the value of the displacement constraint.

Finally, the numerical values of the integrals of $U_{ij}\ N^e$ are, in general, several orders of magnitude smaller than those of $T_{ij}\ N^e$. To ensure proper conditioning of the set of equations, the equations are scaled to be non-dimensional. The integrals of $T_{ij}\ N^e$ are not scaled as they are already non-dimensional but integrals of $U_{ij}\ N^e$ are multiplied by $(E/l_o)$ where $l_o$ is the greatest dimension of the structure. Prescribed values of tractions and displacements are divided by $E$ and $l_o$, respectively, and after the solution of the equations, the calculated values of tractions and displacements are, of course, multiplied by these quantities, respectively.

## 4.4 SOLUTION OF THE SYSTEM OF EQUATIONS

The solution of the system of equations can be done by Gaussian elimination. But the matrix of the equation set is, in general, fully populated and non-symmetric, and for practical three-dimensional problems, the matrix may be too large to be retained in the central memory of the computer. This is despite the fact that the dimensionality of the problem has been numerically reduced by one with the boundary integral formulation. It is thus necessary then to store the coefficients of the matrix on a disc file. This being said, the reduction of equations must be carried out in such a way that the input-output time for this file is low. An effective and efficient strategy is the block elimination technique in which several unknowns are eliminated during each sweep of the disc file. One such block solver has been presented by Das (1978) where the matrix coefficients are stored in a sequential file. Another, arguably more efficient, solver has been presented by Lachat (1975) and Lachat & Watson (1977) and is the

block solver used in the present work.

The matrix coefficients are written to a random access file in rows and as many complete rows as possible are put in each record. During the reduction of the equations, there are five arrays in central memory:

i) The "Slow Block" of length equal to an integral multiple of the file record length.

ii) The "Slow Output Buffer" of length equal to that of a file record.

iii) The "Fast Block" of length equal to that of a file record.

iv) The "Fast Output Buffer" of length equal to that of a file record.

v) The second member.

The length of the file record can be easily modified to suit the computer system characteristics. A flowchart, as presented and discussed in much greater detail by Lachat (1975), is shown in Figure 4.6. Referring to this figure, it may be seen that each time the file is read and re-written, LC unknowns are eliminated. When re-writing the file, the number LCF of complete partially reduced equations per file record is increased whenever possible. Eventually, all the remaining partially reduced equations can be put into slow block and forward reduction ends as a wholly fast-core operation. The reduction of the second member takes place at the same time as that of the matrix to avoid creating a file of pivots. The solution of the equations is then obtained by direct back-substitution.

## 4.5 EVALUATION OF THE SURFACE STRESS TENSOR

The stress tensor at surface points may be obtained from the tractions and tangential strains at the surface. The tractions at the surface would all be known immediately after the solution of (4.12), but the surface strains would still have to be determined first before the surface stress tensor could be obtained.

In general, the vector tangents to the local coordinate lines of the quadrilateral surface element, i.e. $S_{i\beta}$, are not orthogonal. But a local orthogonal system of axis may be defined as follows. Let $m_{1j}$ and $m_{2j}$ be the unit vectors in the coordinate directions $\xi_1$ and $\xi_2$, respectively, and $m_{3j}$ the unit normal to the element (i.e. $\equiv n_j$). If $u_{ij}$ are the direction cosines of this orthogonal system of axes in the global Cartesian system, then the local orthogonal system is defined by taking $\mu_{ij} = m_{1j}$, $\mu_{3j} = m_{3j}$ and $\mu_{2j}$ the vector product of $m_{1j}$ and $m_{3j}$ (Figure 4.7).

Further, let $\bar{u}_i$, $\bar{e}_{ij}$, $\bar{\sigma}_{ij}$ and $\bar{t}_i$ be the displacements, strains, stresses and tractions, respectively, in this orthogonal local system defined by $\mu_{ij}$. The displacements in the orthogonal tangential directions are thus given by:

$$\bar{u}_\alpha(\xi) = N^c(\xi)\, u^c_j\, \mu_{\alpha j} \tag{4.19}$$

Differentiating (4.19) with respect to the local orthogonal coordinates in the surface tangential directions, $\mu_{1j}$ and $\mu_{2j}$, the tangential strains in thic local system of coordinates are obtained (see Appendix C).

$$\bar{e}_{11}(\xi) = \frac{\partial N^c(\xi)}{\partial \xi_1}\, u^c_j\, \frac{\mu_{1j}}{|S_{11}|} \tag{4.20a}$$

$$\bar{e}_{22}(\xi) = -\frac{\partial N^c(\xi)}{\partial \xi_1}\, u^c_j\, \frac{\mu_{2j}\cos\theta}{|S_{21}|\sin\theta} + \frac{\partial N^c(\xi)}{\partial \xi_2}\, u^c_j\, \frac{\mu_{2j}}{|S_{22}|\sin\theta} \tag{4.20b}$$

$$\bar{e}_{12} = \bar{e}_{21} = \frac{\partial N^c(\xi)}{\partial \xi_1} u_j^c \frac{\mu_{2j}}{|S_{21}|} - \frac{\partial N^c(\xi)}{\partial \xi_1} u_j^c \frac{\mu_{1j} \cos\theta}{|S_{11}| \sin\theta}$$

$$+ \frac{\partial N^c(\xi)}{\partial \xi_2} u_j^c \frac{\mu_{1j}}{|S_{12}| \sin\theta} \tag{4.20c}$$

In (4.20), $\theta$ is the angle between the two tangent vectors $m_{1j}$ and $m_{2j}$ (Figure 4.7). Using Hooke's law, the stress tensor $\sigma_{ij}$ may then be obtained from the tractions and these surface strains, viz:

$$\bar{\sigma}_{11} = \frac{E}{1-\nu^2} (\bar{e}_{11} + \nu \bar{e}_{22}) + \frac{\nu}{1-\nu} \bar{t}_3 \tag{4.21a}$$

$$\bar{\sigma}_{12} = \bar{\sigma}_{21} = \frac{E}{2(1+\nu)} \bar{e}_{12} \tag{4.21b}$$

$$\bar{\sigma}_{22} = \frac{E}{1-\nu^2} (\bar{e}_{22} + \nu \bar{e}_{11}) + \frac{\nu}{1-\nu} \bar{t}_3 \tag{4.21c}$$

$$\bar{\sigma}_{33} = \bar{t}_3 \tag{4.21d}$$

$$\bar{\sigma}_{32} = \bar{\sigma}_{23} = \bar{t}_2 \tag{4.21e}$$

$$\bar{\sigma}_{31} = \bar{\sigma}_{13} = \bar{t}_1 \tag{4.21f}$$

The stress tensor in the global Cartesian system may then be obtained by the simple transformation:

$$\sigma_{ij} = \mu_{ki} \mu_{lj} \bar{\sigma}_{kl} \tag{4.22}$$

The surface stress tensor may alternatively be calculated directly from the integral equations by taking the limit of $p(x) \to P(x)$ in (3.48),

but this procedure would be very much more expensive that the procedure described above.

## 4.6 EVALUATION OF STRESSES AND DISPLACEMENTS AT INTERIOR POINTS

The evaluation of stresses and displacements at any point in the interior of the body follows only after the solution of (4.12). To do this, the Somigliana's identities for stresses and displacements, i.e. (3.48) and (3.45), respectively, are discretized in the same way as the boundary integral equation (4.12). Since all the boundary displacements and tractions are now known, the internal point stresses and displacements can be obtained directly by integrating over all the surface elements.

$$\sigma_{ij}(p) = \sum_{b=1}^{M} \sum_{c=1}^{8} \{ \int_{S_b} D_{ijk}(p,Q(\xi))\, N^c(\xi)\, t_k(P_{d(b,c)})\, |J(\xi)|\, d\xi - \int_{S_b} S_{ijk}(p,Q(\xi))\, N^c(\xi)\, u_k(P_{d(b,c)})\, |J(\xi)|\, d\xi \} \tag{4.23}$$

$$u_i(p) = \sum_{b=1}^{M} \sum_{c=1}^{8} \{ \int_{S_b} U_{ij}(p,Q(\xi))\, N^c(\xi)\, t_j(P_{d(b,c)})\, |J(\xi)|\, d\xi - \int_{S_b} T_{ij}(p,Q(\xi))\, N^c(\xi)\, u_j(P_{d(b,c)})\, |J(\xi)|\, d\xi \} \tag{4.24}$$

The integrals in (4.23) and (4.24) are evaluated using the Gaussian quadrature formula (4.13), as before.

## 4.7 FINAL REMARKS

It is now generally acknowledged that the isoparametric formulation based on the shape functions, presented in this chapter, is near the limit of its development for elastostatics. Exceptions perhaps arise for the

generalizations to non-linear analysis and the modelling of cracks and other forms of singularities. It has been suggested (Watson (1979)) that computational efficiency of the boundary integral equation method could probably be still significantly improved by replacing the present shape functions by cubic splines or cubic Hermitian functions.

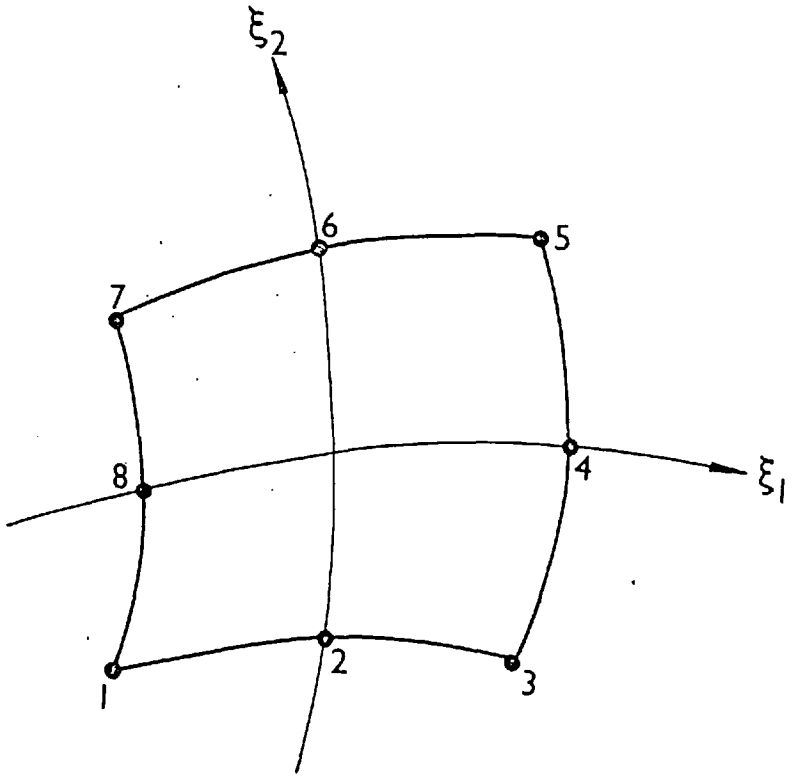



Figure 4.1: The eight-node isoparametric quadrilateral surface element

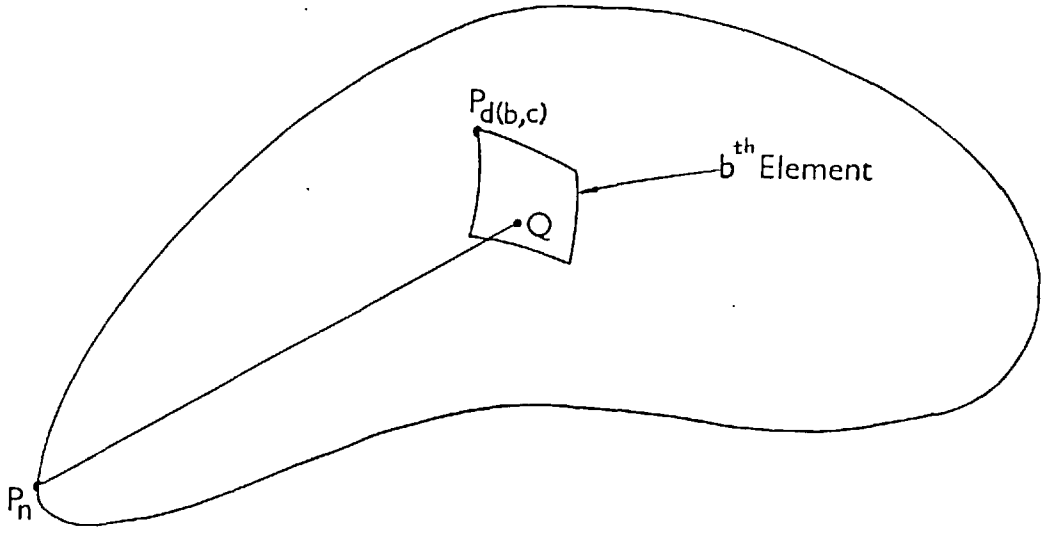
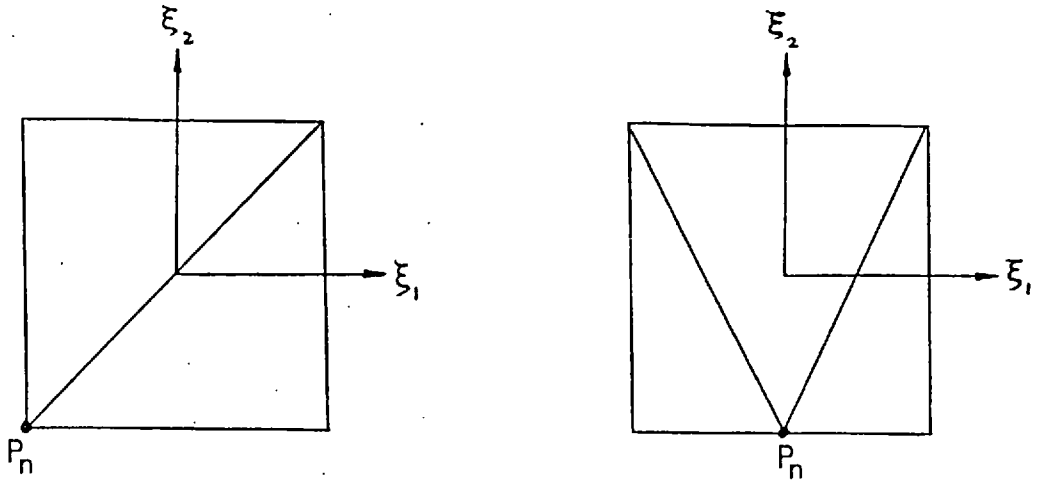



Figure 4.2: Parameters of equation (4.12)




(a) $P_n$ at corner of element (b) $P_n$ at mid-side of element

Figure 4.3: Triangular sub-elements of a quadrilateral element

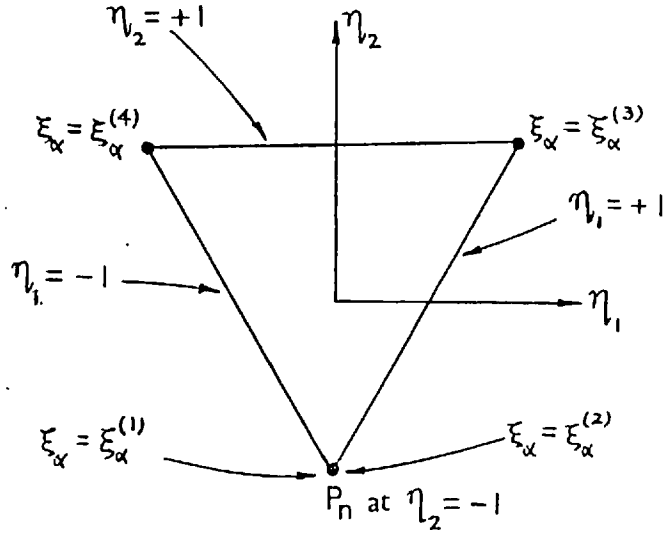



Figure 4.4: Coordinates for integration over a sub-element

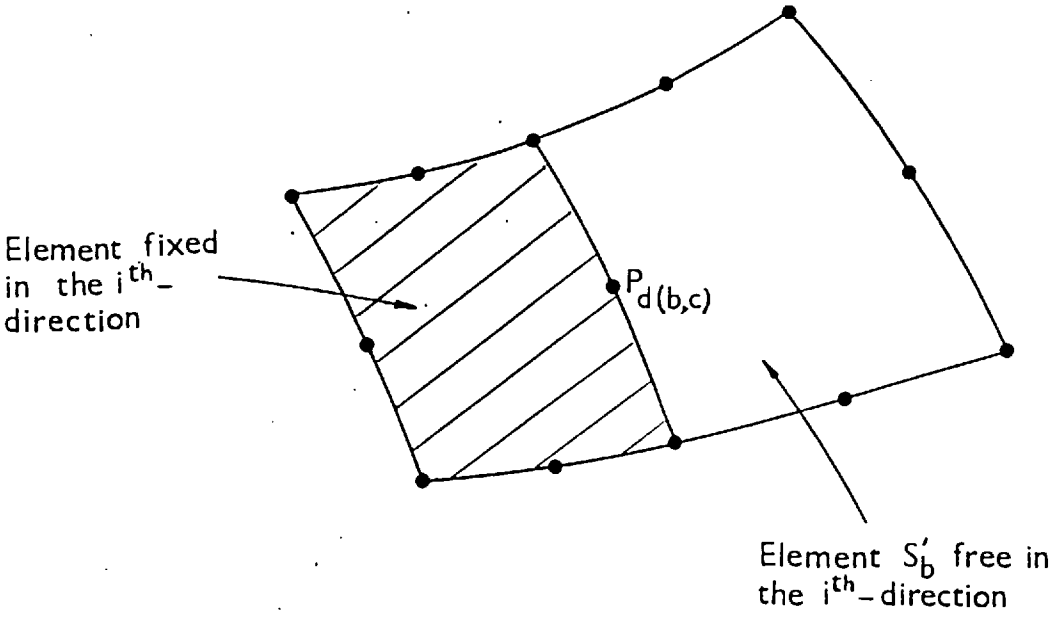



Figure 4.5: Shared nodes of fixed and free elements

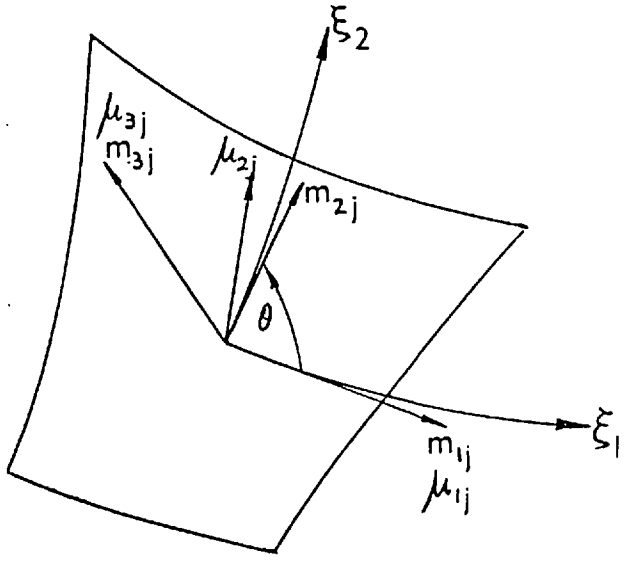



Figure 4.7: Local coordinate axes for stress calculations

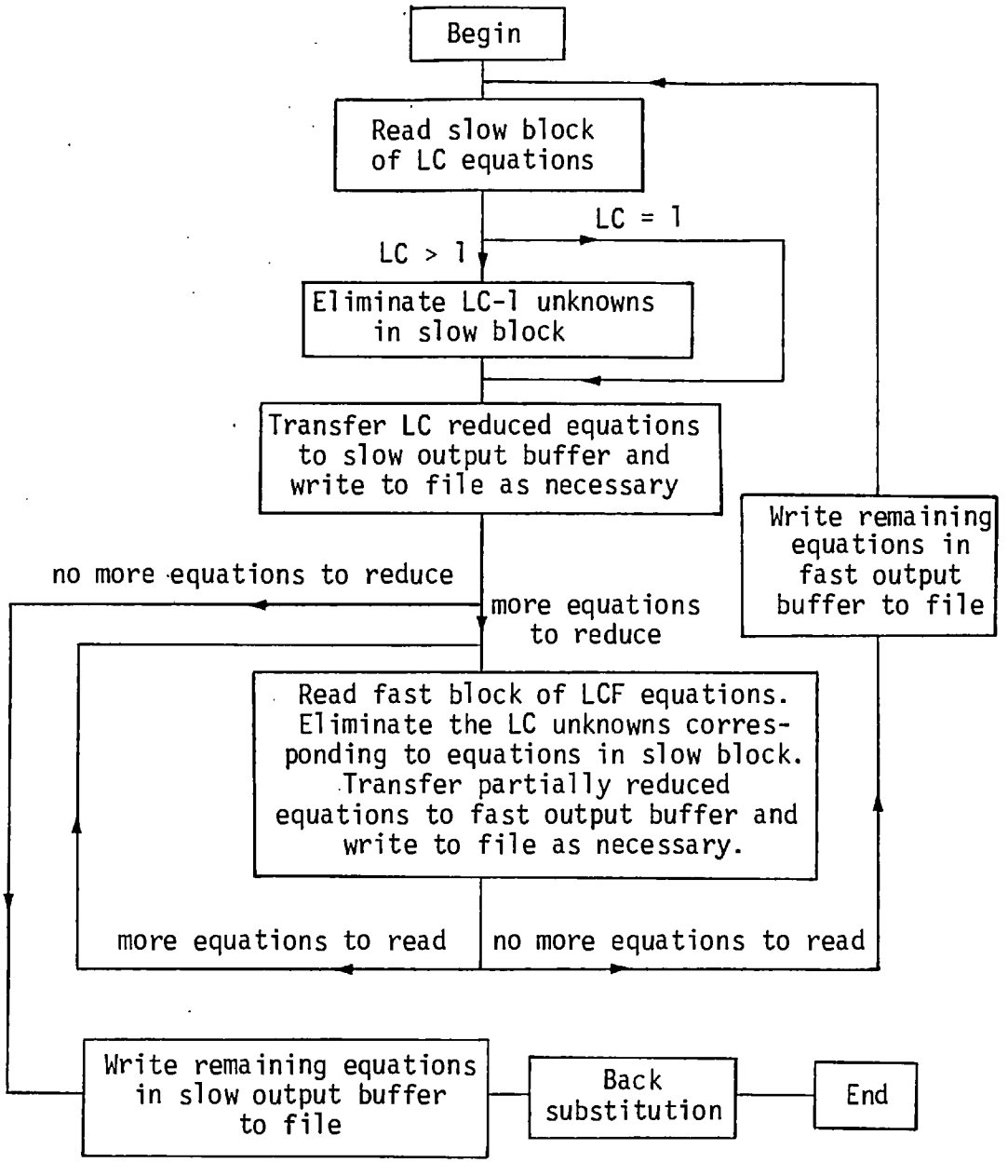



Figure 4.6: Flowchart of block solver

# CHAPTER 5

# APPLICATION OF THE BOUNDARY INTEGRAL EQUATION METHOD TO LINEAR ELASTIC FRACTURE MECHANICS

The determination of crack front stress intensity factors, as mentioned in Chapter 2, forms an essential part of the solution of the problem in elastic fracture mechanics analysis. The importance of the stress intensity factor in the methodology, such as the estimation of the static strength of cracked components or of the residual fatigue life, has, over the past decade, stimulated the search for and development of effective and efficient methods for the solution of complex crack problems. These methods inevitably have to be numerical in approach and probably the most widely used in fracture mechanics analysis in recent years has been the finite element method; a comprehensive review on its progress to date has been presented by Gallagher (1978). But, despite its versatility, it has serious drawbacks, particularly when singularities occur, as in fracture problems. The numerical problem size becomes very large if accurate solutions are required, and is often limited by the capacities of present generation computers. In contrast, the singularity-based boundary integral equation method, described in the previous chapter in which only the boundary of the physical problem is discretized, has proved to be a more accurate and efficient method. Nevertheless, the finite element method is mentioned here because many of the techniques for fracture mechanics analysis by the boundary integral equation method were developed originally for finite element solutions.

In this chapter, these techniques will be reviewed, followed by the results of several test problems. Questions pertaining to the order of stress (strain) singularity for surface crack problems where the crack

intersects a free surface (which may no longer be the classical $r^{-\frac{1}{2}}$) will also be discussed and numerical solutions presented.

## 5.1 NUMERICAL EVALUATION OF THE STRESS INTENSITY FACTOR

The numerical evaluation of crack front stress intensity factors involves essentially two phases: (a) modelling the physical problem, and (b) development of the technique for the determination of the stress intensity factor. In the present study, only problems symmetric about the plane of the crack and under Mode I loading will be investigated. Advantage can therefore be taken of the crack-plane by replacing it with a boundary in the discretized model with the appropriate boundary conditions applied, namely zero normal displacement and shear tractions on this plane ahead of the crack.

The various techniques for determining $K_I$ by the boundary integral equation method can be broadly classified under (i) "direct" methods, and (ii) the "indirect" method. In direct methods, the evaluation of $K_I$ is based on either the classical displacement field solution (displacement method) or the stress field solution (stress method) in the vicinity of the crack front. The indirect method, on the other hand, is an energy-based method in which the strain energy release rate, $G_I$, is employed.

### 5.1.1 The Displacement Method

The classical field solution for displacement in the immediate vicinity of the crack front was given in (2.11) in Chapter 2. For points along a radial line normal to the crack front and in the plane of the crack, the displacement normal to the crack face (i.e. $\theta = \pi$ in Figure 2.3) is:

$$u_2 = \frac{4 K_I}{H'} \sqrt{\frac{r}{2\pi}} \tag{5.1}$$

where $r$ is the distance from the crack front, and $H'$ is the material stiffness, equal to the Young's modulus, $E$, for plane stress conditions and equal to $E/(1-\nu^2)$ for plane strain.

If the computed value of $u_2$ at radial distance $r$ from the crack front is $V$, the corresponding value of $K_I$, say $K_I^*$, is obtained from (5.1), i.e.

$$K_I^* = \frac{H' \sqrt{2\pi}}{4} \frac{V}{\sqrt{r}} \tag{5.2}$$

Equation (5.2) is strictly only valid in the limit when $r$ approaches zero. Thus, values of $K_I^*$ are obtained using (5.2) from the computed displacements $V$ at a series of nodal points along a radial line on the crack face and extrapolated to $r = 0$ to yield the crack front stress intensity factor.

The computed values $V$ at regions very close to the crack front are, however, less reliable and it is therefore necessary to extrapolate from relatively large values of $r$. This does not present problems for it can be shown by retaining higher order terms in (2.11) (see, for example, Pereira (1977)) that a plot of $K_I^*$ versus $r$ should be linear up to relatively large values of $r$. The point of intersection between the tangent to the constant slope portion of the curve with the $K_I^*$ axis will thus be the value of $K_I$ required.

### 5.1.2 The Stress Method

For points along a radial line normal to the crack front and in the plane of the crack, the direct stress component in the direction normal to the crack plane and ahead of the crack (i.e. $\theta = 0$ in Figure 2.3) is given by:

$$\sigma_{22} = \frac{K_I}{\sqrt{2\pi\, r}} \tag{5.3}$$

The computed values of $\sigma_{22}$, say $\sigma_y$, can be found at nodal points at distances $r$ ahead of the crack front and the corresponding values of $K_I$, $K_I^*$, obtained from (5.3), i.e.

$$K_I^* = \sigma_y \sqrt{2\pi r} \tag{5.4}$$

To obtain $K_I$, the extrapolation procedure to $r = 0$, as described in the previous section, has to be used.

Accurate results of $K_I$ can, however, only be obtained at the expense of a highly refined mesh by this method. In general, the $K_I$ solutions are inferior to those obtained by the displacement method (see Cruse (1972), Chan et al (1970)). This is not very surprising as displacements are the primary variables in the boundary integral equation method and are more accurately known than stresses.

### 5.1.3 The Indirect Method

The extrapolation methods above do not contain any special provision for the singularity at the crack front in the numerical formulation. Although the boundary integral equation method gives good resolution of the solution parameters, a relatively fine grid around the crack front is still necessary in order to obtain reasonably accurate values of $K_I$ by these extrapolation methods. To overcome this major disadvantage, two other methods may be used. The first is by the introduction of special "singularity elements" at the crack front in the numerical formulation of the fracture problem; this will be discussed in the next section. The second approach, to be discussed here, calculates $K_I$ via the strain energy release rate, $G_I$, making use of equation (2.18):

$$G_I = \frac{dU}{dA} = \begin{cases} \frac{1-\nu^2}{E} K_I^2 & \text{for plane strain} \\ \frac{K_I^2}{E} & \text{for plane stress} \end{cases} \tag{5.5}$$

In (5.5), $dU$ is the change in strain energy, $U$, in advancing the crack front, thereby exposing an incremental area of crack surface, $dA$.

The rationale behind the use of this energy method is that the crack front stress field will make only a relatively small contribution to the total strain energy of the body, so that adequate representation of the crack front stress field is not very necessary. Consequently, this method can allow for a coarser mesh compared to that admissible for the displacement method above. Extra computational effort is, however, needed in the solution, for, in principle, the strain energy release rate can only be accurately evaluated by differentiating a set of strain energy distributions of the body corresponding to different crack sizes. In practice, a simple differencing approach from two computer runs is sufficient to give very accurate results, as experienced in both the finite element and boundary integral equation methods applied to plane problems. The two computer runs are identical in all respects, except for a very small difference in crack size, from which the strain energy release rate is evaluated as:

$$G_I \simeq \frac{\Delta U}{\Delta A} \tag{5.6}$$

For plane problems, $K_I$ can be obtained directly from (5.5) and (5.6) after the two computer runs, thus obviating the need to extrapolate $K_I^*$ versus $r$ curves to $r = 0$. But in three-dimensional applications, the problem becomes very much more complicated, for the crack front will normally be curved and the stress intensity factor may vary along the

periphery of the crack. If the analogous procedure to that used in plane problems were to be used to obtain local values of $K_I$, a set of computer runs must be carried out with a succession of small and localized extensions of the crack front. This can be a very expensive procedure.

A technique to improve on the efficiency of this energy method in three-dimensional crack problems was proposed by Cruse & Meyers (1977) for use with the boundary integral equation method. This technique employs both the crack face displacements and the strain energy release rate. Only two computer runs are needed, one with the original crack front and the other with a perturbed crack front. The perturbed geometry is obtained from the original geometry by moving the crack front nodes, as well as the adjacent nodes along the same radial line on either side of the crack front, in a direction normal to it, by a small distance (typically 1% of the crack length). The strain energy release rate thus obtained is related to the root-mean-square value of $K_I$ along the crack front, say $\overline{K}_I$:

$$G\,H' \;=\; \overline{K}_I^{\,2} \;=\; \frac{1}{\Delta A}\int_{\Delta A} K_I^{\,2}(s)\;\delta\ell(s)\;ds \tag{5.7}$$

where $\delta\ell(s)$ is the distance between the original and perturbed crack fronts, and $s$ is the linear distance along the crack front, as shown in Figure 5.1.

To obtain $K_I(s)$, assume that the value of $K_I$ can be given by:

$$K_I(s) \;=\; B\,\frac{V(s)}{\sqrt{r(s)}} \tag{5.8}$$

where $V$ is the crack face normal displacements at distance $r$ from the crack front, and $B$ is a constant (cf. equation (5.2)). The variation of

$K_I$ along the crack front can be obtained by referencing all nodal point values to that at one of the nodes which has the following value:

$$K_{I_{ref}} = B \frac{V_{ref}}{\sqrt{r_{ref}}} \tag{5.9}$$

From (5.8) and (5.9):

$$\frac{K_I(s)}{K_{I_{ref}}} = \frac{V(s)/V_{ref}}{\sqrt{r(s)/r_{ref}}} = \frac{V^*(s)}{\sqrt{r^*(s)}} \tag{5.10}$$

Using (5.10), (5.7) becomes:

$$G\,H = \frac{1}{\Delta A} \int_{\Delta A} K_{I_{ref}}^2 \left[\frac{V^*(s)}{\sqrt{r^*(s)}}\right]^2 \delta l(s)\, ds \tag{5.11}$$

and on re-arranging:

$$\frac{1}{K_{I_{ref}}} = \frac{1}{\Delta A} \int_{\Delta A} \frac{1}{G\,H'} \left[\frac{V^*(s)}{\sqrt{r^*(s)}}\right]^2 \delta l(s)\, ds^{\frac{1}{2}} \tag{5.12}$$

The values $V^*$ and $r^*$ in (5.12) are obtained from nodal point values from the computer run with the original crack size. Cruse & Meyers, in their work, assumed these values to vary in a piecewise linear manner between the nodal points. Their numerical formulation was based on flat triangular surface elements as described in the previous chapter, and under the circumstances the linear approximation was perhaps the best approximation that could be made. In the present work with quadratic isoparametric formulation, these quantities are assumed to vary quadratically along the side of each element modelling the crack front, which should provide a better approximation. The terms on the right hand side of (5.12) are thus all known and so $K_{I_{ref}}$ can be obtained. Use of

this reference value in (5.10) gives $K_I(s)$, the distribution of stress intensity factor along the crack front.

The determination of $G_I$ need not involve two completely separate computed solutions, each of which can be expensive, in absolute terms, for a practical three-dimensional problem. As only relatively few coefficients in the equations are affected when the crack front is changed, the second solution can be obtained without re-establishing all the coefficients of the equations. Those coefficients which are affected correspond to those nodes that are moved when the crack front is perturbed. Indeed, both solutions can be obtained in just one computer run. This facility was implemented in the computer program developed for the present study.

The computer programming involves transferring all the coefficients obtained for the first solution onto a scratch file; these coefficients are recalled and, where appropriate, modified for the second solution. The equations, of course, have to be solved again, but nevertheless significant economy arises because the integration of the kernel-shape function products in equation (4.12) to obtain the equation coefficients normally takes up much of the computing effort.

A point perhaps ought to be made here as regards the use of (5.10). Provided the value is accurate, there is no reason why $K_{I_{ref}}$ should not be obtained by some other means, such as the direct method, and (5.10) then used to estimate the variation of $K_I$ along the crack front. Indeed, the computation of $G$ can still be relatively expensive despite the economy offered by the computational technique described above.

## 5.2 THE SINGULARITY ELEMENT

Special "singularity elements" which exhibit the stress (strain) singularity occurring at the crack front may be used to model the crack periphery. This reduces the amount of mesh refinement necessary, around that region, for obtaining accurate values of $K_I$ by the extrapolation method described earlier. Henshall & Shaw (1975) and Barsoum (1976), in their finite element work, independently perceived that the transformation from physical to isoparametric coordinates can be singular if nodal points along the sides of the element are positioned in a certain way, and this consideration could be employed to represent the singularity sought in fracture mechanics analysis. This concept can, of course, be extended as well to the boundary integral equation method with the isoparametric formulation.

For simplicity, consider just the side of the 8-node isoparametric element with nodes 1, 2, 3 and treat this as a one-dimensional element of unit length (Figure 5.2). The shape functions along the element are:

$$N^1(\xi) = -\tfrac{1}{2}\,\xi\,(1-\xi) \tag{5.13a}$$

$$N^2(\xi) = (1+\xi)(1-\xi) \tag{5.13b}$$

$$N^3(\xi) = \tfrac{1}{2}\,\xi\,(1+\xi) \tag{5.13c}$$

The physical coordinate $x$ along the element is thus given by:

$$x = -\tfrac{1}{2}\,\xi\,(1-\xi)\,x^{(1)} + (1+\xi)(1-\xi)\,x^{(2)} + \tfrac{1}{2}\,\xi\,(1+\xi)\,x^{(3)} \tag{5.14}$$

where the superscripts denote nodal point values.

Putting $x^{(1)} = 0$, $x^{(2)} = a$ and $x^{(3)} = 1$ into (5.14):

$$x = (1+\xi)(1-\xi)\,a + \tfrac{1}{2}\,\xi\,(1+\xi) \tag{5.15}$$

The Jacobian $\partial x/\partial \xi$ is then:

$$\frac{\partial x}{\partial \xi} = \tfrac{1}{2} + (1-2a)\,\xi \tag{5.16}$$

But, from (5.15):

$$\xi = \frac{-1 + \sqrt{1 - 8(1-2a)(a-x)}}{2(1-2a)} \tag{5.17}$$

therefore:
$$\frac{\partial x}{\partial \xi} = \tfrac{1}{2}\sqrt{1 - 8(1-2a)(a-x)} \tag{5.18}$$

The Jacobian becomes zero at node 1 ($x = 0$) if:

$$1 - 8(1-2a)\,a = 0$$

i.e.
$$a = \tfrac{1}{4} \tag{5.19}$$

Substitution of (5.19) into (5.17) gives:

$$\xi = -1 + \sqrt{4x} \tag{5.20}$$

thus:
$$\frac{\partial \xi}{\partial x} = \frac{1}{\sqrt{x}} \tag{5.21}$$

The displacement along the element, $u$, is given by:

$$u = -\tfrac{1}{2}(-1+2\sqrt{x})(2-2\sqrt{x})\,u^{(1)} + (4\sqrt{x}-4x)\,u^{(2)} + \tfrac{1}{2}(-1+2\sqrt{x})(2\sqrt{x})\,u^{(3)} \tag{5.22}$$

The strain in the $x$-direction is then:

$$\frac{\partial u}{\partial x} = \frac{\partial u}{\partial \xi}\frac{\partial \xi}{\partial x} = -\tfrac{1}{2}\left[\frac{3}{\sqrt{x}} - 4\right] u^{(1)} + \left[\frac{2}{\sqrt{x}} - 4\right] u^{(2)} + \tfrac{1}{2}\left[-\frac{1}{\sqrt{x}} + 4\right] u^{(3)} \qquad (5.23)$$

which clearly shows the required singularity of the order $r^{-\frac{1}{2}}$.

This result suggests that the required $r^{-\frac{1}{2}}$ singularity in the 8-node quadrilateral elements can be achieved by placing the mid-side node near the crack edge at the quarter point (Figure 5.3). It is important to note that these elements are in no way special in the isoparametric coordinate space and therefore does not require any different computer sub-programs for, say, integration over the elements. The singularity conditions, however, only prevail along the sides of such elements and not on an arbitrary ray emanating from the point of singularity, i.e. the crack edge. But this can be resolved by collapsing a pair of nodes to form a triangular element and positioning the nodes as shown in Figure 5.3(b) (Hibbitt (1977)).

## 5.3 FURTHER NOTES ON THE EVALUATION OF STRESS INTENSITY FACTORS

In Section 5.1, it was mentioned that because the problems that are treated in the present work are symmetric about the crack plane, a physical boundary is used to replace the crack plane in the discretized model, thus reducing the physical problem size to be analysed. However, it must also be pointed out that with the formulation of the boundary integral equation method as described, a very important difficulty arises if the whole physical problem containing the planar crack is modelled. The two crack surfaces which lie on the same plane cannot be resolved by the boundary integral equations and the resultant equation matrix becomes singular (see, for example, Cruse (1975), Montulli (1975)). It is

therefore not possible to obtain any solution for the unknowns which are necessary for the evaluation of the stress intensity factor. This difficulty can, however, be circumvented by modifying the formulation described earlier, but at a greater computer cost.

Snyder & Cruse (1975) have presented a modified formulation of the boundary integral equation method for two-dimensional problems that incorporates a modified fundamental solution or Green's function which contains the full elastic representation of a flat, traction-free crack. The formulation inherently includes the presence of the crack without the need to model the crack surface geometry or crack face displacements and only the external physical boundary of the problem is modelled. Once the boundary solutions are obtained, the stress intensity factors for both Mode I and Mode II can be evaluated directly using these boundary data; the equations for doing so being derived with the use of the classical field solution with the $r^{-\frac{1}{2}}$ stress (strain) singularity. But for the general three-dimensional planar crack problem, no such special Green's function has hitherto been devised in closed form.

To overcome this difficulty in the three-dimensional crack problem, Weaver (1977) obtained additional integral equations for the crack surface in which the unknown functions are the dislocations across the crack. When these unknowns have been solved for, the stress intensity factors for all the three basic modes can be calculated directly from these data; the classical singular stress (strain) field solution having again been incorporated in the formulation.

These methods therefore result in specialized computer programs for crack problems; they will not be discussed any further. The quarter-point node shifting technique, discussed in the previous section, to create the $r^{-\frac{1}{2}}$ stress (strain) singularity at the crack front, can be easily

implemented on to any "conventional" boundary integral equation computer program based on the isoparametric formulation. Therefore, this technique is used most extensively in the present work.

## 5.4 NUMERICAL ANALYSIS OF FATIGUE CRACK GROWTH

To analyse the growth of a three-dimensional crack under cyclic loading is generally difficult primarily because the crack periphery is usually curved and no one value of $K_I$ may be assigned to characterize the whole crack front. In order to carry out such an analysis, the geometry of the growing crack is approximated with a finite number, $n$, of characteristic dimensions, $l_i$ ($i = 1,n$), referred to as degrees of freedom (DOF). The crack propagation is then described by keeping track of the $l_i$, each of which may be allowed to grow independently. The stress intensity factor around the crack front, $K_I(s)$, is similarly approximated with a set of discrete stress intensity factors, $K_{I_i}$, each associated with a DOF. Corresponding to each of these $l_i$, the empirical fatigue law, say, expression (2.29) may be written, resulting in a set of $n$ equations, i.e.

$$\frac{dl_i}{dN} = C_i \left(\Delta K_{I_i}\right)^{m_i} \tag{5.24}$$

where $C_i$ and $m_i$ are the empirically determined material constants corresponding to the $i$th DOF.

Fatigue crack growth prediction is accomplished by solving (5.24), the numerical algorithm for which is relatively simple and routine. The determination of stress intensity factors therefore forms the most important part in the numerical analysis of the fatigue crack problem. The task is then to model the propagating crack with a sufficient number of DOF at which points on the crack front the stress intensity factors are

determined. Further, an algorithm to compute all of the $K_{I_i}$ as a function of the changing crack geometry, $l_i$, must be obtained so that (5.24) can be formulated.

Perhaps the most obvious means of attack is to compute $K_I$ accurately by the direct methods, described in Section 5.1, at the different points characterizing the crack periphery. This is carried out for a series of actual propagating crack geometries. The $\Delta K_I$ can then be expressed as polynomial functions of the crack geometry for use in (5.24). Typically 8 to 15 computer runs, each for a different crack geometry, are required to obtain satisfactory polynomial functional fits. This procedure can therefore be very expensive.

The alternative indirect method for determining $K_I$ is relatively less costly, especially for this purpose, since it is less critically dependent upon the mesh refinement around the crack front. For each crack geometry, the strain energy $U$ and the integral of $(V^*/\sqrt{r^*})^2$ in (5.11) are calculated. $U$ may now be represented by a simple polynomial function and hence differentiated with respect to the crack area, $A$, for use in this equation. The stress intensity factor can therefore be obtained at any number of points along the crack front, over a range of crack geometries. The stress intensity factor range, $\Delta K_{I_i}$, corresponding to each of the characteristic dimensions, may then be expressed as a function of the crack geometry. Given these functions, crack growth can be calculated using (5.24).

The details of the numerical analysis of fatigue crack growth by this method will not be addressed any further in this chapter. Instead, they will be left to the next chapter where this procedure is used to predict the growth of a semi-elliptical surface crack in an internally pressurized thick-walled cylinder.

## 5.5 TEST PROBLEMS

A general three-dimensional boundary integral equation computer program for elastostatics, called BIESIF, was developed for the present work; the numerical formulation being that described in the previous chapter. Several test cases were treated to assess the accuracy of the solution by this numerical technique, especially for the stress intensity factor using the various schemes described earlier. The cases presented here are all fracture problems with known published results and hence are useful checks before problems without any known published solutions are treated.

Most of the data required for program BIESIF are for defining the position of the boundary nodes and elements used to model the physical problem. As the amount of these data is relatively small, no mesh generation programs were developed for any of the problems treated. These data are, however, checked with another computer program DRAW before they are used with BIESIF. The DRAW code enables the mesh discretization of the physical problem to be plotted using some of the off-line graphic facilities available at the Imperial College Computer Centre (ICCC). This enables a visual check of the description of the mesh. In fact, all the boundary mesh illustrations that are being presented were prepared by DRAW. Program DRAW also calculates the direction cosines of the unit outward normal to each of the surface elements, thus providing a further check of any error which may occur in the nodal numbering of each element.

The program BIESIF can be run on any of the Cyber 174, CDC 6500, 6600 or 7600 computers which are available in Imperial College. Where computing costs are compared for different computer runs in the present work, they are in terms of composite units used for accounting purposes in Imperial College. These units do take account of the different

performances of these machines and hence could provide a reasonable basis for comparing usage of computing resources.

### 5.5.1 Compact Tension Specimen

The compact tension specimen used for fracture toughness testing (ASTM E399-74) was represented by a single-edge-crack (SEC) specimen, as shown in Figure 5.4, with crack length $c$, width $W$, thickness $T$, and length $2H$, such that $c/W = T/W = 0.5$ and $H/W = 0.6$. Poisson's ratio was taken to be 0.3. Taking advantage of the two planes of symmetry, only one quarter of the specimen was modelled, the boundary mesh idealization being shown in Figure 5.5. It consists of 58 surface elements and 176 nodes. A uniform shear stress was applied to the $y = 0$ plane to produce a total vertical load $F$ in the $z$-direction. To investigate the effectiveness of the quarter-point node shifting described earlier, two computer runs were carried out for this problem: one with the conventional isoparametric elements and the other with the singularity elements around the crack front.

Figures 5.6 and 5.7 show how the stress intensity factors at the crack front were obtained by the extrapolation method with the use of crack face displacements. The results in Figure 5.6 were obtained with the conventional isoparametric elements, while those in Figure 5.7 were obtained with the singularity elements around the crack front. Plane strain conditions were assumed to prevail at all points along the crack front, except where it intersects the free surface; there, plane stress assumptions were made.

The variation of stress intensity factor along the crack front obtained from these two sets of results is shown in Figure 5.8, the values of $K_I$ are normalized by $(F\sqrt{c}/TW)$. Also shown is the two-dimensional plane

strain solution for the actual test specimen geometry obtained by Newman (1974) using the boundary collocation method, which is 13.68. Another two-dimensional plane strain solution (not shown in the figure), obtained by Srawley & Gross (1972) for the geometry modelled here, gives a value of 13.62. With the quarter-point node shifting at the crack front elements, normalized stress intensity factor values of 13.68 and 11.96 were obtained at the mid-plane ($X = 0$) and the free surface ($X = T/2$), respectively. The corresponding values obtained using the conventional isoparametric elements alone were 13.19 and 11.50, respectively, this being about 4% lower at the mid-plane compared with Newman's results. The improvement due to the singularity elements at the crack front are therefore significant.

The determination of the stress intensity factor by the extrapolation method using the stress data, obtained with and without the singularity elements, is shown in Figures 5.9 and 5.10, respectively. It can be seen that there is considerably more scatter in the results compared to those in Figures 5.6 and 5.7, so the least-square line fit for extrapolation to obtain the value of $K_I$ was subject to more arbitrariness. With the quarter-point node shifting at the crack front elements, the value of the normalized stress intensity factor at the mid-plane was 14.95, while that at the free surface was 11.10. The corresponding values without the singularity elements were 12.76 and 8.53, respectively. These results are thus inferior to those obtained by extrapolation of the displacement data which is consistent with the findings of most, if not all, workers in both boundary integral equation and finite element methods. The stress method of evaluating $K_I$ will therefore not be used hereafter. Further, singularity elements will be used to model the crack front in all the problems treated, unless otherwise stated.

To see the variation of the state of stress in the specimen, a lateral constraint parameter denoted by $\alpha_c$ may be defined and it is the ratio of the transverse stress, $\sigma_{xx}$, to the value for plane strain, $\nu(\sigma_{yy} + \sigma_{zz})$, i.e.

$$\alpha_c = \frac{\sigma_{xx}}{\nu(\sigma_{yy} + \sigma_{zz})} \tag{5.25}$$

The plot of this parameter across the thickness of the specimen at different radial distances in the same plane and ahead of the crack is shown in Figure 5.11. It can be seen that at the free surface, there is a total loss of lateral constraint at all radial distances ahead of the crack thus justifying the assumptions of plane stress conditions in the evaluation of stress intensity factors there. At a distance 0.0375 $c$ ahead of the crack front, the computed value of $\alpha_c$ at the mid-plane was 0.78. This parameter is expected to tend to unity as the crack front is approached, dropping dramatically to zero only as the free surface is reached. Figure 5.12 shows the variation of the ratio of the flow stress, $\tau_o$, to the mean stress, $\sigma_m$, across the thickness at a distance 0.15 $c$ ahead of the crack front. The flow stress and mean stress are given by:

$$\tau_o^2 = \frac{2}{9}\{\sigma_{xx}^2 + \sigma_{yy}^2 + \sigma_{zz}^2 - \sigma_{xx}\sigma_{yy} - \sigma_{yy}\sigma_{zz} - \sigma_{zz}\sigma_{xx} + 3(\sigma_{xy}^2 + \sigma_{yz}^2 + \sigma_{zx}^2)\} \tag{5.26}$$

$$\sigma_m = \frac{1}{3}(\sigma_{xx} + \sigma_{yy} + \sigma_{zz}) \tag{5.27}$$

The ratio $\tau_o/\sigma_m$ can be seen to increase rapidly as the free surface is approached, reflecting the loss in lateral constraint there. As this ratio increases, there is increased tendency to plastic flow or a decreased

tendency from brittle fracture.

Another problem was analysed using the same specimen. In this case, a uniform tensile stress, $\sigma_o$, was applied at the $Z = \pm H$ planes. The stress intensity factors were again calculated using the displacement method and their variation across the thickness of the specimen is shown in Figure 5.13. The results are qualitatively similar to those shown in Figure 5.8. Stress intensity factors were normalized by $\sigma_o \sqrt{\pi c}$ in this case, and at the mid-plane, the value obtained was 2.93, while that at the free surface was 2.66. Again, plane strain conditions were assumed to prevail at all nodal points along the crack front, except at the free surface.

No results for the same geometry and loading are apparently available in the literature for comparison. But Bowie (1973), using the conformal mapping method, obtained a two-dimensional plane strain solution of 2.86 for a specimen with the same crack depth but with $H/W = 1$, and a value of 3.01 when $H/W = 0.5$. As $K_I$ is expected to decrease with increasing $H/W$, the results obtained here must therefore be very close to the two-dimensional plane strain solution. Figure 5.14 again shows rapid increase in the ratio of $\tau_o/\sigma_m$ as the free surface is approached, which reflects the loss of lateral constraint there.

### 5.5.2 Embedded Penny-Shaped Crack in a Square Prism

For a penny-shaped crack of radius $c$ in an infinite body under uniform tension, $\sigma_o$, normal to the plane of the crack at infinity, Sneddon (1964) showed that $K_I = 2\sigma_o \sqrt{c/\pi}$, i.e. approximately $1.128\ \sigma_o \sqrt{c}$, around the crack front. In using this problem as a test case, the body is taken to be a square prism with the ratio of the crack radius to the prism width equal to 0.1. As this crack is small compared to the size of the prism,

the computed $K_I$ should not differ much from the analytical solution. There are three planes of symmetry so only one-eighth of the physical problem was modelled. Both the displacement method and the indirect (energy) method were used to obtain values of $K_I$ around the crack front. In the extrapolation method, the mesh shown in Figure 5.15 was used; this mesh being made up of 61 surface elements and 185 nodes, of which 11 elements were used to represent the crack surface. The mesh in Figure 5.16 was used for the indirect method; this mesh consists of 53 surface elements and 161 nodes, of which only 5 elements were used to model the crack surface.

The computed values of $K_I/\sigma_o\sqrt{c}$ by the displacement method at $22\frac{1}{2}^o$ intervals around the crack front were 1.131, 1.128, 1.132, 1.128 and 1.131, with plane strain conditions being assumed. Agreement with the analytical solution is indeed excellent, the maximum deviation being less than 0.4%. The values of $K_I/\sigma_o\sqrt{c}$ obtained by the indirect method at $30^o$ intervals around the crack front were 1.118, 1.116, 1.118, which are all within 1.2% of the analytical solution. The mesh in Figure 5.16 is too coarse at the crack front region for values of $K_I$ to be evaluated by the extrapolation method, although it appears adequate for the indirect method. But with this mesh discretization, the indirect method used about 5% more computer units for this problem, even though the solutions were not as good!

### 5.5.3 Corner Quadrant Crack in a Long Square Prism

To solve the problem of a corner quadrant crack embedded in a long square prism which is subject to a uniform tensile stress $\sigma_o$ in the direction normal to the crack, the same boundary mesh in Figure 5.15 and in Figure 5.16 were used. There is now only one plane of symmetry,

i.e. the crack plane, so each mesh represents a half of the physical problem. The width of the square prism $W$ was taken to be 5 times the crack radius $c$, and Poisson's ratio was 0.3. The mesh representation in Figure 5.15 was again used for the displacement method of evaluating $K_I$, while that in Figure 5.16 for the indirect method.

Figure 5.17 shows the computed variation of $K_I$ along the crack front, results obtained by both the extrapolation procedure and the indirect method being presented. Also shown are results obtained by Tracey (1973) for a quadrant crack in a quarter circular cross-section prism with diameter ratio of 0.2. As the crack is small compared with the size of the prism, the computed results should be close to those obtained by Tracey, which indeed they are. The results presented are all based on plane strain assumptions at the crack front and they are normalized by the Sneddon solution for the buried penny-shaped crack, i.e. $2\sigma_o\sqrt{c/\pi}$. The normalized values of $K_I$ obtained by Tracey at the surfaces are 1.28, while that at the middle of the crack front, i.e. $\theta = 45^o$ (Figure 5.17), is 1.10. The corresponding boundary integral equation results are 1.29 and 1.09, respectively, by the extrapolation method, and 1.29 and 1.08 by the indirect method. If plane stress assumptions were made at the free surfaces, the computed results here gave values of 1.17 there.

### 5.5.4 Semi-Circular Surface Crack in a Long Rectangular Prism

The next problem to be treated is one which has been investigated by a great many numerical analysts in fracture mechanics. It is the problem of a semi-circular surface crack in a rectangular prism which is subject to a uniform tensile stress $\sigma_o$ in the direction normal to the crack plane. The radius of the crack $c$ was taken to be one-fifth of

the thickness and one-tenth of the width and the length of the prism. The boundary mesh in Figure 5.15 was again used to model the problem. It represents a quarter of the physical problem as there are two planes of symmetry. Poisson's ratio was taken to be 0.3.

Stress intensity factors were obtained by both the displacement method and the indirect method using the same boundary mesh; the computed variation of $K_I$ along the crack front is shown in Figure 5.18, the values being normalized by $2\sigma_o\sqrt{c/\pi}$. Also shown are the results obtained by Smith & Alavi (1971) for a semi-circular crack in a semi-infinite body, and those presented by Tracey (1973) for a semi-circular surface crack in a rod of semi-circular cross-section (with a ratio of crack radius to rod radius of 0.2). The present results should be in close agreement with these other solutions as the surface crack is small compared with the size of the prism, which indeed they are. The values of $K_I$ obtained by the displacement method and the indirect method differed by less than 0.5% for all the points along the crack front at which they were evaluated. At the point of maximum penetration, the normalized value of $K_I$ obtained was 1.02, remaining fairly constant along most of the crack front until the free surface is approached, whereupon the normalized value of $K_I$ rapidly increased to a value of 1.28 there. The corresponding values obtained by Smith & Alavi (1971) and by Tracey (1973) are 1.04 and 1.21, and 1.04 and 1.26, respectively. In all the results shown in Figure 5.18, plane strain conditions were assumed in calculating $K_I$. If plane stress assumptions were made at the free surface, the present results gave a value of 1.16 for the normalized $K_I$.

Figure 5.19 shows the variation of the flow stress to mean stress ratio, $\tau_o/\sigma_m$, with the angular orientation around the crack front for different radial distances ahead of the front, the angle $\theta$ being

defined in Figure 5.18. A feature shown in this figure which is characteristic of the stress state near the free surface, also seen previously in Figures 5.12 and 5.14 is that the flow stress to mean stress ratio increases rapidly as the surface is approached. This reflects the loss of lateral constraint there. Further, with decreasing radial distance ahead of the crack front, this ratio decreases significantly at all angular orientations, except perhaps near the free surface. At a distance of 0.05 $c$ ahead of the front, the computed value of $\tau_o/\sigma_m$ was 0.51 at $\theta = 0^o$; this value increased to 0.66 at 0.20 $c$ and 0.88 at 0.35 $c$ for the same angular position. These results are consistent with the assumptions of plane strain state of stress around the crack periphery, except where it intersects the free surface; there, plane stress conditions should be assumed.

The indirect method used about 48% more computer units than the direct method, employing the same mesh idealization. The level of refinement of the mesh, especially around the crack front, for the indirect method was in fact more than adequate for the order of accuracy sought in practice. But this percentage figure serves to show the savings in computing resources that were due to not re-establishing completely the equation matrix for the second computer run using the energy method for evaluating $K_I$.

## 5.6 SINGULARITY ANALYSIS

So far, the concepts of fracture mechanics discussed have been based upon the planar analyses such as those advanced by Inglis and Griffith described in Chapter 2. While it is generally recognized that in the vicinity of a planar crack, plane strain conditions prevail, the presence of a free surface in three-dimensional problems does act to reduce the

plane strain constraint. This has been shown in the test problems above, as well as in experiments. Based upon the classical plane analyses, it has also been hitherto assumed that the stress singularity for all points around the crack front is of order $r^{-\frac{1}{2}}$. Therefore, singularity elements were used in numerical analyses to impose such a stress behaviour in the vicinity of the crack periphery. But where the crack intersects the free surface, this may not be representative of the actual behaviour of the elastic solution at that point. Indeed, the question as to whether the usual $r^{-\frac{1}{2}}$ singularity in stress exists for the intersection point has, in recent years, been much debated and, to date, is still an unresolved issue. If at these points the stress singularity is no longer of the inverse square root form, then doubts must be expressed over the meaning of the numerical $K_I$ values evaluated there.

Hartranft & Sih (1970) investigated analytically the three-dimensional stress behaviour in the vicinity of the crack border in a thick plate, using variational principles. They emphasized, however, that the analysis is still only an approximation to the truly three-dimensional problem. In the analysis, they assumed that the local stress field in the interior to the plate is in a state of plane strain, and the direct stress normal to the plate faces was forced to vanish in the boundary-layer sense. Their results show that the state of stress depends on the ratio of the plate thickness, $T$, to the crack length, $c$, and a dimensionless parameter characterizing the stress distribution across the thickness. Further, the stress intensity factors in this thin boundary layer near the free surface decrease very rapidly to zero at the surface. The boundary layer thickness was estimated to be $T/(4 + 16\ T/c)$ but no attempt was made to determine the nature of the stress singularity there, although the assumptions imply that the singularity is one weaker than $r^{-\frac{1}{2}}$.

Folias (1975) showed analytically that in the vicinity of the crack front/free surface intersection, displacements are proportional to $r^{(\frac{1}{2}-2\nu)}$ and the stresses are proportional to $r^{-(\frac{1}{2}+2\nu)}$. This result implies that displacements at these points are also singular for Poisson's ratio greater than $\frac{1}{4}$. Folias therefore suggested that linear elastic analysis may be inadequate to predict the actual behaviour at the surface. Benthem (1975), in his semi-analytical eigenfunction expansion investigation of the state of stress at the vertex of a quarter-infinite crack in half-space, also showed that the local direct stresses normal to the crack-plane is singular and that the order of singularity depends on the Poisson's ratio. His results showed, however, that the local stresses are proportional to $r^{-\bar{n}}$ with $\bar{n} < \frac{1}{2}$ for the practical range of Poisson's ratio, except at $\nu = 0$ when $\bar{n} = \frac{1}{2}$ exactly. This implies that for positive values of $\nu$, the stress intensity factor as conventionally defined vanishes at the intersection with the free surface, despite the fact that the stresses are still singular.

An investigation similar to that by Benthem (1975) was also carried out by Bazant & Estenssoro (1977,1979), but the numerical determination of the stress singularity index was by a special finite element method. A variational principle for the angular variation of displacements on a unit sphere with its centre at the singular point was derived. Based on this principle, finite element concepts were applied to the unit sphere to obtain a non-linear eigenvalue problem for the singularity index. The results obtained by Bazant & Estenssoro (1977,1979) agree to within about 0.4% with those obtained by Benthem (1975) for Mode I cracks. Results for Modes II and III were also obtained by the former authors for this intersection point on a half-space, where it was suggested that these two basic modes cannot exist independently.

Other numerical investigations of this problem have been carried out by several authors (see, for example, Cruse & Van Buren (1971), Hartranft & Sih (1973), Raju & Newman (1977,1979)), but without elucidating the nature of the singularity other than to suggest that it may not be of order $r^{-\frac{1}{2}}$. With considerable refinement in the numerical discretization of the physical problems they solved, which include edge cracks and semi-elliptical surface cracks in plates, these authors found that the $K_I$ solutions near the crack front/free surface intersection were quantitatively as well as qualitatively different from the solutions already in the literature. A dramatic drop in the value of $K_I$ was observed in this small region near the free surface, a feature which had not showed up in the results before; away from this region, the solutions were in close agreement.

An attempt to determine the order of the singularity numerically by the boundary integral equation method at these intersection points will now be presented. Two problems were considered, namely, (i) a centre-crack specimen in uniform tension, and (ii) the semi-circular surface crack problem similar to that in Section 5.5.4. The quarter-point shifting of the mid-side nodes of the elements adjacent to the crack front were not employed in these cases, and the boundary meshes made more refined, especially in the region near the intersection in order to obtain good resolution of the variables there.

### 5.6.1 Centre-Crack Tension (CCT) Specimen

A centre-crack tension specimen of length $2H$, width $2W$, thickness $T$ and crack length $2c$ was analysed, with $H/W = 0.875$, $c/W = 0.5$ and $T/c = 3$. Taking advantage of symmetry, one-eighth of the specimen was modelled, the region being $x \geq 0$, $y \geq 0$ and $z \geq 0$ in Figure 5.21.

The boundary mesh idealization is shown in Figure 5.20; it contains 80 quadrilateral elements (with relatively small ones being used near the free surface) and 242 nodal points. Five different values of Poisson's ratio were considered, namely $\nu$ = 0.1, 0.2, 0.3, 0.4 and 0.5.

To obtain the order of singularity in stresses at the surface, the crack face displacements in the vicinity of the crack front were assumed to be given by:

$$V = \frac{4C_I}{E\sqrt{2\pi}} r^{(1-\bar{n})} \tag{5.28}$$

so that stresses, $\sigma \sim r^{-\bar{n}}$. In the event that $\bar{n} = \frac{1}{2}$, $C_I$ would be equivalent to $K_I$.

Table 5.1 shows the variation with Poisson's ratio of the stress (strain) singularity index, $\bar{n}$, at points along the crack front approaching the free surface from the mid-thickness plane. These values were obtained by least-square fitting of straight line portions of logarithmic plots of computed crack-face displacements in the vicinity of the crack periphery, against distance from it. Such logarithmic plots for the mid-thickness plane and the free surface are shown in Figures 5.22 and 5.23, respectively. The displacements in each plot have been normalized by the maximum crack-face displacement in the ray emanating from the front along which the distance $r$ was measured. At points remote from the surface, the computed values of $\bar{n}$ are very close to the expected value of $\frac{1}{2}$, thus providing confirmation of the level of accuracy obtainable. At and near the free surface, however, the value of $\bar{n}$ falls significantly below $\frac{1}{2}$, a trend which becomes more pronounced with increasing Poisson's ratio. For example, the value of $\bar{n}$ at the surface was found to be 0.393 with $\nu$ = 0.5. Table 5.2 presents the computed values of $C_I$ at the surface corresponding to each of the values of Poisson's ratio.

The variations of computed values of $K_I$ with distance from the mid-thickness of the specimen for different values of Poisson's ratio are shown in Figure 5.21. The effect of increasing the Poisson's ratio can be seen to increase the magnitude of $K_I$ at a given point on the crack front, except perhaps at the free surface. For all values of $\nu$ considered, $K_I$ increases from the mid-thickness to a position very close to the free surface after which it drops rapidly as the free surface is approached. The computed value of $K_I$ at the mid-thickness plane, for $\nu = 0.1$, was $1.336\ \sigma_o \sqrt{\pi c}$, increasing to $1.418\ \sigma_o \sqrt{\pi c}$ for $\nu = 0.5$; $\sigma_o$ being the applied uniform tensile stress. Shah & Kobayashi (1973) suggested that for the practical range of $\nu$, its effect on the value of $K_I$ would be small (within about 6% variation for the range between $\nu = 0.1$ and $\nu = 0.4$). Although the computed results here show the difference in $K_I$ values for different $\nu$ to be within about 6% of each other at the mid-thickness plane, near the free surface the difference is as high as 30%. Raju & Newman (1977) have also solved this problem with the same geometry, but only for $\nu = 1/3$, using a very refined finite element mesh; their results are shown in Figure 5.24. Using the results for $\nu = 0.3$ here for comparison, there is only a marginal difference in the value of $K_I$ at the mid-thickness plane which is $1.403\ \sigma_o \sqrt{\pi c}$ as compared to their value of $1.401\ \sigma_o \sqrt{\pi c}$. But near the free surface, the computed values are about 7% higher than those obtained by them. The solutions are nevertheless in very good qualitative agreement with each other.

The estimate of the size of the boundary layer from the analysis by Hartranft & Sih (1970), mentioned earlier, gives a thickness of $0.019\ T$; this also agrees reasonably well with the present results which show the values of $K_I$ dropping very rapidly at a distance of between $0.033\ T$ and $0.017\ T$ from the free surface for different values of $\nu$.

Figure 5.25 shows the variation of the lateral constraint factor $\alpha_c$, defined in (5.25), with the distance from the mid-thickness plane. The plots are almost identical for all values of $\nu$, so only this figure for $\nu = 0.3$ is shown. The value of $\alpha_c$ can again be seen to tend to unity as the crack front is approached, except near the free surface where there is a rapid loss of lateral constraint with $\alpha_c$ dropping to zero. This feature is again reflected in the plot of the flow stress to mean stress ratio, $\tau_o/\sigma_m$, with the distance from the mid-thickness at a distance of 0.1 $c$ from the crack-front shown in Figure 5.26. Near the free surface, this ratio increases very rapidly for all the values of $\nu$ considered after being at a fairly constant value, which is different for each $\nu$, for most of the thickness. These constant values of $\tau_o/\sigma_m$ decreased with increasing values of Poisson's ratio as expected.

### 5.6.2 Semi-Circular Surface Crack in a Long Rectangular Prism

For this problem, the geometry is identical to that considered in Section 5.5.4 with the exception that the radius of the crack front is now 30% of the prism thickness. The boundary mesh was altered and is shown in Figure 5.27; it contains 81 elements and 245 nodal points. This problem was chosen because, although the intersection is at right angles, the crack front is curved, a feature which may affect the nature of the singularity at the free surface. The effects of varying the Poisson's ratio, using the same five values as in the above problem, were analysed.

Figure 5.28 shows the computed variations of $K_I$ along the crack front for the range of values of $\nu$ considered. The angular coordinate, $\theta$, is measured in the plane of the crack from $\theta = 0^o$ at the point of maximum penetration to $\theta = 90^o$ at the free surface. Increasing the Poisson's ratio again increases the values of $K_I$ at all points of the

crack front, except perhaps at the free surface. In all cases, $K_I$ increases gradually from $\theta = 0^o$ to about $\theta = 70^o$, after which the increase is more rapid until a peak is reached just before the surface, and a rapid drop again occurs. The rapid decrease in the value of $K_I$ occurs in about the last $3^o$; this is consistent with the results obtained by Hartranft & Sih (1973), who used the alternating method with considerable refinement in the solution procedure to solve the problem of a semi-circular surface crack in a semi-infinite body. It is also in agreement with the results of Raju & Newman (1979), who investigated the effect of refining the finite element mesh on the $K_I$ solutions, particularly near the free surface, for this problem but with $c/W = 0.2$. At the point of maximum penetration, the computed values of $K_I$, normalized by $2\sigma_o\sqrt{c/\pi}$, are 0.99, 1.01, 1.03, 1.05 and 1.09 for $\nu = 0.1$, 0.2, 0.3, 0.4 and 0.5, respectively, which is an increase of about 10% over this range of $\nu$.

The displacement field in the vicinity of the crack front was again assumed to be given by (5.28). Logarithmic plots of the crack face displacements corresponding to $\theta = 0^o$ and $\theta = 90^o$ versus the distance away from the crack periphery are shown in Figures 5.29 and 5.30, respectively. Table 5.3 presents the computed singularity index, $\bar{n}$, at points along the crack front. These results again show a reducing order of singularity significantly less than $\bar{n} = \frac{1}{2}$, at and near the free surface for increasing values of Poisson's ratio. The coefficient $C_I$ in (5.28) at the free surface was also computed for each value of $\nu$ and the results are shown in Table 5.4.

### 5.6.3 Further Discussion

Despite the differences in crack front geometry and mesh design, the values of $\bar{n}$ obtained at the free surface for the two problems are very

similar. For the purpose of comparison with the semi-analytical results obtained by Benthem (1975), these values are plotted against Poisson's ratio in Figure 5.31. Both sets of results obtained here do, however, predict order of singularity somewhat higher than Benthem obtained, the greatest difference in $\bar{n}$ of about 16% being for $\nu = 0.5$.

Although the lower order of singularity at and near the free surface implies a vanishing $K_I$ there, it is extremely difficult for any numerical method to detect such a zero value unless such a condition is imposed on the analysis. Until an orderly analytical attack on the problem can be provided, the present numerical approach seems incapable of addressing this question much further. Nevertheless, it is anticipated that as the free surface effect appears to be restricted to the small boundary layer region, the discrepancies introduced by neglecting this region on the overall $K_I$ distribution along the crack front would be small enough to be disregarded for engineering purposes. This seems a practical proposition and has been evidently justified by numerous successful pieces of work on fatigue analysis of surface cracks which have not taken into account this change in the order of singularity at the free surface (see, for example, Bergan & Aamodt (1974), Cruse & Besuner (1975), Besuner (1977)). Therefore, this issue will not be discussed any further in the present work.

TABLE 5.1

Stress (Strain) Singularity Indices, $\bar{n}$ ($\sigma \simeq r^{-\bar{n}}$), at the Crack Front of a Centre-Crack Tension Specimen

| Poisson's Ratio, $\nu$ | Distance from Mid-Thickness Plane, $x/(T/2)$ (see Figure 5.21) | | | | | | | | |
|---|---|---|---|---|---|---|---|---|---|
| | 0 | 0.233 | 0.467 | 0.633 | 0.8 | 0.867 | 0.933 | 0.967 | 1.0 |
| 0.1 | 0.507 | 0.492 | 0.495 | 0.507 | 0.509 | 0.495 | 0.495 | 0.499 | 0.495 |
| 0.2 | 0.507 | 0.492 | 0.495 | 0.507 | 0.491 | 0.508 | 0.495 | 0.499 | 0.480 |
| 0.3 | 0.493 | 0.500 | 0.499 | 0.509 | 0.506 | 0.505 | 0.501 | 0.485 | 0.466 |
| 0.4 | 0.497 | 0.506 | 0.500 | 0.509 | 0.498 | 0.498 | 0.480 | 0.464 | 0.434 |
| 0.5 | 0.496 | 0.506 | 0.497 | 0.503 | 0.498 | 0.492 | 0.461 | 0.436 | 0.393 |

TABLE 5.2

Variation of $C_I$ at the Free Surface with Poisson's Ratio (Centre-Crack Tension Specimen)

| Poisson's Ratio, $\nu$ | $\dfrac{C_I}{\sigma_o \sqrt{\pi\, c}}$ |
|---|---|
| 0.1 | 1.329 |
| 0.2 | 1.439 |
| 0.3 | 1.503 |
| 0.4 | 1.647 |
| 0.5 | 1.804 |

TABLE 5.3

Stress (Strain) Singularity Indices, $\bar{n}$ ($\sigma \simeq r^{-\bar{n}}$), at the Crack Front of a Semi-Circular Surface Crack in a Rectangular Prism

| Poisson's Ratio, $\nu$ | $\theta$ (see Figure 5.28) | | | | |
|---|---|---|---|---|---|
| | 0° | 40° | 70° | 85° | 90° |
| 0.1 | 0.500 | 0.505 | 0.500 | 0.501 | 0.486 |
| 0.2 | 0.500 | 0.502 | 0.502 | 0.500 | 0.476 |
| 0.3 | 0.497 | 0.504 | 0.503 | 0.494 | 0.468 |
| 0.4 | 0.498 | 0.497 | 0.493 | 0.473 | 0.435 |
| 0.5 | 0.492 | 0.496 | 0.472 | 0.420 | 0.395 |

TABLE 5.4

Variation of $C_I$ at the Free Surface with Poisson's Ratio (Semi-Circular Surface Crack in Rectangular Prism)

| Poisson's Ratio, $\nu$ | $\frac{C_I}{2\,\sigma_o\,\sqrt{c/\pi}}$ |
|---|---|
| 0.1 | 0.933 |
| 0.2 | 0.940 |
| 0.3 | 0.968 |
| 0.4 | 1.020 |
| 0.5 | 1.056 |

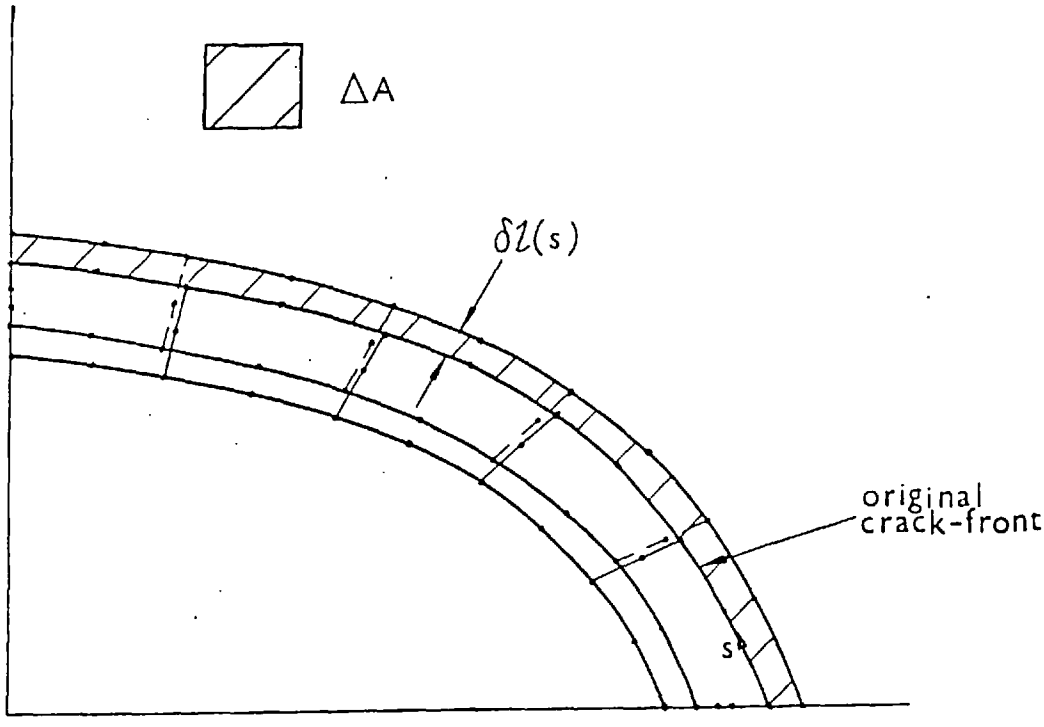



Figure 5.1: Perturbation of crack front

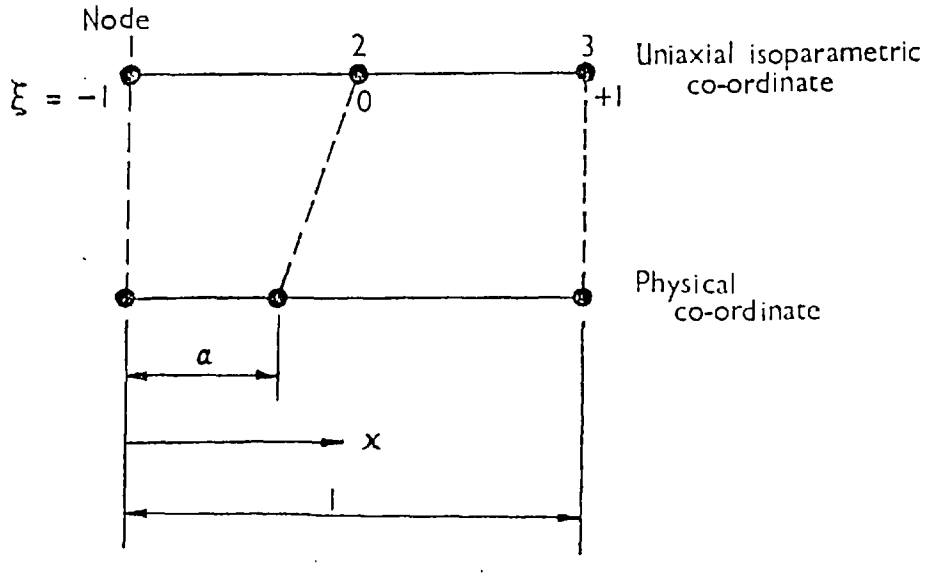
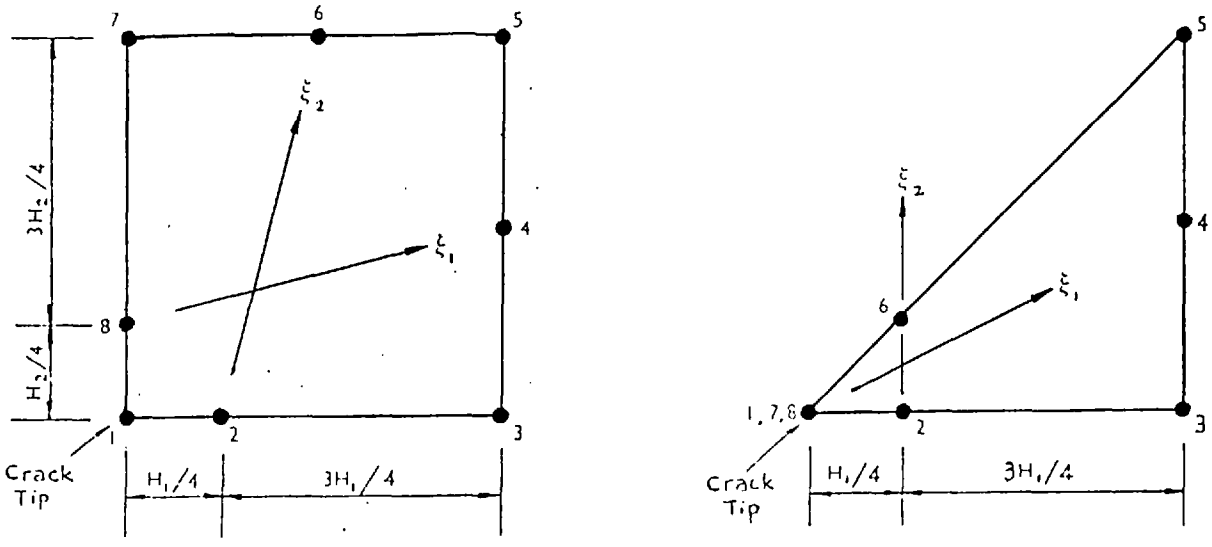



Figure 5.2: Mapping of physical to isoparametric coordinates




(a) Distorted quadrilateral element

(b) Collapsed quadrilateral (triangular) element

Figure 5.3: Isoparametric elements with $r^{-\frac{1}{2}}$ singularity

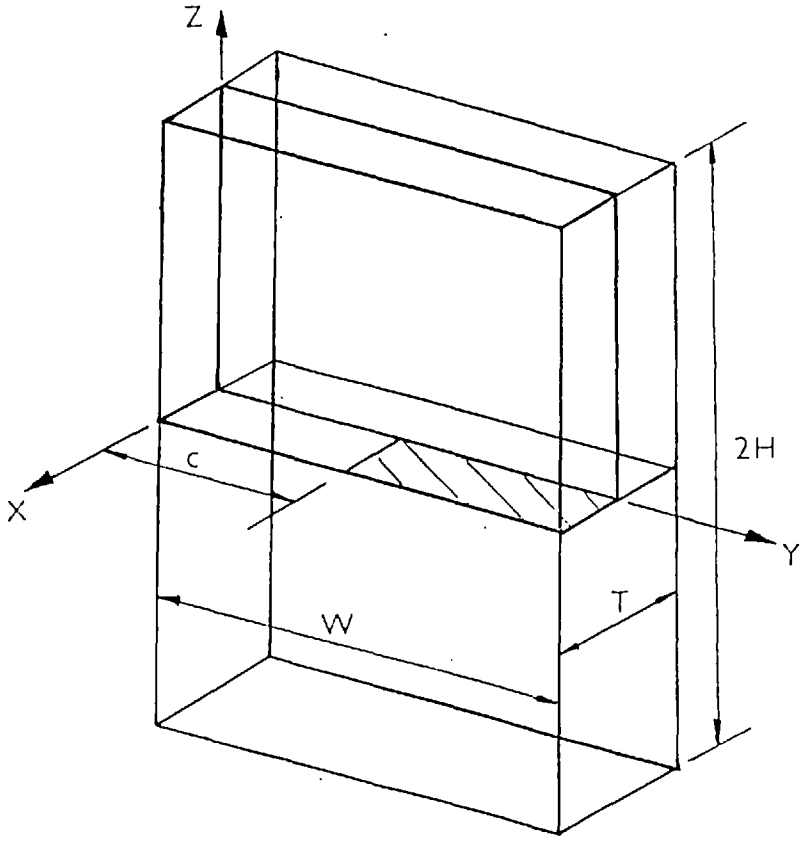



Figure 5.4: Single-edge crack (SEC) specimen

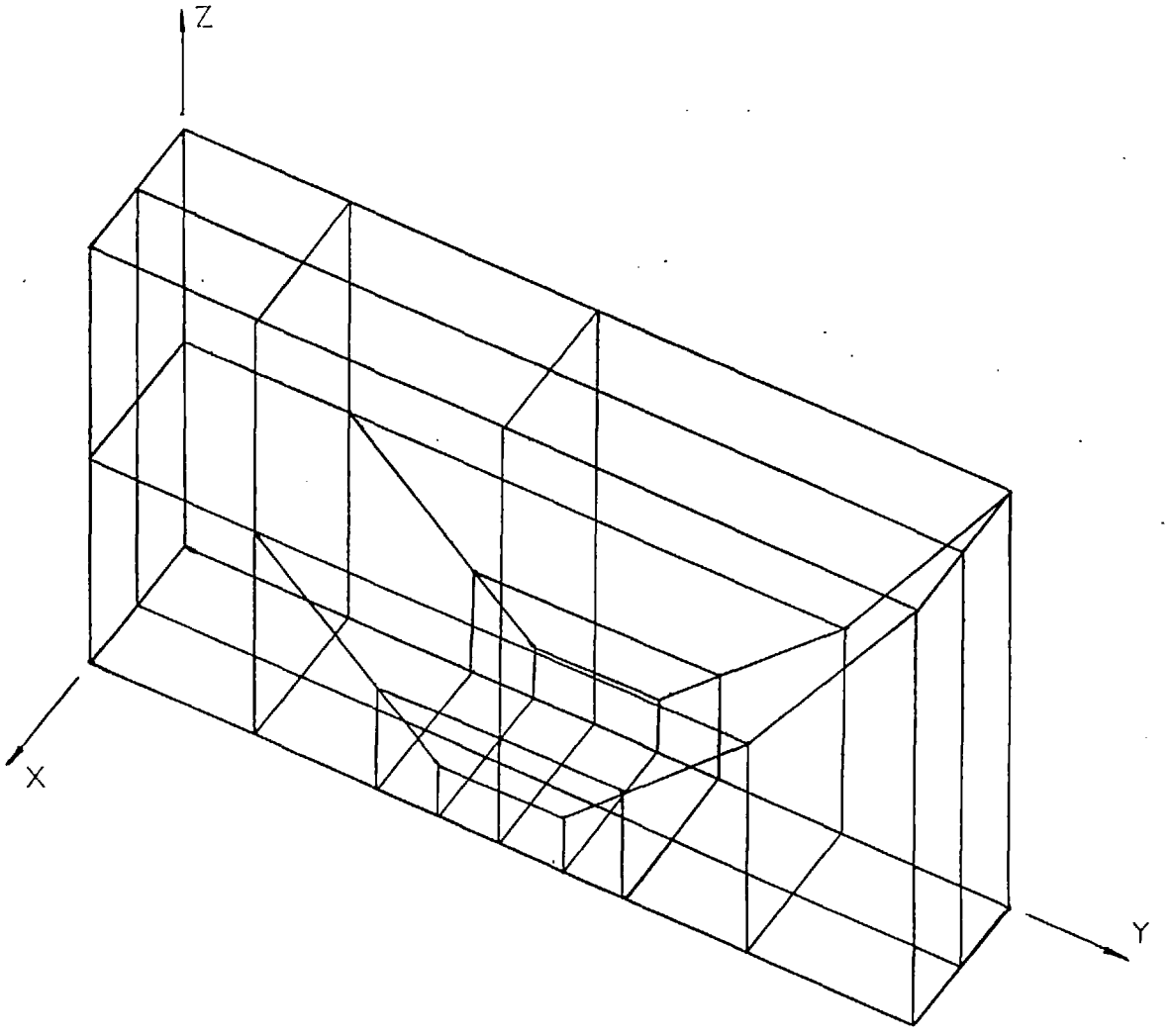



Figure 5.5: Boundary mesh idealization for SEC specimen

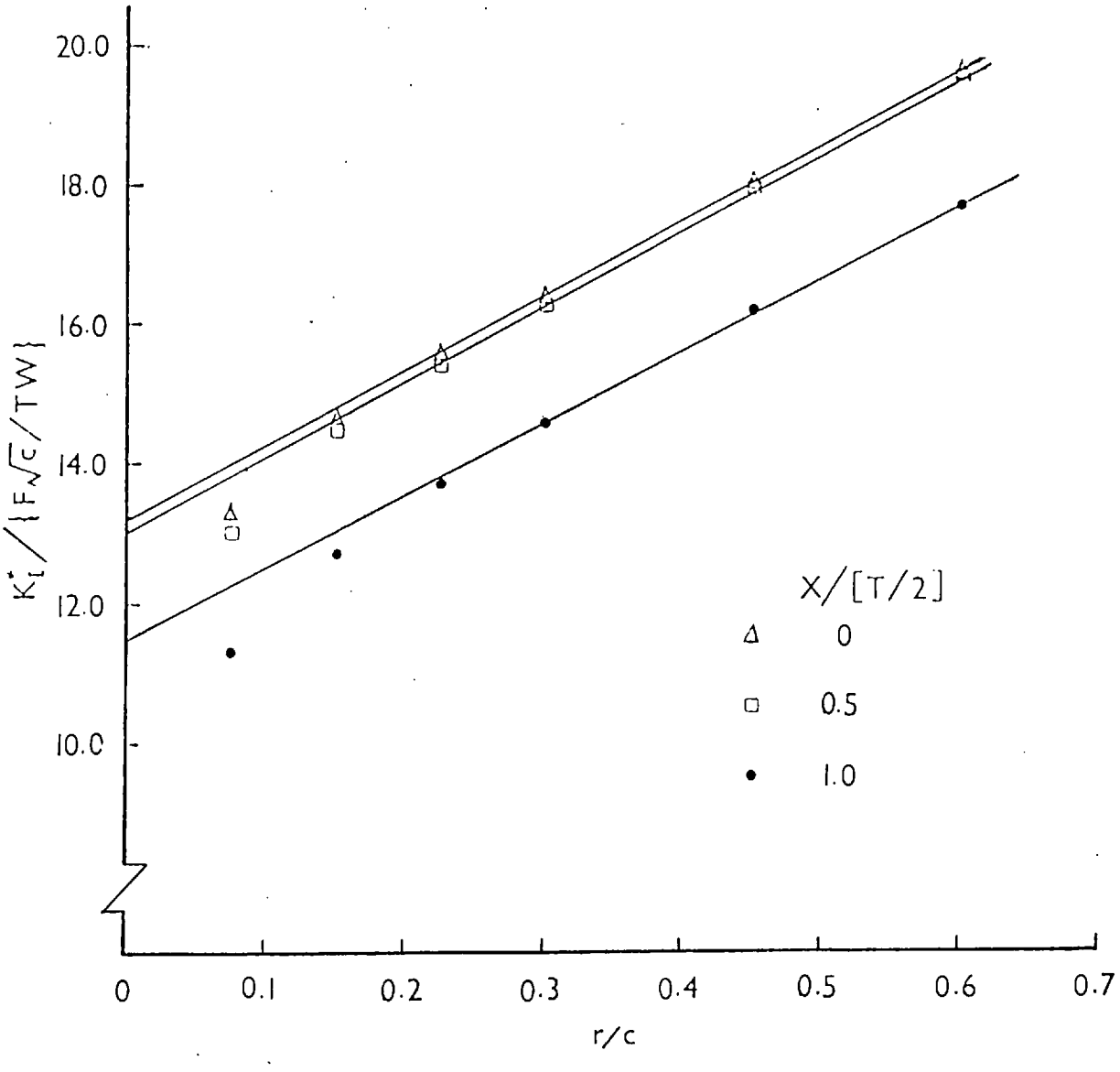



Figure 5.6: Plot of $K_I^*/(F\sqrt{c}/T\,W)$ versus $(r/c)$ for SEC specimen (conventional elements)

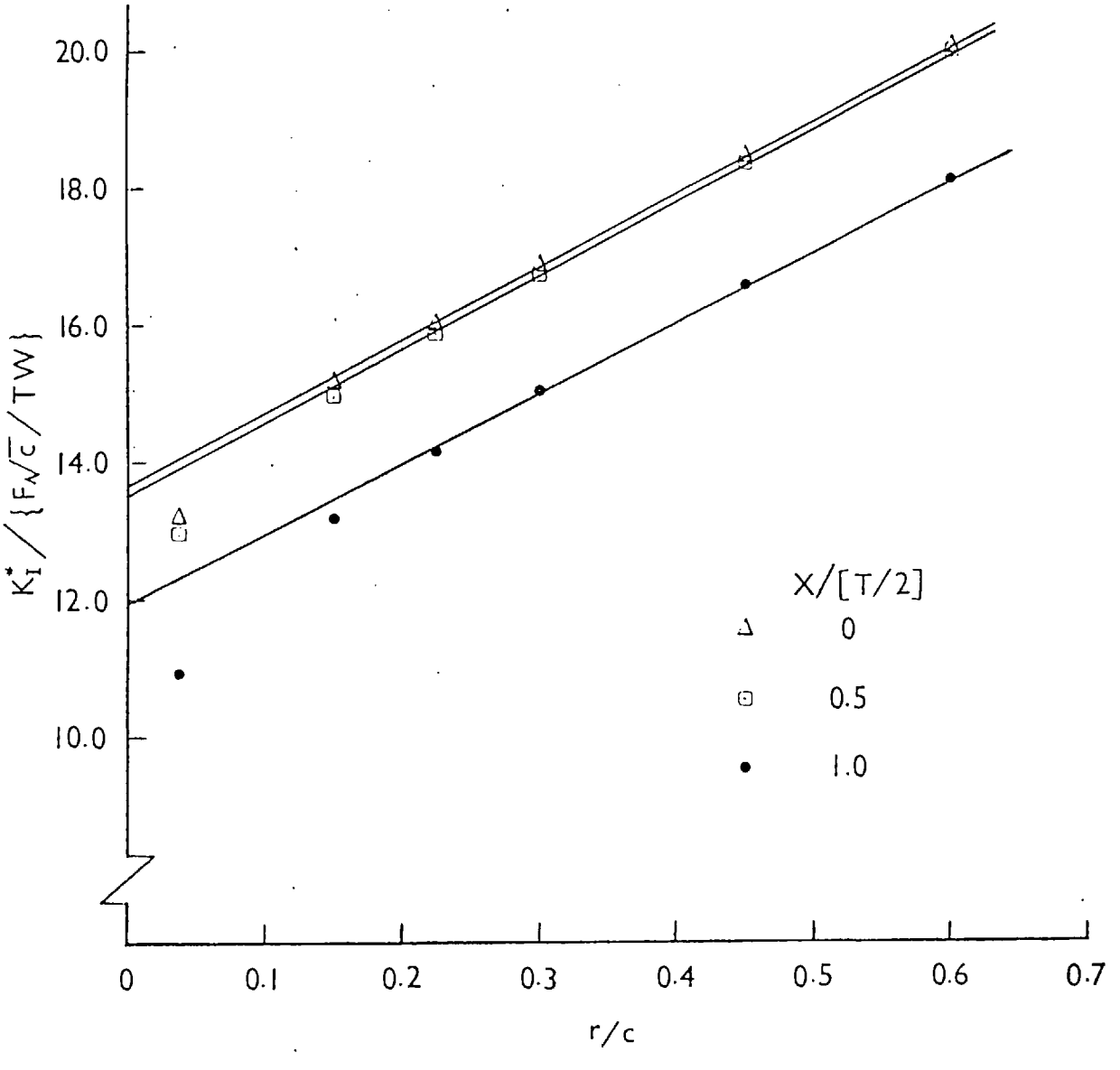



Figure 5.7: Plot of $K_I^*/(F\sqrt{c}/T\,W)$ versus $(r/c)$ for SEC specimen (singularity elements)

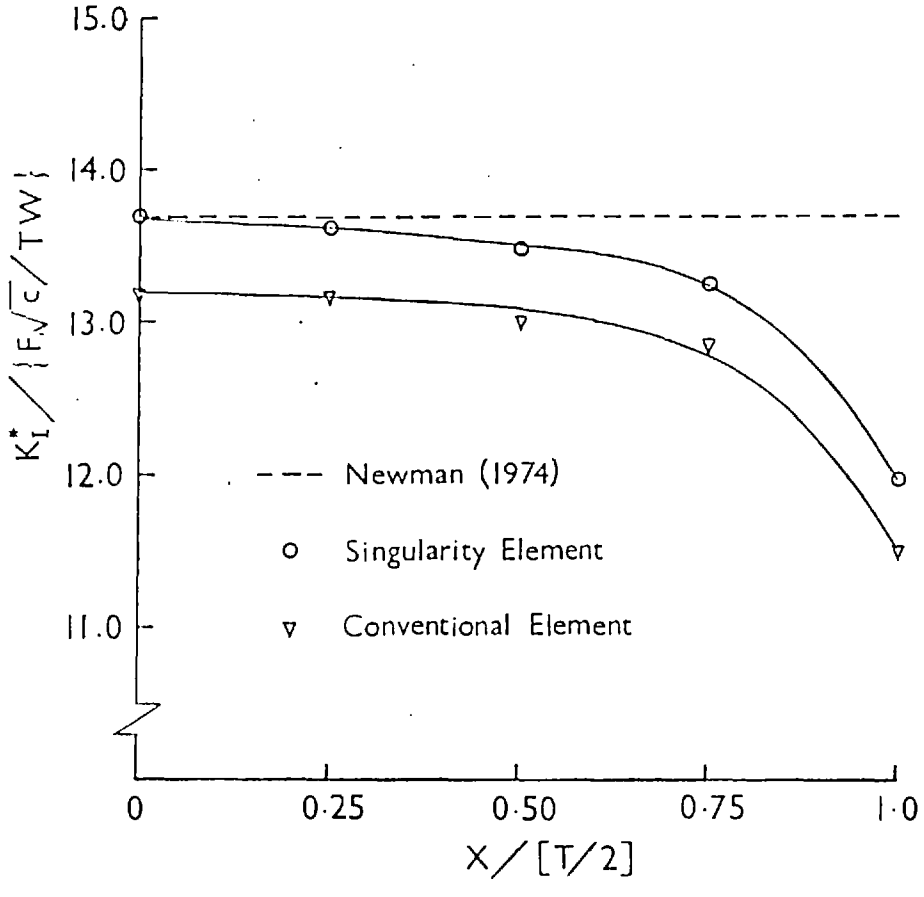



Figure 5.8: Variation of $K_I$ with thickness for SEC specimen

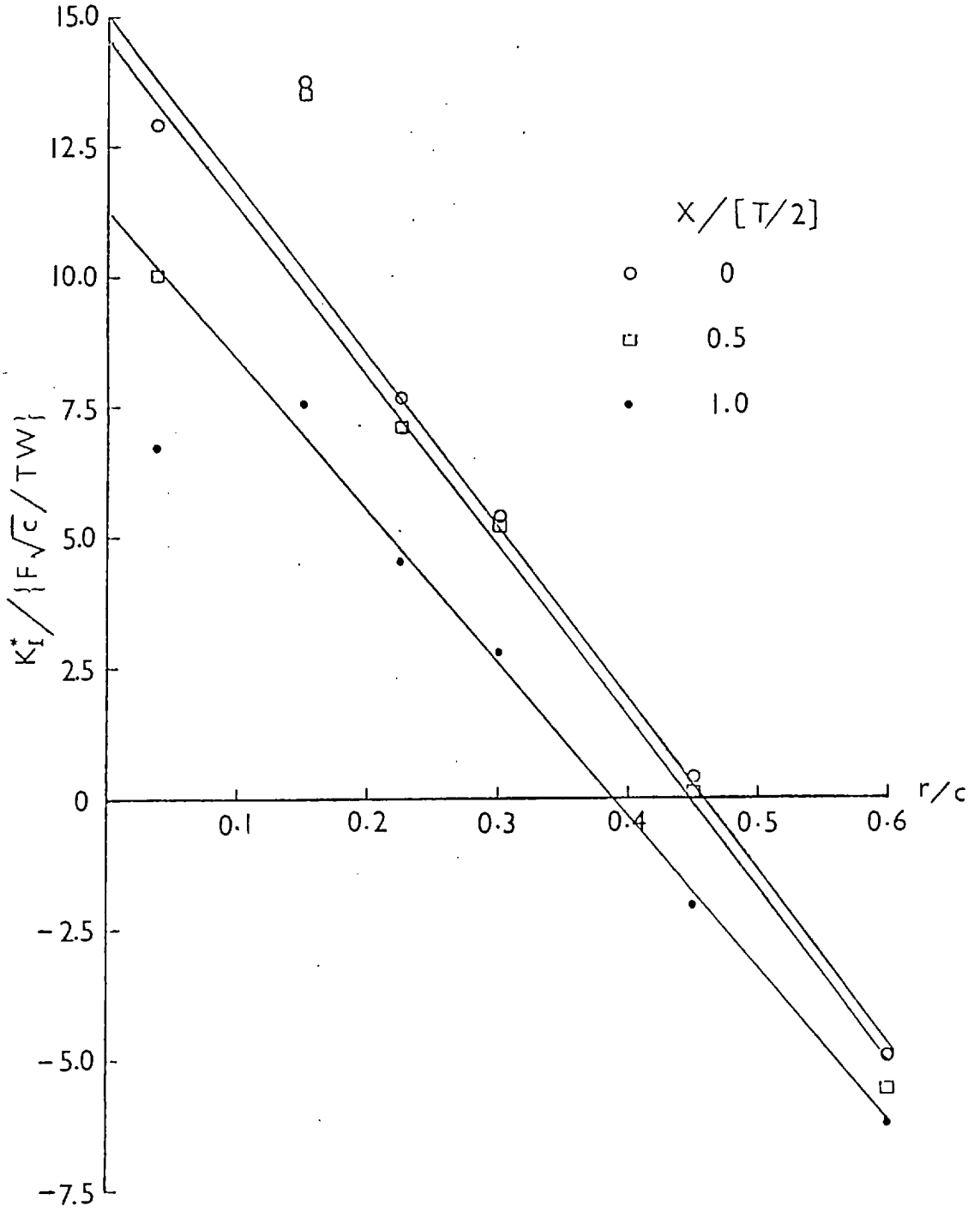



Figure 5.9: Plot of $K_I^*/(F\sqrt{c}/TW)$ versus $(r/c)$ for SEC specimen (singularity elements) - stress method

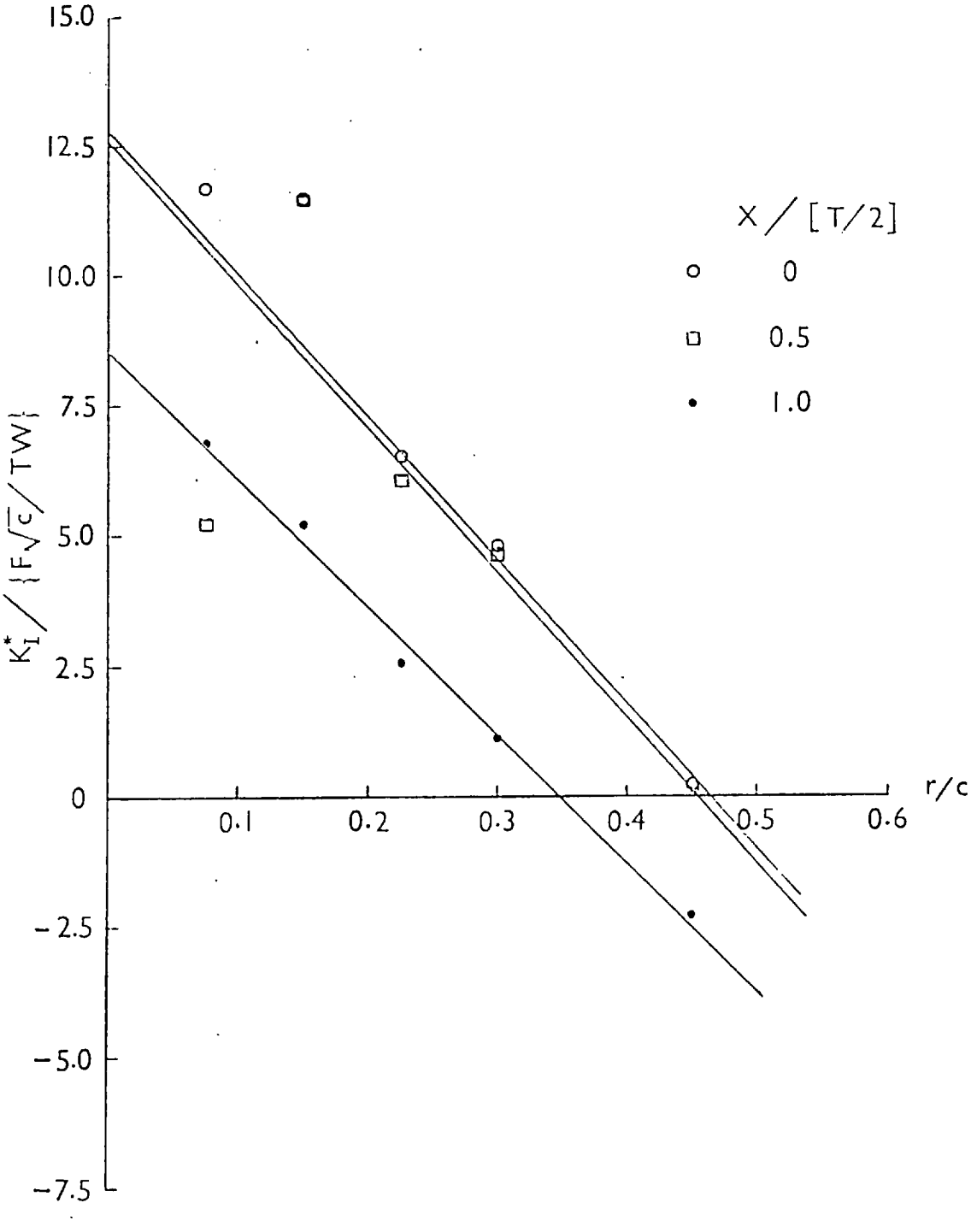



Figure 5.10: Plot of $K_I^*/(F\sqrt{c}/TW)$ versus $(r/c)$ for SEC specimen (conventional elements) - stress method

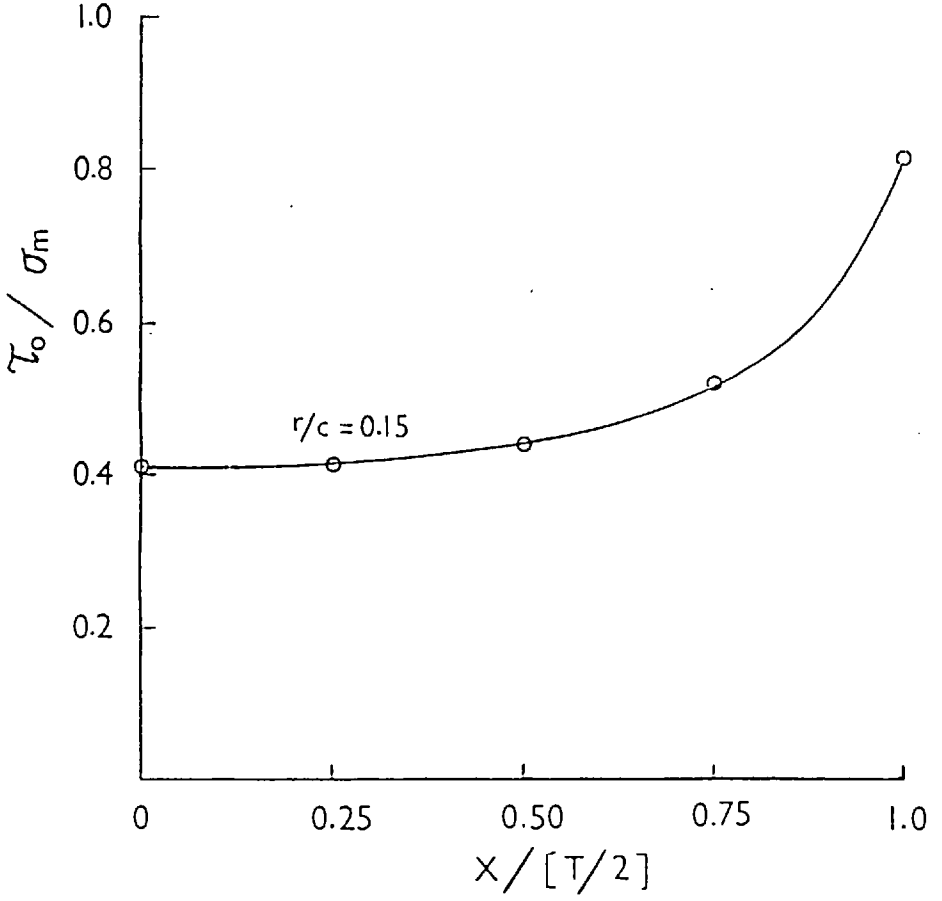



Figure 5.12: Variation of flow stress/mean stress ratio with thickness for SEC specimen

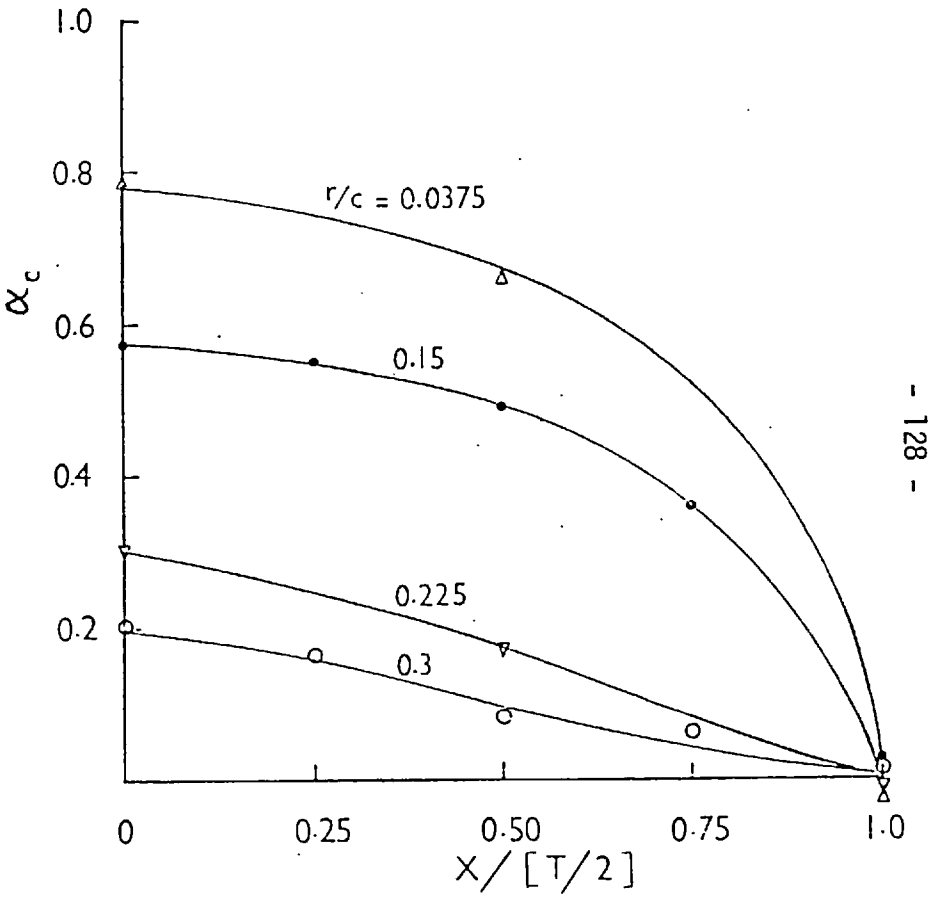



Figure 5.11: Variation of lateral constraint parameter, $\alpha_c$, with thickness for SEC specimen

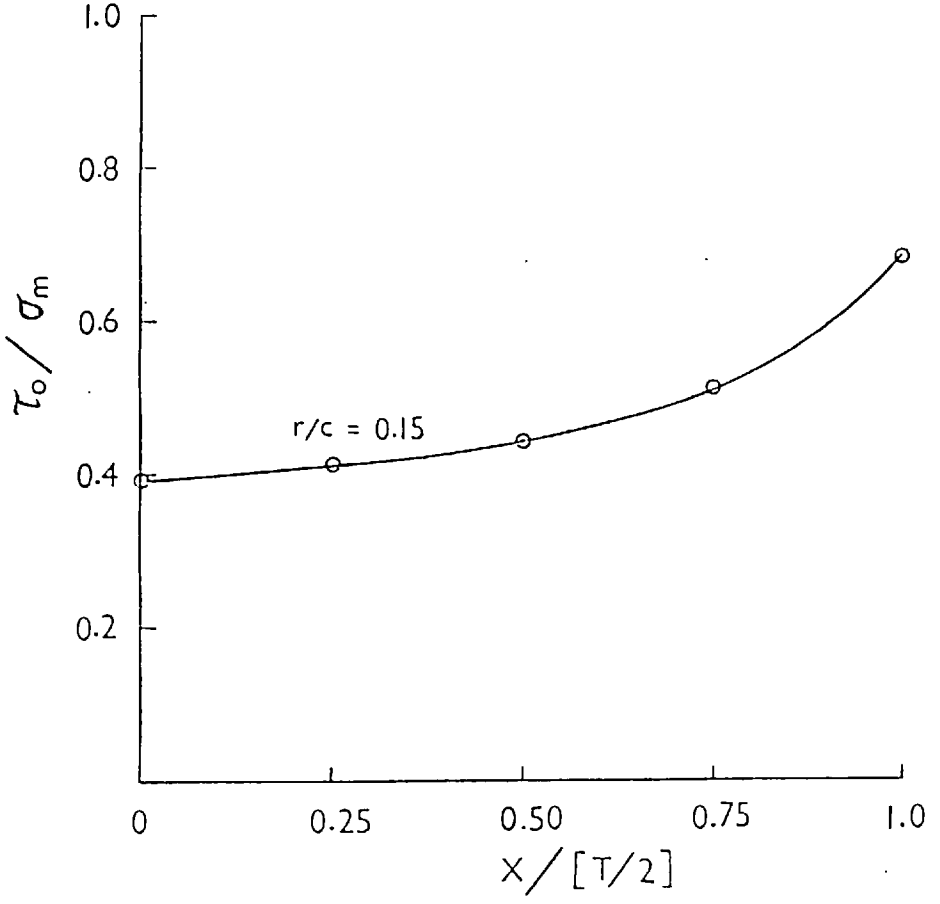



Figure 5.14: Variation of flow stress/mean stress ratio with thickness for SEC specimen (uniform tensile load)

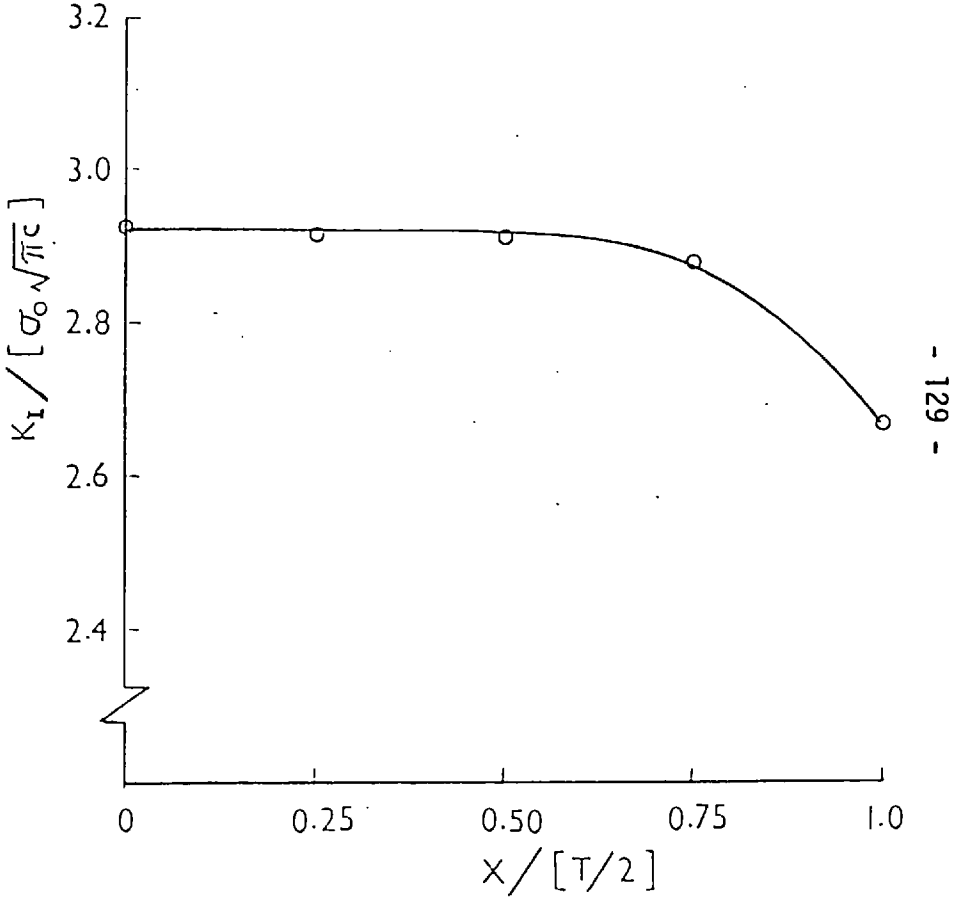



Figure 5.13: Variation of $K_I$ with thickness for SEC specimen (uniform tensile load)

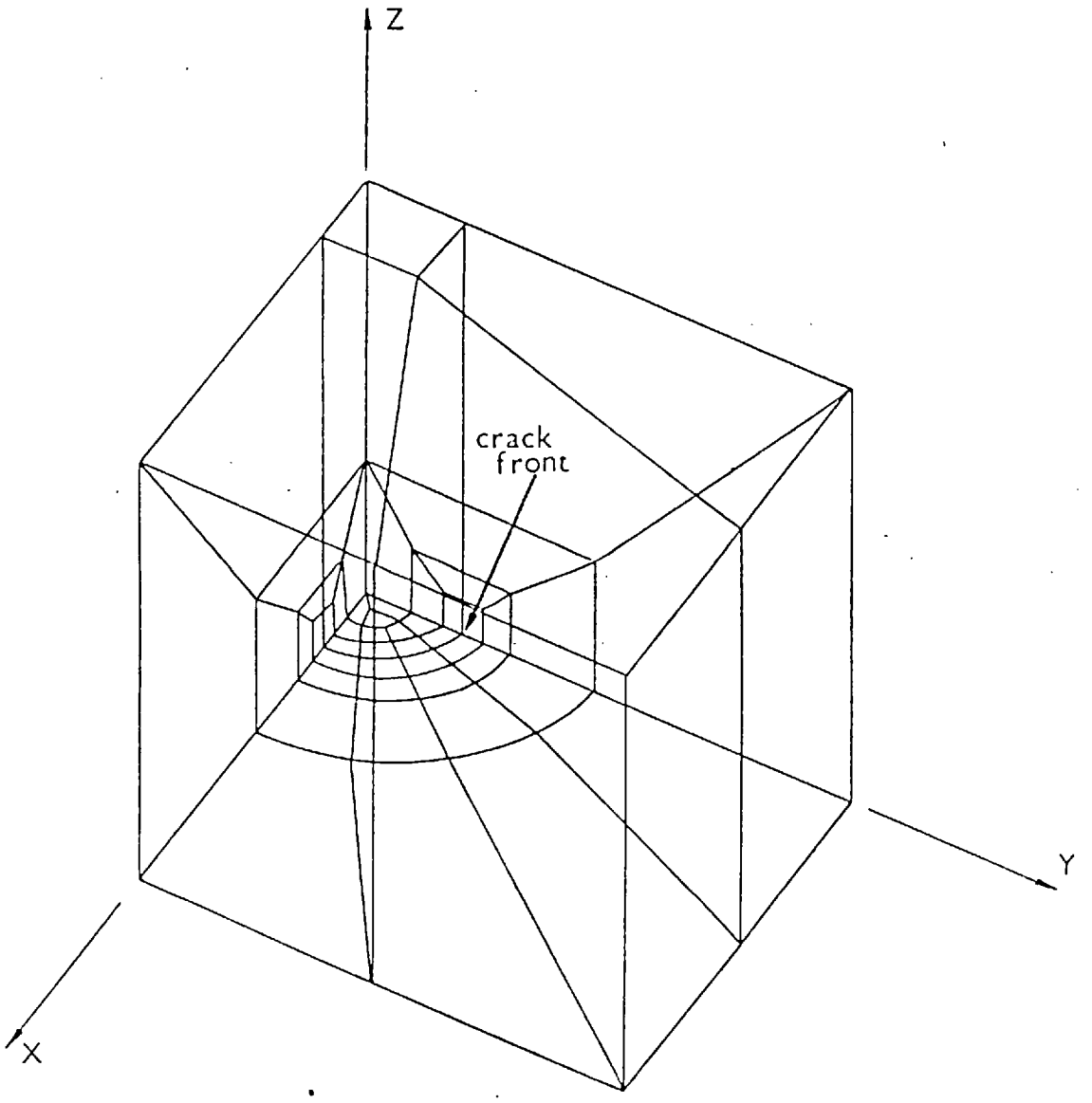



Figure 5.15: Boundary mesh idealization for embedded penny-shaped crack, corner crack and semi-circular surface crack problems

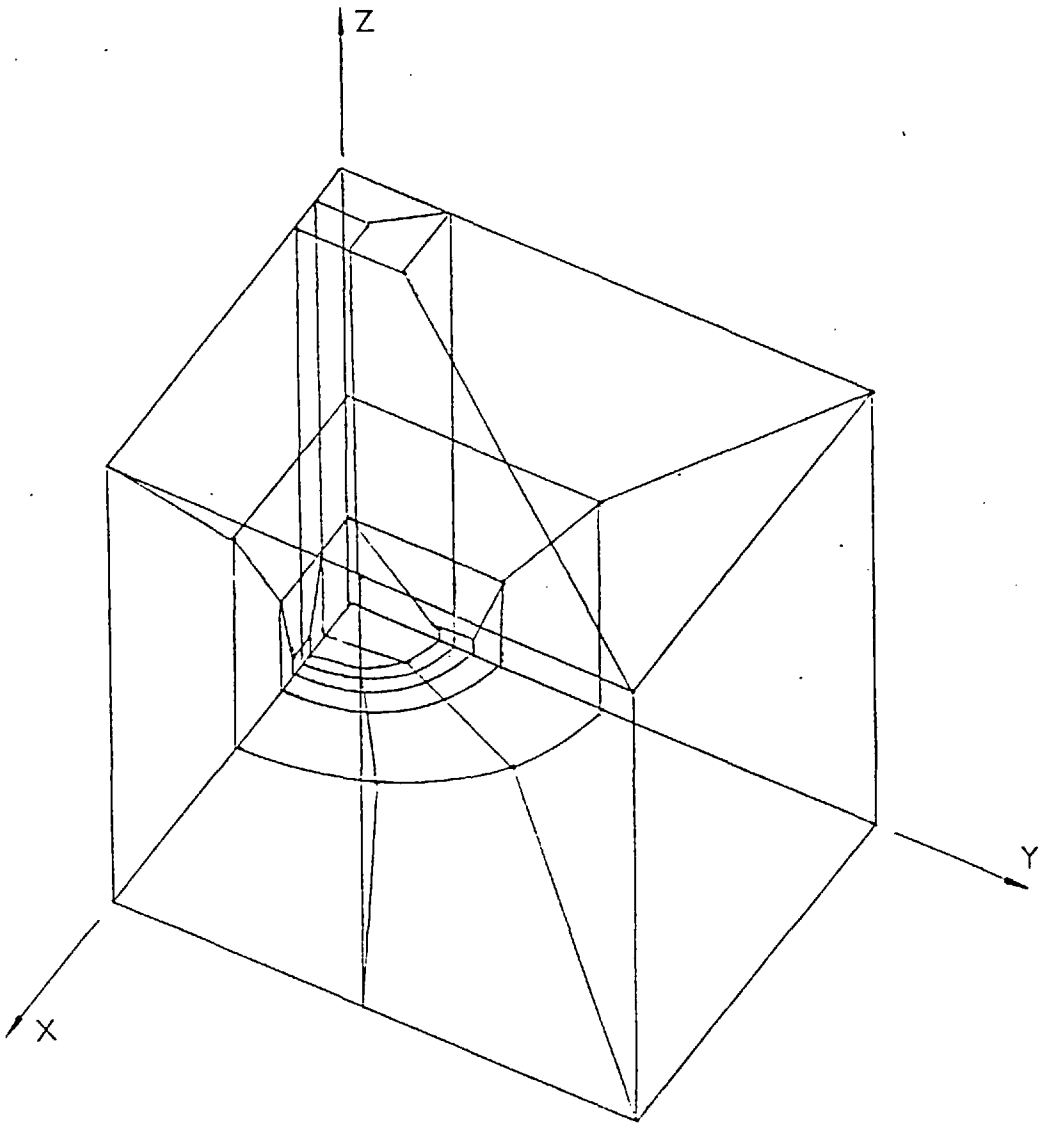



Figure 5.16: Boundary mesh idealization for embedded penny-shaped crack and corner crack problems (indirect method)

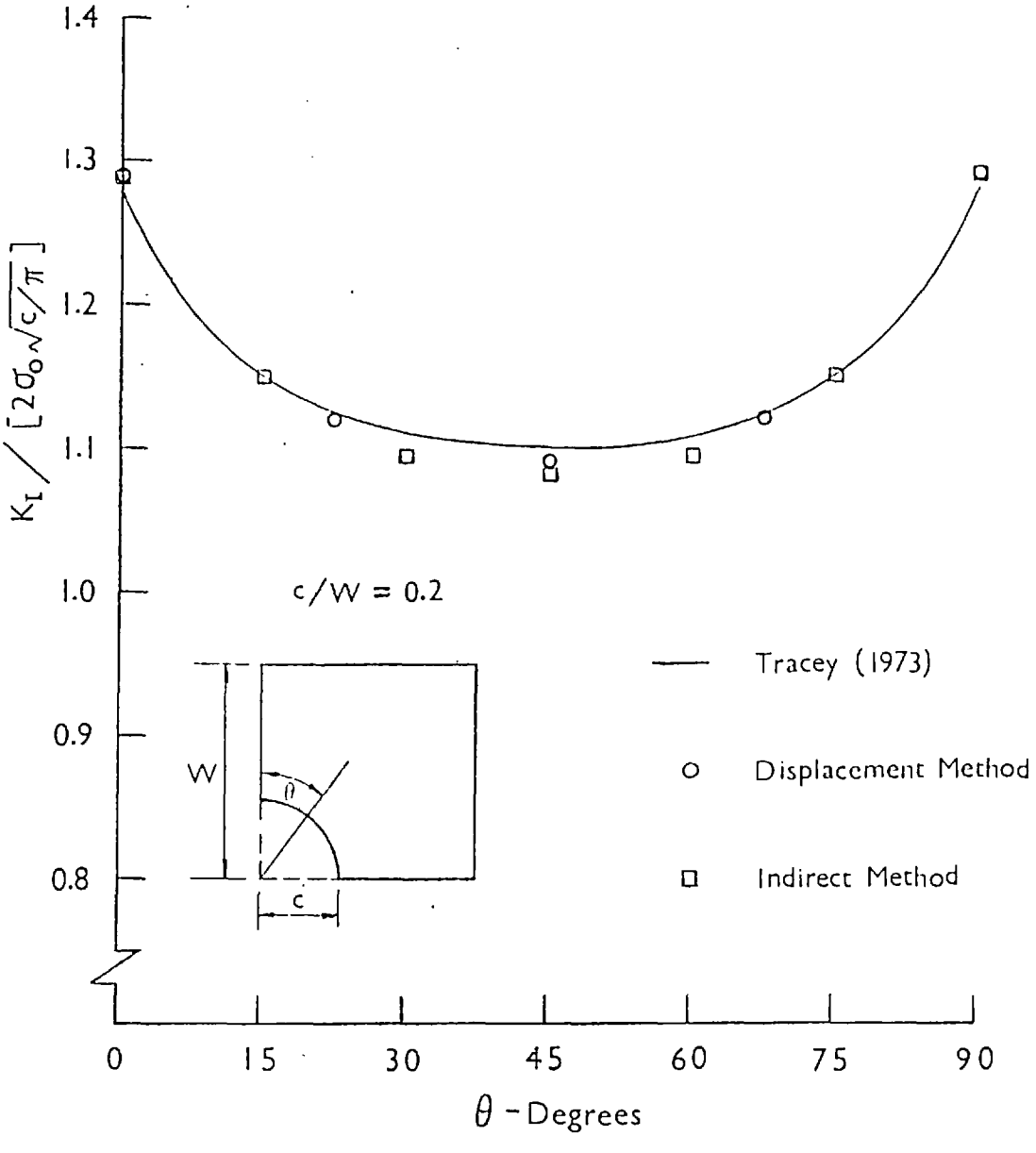



Figure 5.17: Variation of $K_I$ around the crack front of a corner quadrant crack in a square prism

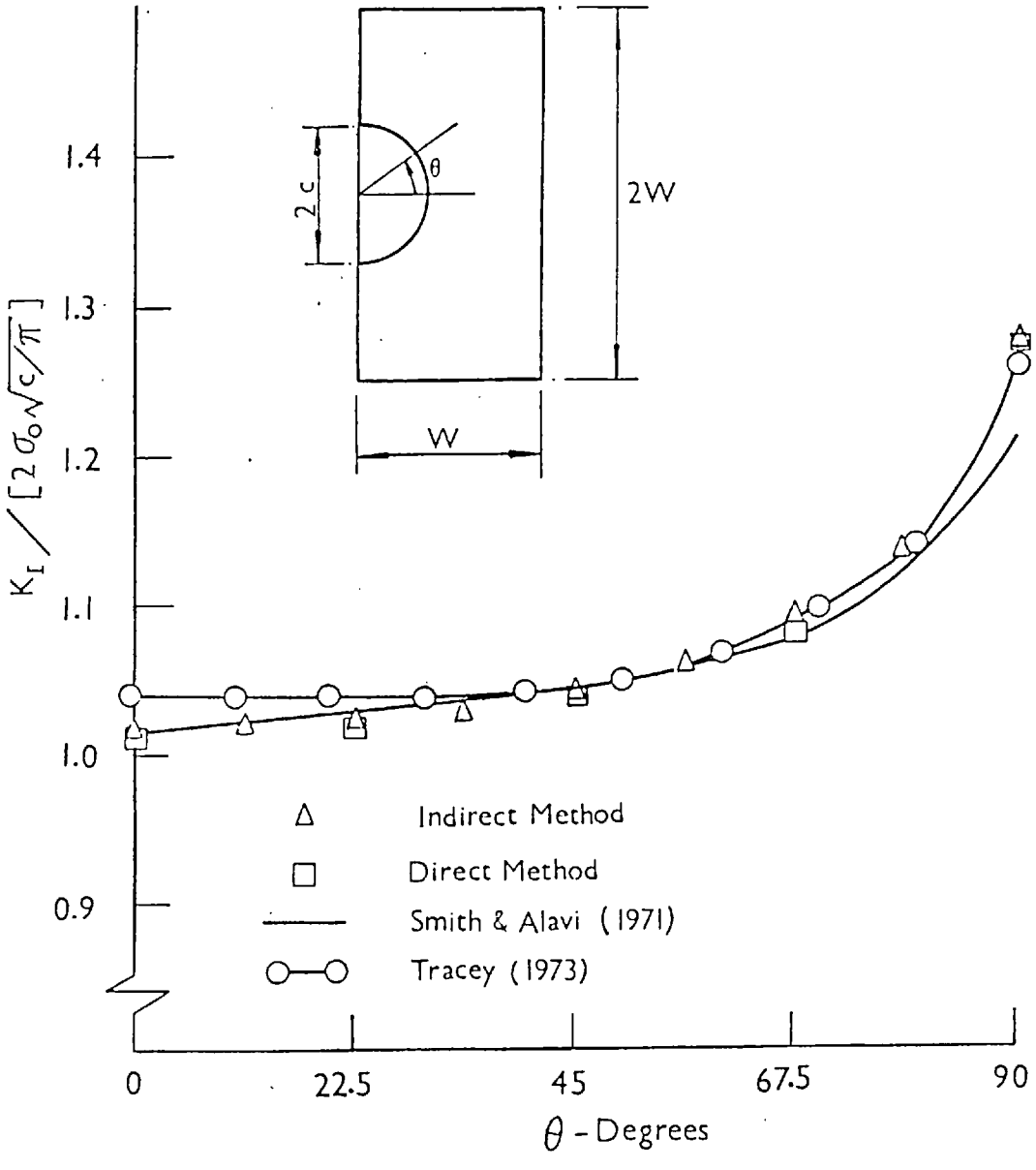



Figure 5.18: Variation of $K_I$ around the crack front of a semi-circular surface crack in a rectangular prism

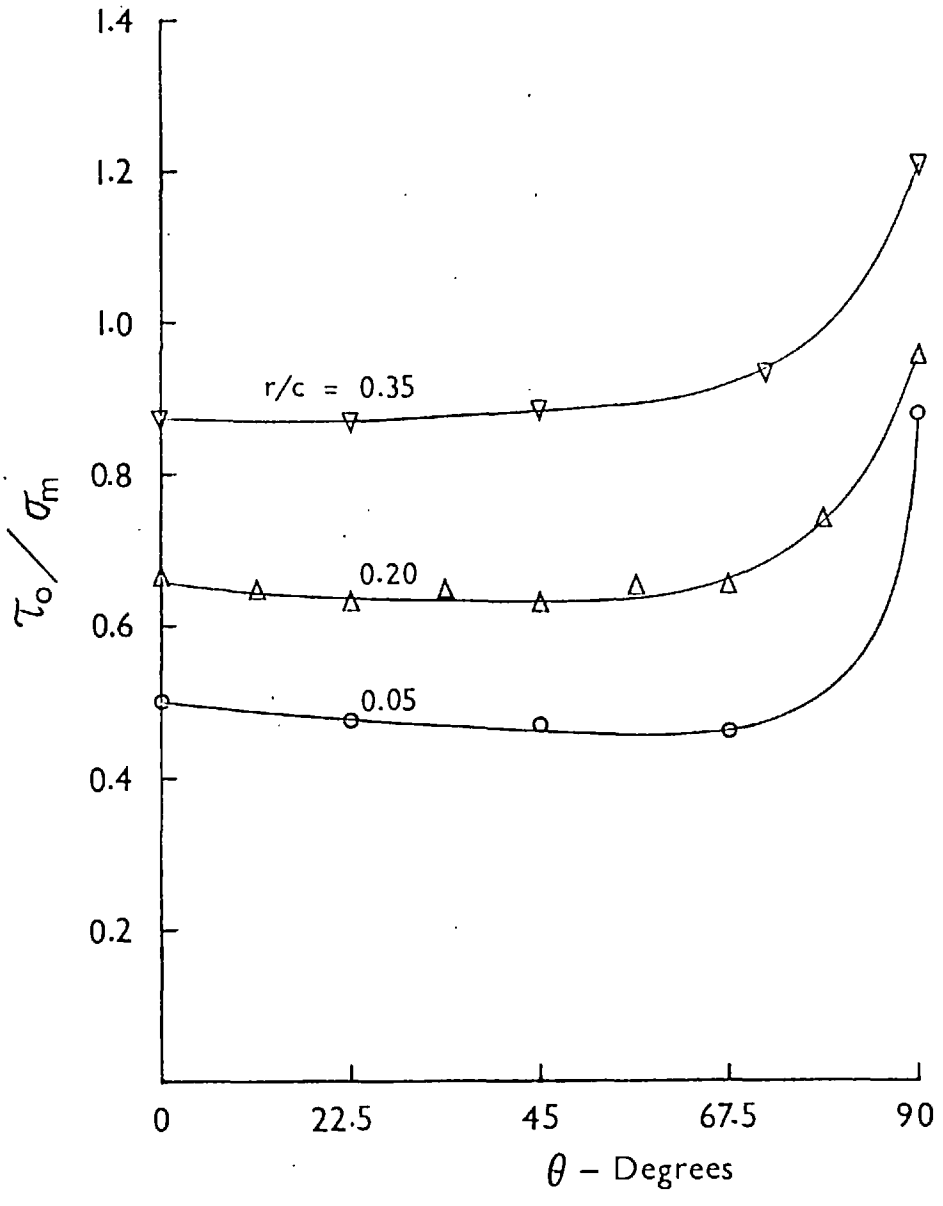



Figure 5.19: Plot of flow stress/mean stress ratio versus the angular orientation for semi-circular surface crack problem

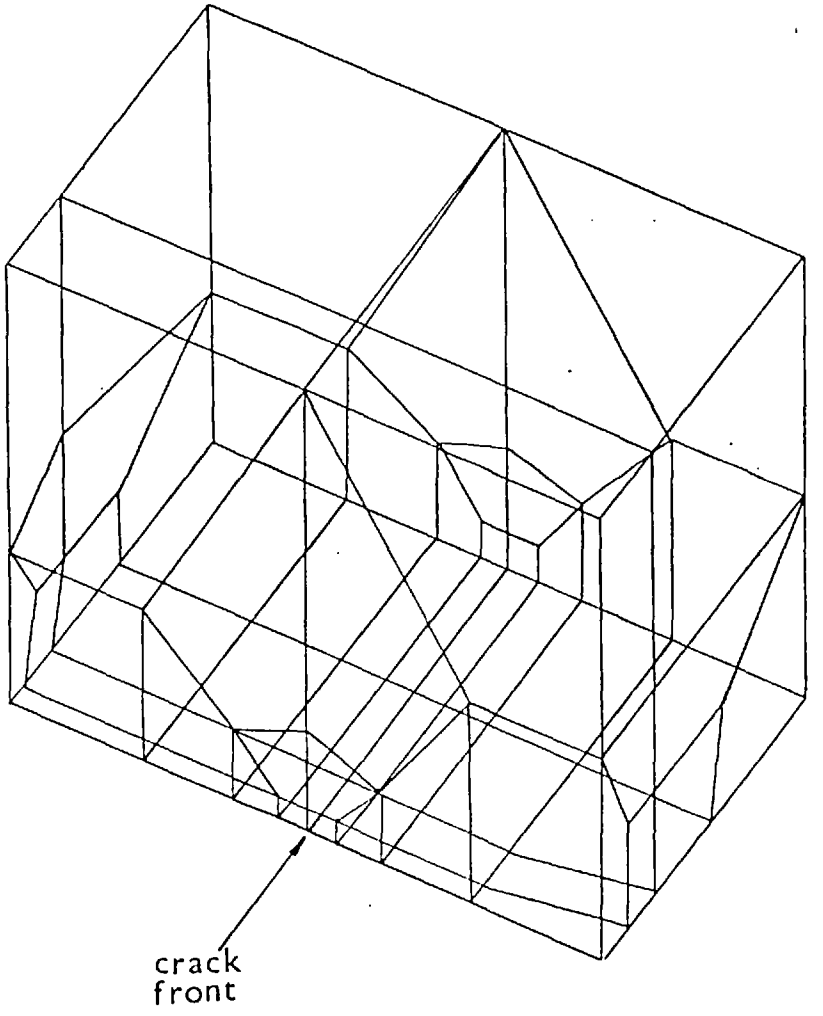



Figure 5.20: Boundary mesh idealization for CCT specimen

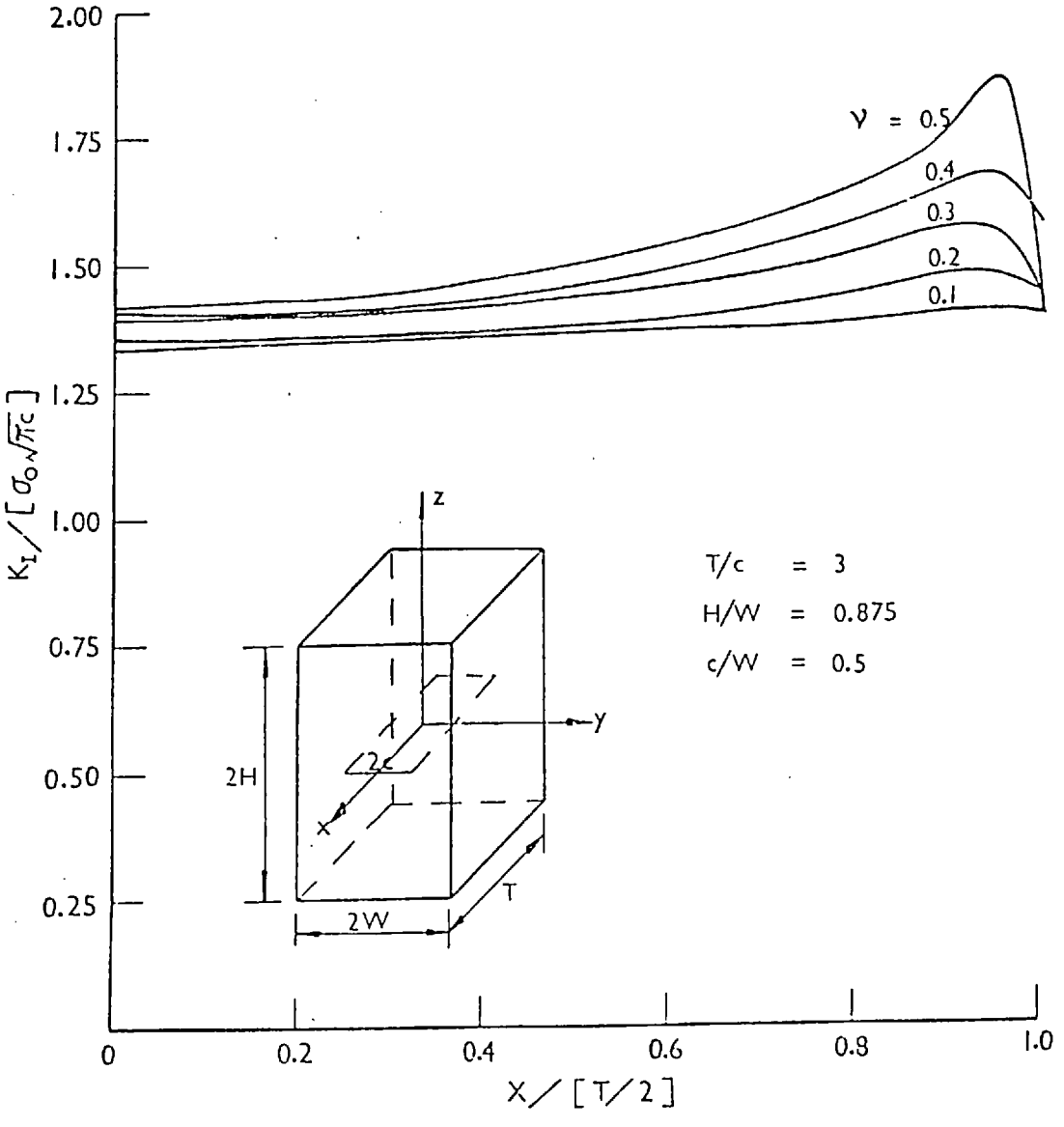



Figure 5.21: Variation of $K_I$ with thickness for CCT specimen

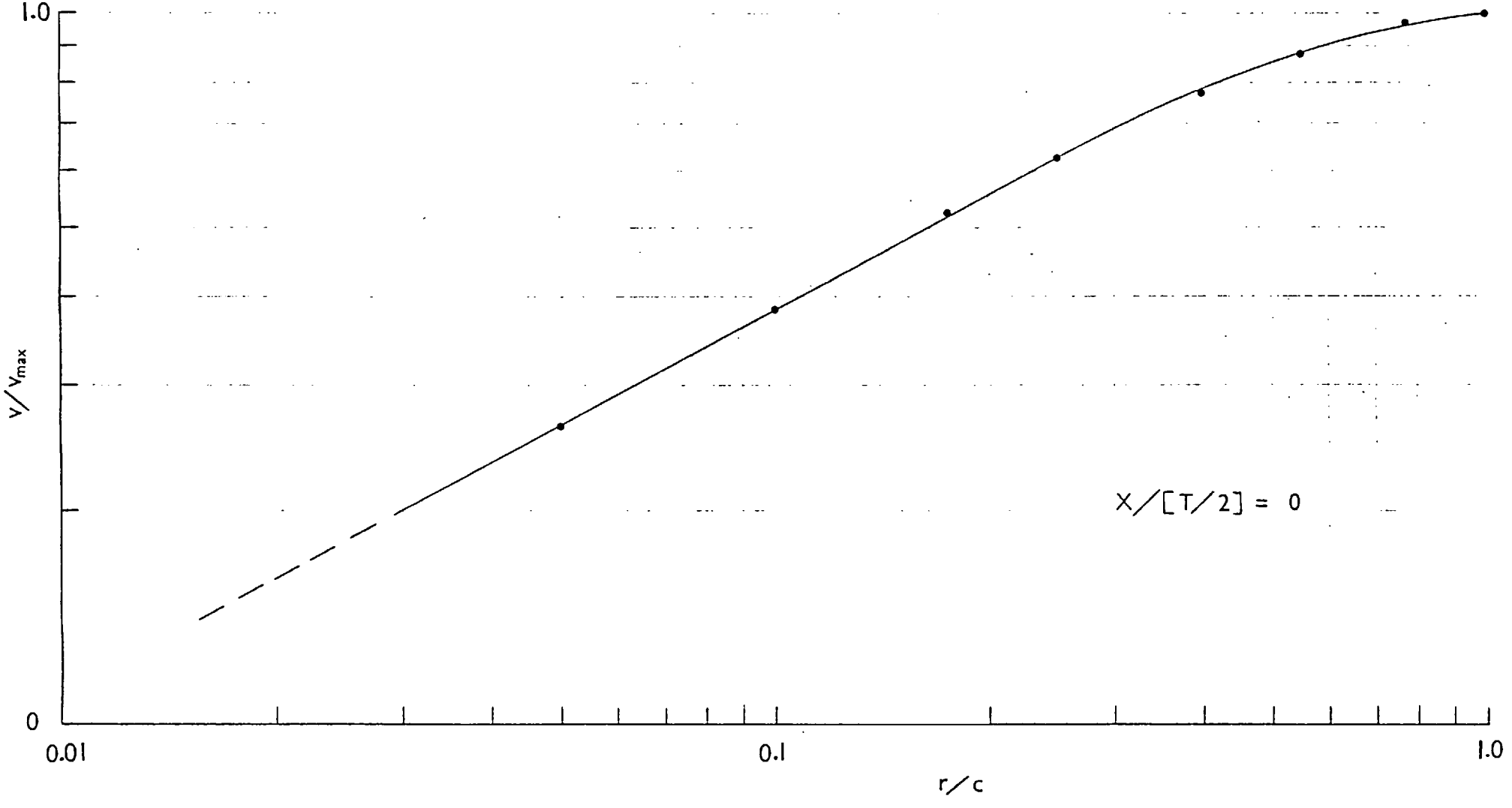



Figure 5.22: Variation of crack face displacements with distance from the crack front (CCT specimen)

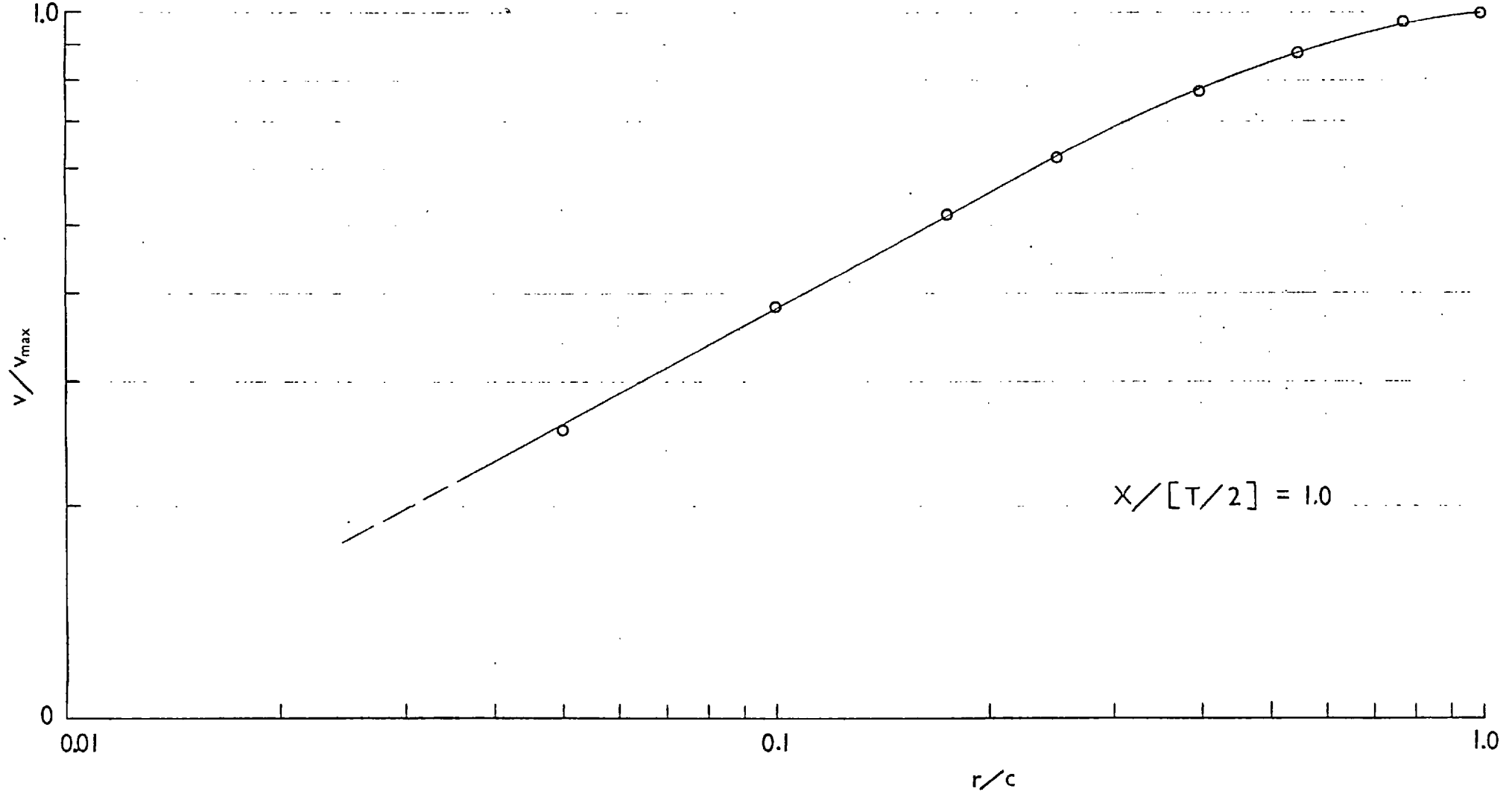



Figure 5.23: Variation of crack face displacements with distance from the crack front (CCT specimen)

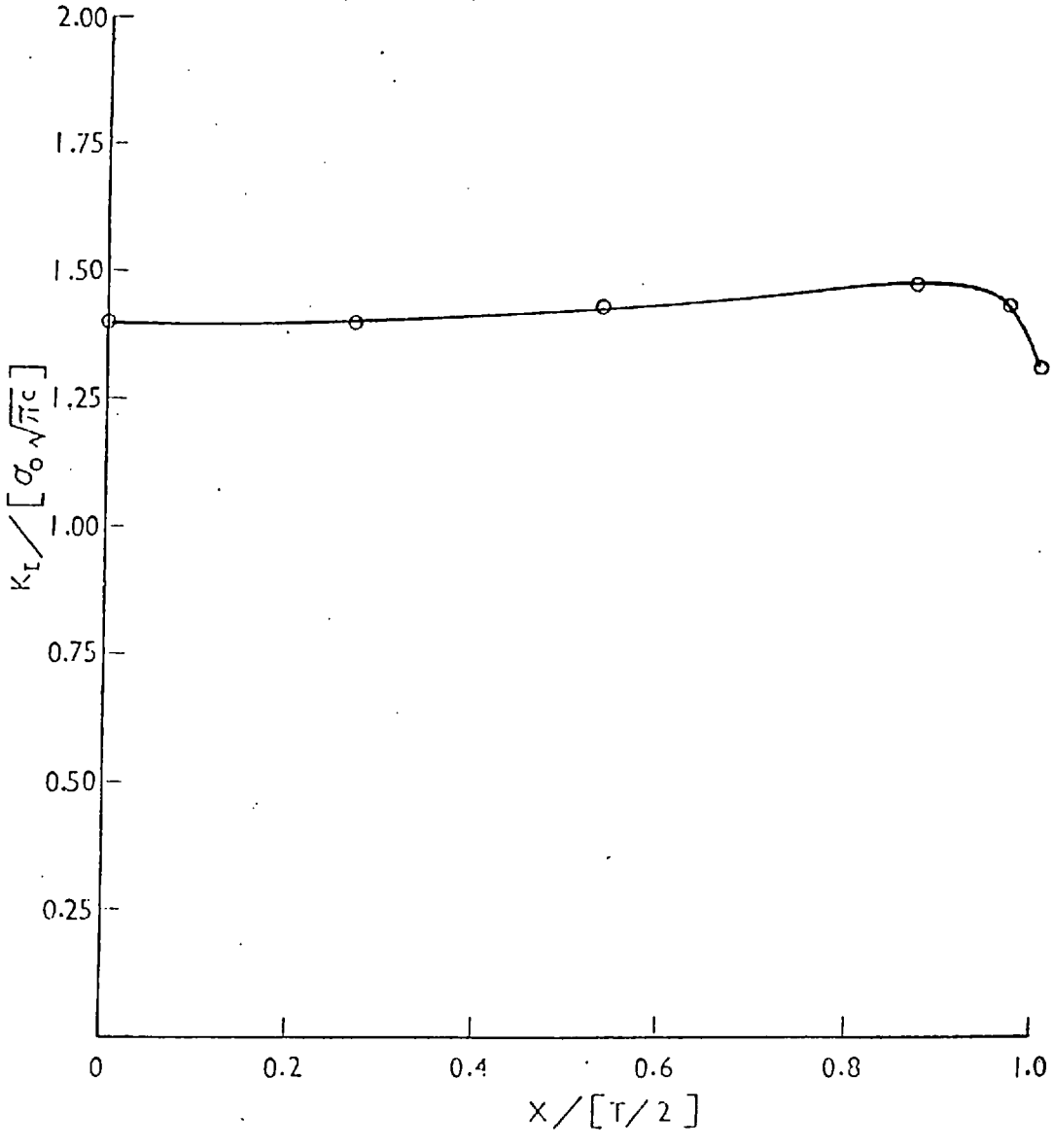



Figure 5.24: Variation of $K_I$ with thickness - CCT specimen (Newman (1977), $\nu$ = 1/3)

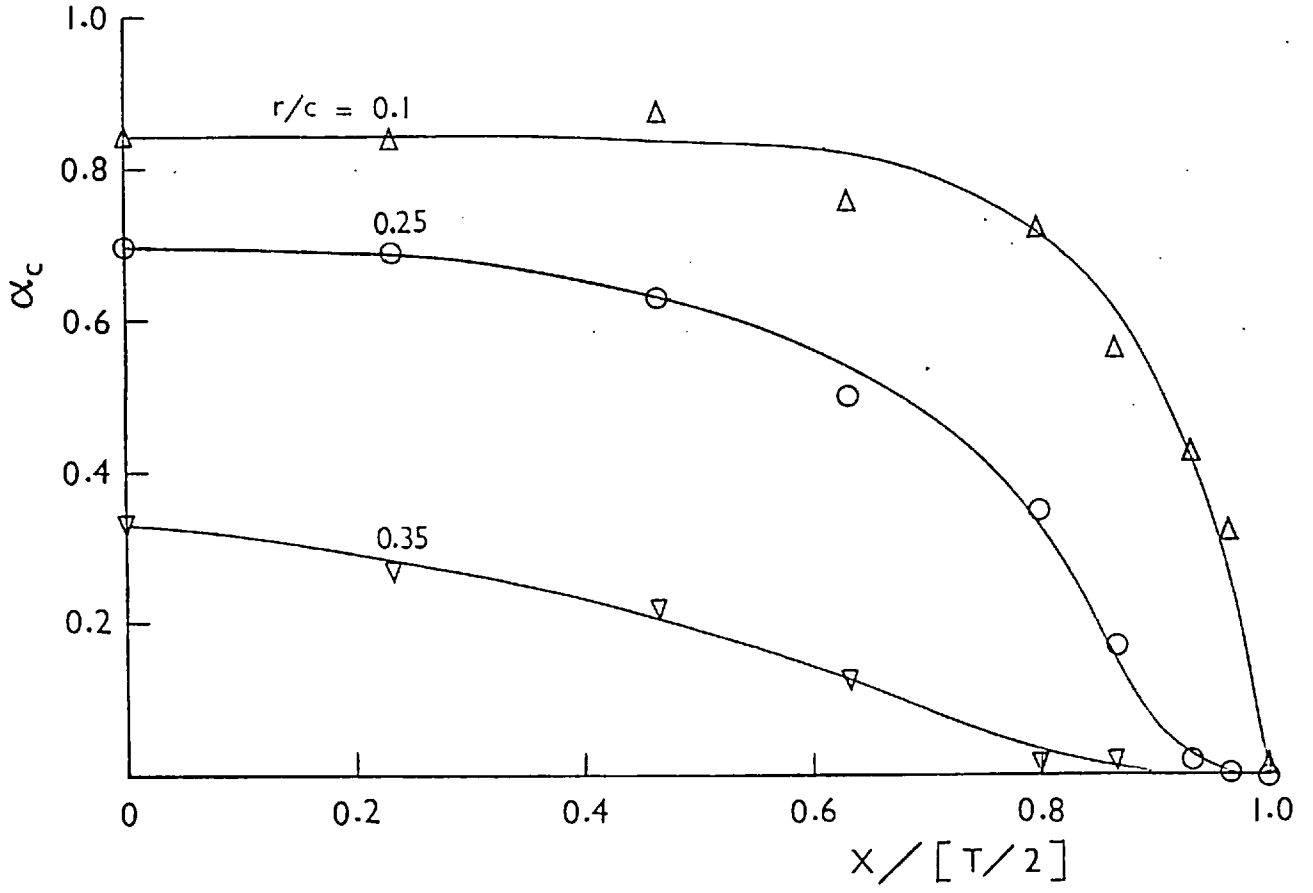



Figure 5.25: Variation of lateral constraint parameter, $\alpha_c$, with thickness (CCT specimen)

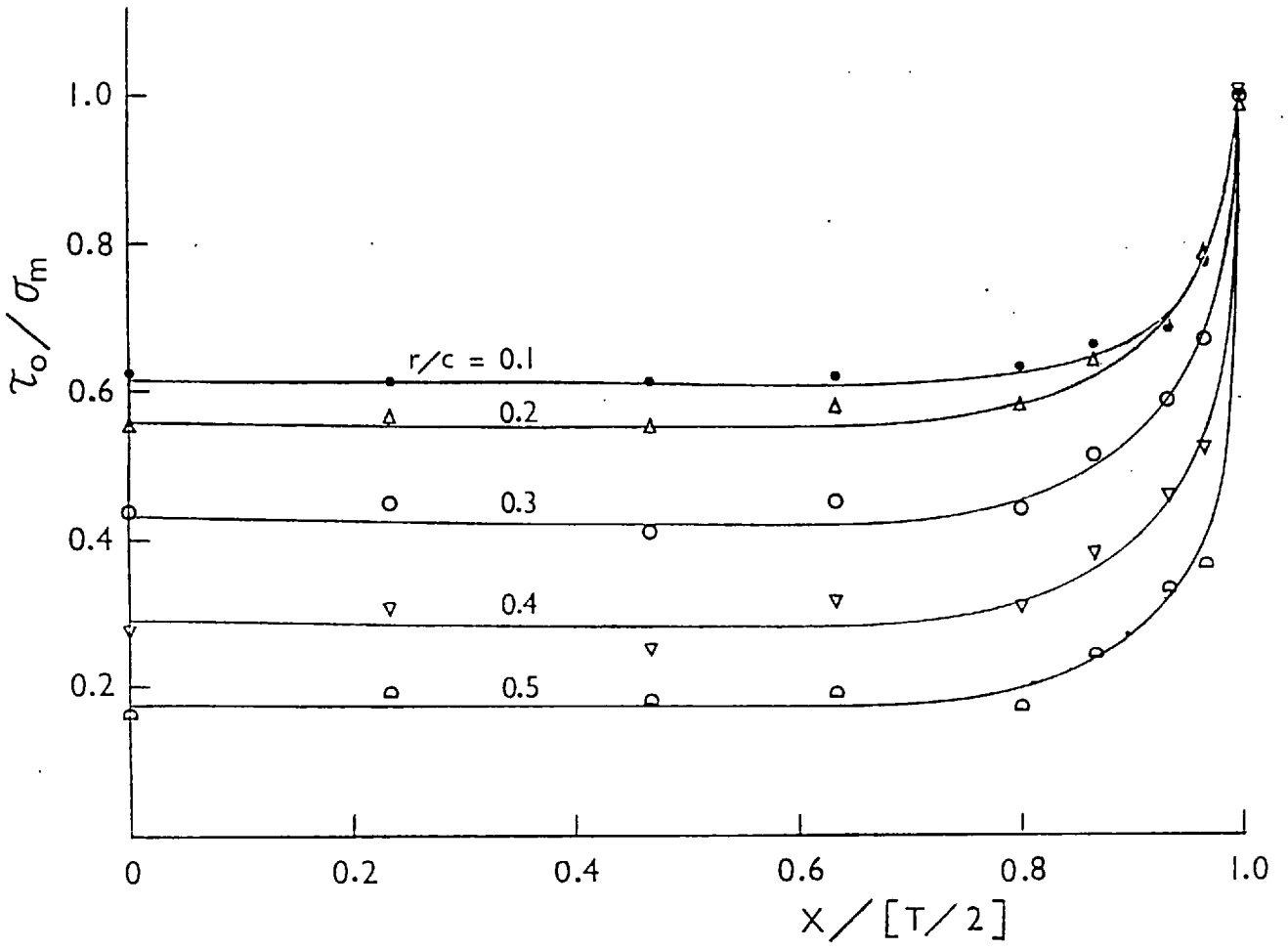



Figure 5.26: Variation of flow stress/mean stress ratio with thickness (CCT specimen)

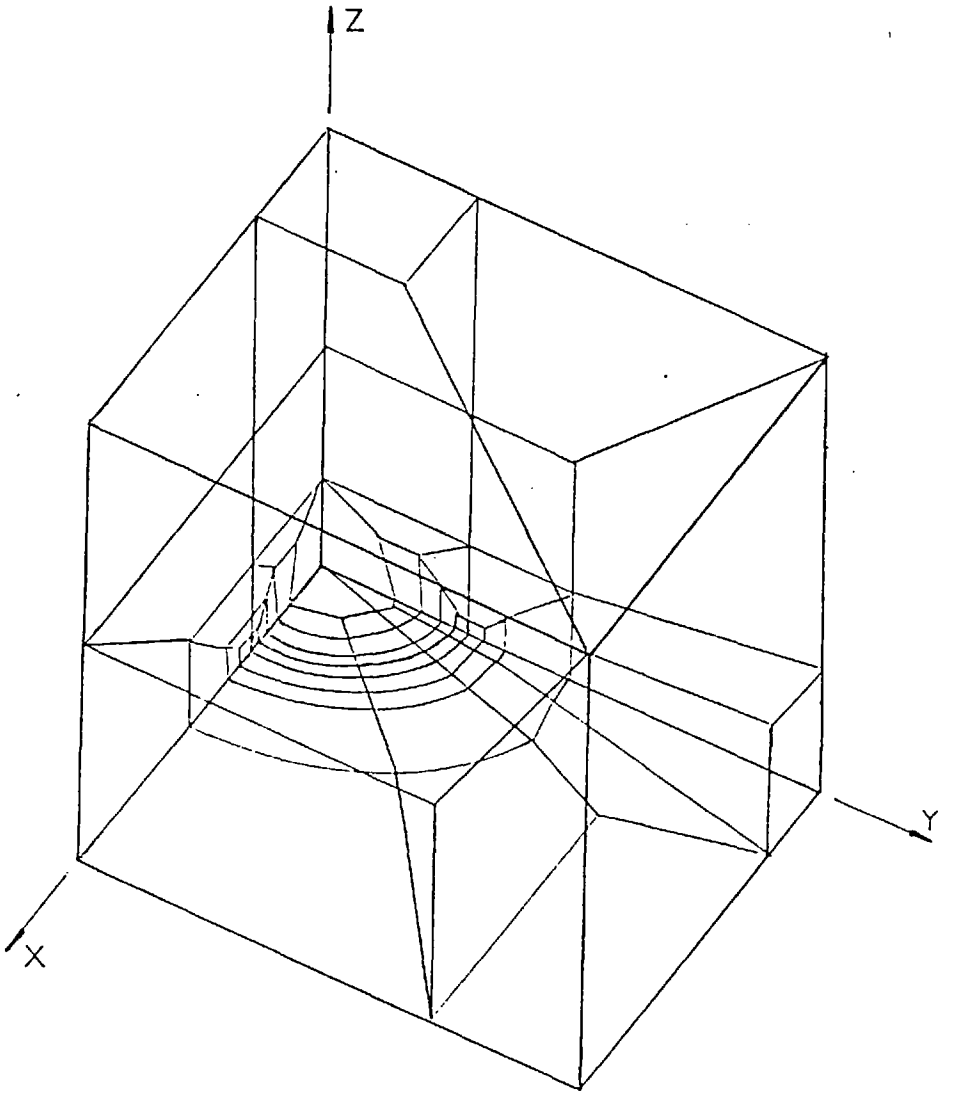



Figure 5.27: Boundary mesh idealization for semi-circular surface crack problem

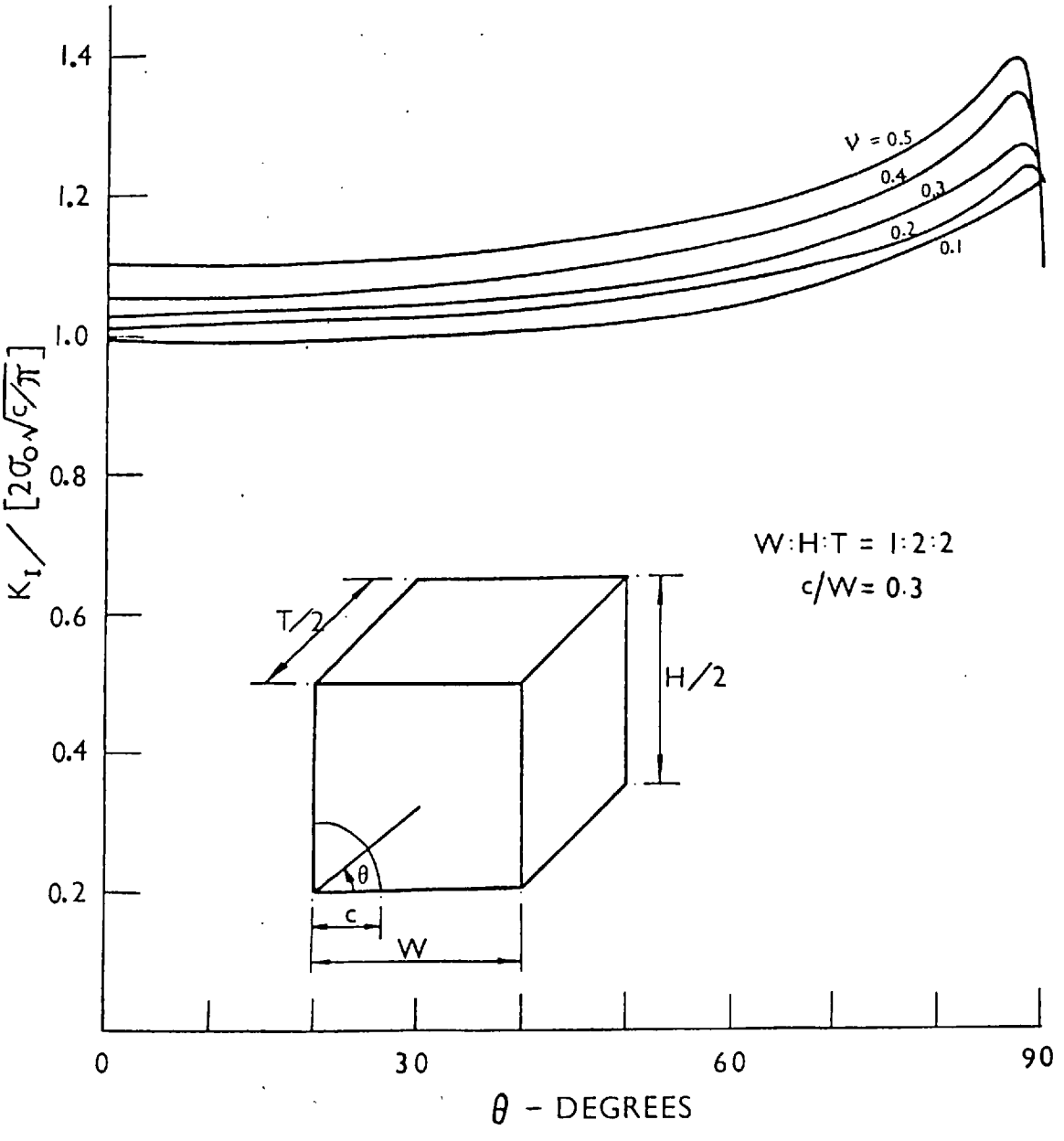



Figure 5.28: Variation of $K_I$ around the crack front of semi-circular surface crack in a rectangular prism

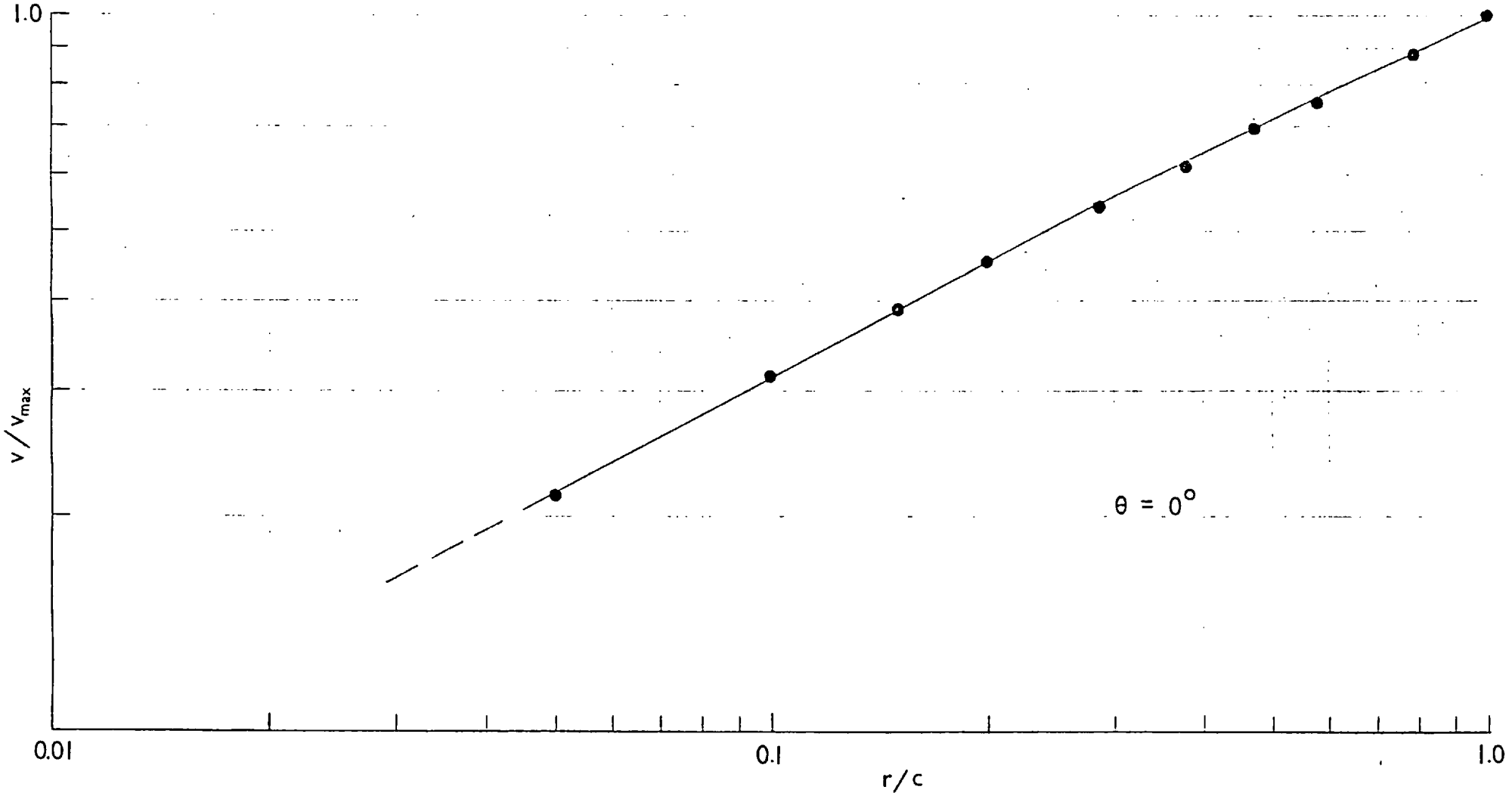



Figure 5.29: Variation of crack face displacements with distance from the crack front (semi-circular surface crack)

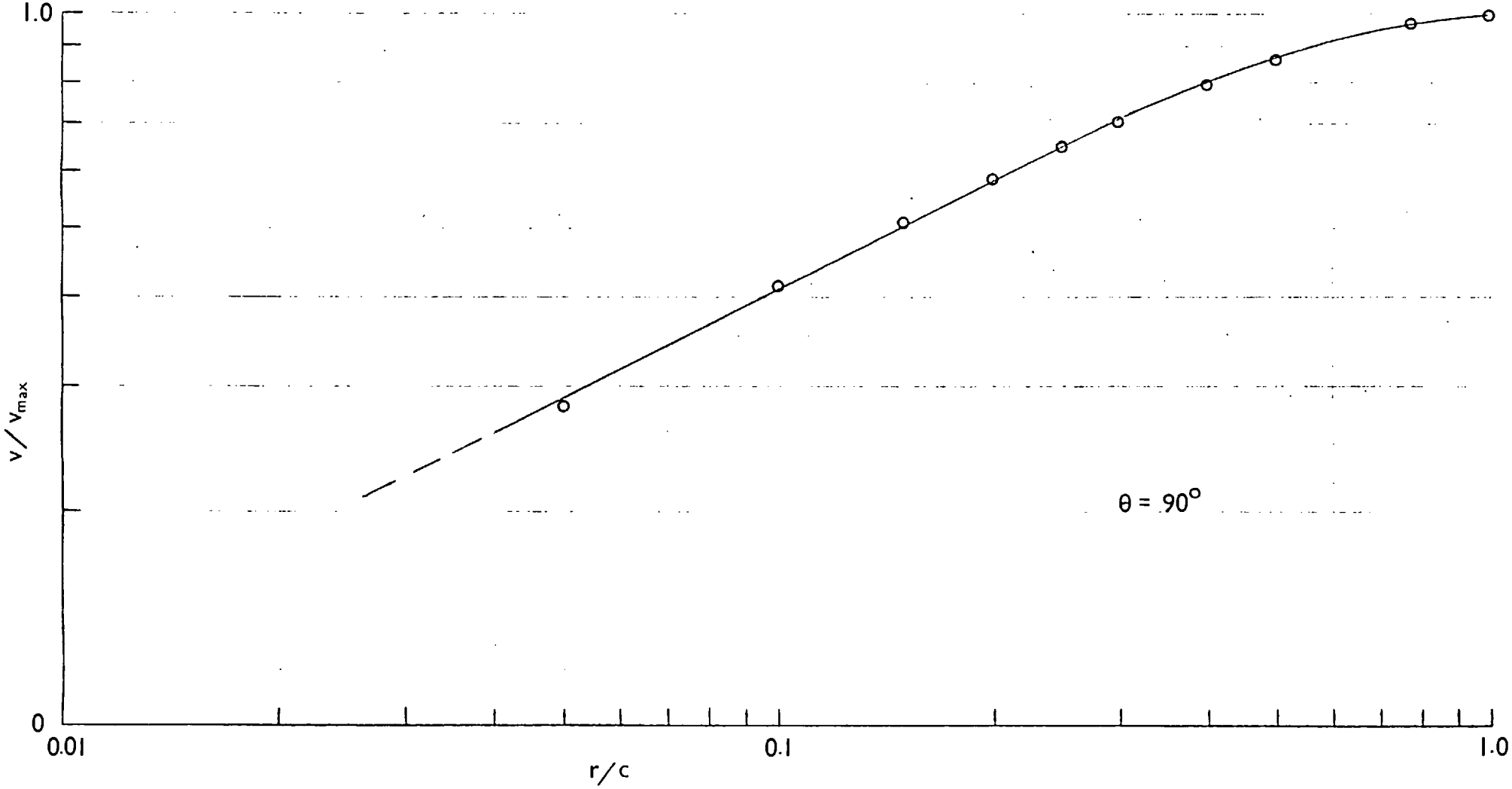



Figure 5.30: Variation of crack face displacements with distance from the crack front (semi-circular surface crack)

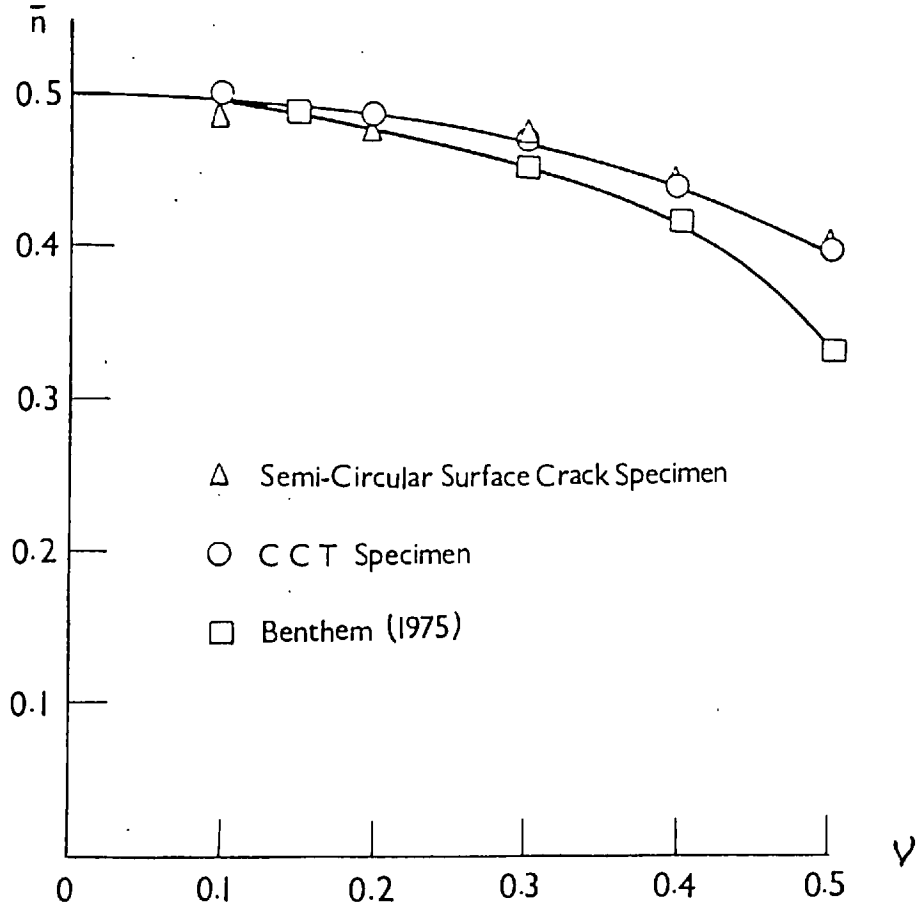



Figure 5.31: Variation of stress (strain) singularity index, $\bar{n}$ ($\sigma \sim r^{-1/\bar{n}}$), with Poisson's ratio

# CHAPTER 6

# ON THE SURFACE FLAW PROBLEM IN INTERNALLY PRESSURIZED THICK-WALLED CYLINDERS

This chapter presents a numerical treatment of the application of fracture mechanics principles to the problem of an internally pressurized thick-walled cylinder with a surface crack. In industrial or military applications, where thick-walled cylinders are used as chemical reactors, isostatic compaction chambers, gun tubes, etc., they are subject to very high pressures and any failure during service can be extremely hazardous and catastrophic. It is therefore of considerable practical importance that there is a good understanding of the fracture behaviour of these pressurized tubes.

## 6.1 INTRODUCTION TO THE PROBLEM

For an internally pressurized thick-walled cylinder, crack initiation usually occurs at the bore of the cylinder due to the presence of local defects such as large inclusions, corrosion pits or tool marks. The crack, once found, would then propagate in a radial plane to final failure by fatigue during service, if left unchecked. It may grow until it reaches the outer surface of the cylinder and continue propagation as a through-crack. In this case, there is a good chance of detection before the size of the through-crack becomes critical, for if the tube is used as a pressure vessel, it would then be leaking. Often, however, the surface crack may become critical in size even before it penetrates the entire wall thickness. This can be a more serious problem, particularly when inspection for cracks and crack growth during service operation is a relatively difficult task. The method of fracture prevention in these

circumstances is therefore primarily one of propagation control. In principle, it involves determining the critical crack size and establishing crack propagation period from the minimum detectable crack to the critical-sized crack. On this basis, a safe inspection period can be selected to ensure that the crack has several chances of detection before it becomes critical in size. Remedial actions can be taken once the crack is detected, either by repair or by exchange of the partially failed tube component.

However, in the study of the growth characteristics of the surface crack in a thick-walled cylinder, several difficulties arise which have so far defied a complete analytical treatment of the problem. The crack front is, for one, usually curved. Further, the crack surfaces may be subject to the internal pressure, either fully or partially, and this is coupled with the fact that the nominal stresses are varying across the wall of the cylinder. As in any surface flaw problem, the crack may be characterized by a length and a depth. But given only these two characterizing parameters, there can, in theory, be an infinite number of crack front profiles and each of these shapes would have its own local variation of $K_I$ along the crack front. Fortunately, in practice, even though the original crack shape may be uncontrollably arbitrary, most of the irregularities in the contours may be expected to be smoothed out and the crack grows in a relatively slow manner to a common shape before the onset of fast fracture. This shape will hardly be unique to all situations but will depend upon the material response to the presence of the crack in whatever stress fields.

Plates 6.1 and 6.2 show typical shapes of cracks which have grown by fatigue in a thick-walled cylinder under cyclic internal pressure. This shape is often very well represented by a semi-ellipse as shown in Figure

6.1. The lengths of the semi-major and semi-minor axes are defined by $a$ and $b$, respectively, while the wall thickness, $W$, is the difference between the outer and inner cylinder radii, $R_2$ and $R_1$. Using oil as the pressurizing medium in Ni-Cr-Mo case hardening (EN36B) steel cylinders of $R_2/R_1 = 2$, it was found that the shape of the propagating crack which was initiated by a "point" defect made by using the electrical discharge method, tends to be similar with the ratio of $b/a$ at about 0.77 (Figure 6.2). This is consistent with the experimental findings of Nishioka & Hirawaka (1975), who used Ni-Cr-Mo steel (AISI 4340) cylinders of radii ratio of 2.3. In their tests, a long initial surface flow (i.e. low aspect ratio), made by using the electrical discharge method, soon developed into a semi-elliptical shape with $b/a$ ratio at a nearly constant value of 0.8 as it propagated across the wall of the cylinder (Figure 6.3).

For the fracture analysis of this cylinder problem, the main task now remains to evaluate the variation of the stress intensity factor along the semi-elliptically shaped crack-front. The approach inevitably has to be numerical due to the complexity of the problem. Other results of stress analysis, such as the hoop strain distribution in the cracked component, could also be useful in the study of the crack-growth characteristics, for hoop strains are experimentally measurable quantities.

A numerical study of this problem was carried out and will be presented in two parts here. First, the overall elastic response due to the presence of the semi-elliptical surface flaw at the bore of the cylinder was investigated and stress intensity factor solutions obtained. The prediction of fatigue crack-growth formed the second part of the study and will be presented separately in Section 6.6. But, before all the results are presented and discussed, a review of previous numerical work on cracked cylinders is perhaps in order.

## 6.2 REVIEW OF PREVIOUS WORK

Analytical and numerical stress intensity factor solutions for surface cracks in thick-walled cylinders are very scarce indeed, this being due primarily to the three-dimensional nature of the problem. Bowie (1956) solved the problem of an infinite plate containing a hole with a radial crack and subjected to biaxial tension. The stress intensity factor solution corresponds to a long straight-fronted axial crack in an internally pressurized cylinder of infinitely large diameter ratio. Solutions for a wide range of diameter ratios and crack depths were later derived by Bowie & Freese (1972) using the modified mapping collocation technique developed by Bowie & Neal (1969). Similar solutions were obtained by Shannon (1974) using a finite element technique, and the two sets of solutions showed very good agreement.

Attempts to approximate the three-dimensional solution were made by Underwood (1972) and Kobayashi et al (1975,1977). These approximations are based on combinations of simpler analyses. Underwood's treatment combined the Bowie & Freese (1972) solution for a straight-fronted crack with that of Rice & Levy (1970) for a part-through semi-elliptical crack in a finite thickness plate. The assumption made was that the effect of a given crack shape on the $K_I$ value of a pressurized cylinder is the same as the effect on the value of $K_I$ for a plate under uniform tension. The proposed combination of the two analyses is thus:

$$(K_I)_e = \alpha_s (K_I)_s \qquad (6.1)$$

where:

$(K_I)_e$ = $K_I$ for a pressurized cylinder with a semi-elliptical crack

$$(K_I)_s = K_I \text{ for a pressurized cylinder with a straight-fronted crack}$$

$$\alpha_s = \frac{K_I \text{ for a plate with a semi-elliptical surface crack}}{K_I \text{ for a plate with a straight, edge-crack}}$$

The parameter $\alpha_s$ is often known as the shape factor and pertains to the point of deepest penetration of the semi-elliptical crack. Rice & Levy (1970) have presented some $\alpha_s$ values for different $b/a$ ratios and relative crack depths. Figure 6.4 shows the $K_I$ solutions at the point of deepest penetration for the case where $R_2/R_1 = 2$, obtained by the Underwood analysis. There must be considerable doubt as to the validity of this approach for very thick-walled cylinders and deep cracks, for increasing either or both of these parameters would make the cylinder behave less like a plate. But for relatively thin walls and shallow cracks of low aspect ratio, $b/2a$, the solutions are believed to be within 10% of the true values.

The approach by Kobayashi et al (1975,1977) involves incorporating a curvature correction factor into the solution for a flat plate with a semi-elliptical surface crack subjected to the same hoop stress distribution as in the cylinder. The alternating method was used to obtain the latter solution, with both the front and back surface accounted for. The curvature correction factors were derived by comparing the stress intensity factors for two-dimensional edge-cracked pressurized cylinders and single edge-cracked plates with appropriate hoop stresses acting on the crack surfaces. Results thus obtained are again only approximate in nature.

The first direct three-dimensional solution for a semi-elliptical crack in an internally pressurized cylinder was possibly by Marcal (1972), using the finite element method. A special crack-tip element with an

embedded $1/r$ stress (strain) singularity was employed, but the $K_I$ solutions were obtained for only one geometry, namely $R_2/R_1 = 1.333$, $b/a = 0.290$ and $b/W = 0.333$. Another finite element solution is by Pereira (1977), who solved for semi-circular surface cracks in pressurized cylinders of radius ratios 1.889 and 1.610. Only one crack depth, namely $b/W = 0.2$, was treated. Tan & Fenner (1978), using the boundary integral equation method with a relatively refined boundary mesh, have also solved one of the cases considered by Pereira (1977), namely for $R_2/R_1 = 1.889$. Although the two sets of results are qualitatively similar (see Figure 6.5), the boundary integral equation solution is believed to be numerically more accurate.

In all the three-dimensional solutions discussed so far, three planes of symmetry were assumed and only one-eighth of the cylinder was modelled with the radial plane containing the crack as one of the assumed planes of symmetry. This representation implies the existence of two similar cracks situated diametrically opposite each other in the same plane through the cylinder axis. While this is reasonable for modelling the problem shown in Figure 6.1, when the crack is small relative to the wall thickness and cylinder length, owing to the constraint provided by the relatively large amount of undamaged material remaining in the crack plane, the solutions for relatively deep cracks are of doubtful validity.

Blackburn & Hellen (1974,1977) have, however, solved the pressurized cylinder problem using both special finite elements which have the embedded $r^{-\frac{1}{2}}$ stress (strain) singularity, and a virtual crack extension procedure applied to a quarter-cylinder model. The $K_I$ solutions obtained are for $R_2/R_1 = 1.444$, $b/W = 0.4$ and $b/a = 0.6$, with both problems of the crack lying either in the inner surface or the outer surface of the cylinder solved for. Again, using the finite element virtual crack extension

method applied to a quarter-cylinder model, McGowan & Raymund (1978) solved the semi-elliptical surface crack problem for $b/a$ = 0.333 but for relatively thin-walled cylinders having radius ratios of 1.1. The relative crack depths treated were 0.25, 0.5 and 0.8. Heliot et al (1978) solved the same problems as McGowan & Raymund (1978) but by the boundary integral equation method. The two sets of results agree well but differ considerably from the solutions obtained using the analysis proposed by Kobayashi et al (1975), especially for the deeper cracks.

Using the displacement hybrid finite element method, Atluri & Kathiresan (1979) have also presented stress intensity factor solutions for internal and external surface cracks in internally pressurized thick-walled cylinders. A quarter-cylinder model was used and for internal surface cracks, the cases treated were $b/a$ = 0.2 and 1.0 for $b/W$ = 0.5 and 0.8, also $R_2/R_1$ = 1.5 and 2.0. Both pressurized and unpressurized cracks were considered for these cases. For external surface cracks, the cases treated were $b/a$ = 0.6 and 1.0 for $b/W$ = 0.4, 0.6 and 0.8 with $R_2/R_1$ = 1.5 only. Agreement with the estimates of Kobayashi et al (1975) was within 6% for the semi-circular internal surface crack with $b/W$ = 0.8 and $R_2/R_1$ = 2.0. For the semi-elliptical internal surface flaws, however, the results differ very significantly, both qualitatively and quantitatively. The solutions for external surface cracks were again significantly different from Kobayashi's estimates but agree reasonably well with the Blackburn & Hellan (1974,1977) solution for a slightly different geometry. Atluri & Kathiresan therefore questioned the validity of obtaining stress intensity factors from solutions for flat plates using curvature correction factors.

## 6.3 PRESENT NUMERICAL INVESTIGATION

For the first part of the present numerical study of the cracked-cylinder problem (Figure 6.1), relative crack depths, $b/W$, ranging from 0.2 to 0.8 were analysed for two different cylinder radius ratios, $R_2/R_1$, of 2.0 and 3.0, but the same crack front geometry was used throughout. This geometry, a semi-ellipse with a ratio of semi-minor to semi-major axis, $b/a$, of 0.8, was chosen because experiments (Crofton (1977), Nishioka & Hitawaka (1975)) have shown that for cylinders with radius ratios between 2 and 3, the crack, once established is indeed semi-elliptical in shape with $b/a$ very close to 0.8. Unless otherwise stated, the crack faces were subject to the same internal pressure acting in the cylinder. In practical applications, this probably represents the worst case. For example, under relatively high frequency cyclic loading using a viscous pressurizing medium, pressures acting on the crack surfaces may be significantly lower than the applied pressure.

One quarter of the cylinder was modelled, taking advantage of symmetry about the plane of the crack and the cylinder cross-section containing its semi-minor axis. Typical boundary mesh idealizations used for the boundary integral equation analyses are shown in Figures 6.6 to 6.9. The element configuration was varied to suit the different radius ratios and relative crack depths. A maximum of 82 surface elements and 248 nodes were used, with the sides of singularity-elements, as used in the previous chapter, modelling the crack front and relatively small elements in the vicinity of it. Indeed, the increase in the number of boundary elements used was all in the region of the crack periphery as the relative crack-depth was increased, so that there was adequate representation of the rapidly varying stress field there. For each cylinder radius ratio, the length of the quarter cylinder modelled was 2.5

times the wall thickness. Plane strain boundary conditions were applied at the end of the cylinder remote from the crack, and Poisson's ratio was taken as 0.3.

## 6.4 OVERALL RESPONSE

Figures 6.10 and 6.11 show the predicted deflections of the outer surface of one symmetrical half of a cylinder with $R_2/R_1 = 2$ and $R_2/R_1 = 3$, respectively, in the cross-sectional plane through the point of maximum penetration of the crack. Results are shown for a range of crack-depths in both cases, the plate of the crack lying along the right hand side of the horizontal axes, i.e. $\theta = 0^{o}$. The deflections in these polar plots are normalized with respect to the Lamé solution deflections for an uncracked cylinder with the appropriate radius ratio. It can be seen that for relative crack depths beyond about 0.3, the distortion of the cylinder with either of the radius ratios considered is too severe for symmetry about the vertical axes of Figures 6.10 and 6.11 to be assumed and only one-eighth of the cylinder modelled. The presence of the crack creates a bending effect which tends to reduce the radial deflections in the crack plane to less than those for an uncracked cylinder. This bending effect increases with increasing crack depth and is greatest at the cross-sectional plane through the point of maximum penetration of the crack, diminishing with distance, $Z$, away from it.

### 6.4.1 Stress Distributions

The discussion here will be confined to hoop stresses as they are generally the largest components of stresses acting in the cylinder. For a cylinder under internal pressure, $P$, the hoop stress is, in the absence of the surface crack, largest in magnitude at the bore and is

given by the Lamé solution:

$$\sigma_h^* = \frac{(R_2/R_1)^2 + 1}{(R_2/R_1)^2 - 1} P \qquad (6.2)$$

The presence of the surface flaw will redistribute the stresses such that the Lamé solution will not be valid in the vicinity of the crack front. Figures 6.12 and 6.13 show, for $R_2/R_1 = 2$ and $R_2/R_1 = 3$, respectively, the variation of the computed hoop stresses, $\sigma_h$, at the inner surface of the cylinder in the radial plane containing the crack; the results are normalized to the value of $\sigma_h^*$ obtained from (6.2). The broken lines in the figures denote the position of the crack edge at the bore of the cylinder, $H$ being the half-length of the cylinder and $Z$ the axial distance from the cross-sectional plane through the point of maximum crack penetration. As can be seen, the hoop stress rapidly decreases away from the crack edge in all cases and tends to the value of $\sigma_h^*$, although for $R_2/R_1 = 2$ it was still 20% greater in magnitude than $\sigma_h^*$ when $b/W = 0.8$ at the ends of the cylinder ($Z/H = 1.0$). On the other hand, for $R_2/R_1 = 3$, the deviation of $\sigma_h$ from $\sigma_h^*$ at the ends were less than 3.5% for all the crack depths considered. When $b/W$ is less than or equal to 0.4, the computed values of $\sigma_h$ were found to be within about 5% of the Lamé solution value at $Z/H$ greater than 0.55 for both the radius ratios analysed, the percentage deviation being smaller for decreasing crack depths. The results perhaps confirm the adequacy of the boundary meshes used here for obtaining solutions to be sufficiently accurate for engineering applications.

Figure 6.14 shows the computed variation at the inner surface of the cylinder with $R_2/R_1 = 2$, in the radial plane diametrically opposite to that containing the crack ($\theta = 180^0$ plane). The effect of increasing the crack depth is shown to increase the hoop stresses in this plane,

although the stresses tend to decrease with increasing distance from the cross-sectional plane through the point of maximum penetration of the crack. But at the ends of the cylinder, the computed value of $\sigma_h$ was still 11% higher than the value from the Lamé solution, $\sigma_h^*$. The corresponding variation in hoop stresses at the bore of the cylinder for $R_2/R_1 = 3$ is shown in Figure 6.15. The features are qualitatively similar to those in Figure 6.14, except that here the increase in the computed values of $\sigma_h$ at the bore diametrically opposite the crack with increasing crack depth is more pronounced than in the case where $R_2/R_1 = 2$. For example, at $b/W = 0.8$, the computed value of $\sigma_h/\sigma_h^*$ was 1.45 at $Z/H = 0$ for $R_2/R_1 = 3$, while the corresponding value for $R_2/R_1 = 2$ was only 1.15. The decrease of the hoop stress towards the Lamé solution value with increasing $Z/H$ was also more rapid here than in the case where $R_2/R_1 = 2$; in fact, at the ends of the cylinder, the computed values of $\sigma_h$ were within 4% of $\sigma_h^*$ for all crack-depths analysed.

While in the $\theta = 180^0$ radial plane, the computed hoop stresses were generally found to increase with increasing crack depths, the reverse was found to be true in the radial plane perpendicular to that containing the crack, i.e. the $\theta = 90^0$ plane. This is shown in Figures 6.16 and 6.17 for the cases $R_2/R_1 = 2$ and $R_2/R_1 = 3$, respectively. An interesting feature here is that the computed minimum hoop stress along the bore was not at $Z/H = 0$ but instead at about $Z/H = 0.2$. The decrease in the values of $\sigma_h$ was again more pronounced for $R_2/R_1 = 3$ than it was for $R_2/R_1 = 2$. For example, the computed minimum value of $\sigma_h/\sigma_h^*$ for $R_2/R_1 = 3$ was 0.71 at $Z/H = 0.2$, while that for $R_2/R_1 = 2$ was 0.86 also at $Z/H = 0.2$. At the ends of the cylinder with the radius ratio of 3, the deviation from the Lamé solution value $\sigma_h^*$ was less than 5% for all crack depths analysed, but for the case where $R_2/R_1 = 2$, the computed value of $\sigma_h$ differed from

$\sigma_h^*$ by as much as 10% at $b/W = 0.8$. All these results suggest perhaps that while the length of the cylinder, taken as 2.5 times the wall thickness, may be sufficient, for the case where $R_2/R_1 = 3$, to represent a long cylinder with a crack of relative depth of as high as 0.8 such that the stresses remote from the crack could be those calculated from the Lame solution, it may not be so for the case where $R_2/R_1 = 2$, especially for the deeper cracks. In this respect, the parameter $H/R_2$ is probably more important than $H/W$.

Figure 6.18 shows the variation of the computed hoop stress at various crack depths around the inner circumference of the cylinder in the cross-sectional plane through the point of maximum penetration of the crack, i.e. the $Z = 0$ plane, for $R_2/R_1 = 2$. The corresponding variation for $R_2/R_1 = 3$ is shown in Figure 6.19. Both sets of results show very similar features, with part of the bore in hoop compression which decreases in magnitude as one traverses around the inner surface from the crack plane until the tangential stress becomes tensile again. This stress then increases to a maximum at about $\theta = 160^0$, and thereafter it decreases slightly until $\theta = 180^0$. The compressive hoop stress state spanned over a larger part of the inner surface of the cylinder the greater the crack depth, in both cases of the two radius ratios considered. The computed region of compressive tangential stress at the bore in this $Z = 0$ axial plane was in turn larger for $R_2/R_1 = 3$ than it was for $R_2/R_1 = 2$. This is not an unexpected feature, for larger cracks would imply a larger surface area in the radial crack plane being subjected to the pressure which is a direct compressive stress.

For $R_2/R_1 = 2$, the hoop stresses at the inner surface of the cylinder in the $Z = 0$ axial plane were found to be only compressive up to about $\theta = 11^0$ when $b/W = 0.2$. At this crack depth, the computed hoop

stresses were within 2% of the Lamé solution value, $\sigma_h^*$, from about $\theta = 45^0$. When $b/W = 0.8$, however, the hoop stresses at the bore were compressive up to about $\theta = 40^0$ in the same axial plane, then increased in magnitude in the tensile state to 1.24 $\sigma_h^*$ at $\theta = 157.5^0$ before they decreased to 1.15 $\sigma_h^*$ at $\theta = 180^0$. It is interesting to note that for this radius ratio, the computed hoop stresses at the bore were within 4% of $\sigma_h^*$ at $\theta = 90^0$ at all the crack depths considered, being progressively lower in magnitude than this value $\sigma_h^*$ when $\theta < 90^0$ and increasingly greater when $180^0 \geq \theta > 90^0$, with increasing crack depths. For $R_2/R_1 = 3$ (Figure 6.19), this "cross-over" point was not at $\theta = 90^0$, but instead was at about $\theta = 108^0$. In this case, the computed hoop stresses at the bore in the $Z = 0$ axial plane only became tensile at about $\theta = 27^0$ when the relative crack depth was 0.2; the corresponding angular position when $b/W = 0.8$ was found to be at about $\theta = 64^0$. Also, beyond $\theta \simeq 108^0$, the magnitude of $\sigma_h/\sigma_h^*$ was higher than it was for $R_2/R_1 = 2$ with the same relative crack depth; when $b/W = 0.8$, the computed value of $\sigma_h$ was 1.64 $\sigma_h^*$ at $\theta = 157.5^0$.

### 6.4.2 Hoop Strains

As strains are experimentally measurable quantites, they can be used to monitor crack growth if there exists a relationship between, say, the hoop strain, $\varepsilon_h$, at the outer surface of the cylinder and the crack depth. Shannon & Austin (1971), working on cylinders with long straight-fronted surface crack, measured the hoop strains at the outer diameter in the same plane of the crack for a range of different crack depths, and showed that there was indeed such a relationship. Similar experiments were carried out by Crofton (1977) but on cylinders with semi-elliptical surface cracks; the hoop strains in this case were measured at the outer diameter through the point of maximum crack penetration (point A

in Figure 6.1(b)). His results for $R_2/R_1$ = 2 are shown in Figure 6.20. Also shown are the computed variations of hoop strains obtained from the present numerical study for this radius ratio, and the range of crack depths analysed. The hoop strains are normalized with respect to the corresponding Lame solution hoop strain, $\varepsilon_h^*$, for an uncracked cylinder. For $b/W$ up to about 0.5, there is a slight reduction in the hoop strain compared with an uncracked cylinder, but for deeper cracks the hoop strain increases rapidly. The general agreement between the computed and experimental results is very good indeed, the small differences between them possibly being due to the uncertain form of pressure loading on the crack faces. While the computed results were obtained for the full internal pressure acting throughout the crack, which represents the worst situation, this may not have been obtained in the experiments which involved cyclically varying hydraulic oil pressure.

In order to obtain a better perspective of the hoop strain variation at the outer surface of the cylinder, the computed values of $\varepsilon_h$ around the outer circumference at the cross-section through the point of maximum crack penetration are plotted for the range of crack depths considered. The results for $R_2/R_1$ = 2 and $R_2/R_1$ = 3 are shown in Figures 6.21 and 6.22, respectively. Hoop strains are again normalized to the corresponding Lamé solution hoop strain for an uncracked cylinder. The two sets of results are qualitatively very similar. It is interesting to note that for both the radius ratios considered, the hoop strain increases from $\theta = 0^0$ to a maximum which occurs between $\theta = 30^0$ and $\theta = 60^0$, for the range of crack depths analysed, and then decreases to the Lamé solution at about $\theta = 115^0$ beyond which it is lower than the Lamé strain. The computed value of the maximum normalized hoop strain was, however, significantly higher in magnitude for $R_2/R_1$ = 3 than it was for $R_2/R_1$ = 2

with the same relative crack depth. It is perhaps worth noting that Figures 6.21 and 6.22 could be somewhat misleading in that the curves at $\theta = 0^0$ and $\theta = 180^0$ are not horizontal as they should be. This is due to insufficient number of points for plotting the curves around these two positions where $\varepsilon_h$ varies rapidly.

The location of the maximum hoop strain discussed here has important implications for the positioning of strain gauges for maximum sensitivity in the experimental monitoring of crack growth. But because this position may vary somewhat with different crack depths, as predicted by the computational solutions, it may present practical difficulties. Further, due to the rapid change in the magnitude of the hoop strain at about $\theta = 0^0$, especially for the deeper cracks, the measured strains would be more susceptible to error, particularly since the strain gauges are finite in size. Indeed, the experiments by Crofton (1977) showed that a slight misalignment of the strain gauges at $\theta = 0^0$ could give rise to totally erroneous sets of results. Perhaps, instead of measuring $\varepsilon_h$ at the outer diameter of the radial crack plane, a better way to monitor crack growth would be to measure it at the outer diameter of the radial plane diametrically opposite, i.e. at point B in Figure 6.1(b), where, as seen in Figures 6.21 and 6.22, the computed values of $\varepsilon_h$ do not vary so rapidly with $\theta$. Here, the values of $\varepsilon_h/\varepsilon_h^*$ decrease monotonically with increasing $b/W$ as shown in Figures 6.23 and 6.24, the decrease being significantly greater for $R_2/R_1 = 3$ than it is for $R_2/R_1 = 2$. At $b/W = 0.8$, for example, the computed value of $\varepsilon_h$ was 0.78 $\varepsilon_h^*$ for $R_2/R_1 = 2$, but for $R_2/R_1 = 3$, it was 0.35 $\varepsilon_h^*$.

### 6.4.3 Stress Intensity Factors

Stress intensity factors at points around the crack front of the semi-elliptical surface crack were evaluated for each of the radius ratios and the range of crack depths considered. For the calculation of $K_I$, plane strain conditions were assumed at all points along the crack front, except at the internal surface of the cylinder which was treated as being under plane stress. The values of normalized stress intensity factor, $K_I/P\sqrt{\pi b}$, presented in Tables 6.1 and 6.2 were obtained by the direct method using the crack face displacement data as discussed in Section 5.1.1. The only exceptions are the results shown in parentheses in Table 6.1 for $b/W = 0.4$ which were obtained by the indirect method. To obtain the stress intensity factors for this case, the entire crack front was advanced by 1.25% of the crack depth and the procedure outlined in Section 5.1.3 followed. Values obtained by the two methods differed by less than 1.5%, which serves to verify the accuracy of the solutions. Further, when $K_{I_{ref}}$ in (5.10) was taken to be the value obtained by the extrapolation method at the point of maximum crack penetration, for the purposes of calculating $K_I$ around the crack front, all the results so obtained, shown in Tables 6.3 and 6.4, were within 2% of the corresponding values displayed in Tables 6.1 and 6.2. Position around the crack front is defined by the angle $\phi$, ranging from $\phi = 0^o$ at the point of maximum crack penetration to $\phi = 90^o$ at the internal surface of the cylinder, as illustrated in Figures 6.26 and 6.27. While element corner nodes on the semi-elliptical crack front were arranged to be at $\phi = 0^o$, $30^o$, $60^o$ and $90^o$ exactly, the angular positions of the mid-side nodes were only approximately $15^o$, $45^o$ and $75^o$. As the differences were less than $1^o$ in all cases, however, the effects on the tabulated values of $K_I$ are not significant.

Figure 6.25 shows the predicted variation of $K_I$ with relative crack depth, at the point of deepest penetration of the crack, obtained by the present three-dimensional boundary integral equation method. Also shown for comparison are predictions by Shannon (1974) for a straight-fronted axial crack (again, with pressure acting fully on the crack faces) computed using a two-dimensional finite element analysis applied to the cross-sectional plane of the cylinder. The large differences between the two and three-dimensional solutions emphasize the inadequacies of the straight-fronted crack model of what are normally observed in practice to be semi-elliptical cracks. Although a straight-fronted crack represents the worst case for a given crack depth, and therefore leads to a conservative design, Figure 6.25 suggests that the level of over-designing is likely to be excessive.

The variations of $K_I$ along the crack front according to Tables 6.1 and 6.2 are plotted in Figures 6.26 and 6.27 for the two different radius ratios, with curves being shown for two typical relative crack depths, namely 0.2 and 0.5. For both radius ratios, it appears that, moving around the crack front from the point of deepest penetration at $\phi = 0^0$, the value of $K_I$ decreases gradually to a minimum and then increases more rapidly as the free surface at $\phi = 90^0$ is approached. For the cases considered, the minimum value of $K_I$ always occurs between $\phi = 45^0$ and $\phi = 60^0$.

Table 6.5 represents values of the ratio of $K_I$ at $\phi = 90^0$ to that at $\phi = 0^0$ for both radius ratios and the range of crack depths. While the magnifying effect of the free surface is seen to be substantial, it is interesting to note that this ratio attains a maximum value as the crack grows, and then decreases again to almost unity at $b/W = 0.8$ in both cases. The maximum does not, however, occur at the same value of $b/W$ for

the two radius ratios considered. The significance of this result is uncertain, not least because of the doubt concerning the meaning of a stress intensity factor at $\phi = 90^{o}$ as discussed in the previous chapter.

## 6.5 FURTHER NUMERICAL INVESTIGATION

It was mentioned in Section 6.4.2 that the discrepancies between the computed and experimentally measured hoop strains, especially at deeper cracks, shown in Figure 6.20, could be due to the uncertain form of pressure loading at the crack faces. To ascertain that this was indeed a cause, computer runs were made for cylinders with $R_2/R_1 = 2$ having the same crack geometry, namely $b/a = 0.8$, and with relative crack depths $b/W = 0.6$ and 0.7, but with the crack faces free from any applied pressure.

A comparison of the deflections at the outer circumference of the cylinder in the axial plane through the point of maximum penetration of the crack between the case where the crack surfaces are subject to the internal pressure, as treated in the previous sections, and that in which they are not, is presented in Figure 6.28. The results are again normalized to the Lamé solution deflections for an uncracked cylinder. The long broken lines represent the results for the case with pressure acting on the crack faces, seen previously in Figure 6.10, while the continuous solid lines represent the case without the pressure loading on the crack faces. For $\theta$ less than about $20^{o}$, the deflections for the latter case were greater than those when the crack was pressurized at both crack depths considered; beyond this circumferential angle, the reverse was true. At the outer diameter through the point of maximum crack penetration, the increase in the radial deflection as a result of the absence of pressure loading on the crack faces was about 40% for $b/W = 0.6$, while for $b/W = 0.7$, it was about 83%, compared with the values obtained

when the crack was pressurized. These results concur with the remarks made earlier as regards the bending effect due to the pressure acting on the crack faces.

Figure 6.29 shows the hoop stress variations at the inner surface of the cylinder in the same axial plane as above. Also plotted for comparison are the results corresponding to the crack depths seen previously in Figure 6.18 where the crack faces were subject to the internal pressure. As can be seen in this figure, the computed hoop stress at all points at the inner surface of the cylinder in this axial plane was tensile in nature; the computed compressive tangential stress at $\theta = 0^{o}$ was, relatively, very small and was most likely due to numerical truncation errors. As the crack faces were traction-free, these results are not unexpected.

The hoop strain distribution at the outer circumference of the cylinder in this $Z = 0$ axial plane for the two crack depth considered here are shown in Figure 6.30. The features are very similar to those in Figure 6.21 in which the crack faces were subject to the internal pressure. For each of the crack depths analysed, the computed hoop strains for the case where the crack faces were traction-free were found to be less than those obtained when the crack was pressurized below about $\theta = 115^{o}$; beyond this circumferential angle, they were greater. At $\theta = 0^{o}$, the computed value of the hoop strain $\varepsilon_h$ was 1.027 $\varepsilon_h^*$ at $b/W = 0.6$ and 1.109 $\varepsilon_h^*$ at $b/W = 0.7$. The corresponding values obtained previously with pressure acting on the crack faces are 1.087 $\varepsilon_h^*$ and 1.323 $\varepsilon_h^*$, respectively. From the experimentally derived curve in Figure 6.20, at $b/W = 0.6$, the measured hoop strain was 1.01 $\varepsilon_h^*$, while at $b/W = 0.7$, it was 1.22 $\varepsilon_h^*$. These results support the statement made above and in an earlier section about the uncertain form of pressure loading at the crack faces. While the

computed hoop strain with the unpressurized crack at $b/W$ = 0.6 was marginally higher than that obtained from the experimental curve for the same crack depth, at $b/W$ = 0.7, it was significantly lower.

Figures 6.31 and 6.32 show the variation of the computed normalised stress intensity factor, $K_I/P\sqrt{\pi b}$, along the crack front for relative crack depths of 0.6 and 0.7, respectively. The angle $\phi$ is as defined previously in Figures 6.25 and 6.26. The corresponding results, presented in Tables 6.1 and 6.2, are also plotted for comparison. As before, plane strain conditions were assumed to prevail at all points along the crack front, except at the inner surface of the cylinder, where plane stress assumptions were made. For these two relative crack depths, the computed stress intensity factors are significantly lower in magnitude when the crack faces are traction-free, although qualitatively, their variations around the crack front are very similar to those when the crack faces are pressurized. When $b/W$ = 0.6, the computed value of $K_I/P\sqrt{\pi b}$ at the point of maximum penetration of the crack was 0.759, remaining fairly constant at this value along the crack front up to about $\phi = 45^{o}$, beyond which the normalized stress intensity factor increased fairly rapidly to a value of 1.012 at the inner surface of the cylinder. In the case where $b/W$ = 0.7, the computed value of $K_I/P\sqrt{\pi b}$ was 0.769 at the point of maximum crack penetration, decreasing very gradually to a value of 0.744 at $\phi = 45^{o}$ before increasing more rapidly to a value of 1.018 at the inner surface of the cylinder.

No other values of $b/W$ were considered in this part of the numerical investigation where zero pressure on the crack faces was assumed, although the results for a wide range of different crack depths may be of academic interest. The reason is because, in practice, it is extremely unlikely that there is a total absence of pressure acting on the crack faces since

the pressurizing medium is a fluid. The actual form of loading on the crack faces is very difficult to ascertain and will depend on the viscosity of the pressurizing fluid as well as the cyclic frequency, if the cylinder is cyclically pressurized. In any case, for a given crack shape, the results obtained in Section 6.4 where the internal pressure acts fully on the crack faces, would represent the worst case and therefore should be used for, say, design purposes instead of those obtained here.

## 6.6 CRACK PROPAGATION ANALYSIS

The methodology of crack propagation and residual life prediction outlined in the previous chapter (Section 5.4) was applied to the cracked cylinder problem for the radius ratio $R_2/R_1$ of 2.0. The analysis is based on Paris' formula (2.29) which may be written in the form of (5.24) for each degree-of-freedom (DOF) characterizing the crack shape. As post-mortem measurements of the crack shapes have shown that they can be very well represented by semi-ellipses, only a two DOF model was used; the two DOF being the semi-minor and semi-major axes of the semi-ellipse representing the crack. Denoting the stress intensity factors at the ends of these axes by $K_{Ib}$ and $K_{Ia}$, respectively, the propagation rates due to cyclic loading for this two DOF model can be found from the following:

$$\frac{da}{dN} = C_a \left(\Delta K_{Ia}\right)^{m_a} \tag{6.3a}$$

$$\frac{da}{dN} = C_b \left(\Delta K_{Ib}\right)^{m_b} \tag{6.3b}$$

in which $C_a$, $m_a$ and $C_b$, $m_b$ are material constants in the directions of the semi-major and semi-minor axes, respectively.

The material (Ni-Cr-Mo steel) used in the fatigue experiments with

which results the computational predictions are to be compared is known to be isotropic as regards fracture behaviour. Therefore, for the analysis, it was assumed that $C_a = C_b$ and $m_a = m_b$; the subscripts in $C$ and $m$ will now be dropped for convenience. Fatigue data obtained through a series of experimens were processed using the method proposed by McCartney & Cooper (1977) and the following median values of $C$ and $m$ were obtained:

$$C = 1.5463 \times 10^{-16} \qquad \text{(Units: N, mm)}$$
$$m = 3.88 \tag{6.4}$$

The crack propagation analysis was therefore to be carried out using these values for the material constants. The main task left, to be performed numerically, was to model the propagating crack in the cylinder and obtain the stress intensity factor functions, $\Delta K_{Ia}$ and $\Delta K_{Ib}$, in order that (6.3) could be solved.

### 6.6.1 Evaluation of Stress Intensity Factors

Because a relatively large number of computer runs is often required in fatigue analysis, the indirect method for determining the stress intensity factors is to be preferred on cost grounds; this was discussed in Section 5.4. Twelve computer runs were made for a range of different actual crack geometries as measured from the post-mortem experimental specimens. In the numerical model, the total length of the cylinder was taken to be 5.67 times the cylinder wall thickness (this figure was chosen for convenience because of the actual numerical values of the dimensions used). The element configuration and the number used to model the physical problem were varied to suit the different crack depths; a typical boundary mesh is shown in Figure 6.33. It can be seen

that the mesh discretization in the region of the crack front is very much less refined than it was previously (Figures 6.6 and 6.7, for example), where the stress intensity factors were obtained by the direct displacement method. Also, plane strain boundary conditions were applied at the ends of the cylinder for the analysis. For each crack geometry, the strain energy, $U$, of the body was calculated, the variation of $U$ with respect to the crack surface area, $A$, is shown in Figure 6.34 where the values of $U$ have been normalized to the value of the strain energy for an uncracked cylinder of the same geometry, $U_o$.

To obtain the stress intensity factors $K_{Ia}$ and $K_{Ib}$ from the strain energy data, either of two approaches may be followed. For a quarter ellipse, as modelled, the differentiation of the strain energy with respect to the area of the crack as defined in (5.5) can be carried out as follows:

$$\frac{dU}{dA} = \frac{\partial U}{\partial a}\frac{\partial a}{\partial A} + \frac{\partial U}{\partial b}\frac{\partial b}{\partial A} = \frac{4}{\pi}\left(\frac{1}{b}\frac{\partial U}{\partial a} + \frac{1}{a}\frac{\partial U}{\partial b}\right) \tag{6.5}$$

The partial derivatives $\partial U/\partial a$ and $\partial U/\partial b$ in (6.5) can be found by the variation of one of the semi-axes, $a$ or $b$, while the other is kept constant. The stress intensity factors for crack propagation in the directions of the semi-major and semi-minor axes of the ellipse are then given by:

$$\overline{K}_{Ia} = \left\{\frac{4H'}{\pi\, b}\frac{\partial U}{\partial a}\right\}^{\frac{1}{2}} \tag{6.6}$$

$$\overline{K}_{Ib} = \left\{\frac{4H'}{\pi\, a}\frac{\partial U}{\partial b}\right\}^{\frac{1}{2}} \tag{6.7}$$

respectively. In (6.6) and (6.7), the symbols $\overline{K}_{Ia}$ and $\overline{K}_{Ib}$ are used because they are not the local stress intensity factors at the ends of the

semi-axes which are being denoted by $K_{Ia}$ and $K_{Ib}$. Instead, they are "local mean" values because the strain energy release rates from which these quantities are calculated are associated with the creation of the shaded surface areas $\Delta A_a$ and $\Delta A_b$ in Figure 6.35, i.e.

$$G_a = \left(\frac{\partial U}{\partial A}\right)_a = \frac{4}{\pi b}\left(\frac{\partial U}{\partial a}\right) \tag{6.8}$$

$$G_b = \left(\frac{\partial U}{\partial A}\right)_b = \frac{4}{\pi a}\left(\frac{\partial U}{\partial b}\right) \tag{6.9}$$

$\Delta A_a$ and $(\partial U/\partial A)_a$ are, respectively, the change in crack surface area and the strain energy release rate as a result of a perturbation of the value $a$ alone. $\Delta A_b$ and $(\partial U/\partial A)_b$ are similarly defined but with the perturbation in the value of $b$ alone.

This approach implies a necessity of functional fitting to the computed values of $U$, a polynomial in the two variables $a$ and $b$. Bergan & Aamodt (1974) in their numerical fatigue analysis of a semi-elliptical part-through crack in a plate using the finite element method, obtained good results with the following polynomial for $U$:

$$U = B_1 a^2 b^2 + B_2 a b^2 + B_3 b^2 + B_4 a^2 b + B_5 a b + B_6 a + B_7 a^2 + B_8 a + B_9 \tag{6.10}$$

where the coefficients of $a$ and $b$ were determined by least-squares. Further, they found that third and higher order terms of $a$ and $b$ would give rise to undesirable oscillations in the fitted function due to the scatter of the computed values of $U$. The way of obtaining the polynomial in the two variables which would yield good results by this approach seems very much a trial-and-error method. Further, when the fitted function is

to be differentiated to obtain the stress intensity factors, severe errors could still result even though the calculated functional values of $U$ agree very well with the discrete values to which the function was fitted. Indeed, this was found to be the case in the various unsuccessful attempts made to find a suitable two variable function of $U$ for the present analysis which could yield sensible values of the stress intensity factor. In some of these attempts, even negative values of the partial derivatives of $U$ were obtained, which are inadmissible! This approach was therefore discarded.

The alternative approach has already been briefly outlined in the previous chapter (Section 5.4). For each crack size, the integral of $(V^*/\sqrt{r^*})^2$ in the following equation, modified from (5.12):

$$\frac{1}{K_{I_{ref}}} = \left\{ \frac{1}{G\,H'} \int \left[ \frac{V^*(\bar{s})}{\sqrt{r^*(\bar{s})}} \right]^2 d\bar{s} \right\}^{\frac{1}{2}} \tag{6.11}$$

was calculated from the computed results. In (6.11), $\bar{s}$ is the non-dimensional distance along the crack front having the same meaning as the dimensional $s$ in (5.12) if this latter equation is used. This leaves the strain energy release rate $G$ as the only unknown in (6.11) before the stress intensity factors along the crack front can be evaluated.

The next task then is to determine accurately $dU/dA$ corresponding to each of these crack geometries considered. An obvious means of attack would be to least-squares fit a, say, second order polynomial to the discrete values of $U$ with respect to just the area of the crack surface, $A$, as shown in Figure 6.34. The computed values of $U$ and the least-squares fitted values, $U^*$, for the various crack sizes considered are shown in Table 6.6. Also shown in this table are the normalized strain energy release rates, $d(U^*/U_o)/d(A/W^2)$, at each of the

crack size, obtained by differentiating the polynomial function. Although this is a reasonable approach to obtain $G$, the range of crack sizes here is perhaps too large for a second degree polynomial to represent the variation of $U$ satisfactorily over the entire range. Yet higher degree polynomials tend to give rise to undesirable oscillations, especially when differentiated.

An improvement over this approach can, however, be made. Instead of fitting over the entire range of crack sizes, a series of least-squares fits with a second degree polynomial was applied over each possible group of five neighbouring points in Figure 6.34. The derivative $dU/dA$ was then calculated at the third of the five points. With this approach, it was possible to calculate the strain energy release rate at all the points with the exceptions of the crack sizes denoted by points 1 and 2, and 11 and 12 (Figure 6.34). For points 1 and 2, the values of $G$ were obtained by differentiating the polynomial for the first five crack sizes, while for points 11 and 12, that for the last five crack sizes. Table 6.7 shows the least-squares fitted values of the normalized strain energies and the corresponding normalized strain energy release rates for the points 2 to 6 in Figure 6.34. It can be seen that there is considerably less deviation between the computed and least-squares fitted values of $U$ in the limited range, compared to the values of Table 6.6. In effect, this method employs a series of overlapping parabolas instead of just one parabola to represent the strain energy variation over the entire range of crack sizes considered. The strain energy release rates so calculated should therefore be more accurate compared to the previous method.

Having now obtained $G$ for each of the crack sizes, all the terms on the right hand side of (6.11) are known. $K_{I_{ref}}$ could then be calculated and the stress intensity factor at points along the crack front

for each of the crack sizes considered obtained using (5.10). Table 6.8 presents the values of the normalized stress intensity factor so obtained, at the semi-major and semi-minor axes of the semi-ellipse representing the crack, $K_{Ia}/P\sqrt{\pi b}$ and $K_{Ib}/P\sqrt{\pi b}$, respectively. For the calculation of $K_{Ia}$, plane stress assumptions have been assumed.

### 6.6.2 Prediction of Crack Growth

The cyclic pressure acting in the cylinder considered varied from zero to $P$, therefore the stress intensity factor range for crack propagation along the semi-major and semi-minor axes are simply the values of $K_{Ia}$ and $K_{Ib}$, respectively, obtained above. To obtain the $\Delta K_{Ia}$ and $\Delta K_{Ib}$ functions for the solution of (6.3), least-squares fitting by simple polynomials to the discrete values of the stress intensity factors presented in Table 6.8 was again applied. The order of the polynomial would not be so critical here since the solution of the differential equations is in effect an integration process, which in turn is a smoothing process. The following simple polynomials were found to adequately represent the values presented in Table 6.8:

$$\frac{\Delta K_{Ia}}{P\sqrt{W}} = 1.20317 + 0.83201\left(\frac{a}{W}\right) + 0.73712\left(\frac{a}{W}\right)^2 \qquad (6.12)$$

$$\frac{\Delta K_{Ib}}{P\sqrt{W}} = 1.37588 + 0.16655\left(\frac{b}{W}\right) + 1.76986\left(\frac{b}{W}\right)^2 \qquad (6.13)$$

These functions are plotted in Figures 6.36 and 6.37, respectively. Also shown in these figures are corresponding values of stress intensity factors for $b/a = 0.8$, $R_2/R_1 = 2$ from Table 6.1, which were obtained using the displacement method. The agreement between the values from the curve fitted functions (6.12) and (6.13), and those obtained previously for the

crack geometry $b/a$ = 0.8 is very good indeed. In view of the fact that the mean value of $b/a$ experimentally measured for the propagating crack was 0.77, this agreement is to be expected.

The expressions (6.12) and (6.13) can now be substituted into (6.3a) and (6.3b), respectively, for the fatigue crack growth prediction. Given the initial values of $a$ and $b$, the solution to the differential equations can be obtained numerically, such as by the Adams-Bashforth predictor-corrector method. The numerical prediction of the crack growth was compared with the set of experimental results which have not been used previously for the numerical analysis, and therefore provide a check for the accuracy of the prediction. The comparison, shown in Figure 6.38, displays reasonably good agreement between the experimental and predicted results, with the numerical analysis generally predicting a faster rate of crack growth than experimentally measured. The shape of the crack predicted by the numerical analysis is shown in Figure 6.39, being almost similar at all stages of the propagation period considered. A least-squares fit by a straight line to the points in Figure 6.39 yields a slope $b/a$ of 0.77 which is in fact the mean value obtained from post-mortem measurements of the crack shape! The agreement between the predicted and experimental results are thus extremely encouraging indeed.

Although the analysis carried out here is for a two-DOF model, this is superfluous if the shape of the crack as it propagates remains unchanged. The analysis could, in principle, be simplified further using a one-DOF model. For example, given the crack depth, the geometry of the crack would be defined, and the crack propagation analysis would merely keep track of the growing crack depth. However, the initial crack is, in practice, uncontrollably arbitrary, and while the crack may grow towards the common shape under moderate loading conditions, the intermediate crack

shapes are still important, for the critical crack size under the service loading conditions may be in this range. Therefore, a model with at least two DOF should still be used for fatigue analysis of such three-dimensional cracks.

It should be reminded that the analysis presented above has been carried out for materials which are isotropic both in terms of mechanical as well as fracture behaviour. When the material is anisotropic, it is most unlikely that the crack-growth characteristics would remain direction-independent. Under such circumstances, the crack shape developed would, in general, be different from what was observed and predicted above.

TABLE 6.1

Normalized Stress Intensity Factors, $K_I/P\sqrt{\pi b}$, for Semi-Elliptical Surface Crack in Pressurized Cylinder, $R_2/R_1 = 2$, $b/a = 0.8$

| $b/W$ | $\phi$ (see Figures 6.26 and 6.27) | | | | | | |
|---|---|---|---|---|---|---|---|
| | 0° | 15° | 30° | 45° | 60° | 75° | 90° |
| 0.2 | 1.617 | 1.604 | 1.588 | 1.565 | 1.565 | 1.604 | 1.782 |
| 0.3 | 1.550 | 1.546 | 1.532 | 1.515 | 1.528 | 1.613 | 1.707 |
| 0.4 | 1.492 | 1.473 | 1.469 | 1.455 | 1.481 | 1.573 | 1.684 |
| (0.4) | (1.483) | (1.471) | (1.466) | (1.456) | (1.474) | (1.551) | (1.668) |
| 0.5 | 1.477 | 1.450 | 1.447 | 1.432 | 1.468 | 1.551 | 1.677 |
| 0.6 | 1.490 | 1.480 | 1.460 | 1.463 | 1.473 | 1.582 | 1.703 |
| 0.7 | 1.523 | 1.511 | 1.480 | 1.457 | 1.470 | 1.576 | 1.727 |
| 0.8 | 1.623 | 1.607 | 1.582 | 1.526 | 1.520 | 1.536 | 1.669 |

TABLE 6.2

Normalized Stress Intensity Factors, $K_I/P\sqrt{\pi b}$, for Semi-Elliptical Surface Crack in Pressurized Cylinder, $R_2/R_1 = 3$, $b/a = 0.8$

| $b/W$ | $\phi$ | | | | | | |
|---|---|---|---|---|---|---|---|
| | 0° | 15° | 30° | 45° | 60° | 75° | 90° |
| 0.2 | 1.208 | 1.197 | 1.189 | 1.183 | 1.187 | 1.245 | 1.374 |
| 0.3 | 1.123 | 1.112 | 1.110 | 1.101 | 1.124 | 1.188 | 1.271 |
| 0.4 | 1.067 | 1.055 | 1.055 | 1.038 | 1.074 | 1.147 | 1.246 |
| 0.5 | 1.062 | 1.051 | 1.048 | 1.034 | 1.058 | 1.126 | 1.227 |
| 0.6 | 1.087 | 1.075 | 1.070 | 1.052 | 1.072 | 1.107 | 1.213 |
| 0.7 | 1.118 | 1.094 | 1.091 | 1.050 | 1.062 | 1.132 | 1.209 |
| 0.8 | 1.216 | 1.187 | 1.168 | 1.115 | 1.090 | 1.139 | 1.238 |

TABLE 6.3

Normalized Stress Intensity Factors, $K_I/P\sqrt{\pi b}$, for Semi-Elliptical Surface Crack in Pressurized Cylinder, $R_2/R_1 = 2$, $b/a = 0.8$

| $b/W$ | $\phi$ (see Figures 6.26 and 6.27) | | | | | | |
|---|---|---|---|---|---|---|---|
| | 0° | 15° | 30° | 45° | 60° | 75° | 90° |
| 0.2 | 1.617 | 1.604 | 1.588 | 1.577 | 1.571 | 1.604 | 1.800 |
| 0.3 | 1.550 | 1.541 | 1.531 | 1.520 | 1.525 | 1.594 | 1.687 |
| 0.4 | 1.492 | 1.480 | 1.474 | 1.465 | 1.486 | 1.561 | 1.678 |
| 0.5 | 1.477 | 1.458 | 1.442 | 1.423 | 1.465 | 1.563 | 1.686 |
| 0.6 | 1.490 | 1.471 | 1.471 | 1.446 | 1.485 | 1.572 | 1.722 |
| 0.7 | 1.523 | 1.500 | 1.490 | 1.430 | 1.479 | 1.571 | 1.739 |
| 0.8 | 1.623 | 1.603 | 1.600 | 1.526 | 1.530 | 1.536 | 1.647 |

TABLE 6.4

Normalized Stress Intensity Factors, $K_I/P\sqrt{\pi b}$, for Semi-Elliptical Surface Crack in Pressurized Cylinder, $R_2/R_1 = 3$, $b/a = 0.8$

| $b/W$ | $\phi$ (see Figures 6.26 and 6.27) | | | | | | |
|---|---|---|---|---|---|---|---|
| | 0° | 15° | 30° | 45° | 60° | 75° | 90° |
| 0.2 | 1.208 | 1.197 | 1.189 | 1.184 | 1.189 | 1.245 | 1.380 |
| 0.3 | 1.123 | 1.114 | 1.110 | 1.103 | 1.120 | 1.177 | 1.262 |
| 0.4 | 1.067 | 1.055 | 1.056 | 1.043 | 1.072 | 1.132 | 1.236 |
| 0.5 | 1.062 | 1.051 | 1.048 | 1.038 | 1.054 | 1.113 | 1.217 |
| 0.6 | 1.087 | 1.076 | 1.070 | 1.053 | 1.069 | 1.113 | 1.214 |
| 0.7 | 1.118 | 1.098 | 1.091 | 1.057 | 1.069 | 1.128 | 1.214 |
| 0.8 | 1.216 | 1.192 | 1.169 | 1.111 | 1.075 | 1.138 | 1.258 |

TABLE 6.5

Ratio of $K_I$ at the Free Surface ($\phi$ = 90°) to that at the Point of Maximum Crack Penetration ($\phi$ = 0°)

| $b/W$ | $R_2/R_1$ | |
|---|---|---|
| | 2 | 3 |
| 0.2 | 1.102 | 1.137 |
| 0.3 | 1.101 | 1.132 |
| 0.4 | 1.129 | 1.167 |
| 0.5 | 1.135 | 1.155 |
| 0.6 | 1.142 | 1.116 |
| 0.7 | 1.134 | 1.081 |
| 0.8 | 1.028 | 1.018 |

TABLE 6.6

Variation of Strain Energy and Strain Energy Release Rate with Crack Size: Least-Squares Fitted Function

$$U^*/U_o = 1.017230 + 0.021405\ (A/W^2) + 0.307602\ (A/W^2)^2$$

| Relative Crack Depth $b/W$ | Crack Surface Area $A/W^2$ | Computed Strain Energy $U/U_o$ | Curve Fitted Strain Energy $U^*/U_o$ | Strain Energy Release Rate $\frac{d(U^*/U_o)}{d(A/W^2)}$ |
|---|---|---|---|---|
| 0.3031 | 0.09374 | 1.018033 | 1.021939 | 0.007907 |
| 0.3335 | 0.11342 | 1.020563 | 1.023614 | 0.091181 |
| 0.4244 | 0.18373 | 1.031438 | 1.031546 | 0.134437 |
| 0.4547 | 0.21091 | 1.036144 | 1.035427 | 0.151158 |
| 0.4850 | 0.23997 | 1.043445 | 1.040080 | 0.169036 |
| 0.5457 | 0.30371 | 1.055659 | 1.052104 | 0.208249 |
| 0.6063 | 0.37495 | 1.073585 | 1.068500 | 0.252076 |
| 0.6669 | 0.45369 | 1.092798 | 1.090256 | 0.300517 |
| 0.7276 | 0.53993 | 1.118334 | 1.118460 | 0.353572 |
| 0.7882 | 0.63367 | 1.151181 | 1.154307 | 0.411241 |
| 0.8488 | 0.73490 | 1.189765 | 1.199089 | 0.473519 |
| 1.0 | 0.99690 | 1.349018 | 1.344266 | 0.634702 |

TABLE 6.7

Variation of Strain Energy and Strain Energy Release Rate with Crack Size: Least-Squares Fitted Function Over Limited Range

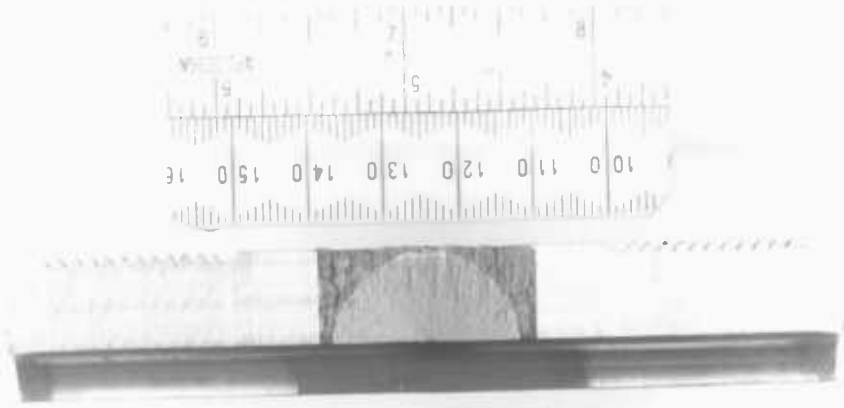
$$U^*/U_o = 1.006224 + 0.101846\ (A/W^2) + 0.203438\ (A/W^2)^2$$

| Relative Crack Depth $b/W$ | Computed Strain Energy $U/U_o$ | Curve Fitted Strain Energy $U^*/U_o$ | Strain Energy Release Rate $\frac{d(U^*/U_o)}{d(A/W^2)}$ |
|---|---|---|---|
| 0.3335 | 1.020563 | 1.020392 | 0.147993 |
| 0.4244 | 1.031438 | 1.031803 | 0.176601 |
| 0.4547 | 1.036144 | 1.036754 | 0.187660 |
| 0.4850 | 1.043445 | 1.042379 | 0.199484 |
| 0.5457 | 1.055659 | 1.055921 | 0.225418 |

TABLE 6.8

Normalized Stress Intensity Factors, $K_{I_a}/P\sqrt{\pi b}$ and $K_{I_b}/P\sqrt{\pi b}$, for Propagating Semi-Elliptical Surface Crack in Pressurized Cylinder, $R_2/R_1 = 2.0$

| $b/W$ | $K_{I_a}/P\sqrt{\pi b}$ | $K_{I_b}/P\sqrt{\pi b}$ |
|---|---|---|
| 0.3031 | 1.696 | 1.616 |
| 0.3335 | 1.633 | 1.569 |
| 0.4244 | 1.655 | 1.539 |
| 0.4547 | 1.603 | 1.545 |
| 0.4850 | 1.687 | 1.561 |
| 0.5457 | 1.640 | 1.508 |
| 0.6063 | 1.659 | 1.520 |
| 0.6669 | 1.727 | 1.590 |
| 0.7276 | 1.754 | 1.611 |
| 0.7882 | 1.763 | 1.657 |
| 0.8488 | 1.868 | 1.720 |



T·L-13

Plate 6.1

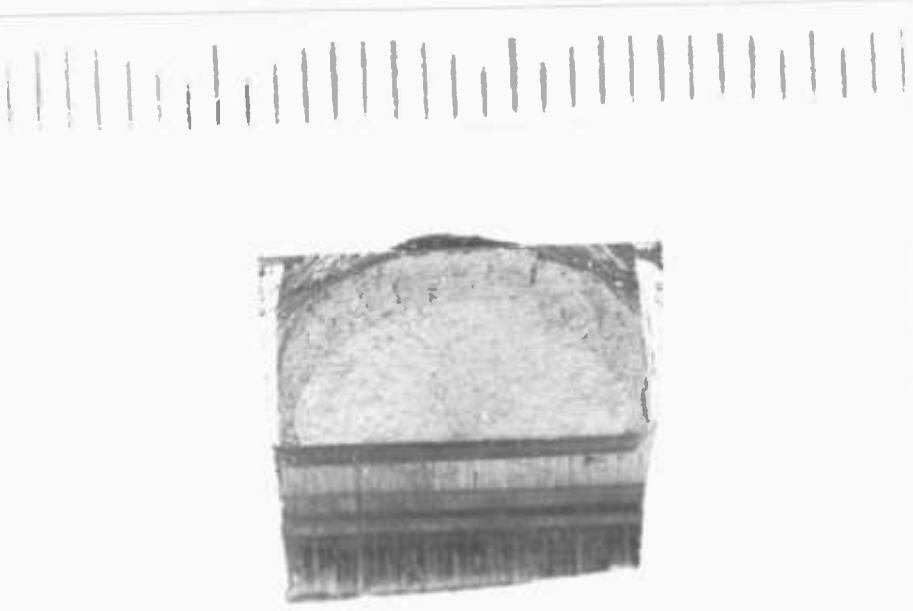


Plate 6.2

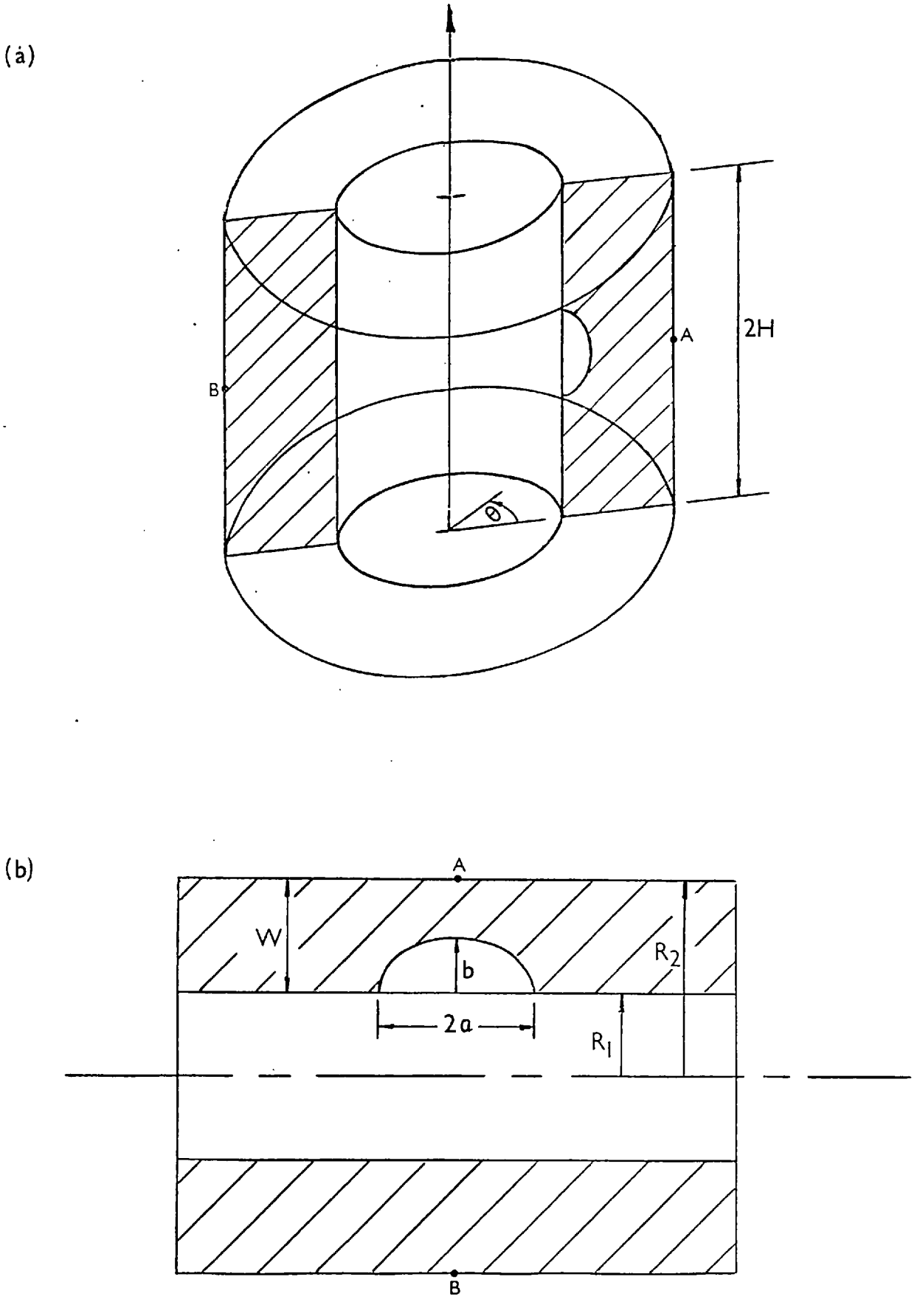



Figure 6.1: Thick-walled cylinder with an internal semi-elliptical surface crack

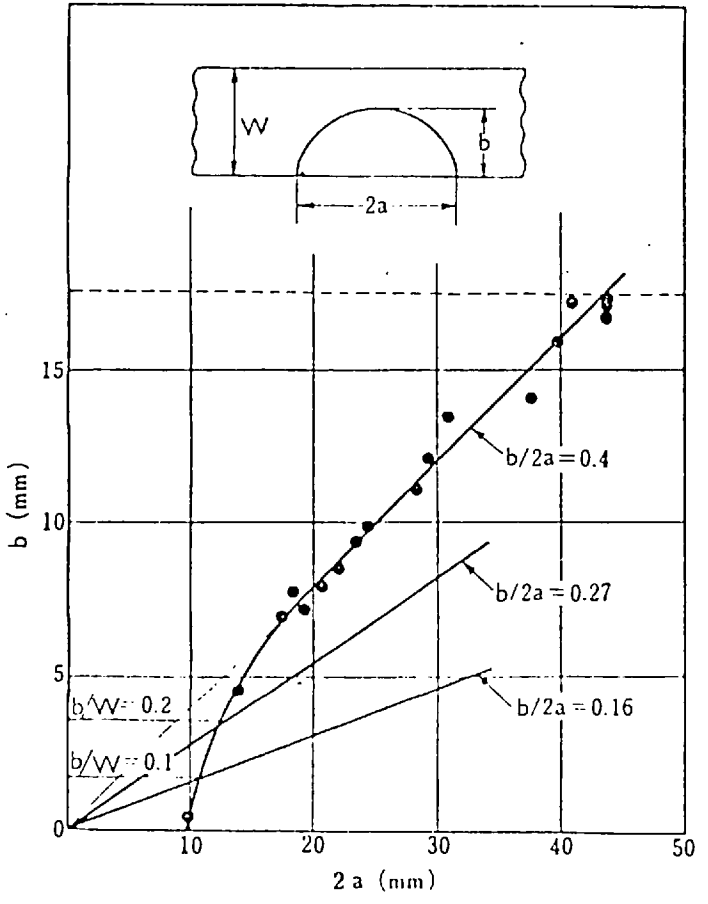



Figure 6.3: Shape of propagating crack in cylinder, $R_2/R_1$ = 2.3
(Nishioka & Hirawaka (1975))

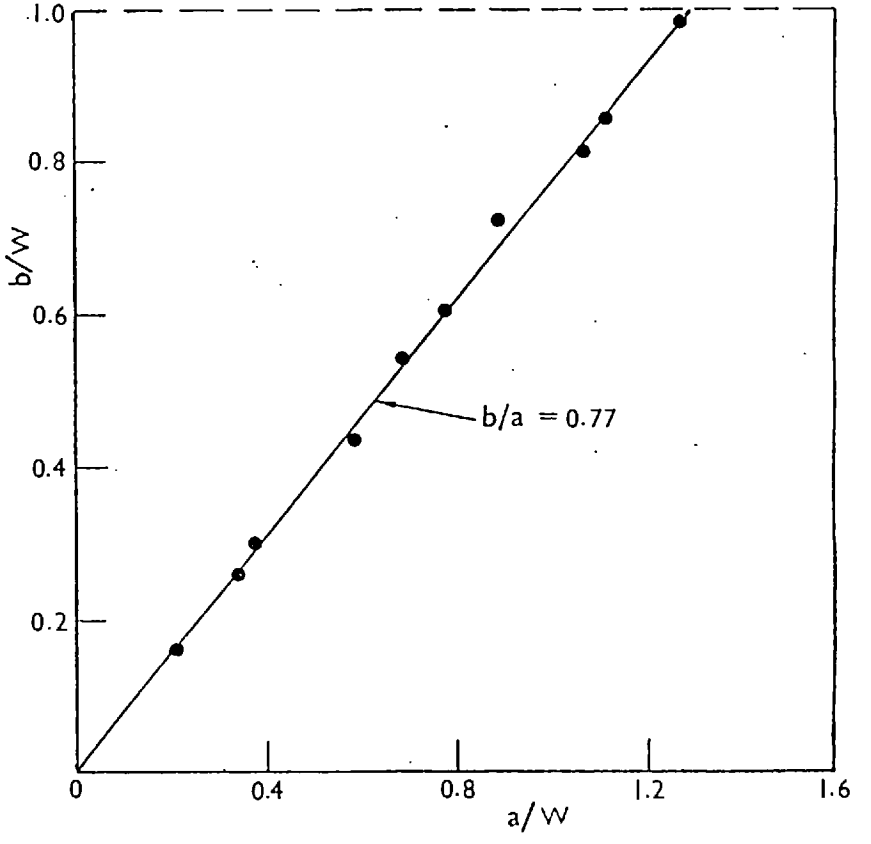



Figure 6.2: Shape of propagating crack in cylinder, $R_2/R_1$ = 2 (Tan & Crofton (1977))

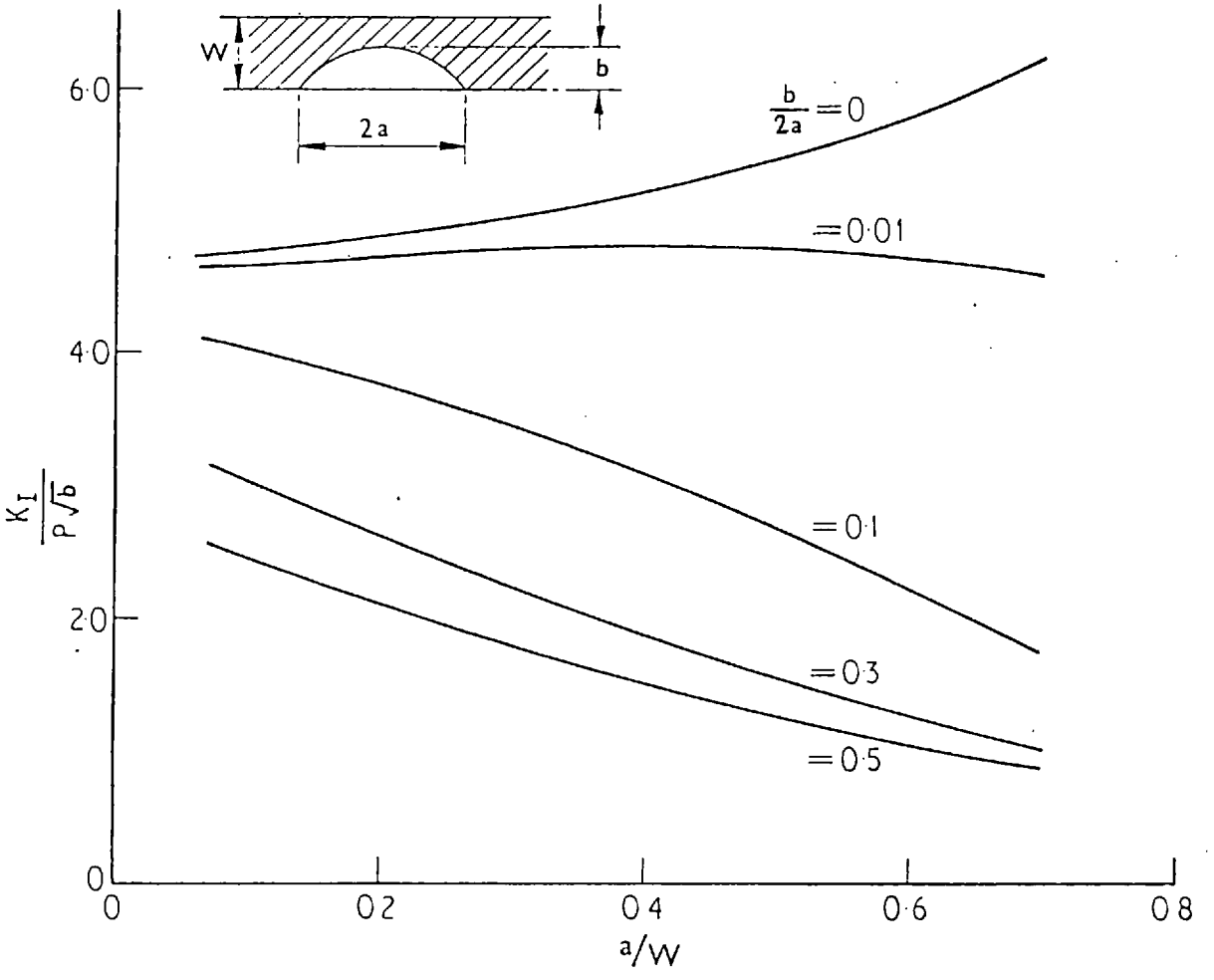



Figure 6.4: Stress intensity factors for a semi-elliptical crack in an internally pressurized cylinder (Underwood (1972))

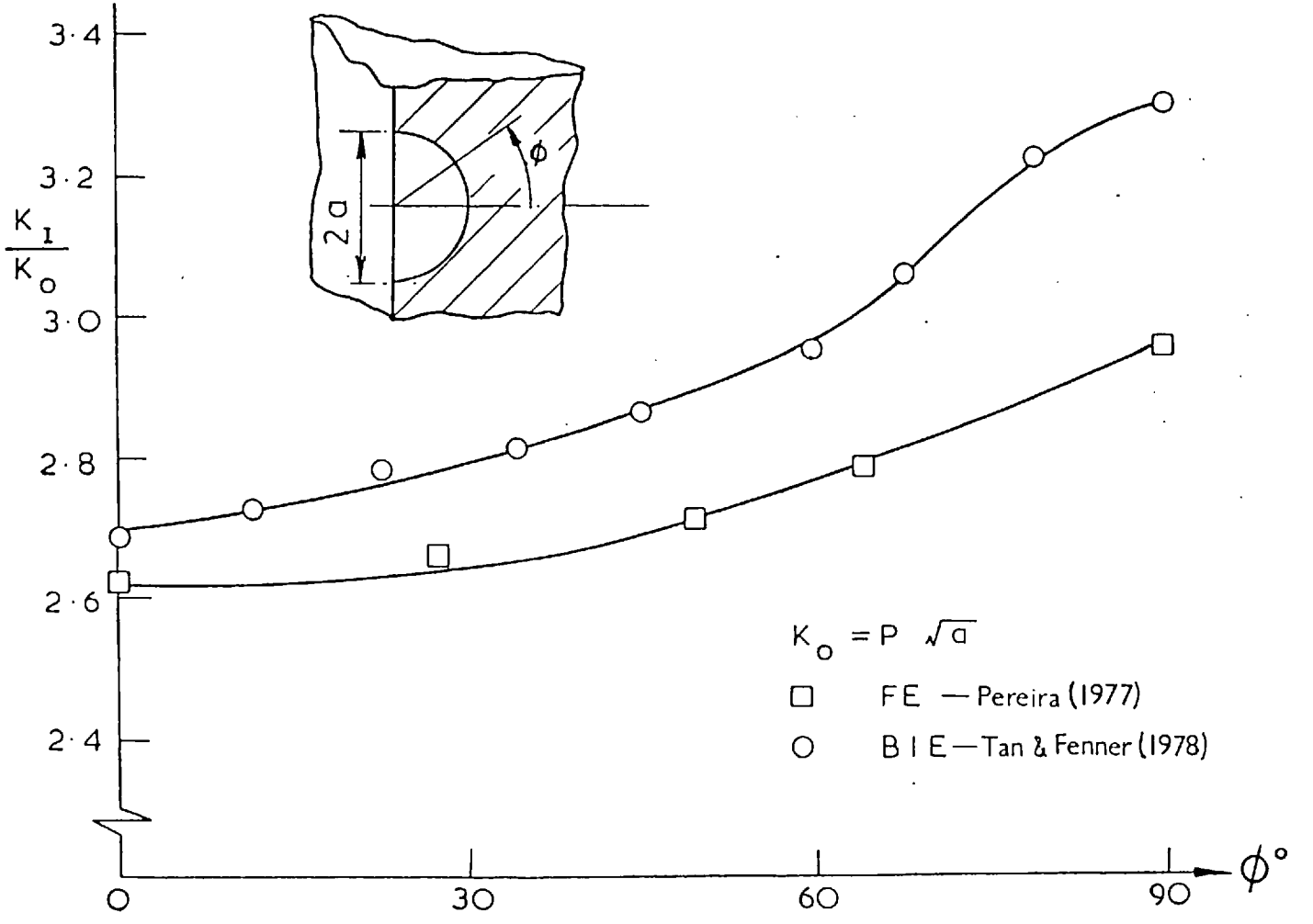



Figure 6.5: Stress intensity factor for a semi-circular crack in an internally pressurized cylinder, $R_2/R_1$ = 1.889, $a/W$ = 0.2

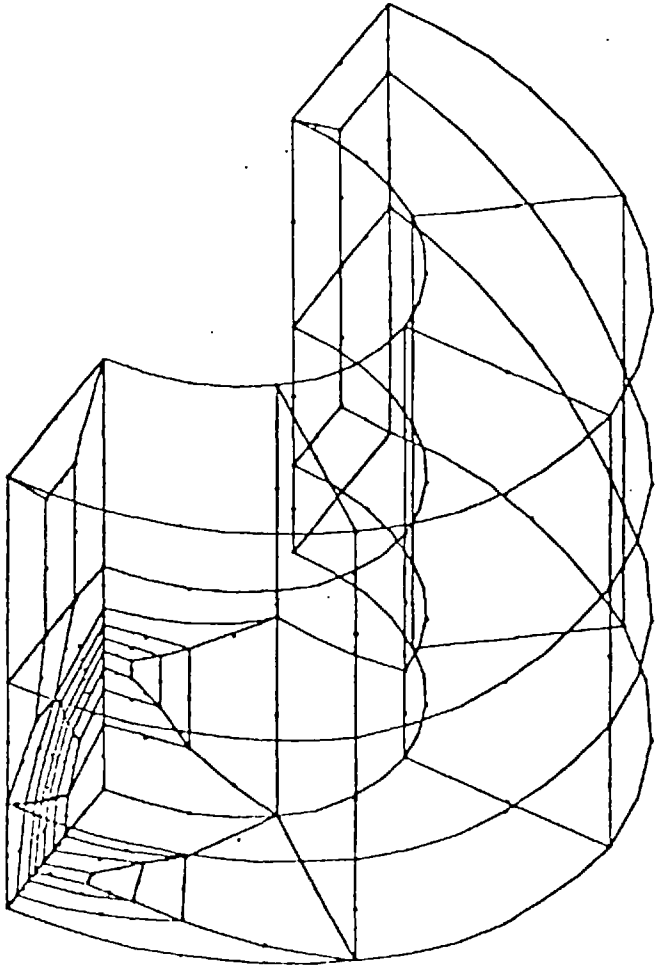


Figure 6.7: Boundary mesh for $R_2/R_1$ = 2, $b/W$ = 0.8, $b/a$ = 0.8

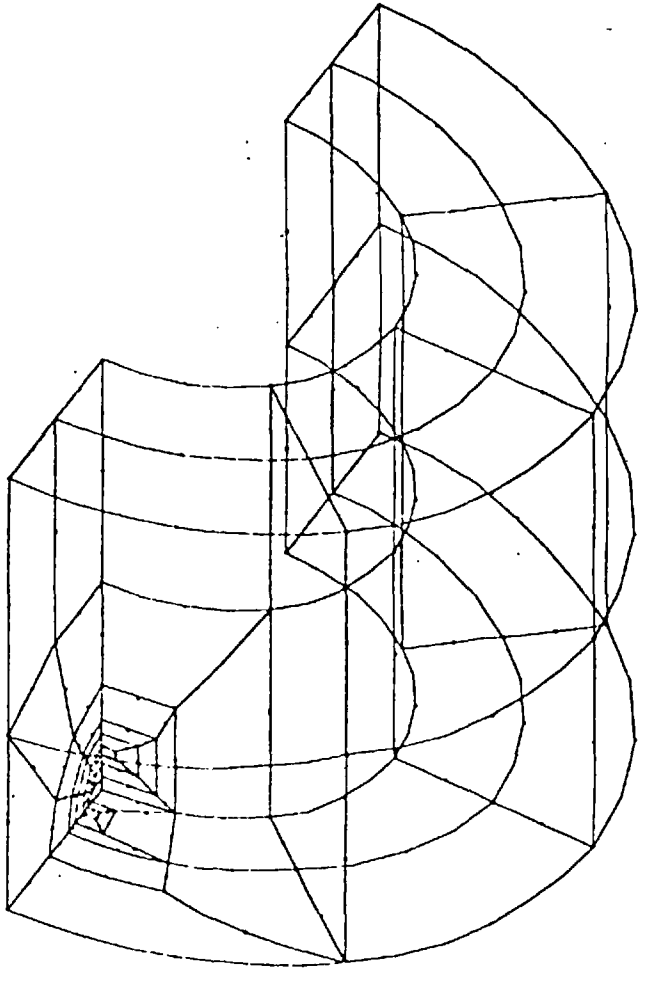


Figure 6.6: Boundary mesh for $R_2/R_1$ = 2, $b/W$ = 0.2, $b/a$ = 0.8

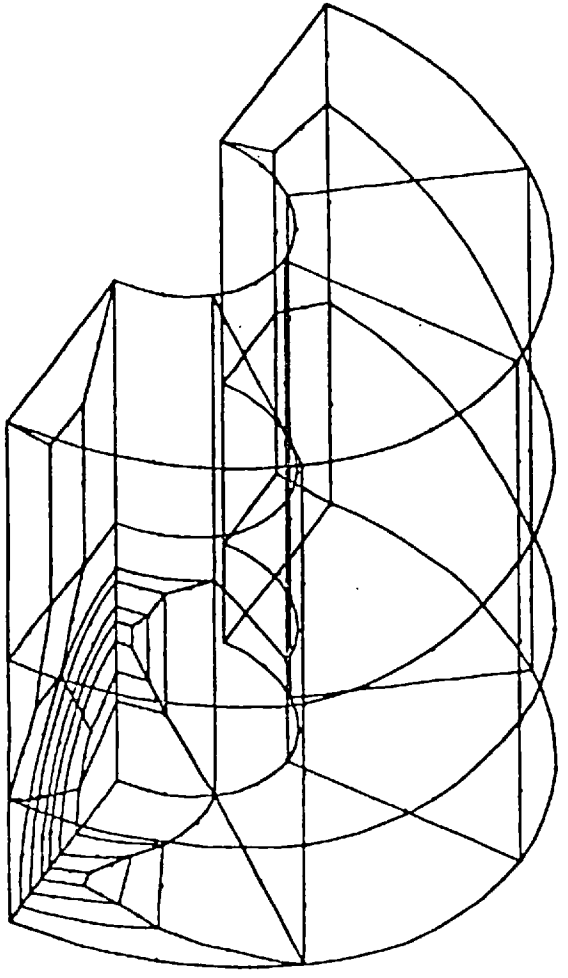


Figure 6.9: Boundary mesh for $R_2/R_1$ = 3, $b/W$ = 0.8, $b/a$ = 0.8

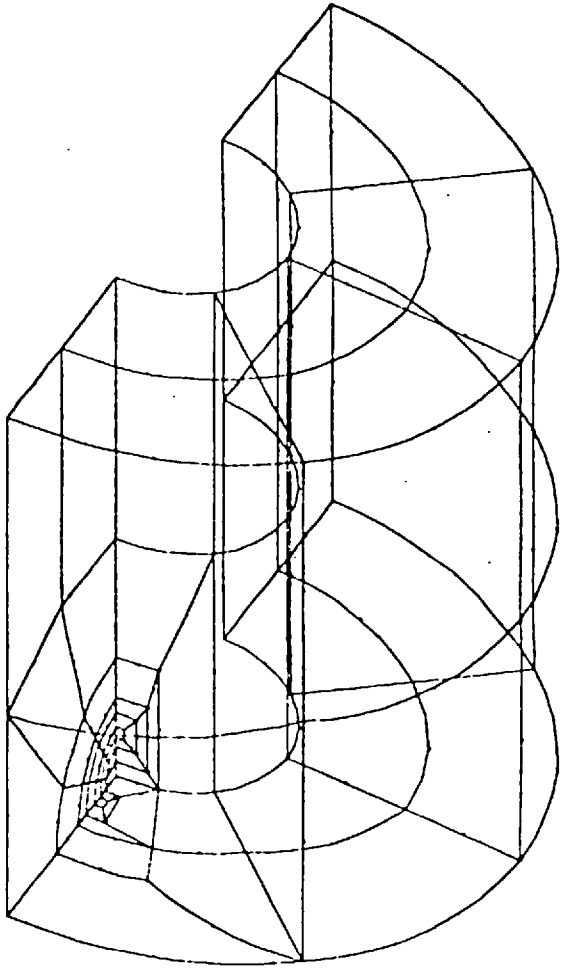


Figure 6.8: Boundary mesh for $R_2/R_1$ = 3, $b/W$ = 0.2, $b/a$ = 0.8

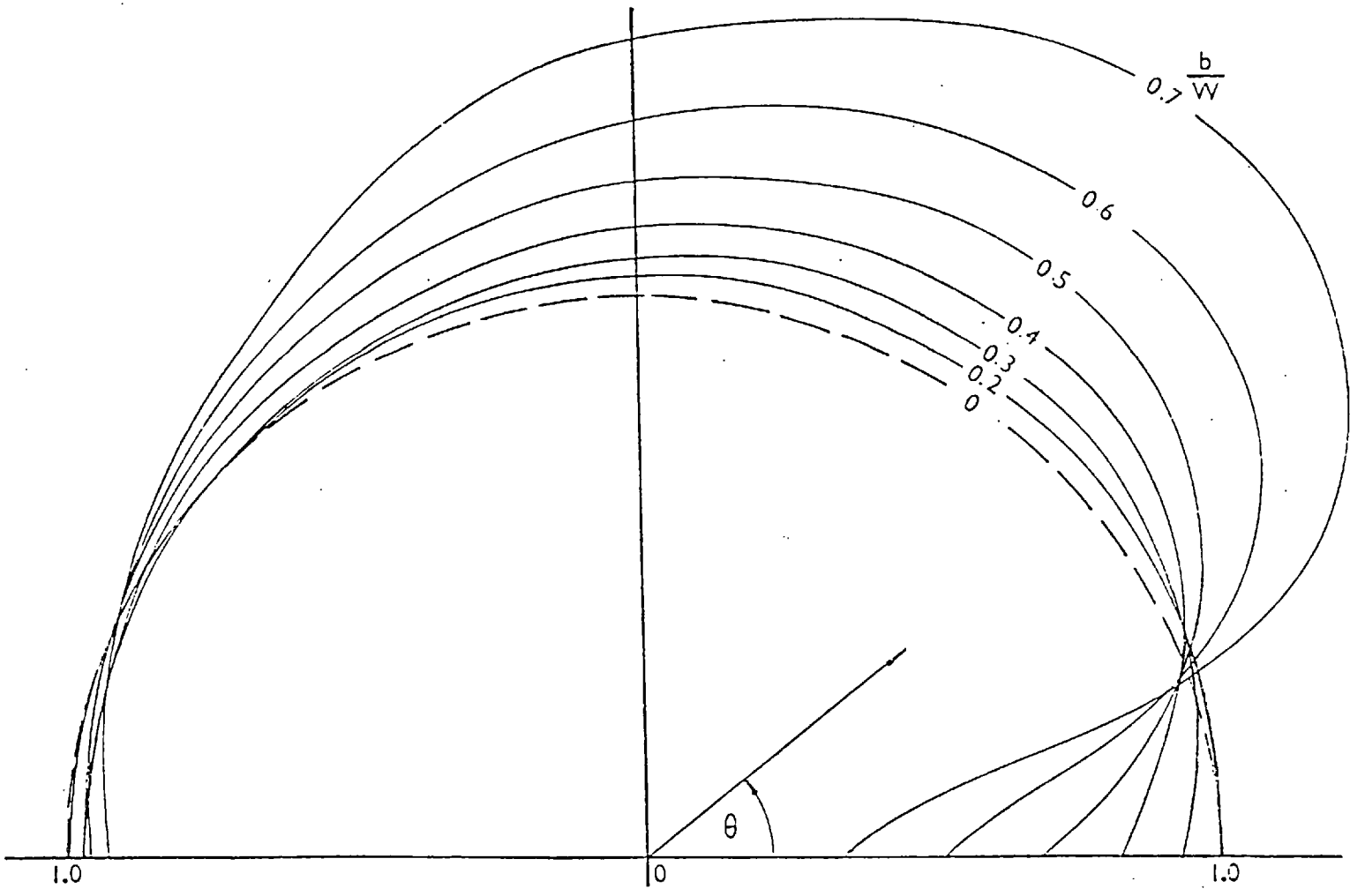



Figure 6.10: Polar plot of deflections at outer circumference of cylinder, $Z/H = 0$, $R_2/R_1 = 2$

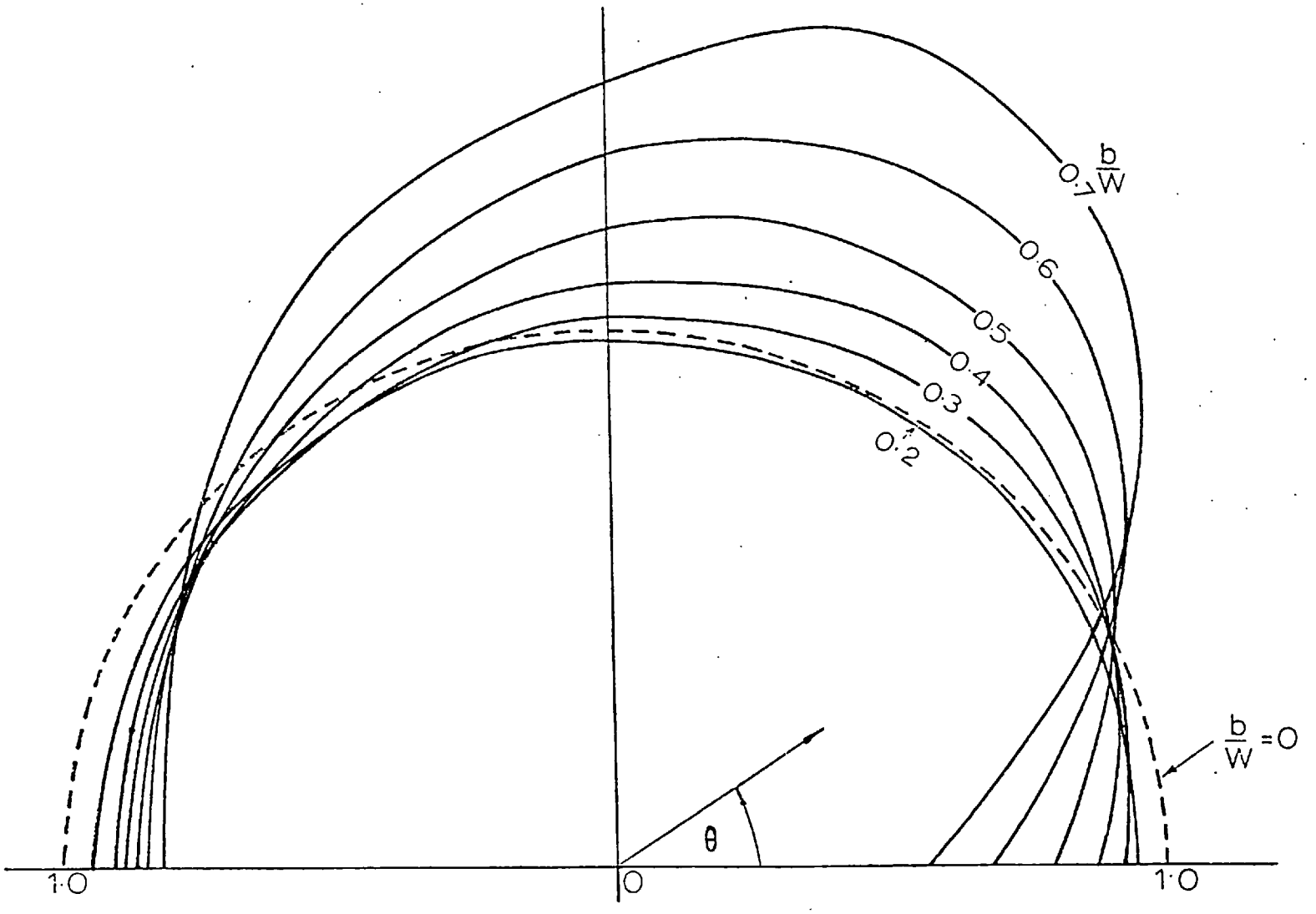



Figure 6.11: Polar plot of deflections at outer circumference of cylinder, $Z/H$ = 0, $R_2/R_1$ = 3

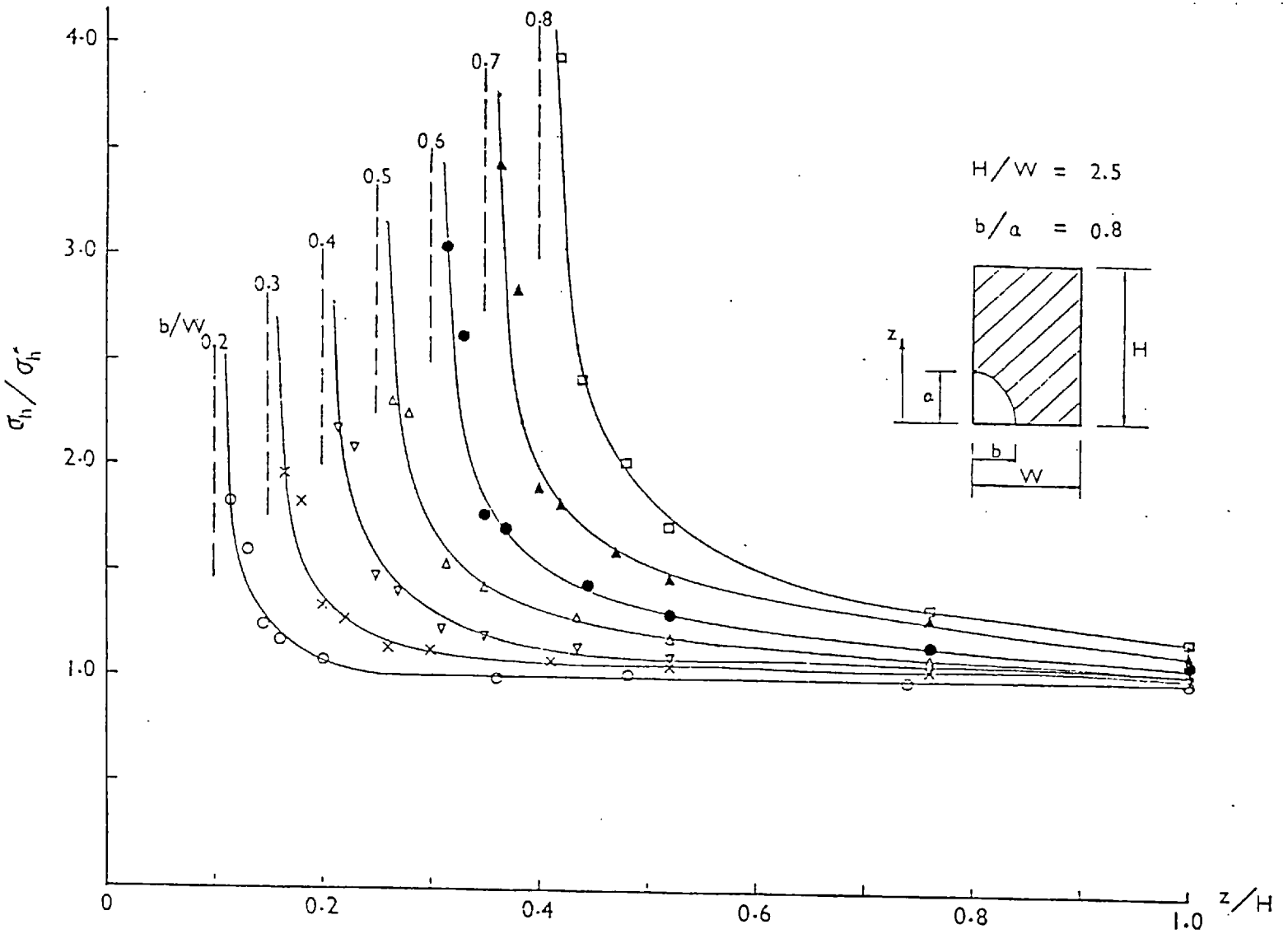



Figure 6.12: Variation of hoop stress at inner surface ($\theta = 0^0$) of cylinder, $R_2/R_1 = 2$

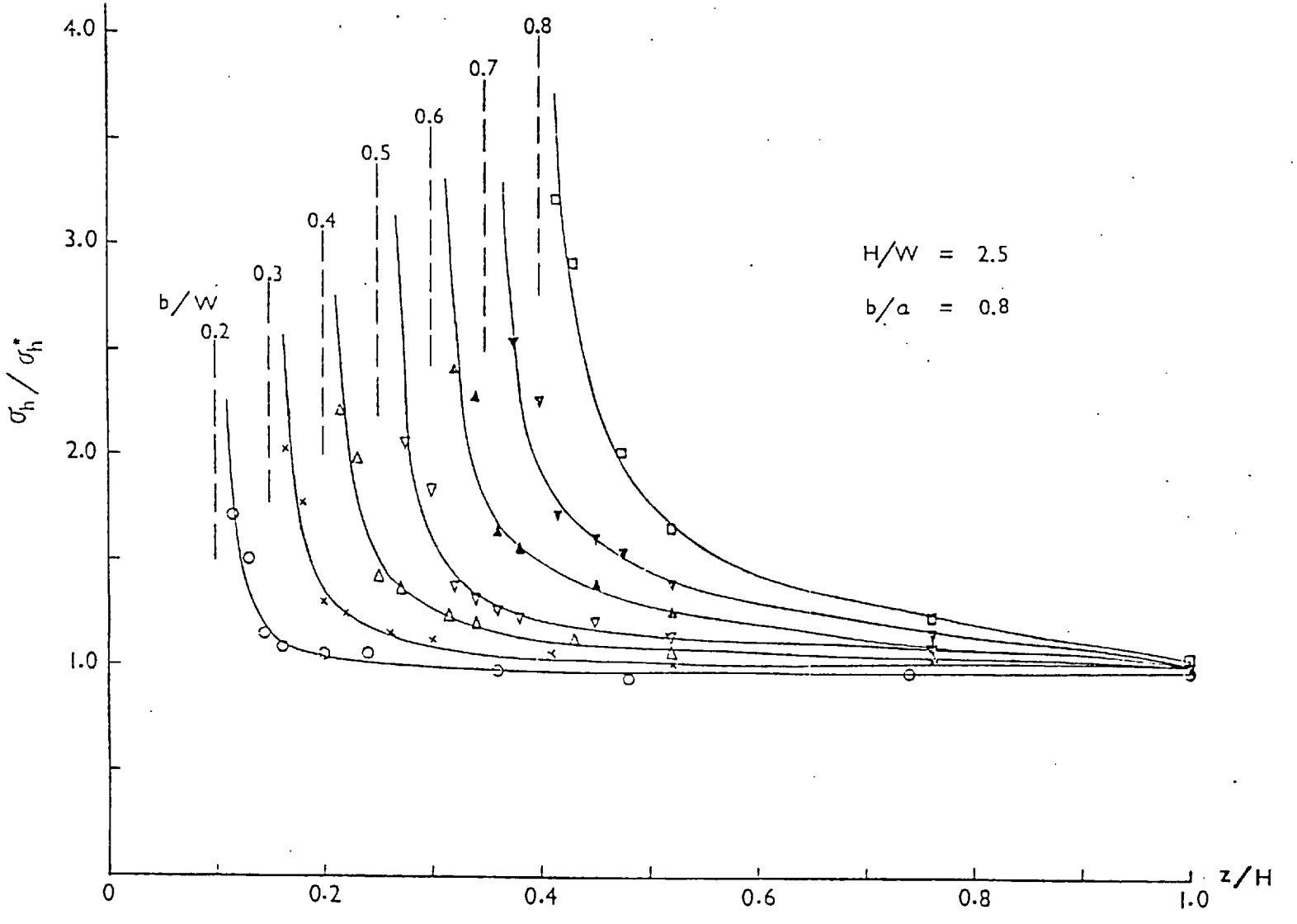



Figure 6.13: Variation of hoop stress at inner surface ($\theta = 0^0$) of cylinder, $R_2/R_1 = 3$

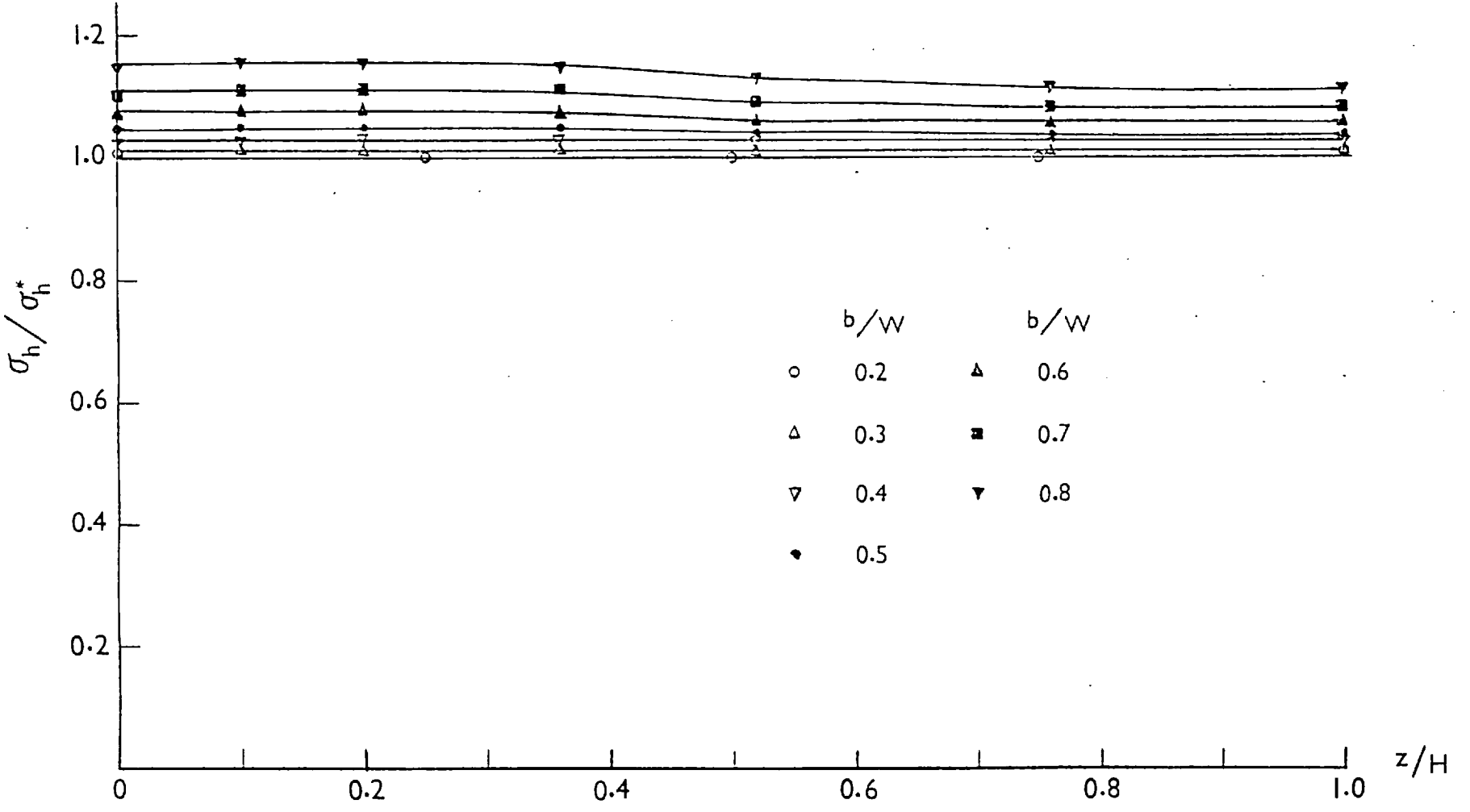



Figure 6.14: Variation of hoop stress at inner surface ($\theta = 180^0$) of cylinder, $R_2/R_1 = 2$

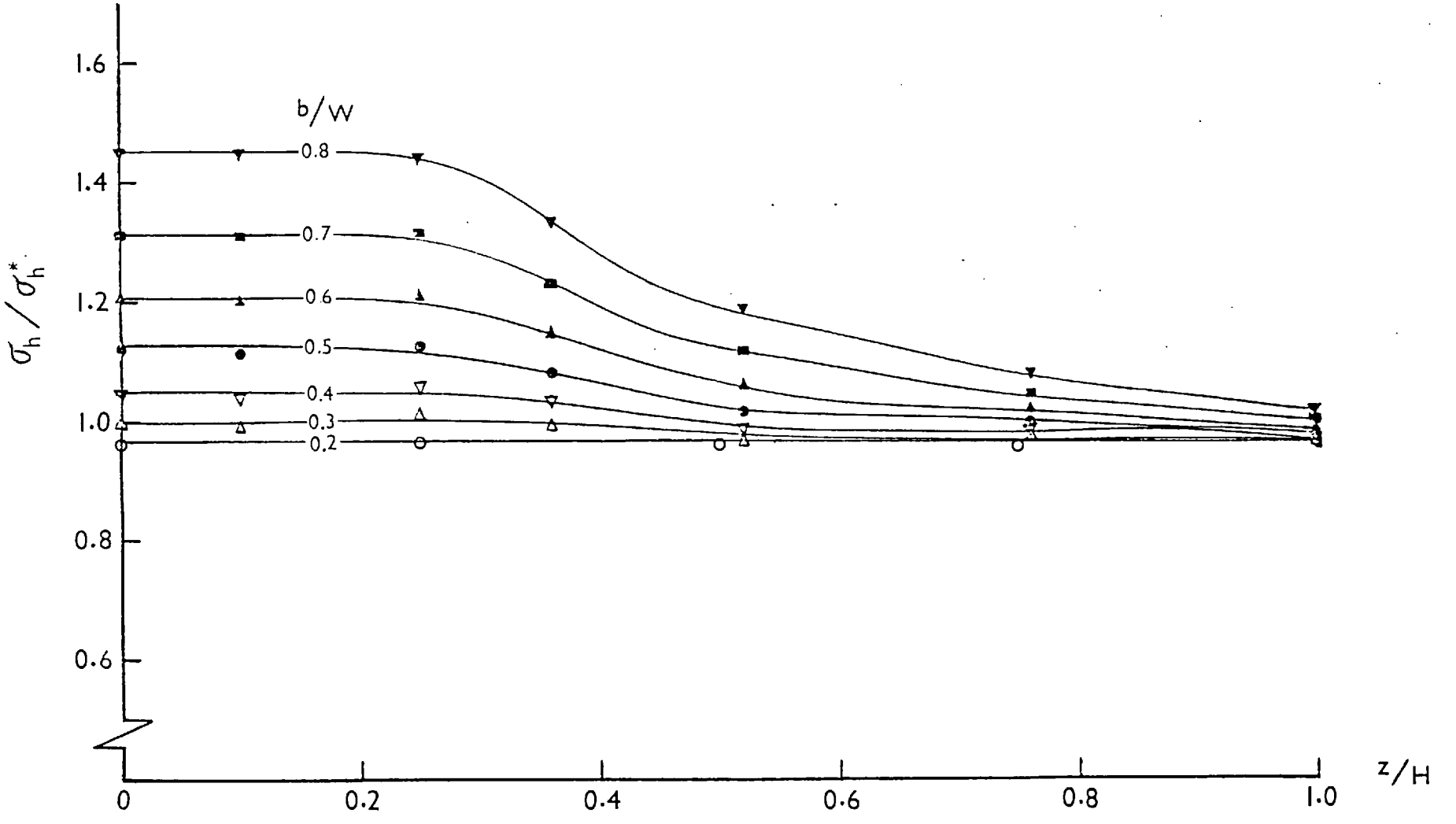



Figure 6.15: Variation of hoop stress at inner surface ($\theta = 180^0$) of cylinder, $R_2/R_1 = 3$

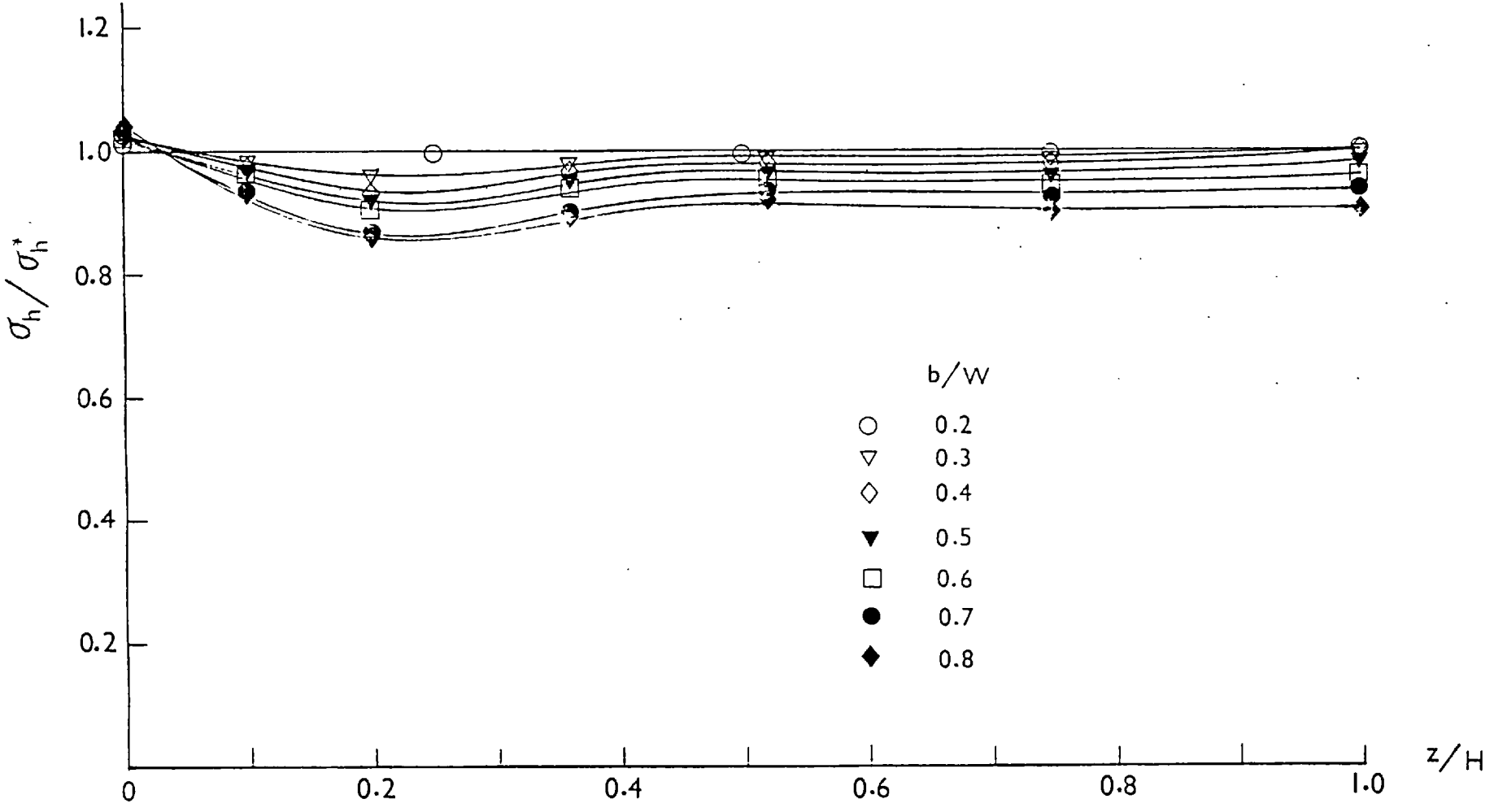



Figure 6.16: Variation of hoop stress at inner surface ($\theta = 90^0$) of cylinder, $R_2/R_1 = 2$

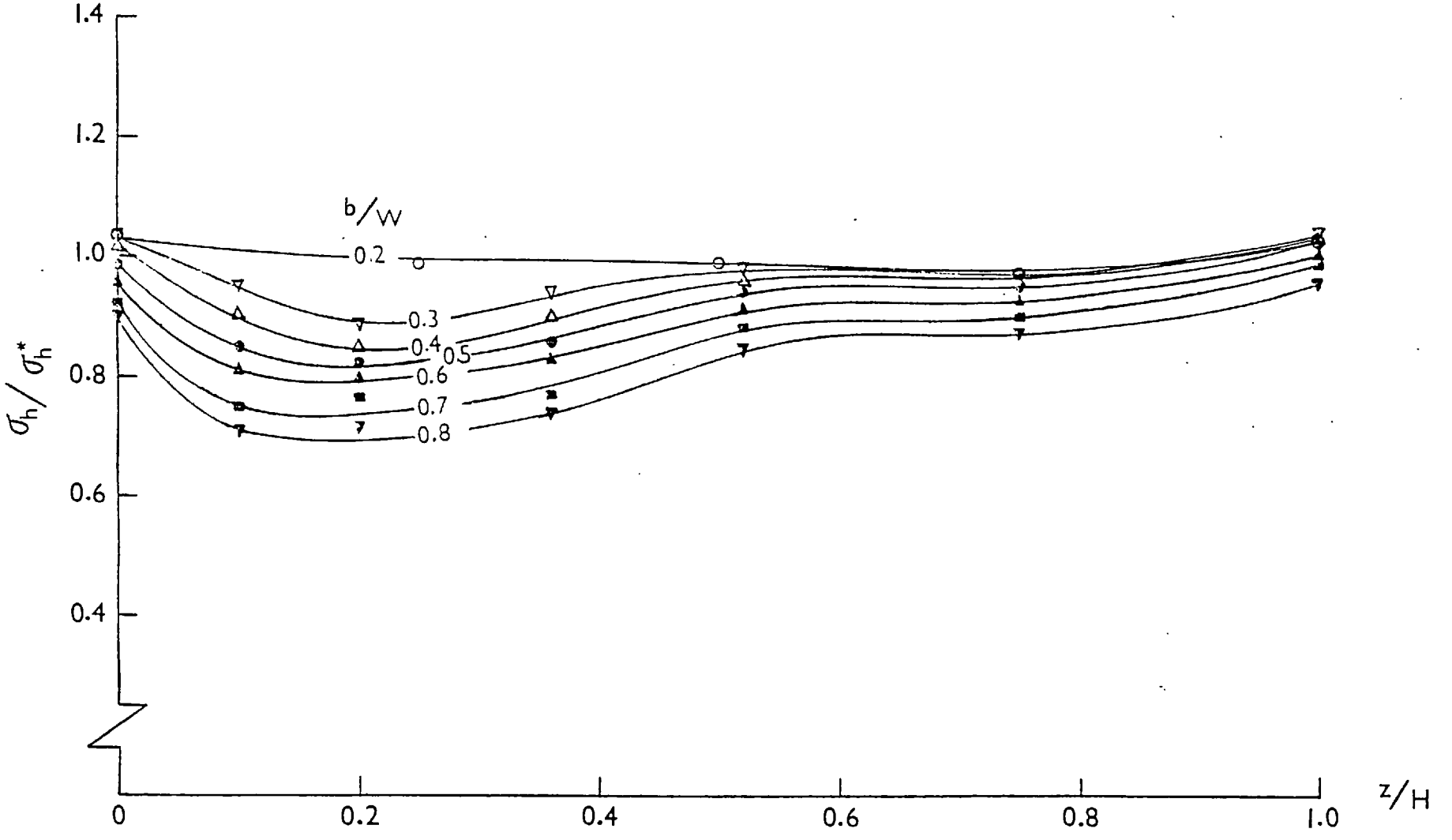



Figure 6.17: Variation of hoop stress at inner surface ($\theta = 90^0$) of cylinder, $R_2/R_1 = 3$

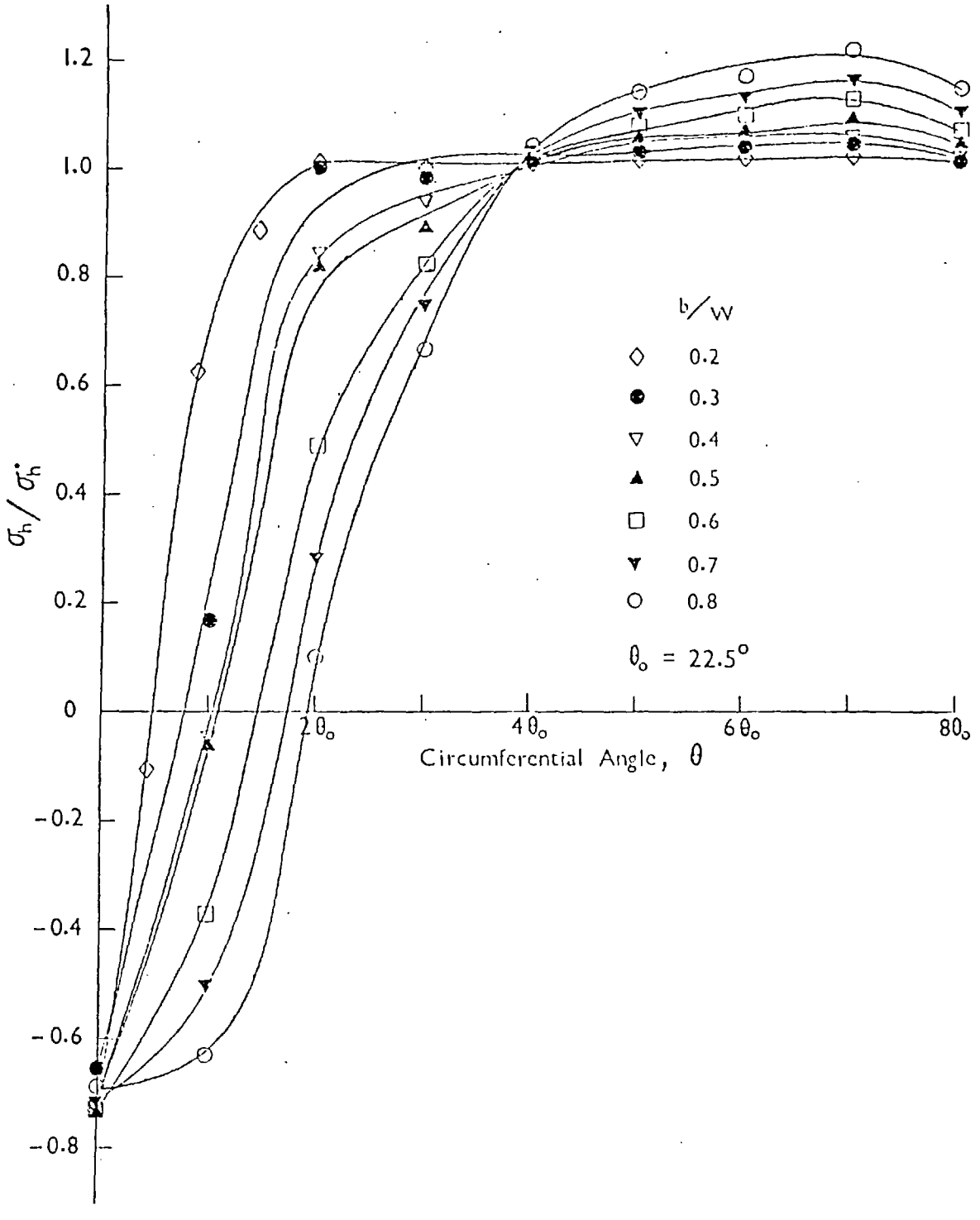



Figure 6.18: Variation of hoop stress at inner circumference of cylinder, $Z/H = 0$, $R_2/R_1 = 2$

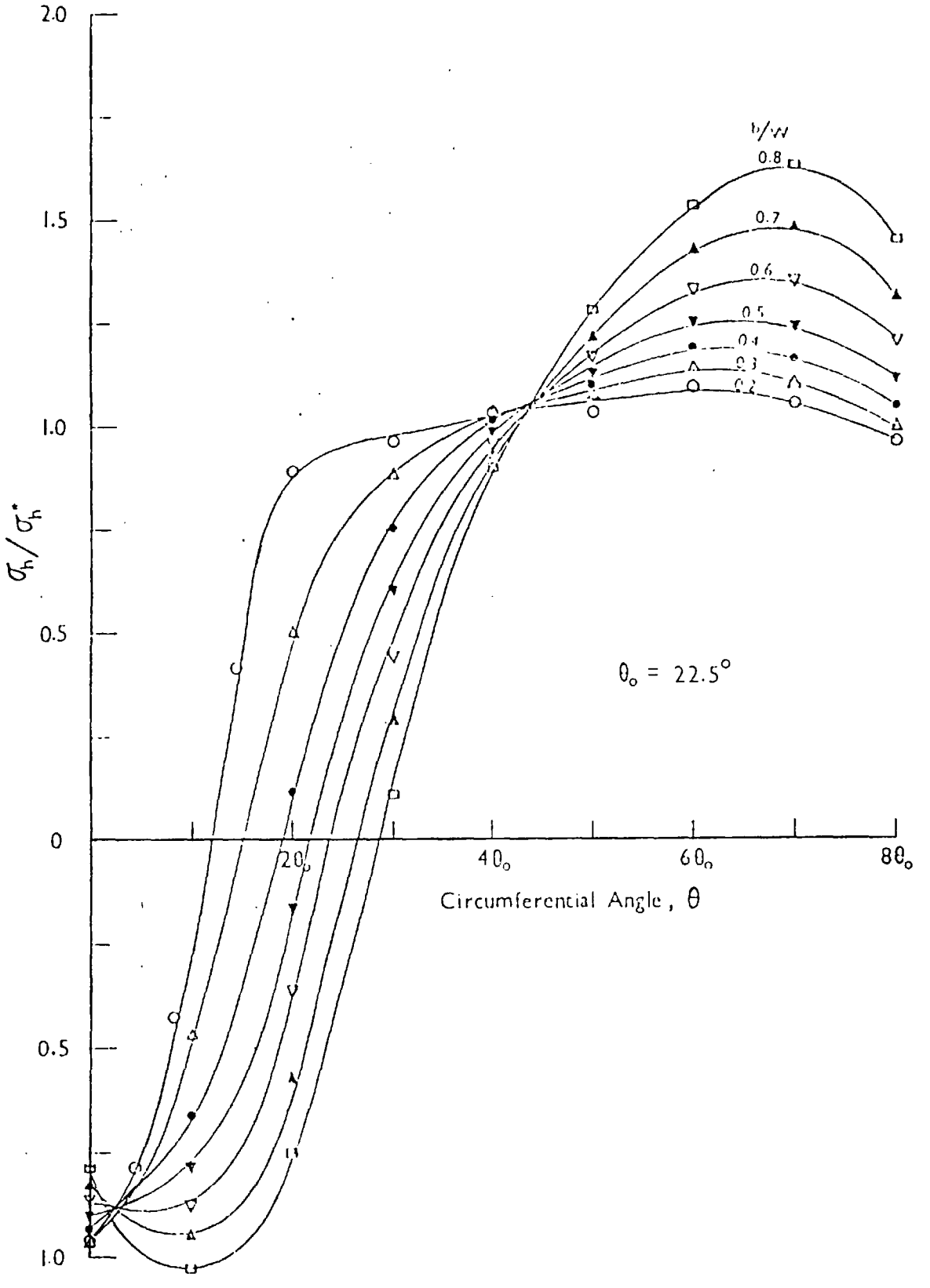



Figure 6.19: Variation of hoop stress at inner circumference of cylinder, $Z/H$ = 0, $R_2/R_1$ = 3

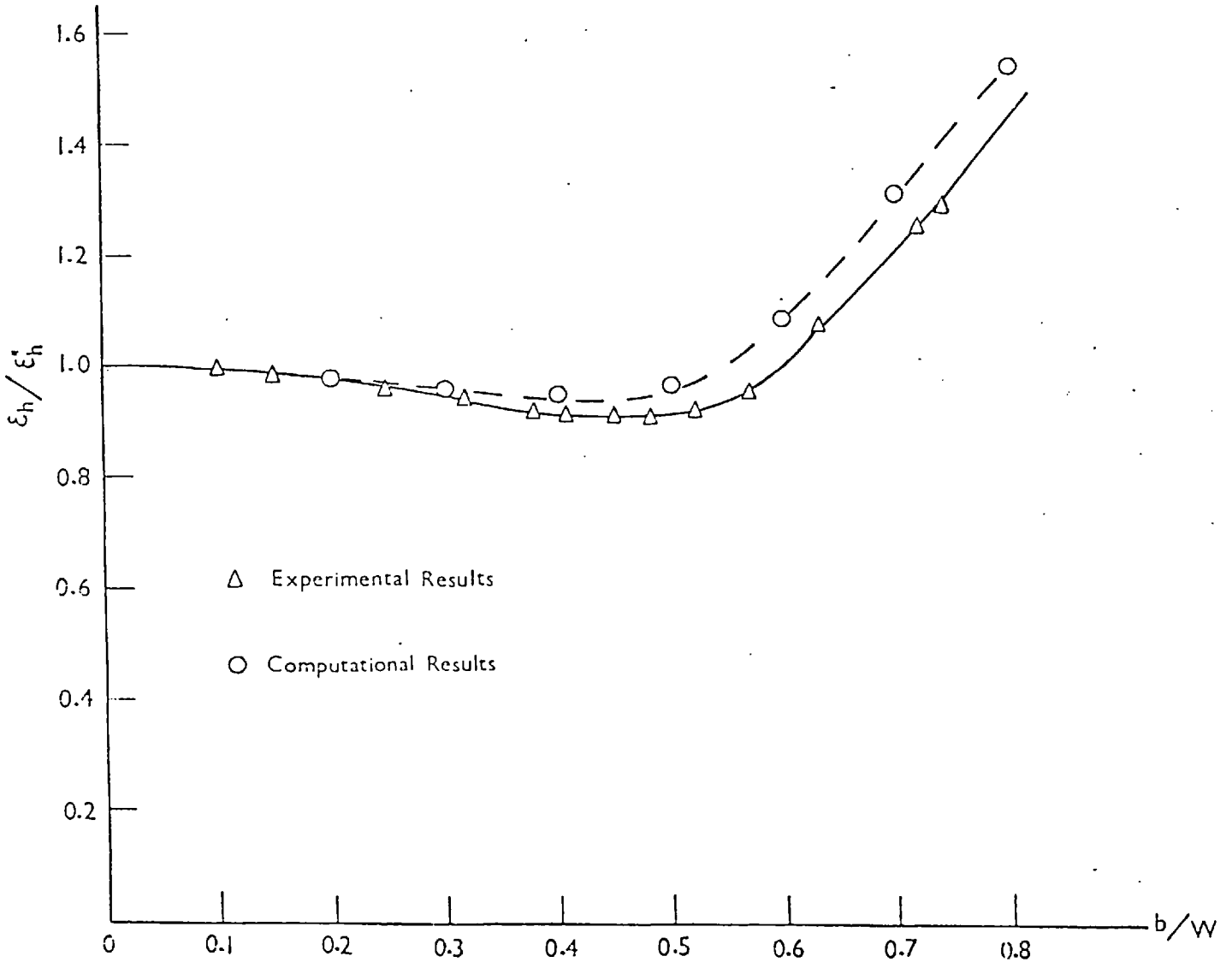



Figure 6.20: Variation of hoop strain at outer diameter ($\theta = 0^o$) with crack depth, $R_2/R_1 = 2$

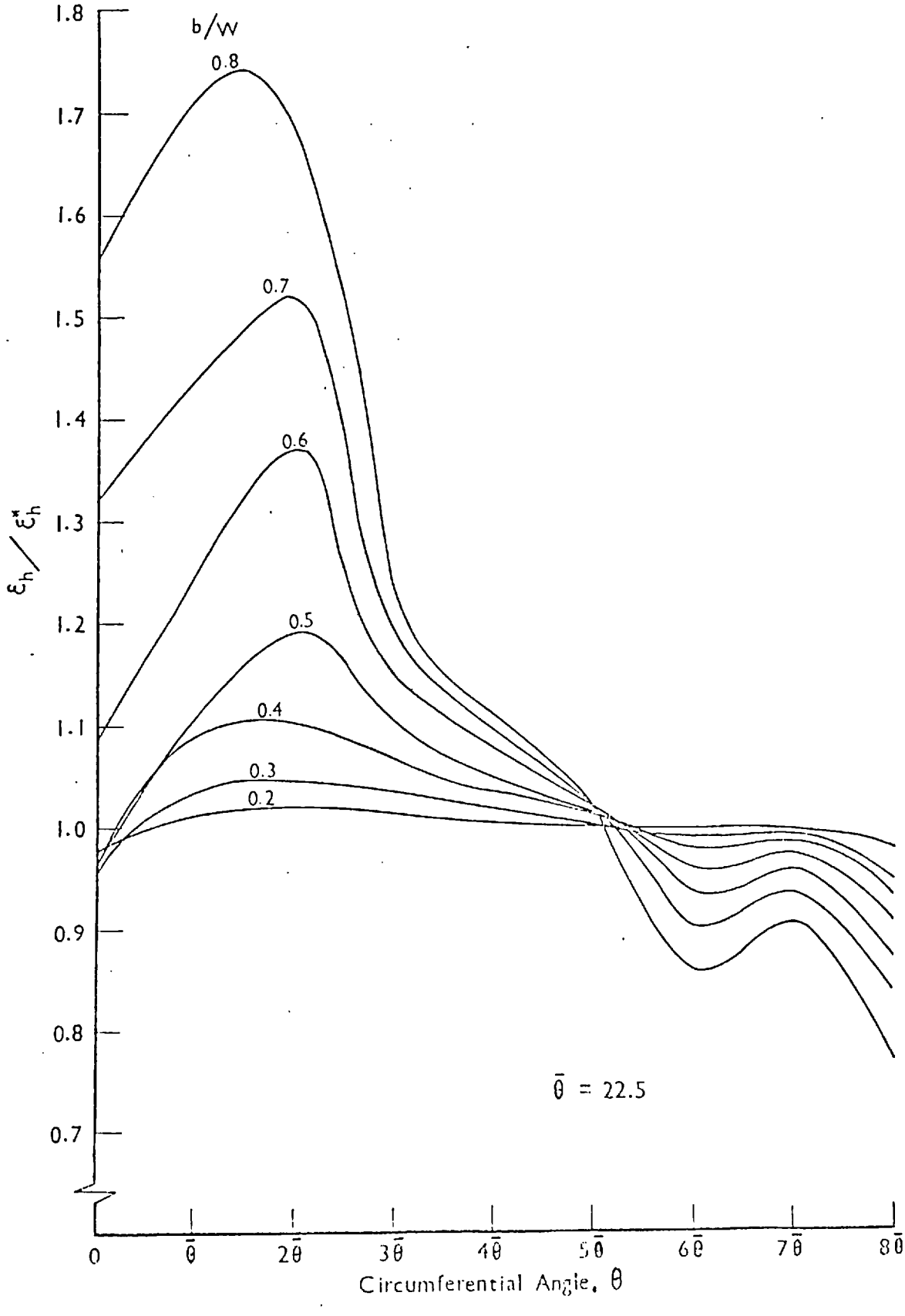



Figure 6.21: Variation of hoop strain at outer circumference, $Z/H = 0$, $R_2/R_1 = 2$

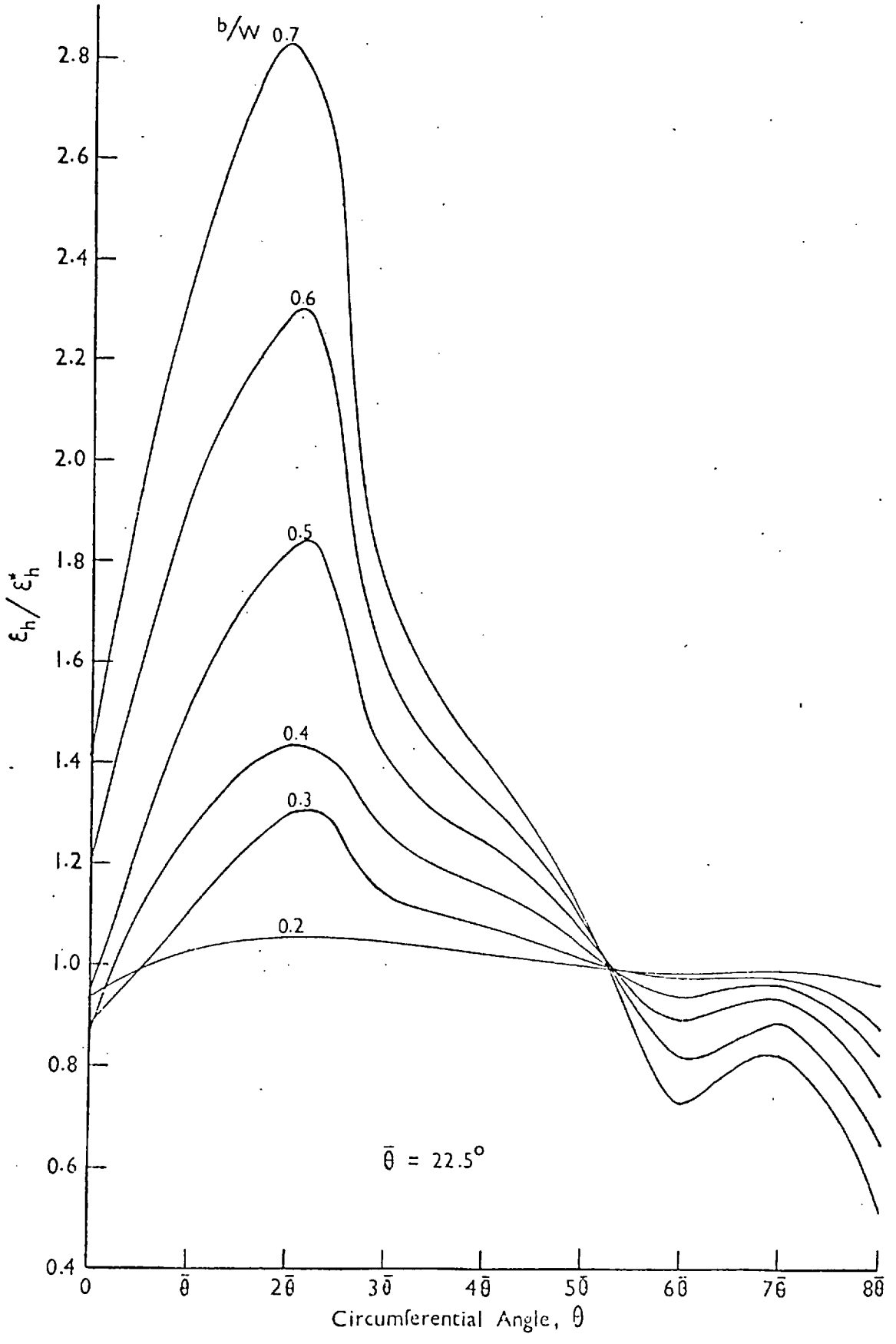



Figure 6.22: Variation of hoop strain at outer circumference, $Z/H = 0$, $R_2/R_1 = 3$

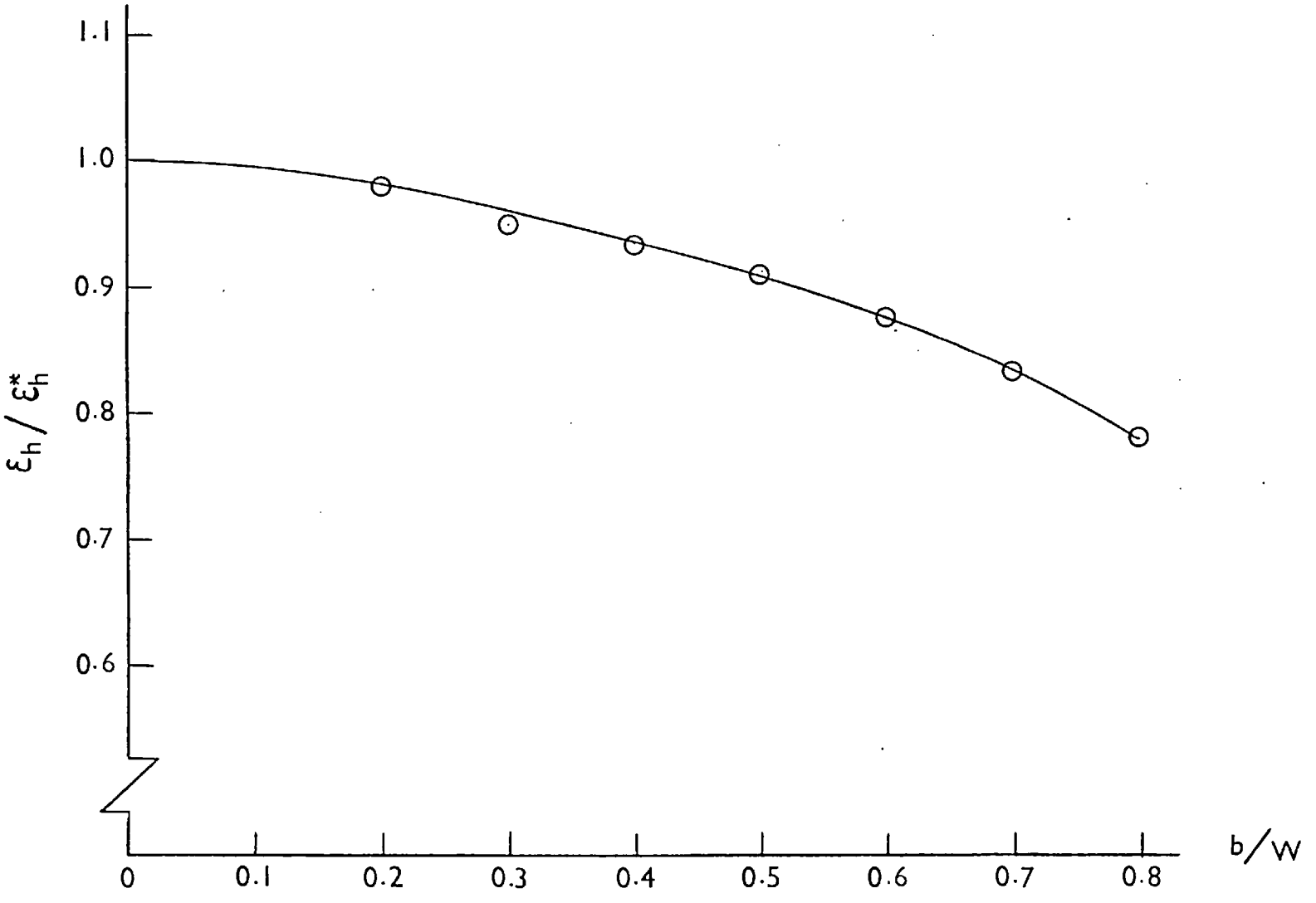



Figure 6.23: Variation of hoop strain at outer diameter ($\theta = 180^0$) with crack depth, $R_2/R_1 = 2$

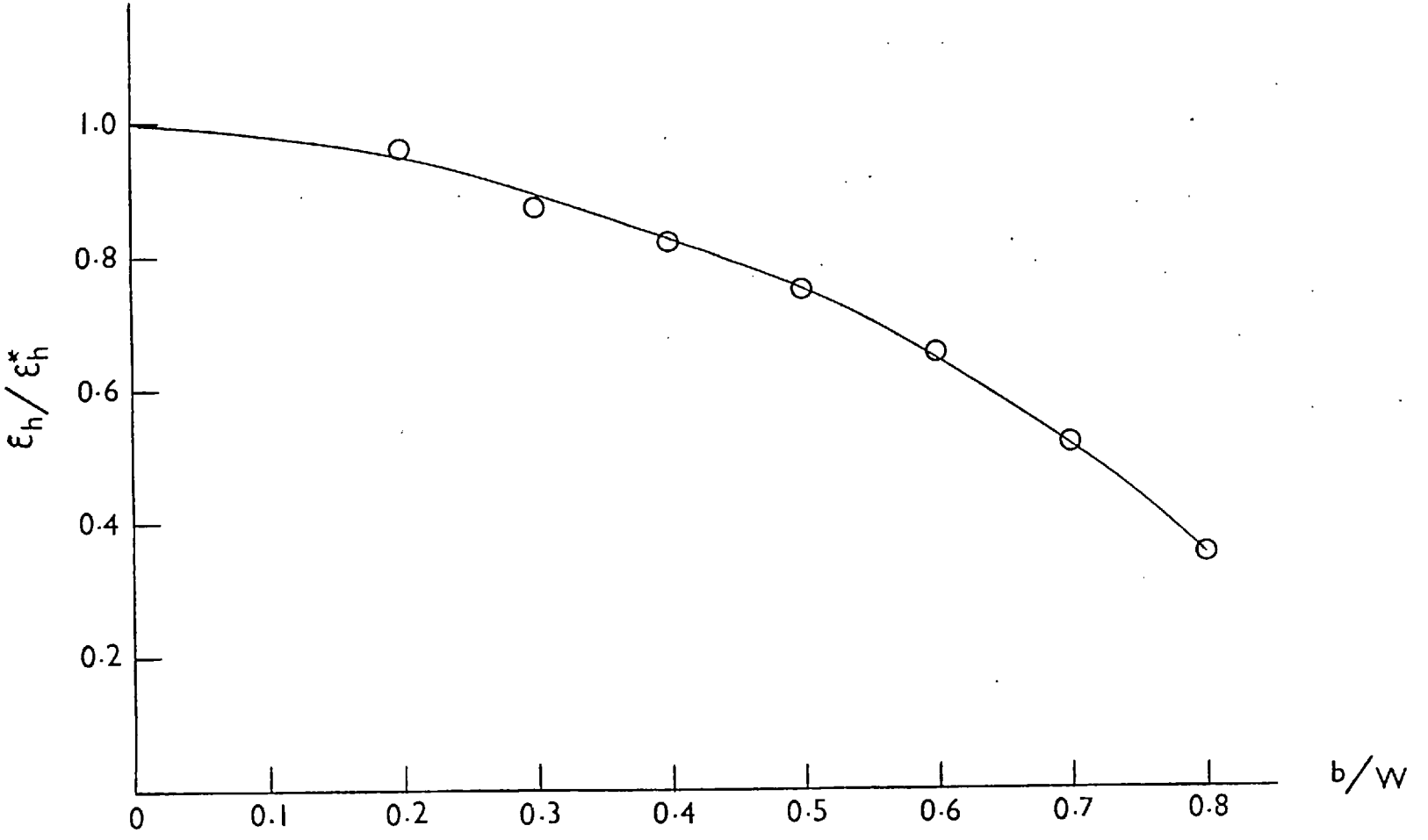



Figure 6.24: Variation of hoop strain at outer diameter ($\theta = 180^{o}$) with crack depth, $R_2/R_1 = 3$

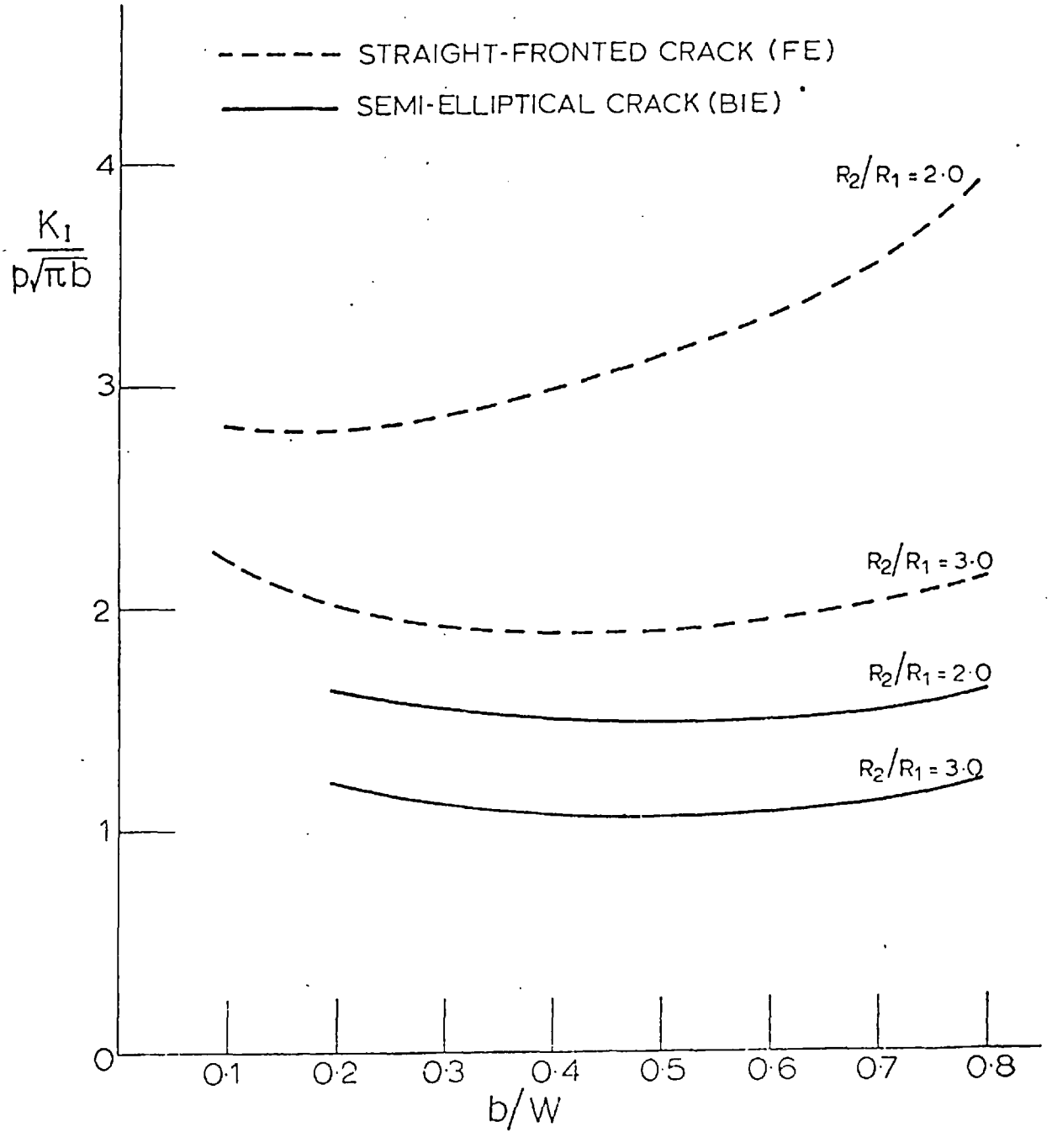



Figure 6.25: Stress intensity factors for a semi-elliptical surface crack in a pressurized cylinder at point of deepest penetration, with $b/a$ = 0.8

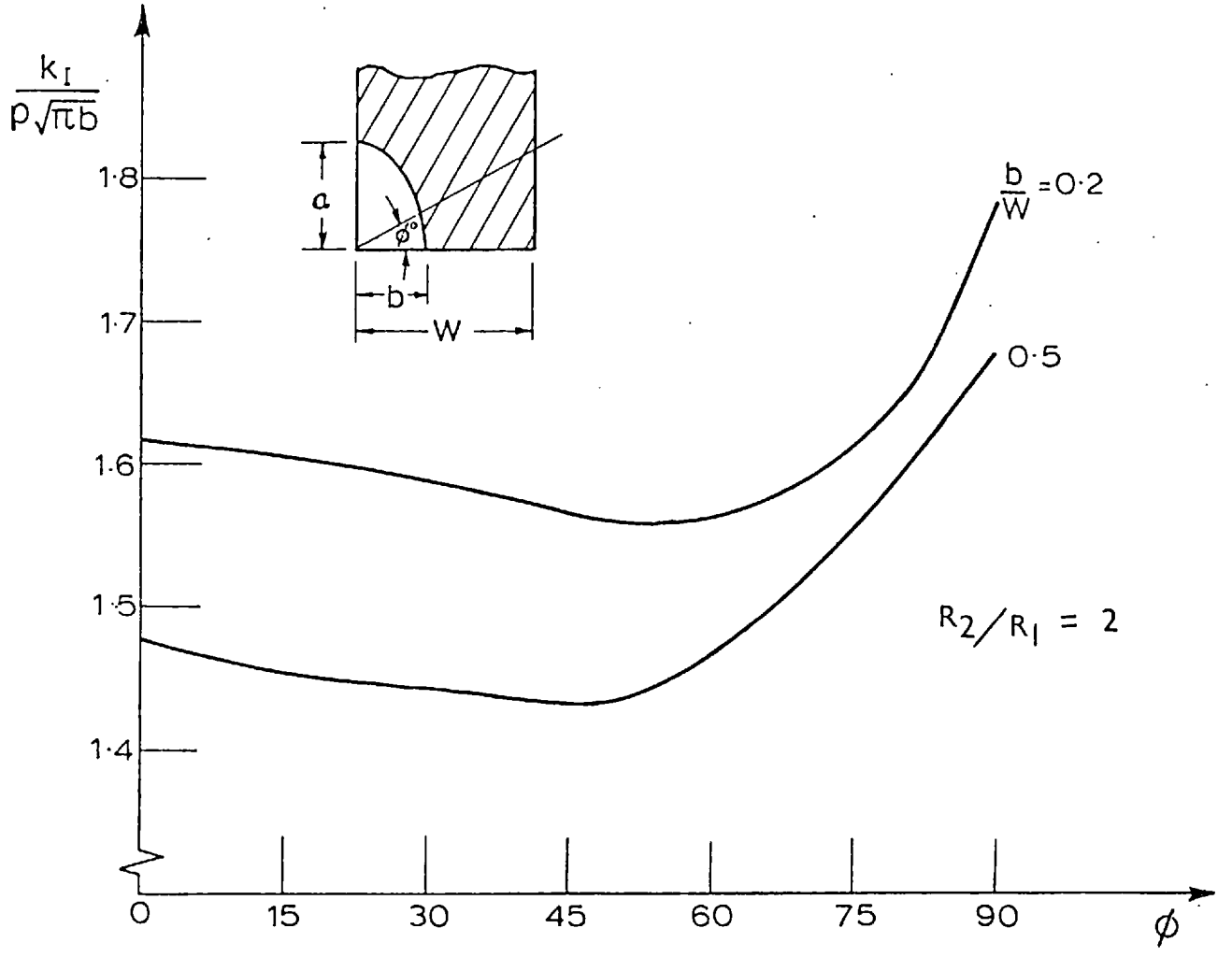



Figure 6.26: Variation of stress intensity factors along the crack front for $b/a$ = 0.8, $R_2/R_1$ = 2

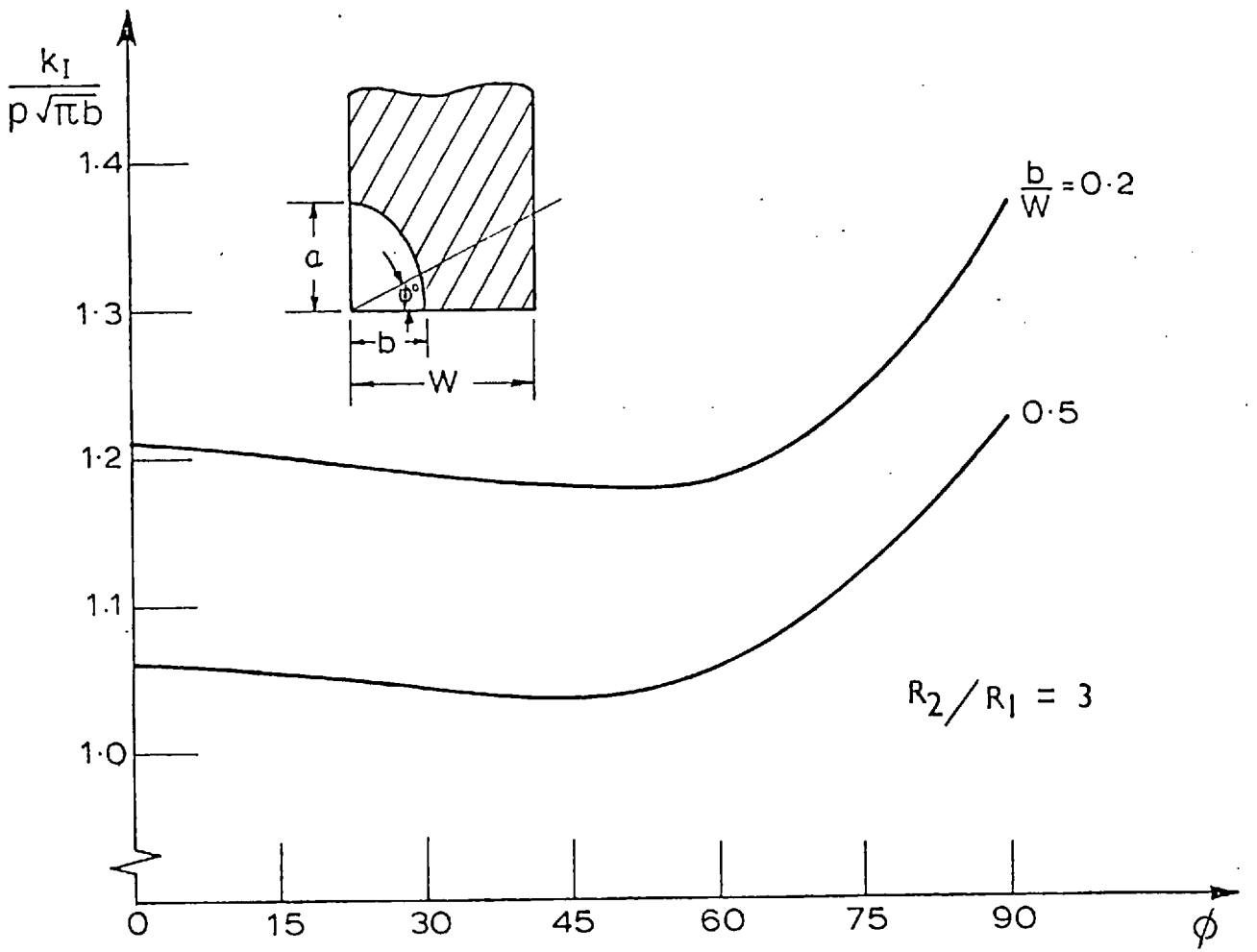



Figure 6.27: Variation of stress intensity factor along the crack front for $b/a$ = 0.8, $R_2/R_1$ = 3

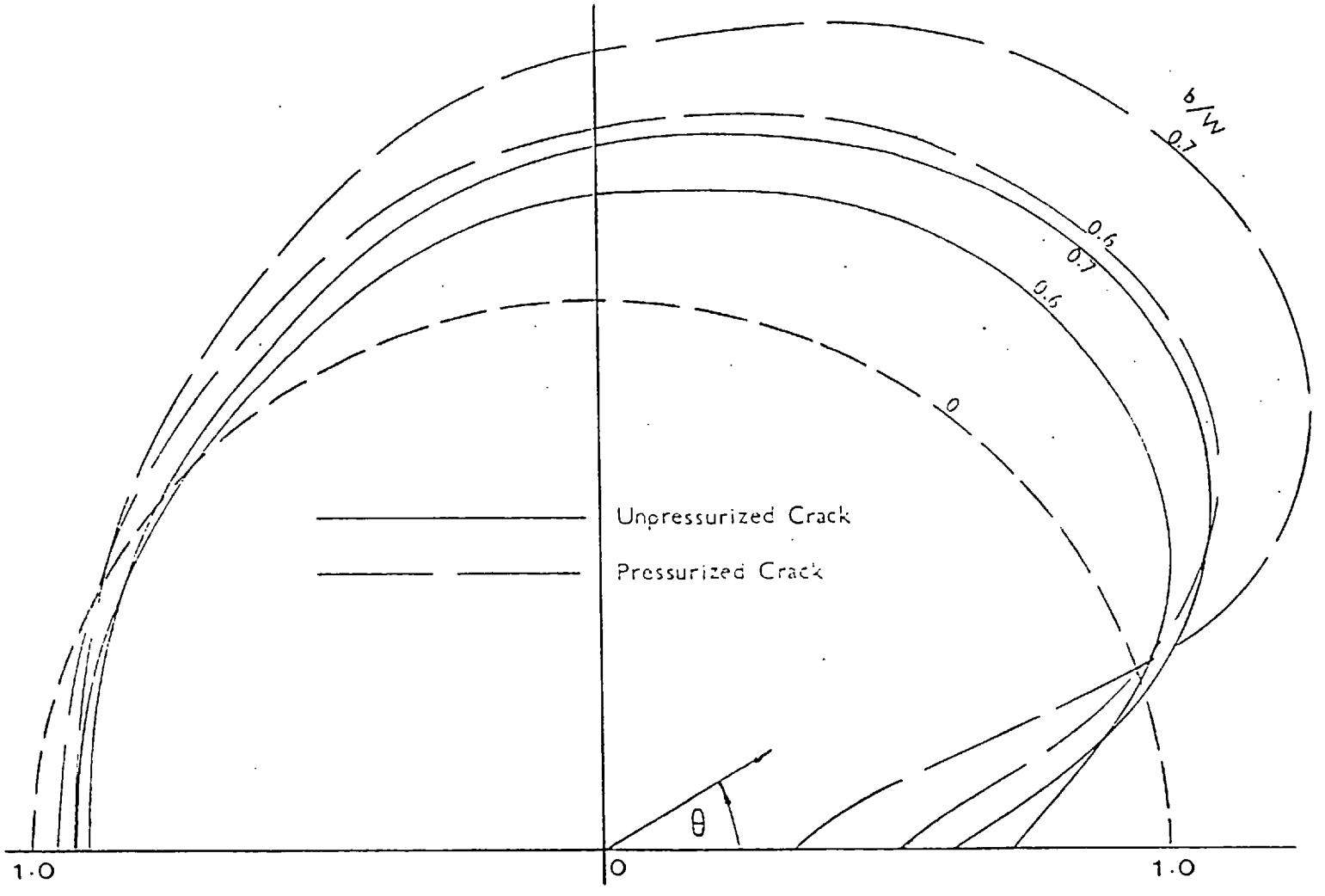



Figure 6.28: Polar plot of deflections at outer circumference of cylinder, $Z/H = 0$, $R_2/R_1 = 2$

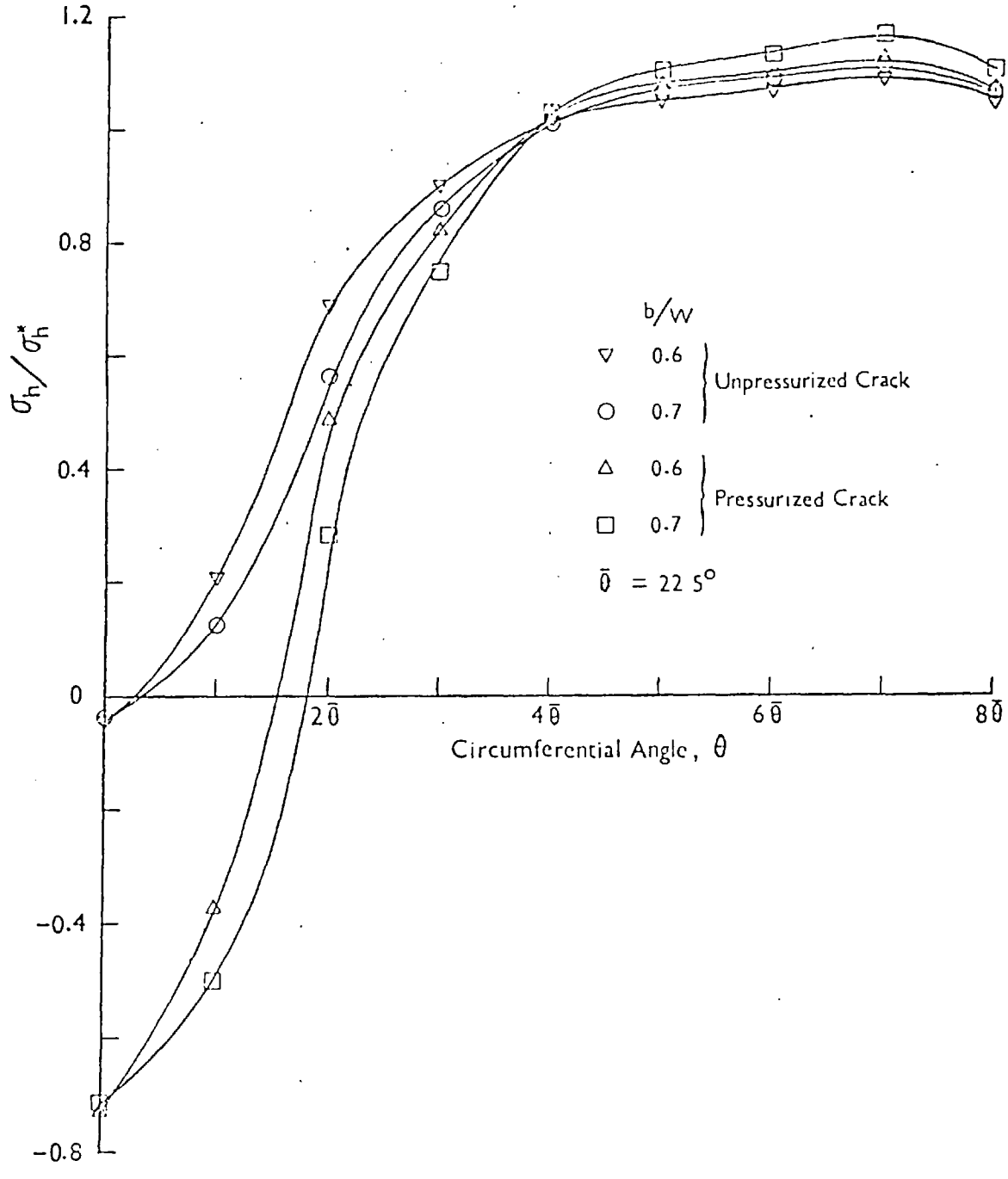



Figure 6.29: Variation of hoop stress at inner circumference of cylinder, $Z/H = 0$, $R_2/R_1 = 2$

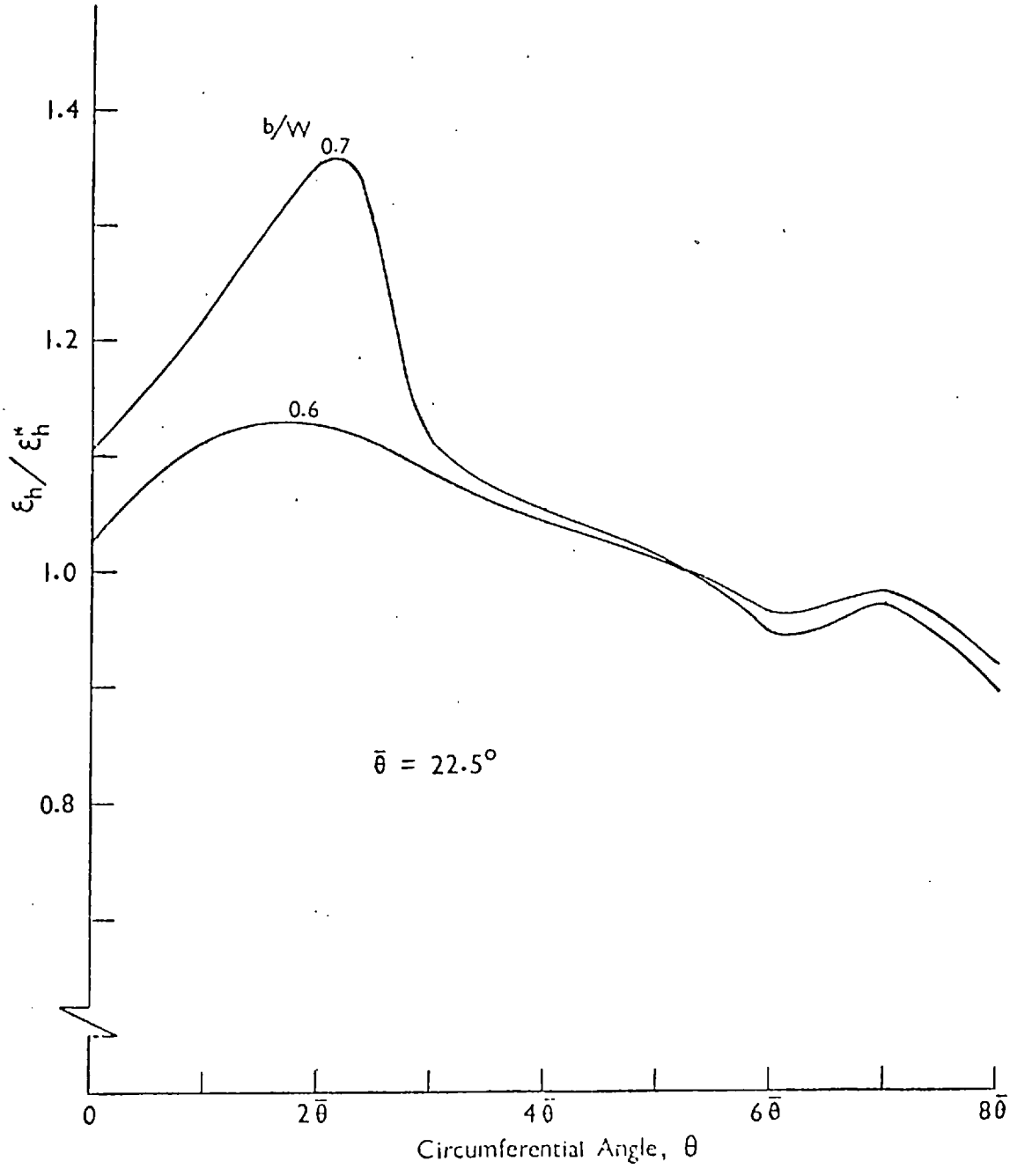



Figure 6.30: Variation of hoop strain at outer circumference of cylinder (unpressurized crack), $Z/H = 0$, $R_2/R_1 = 2$

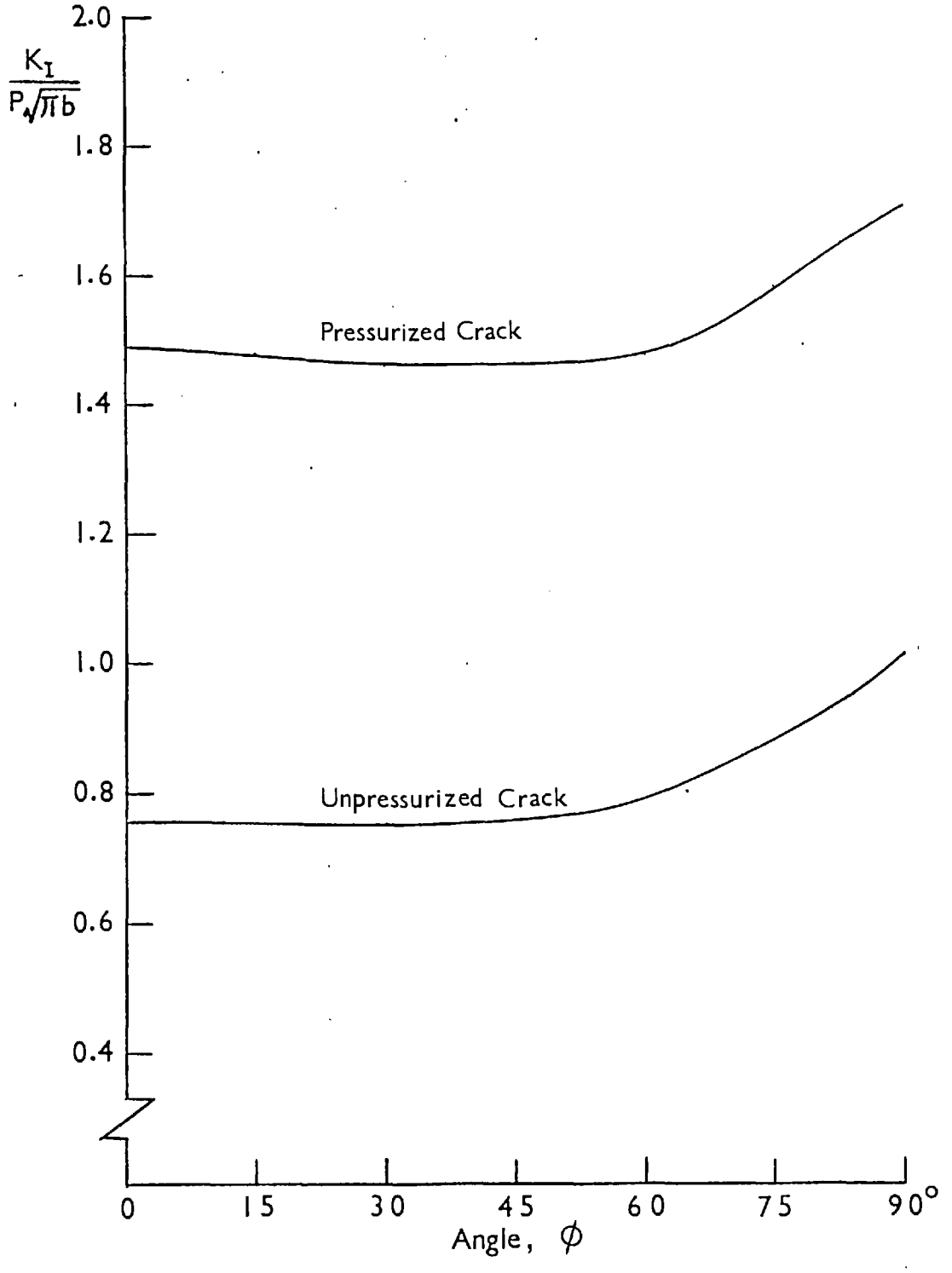



Figure 6.31: Variation of stress intensity factor along the crack front for $b/a$ = 0.8, $R_2/R_1$ = 2, $b/W$ = 0.6

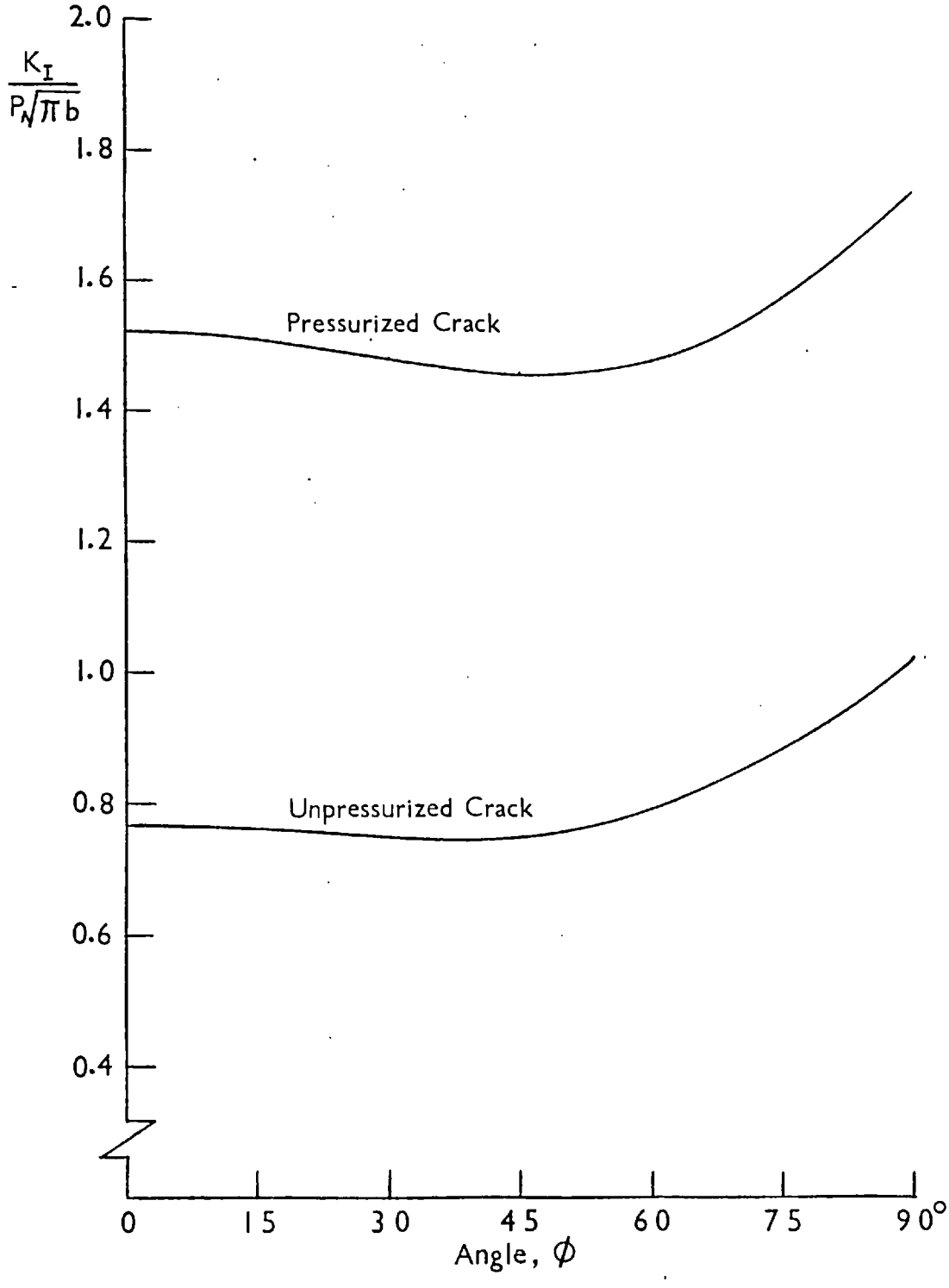



Figure 6.32: Variation of stress intensity factor along the crack front for $b/a$ = 0.8, $R_2/R_1$ = 2, $b/W$ = 0.7

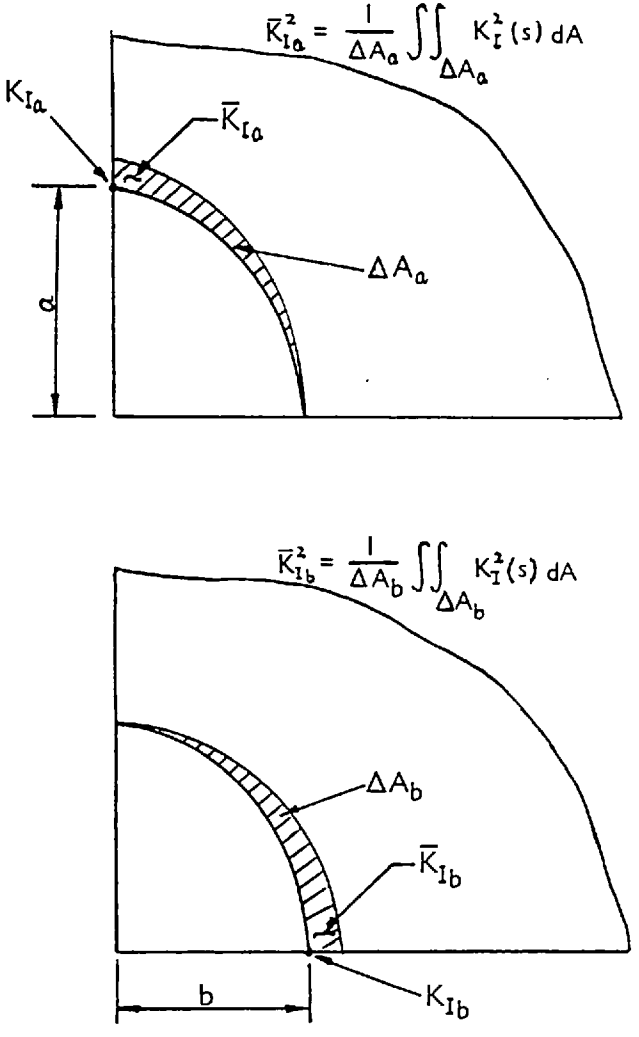



Figure 6.35: Distinction between "local" and "local mean" values of $K_I$ in two DOF elliptical crack model

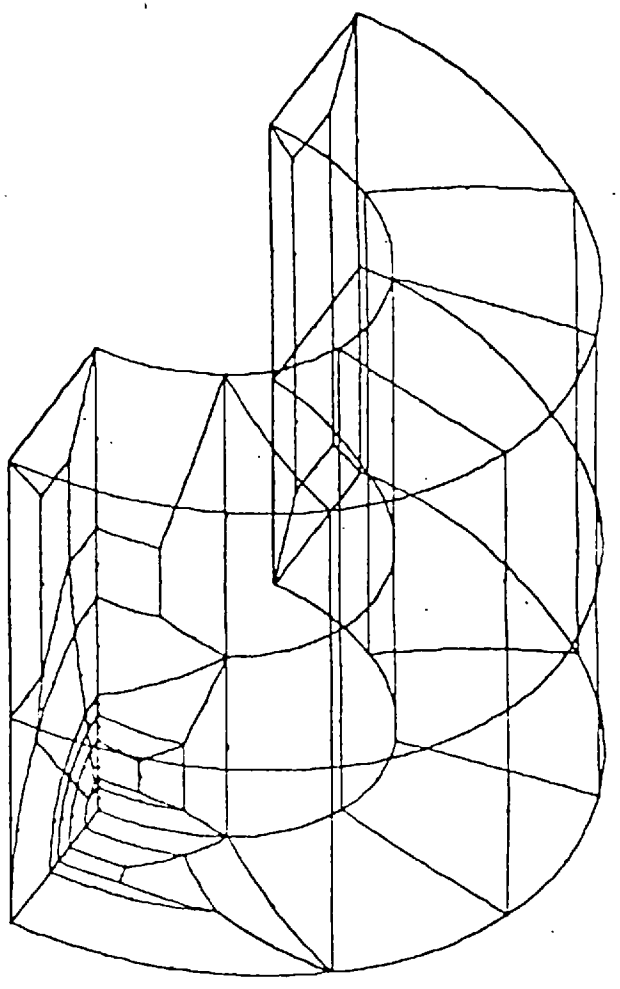


Figure 6.33: Typical boundary mesh of quarter-cylinder model used for fatigue analysis

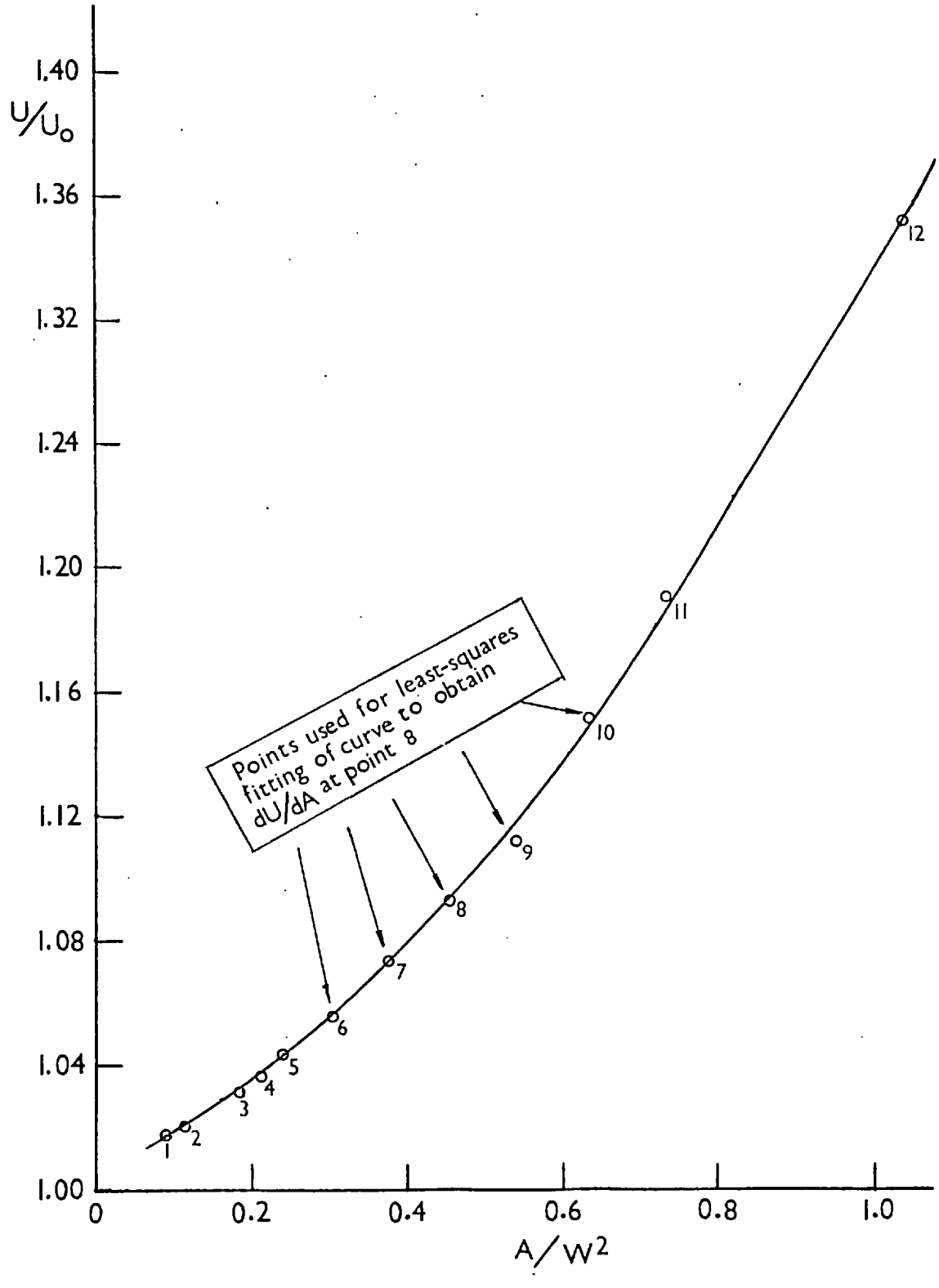



Figure 6.34: Plot of strain energy versus crack surface area

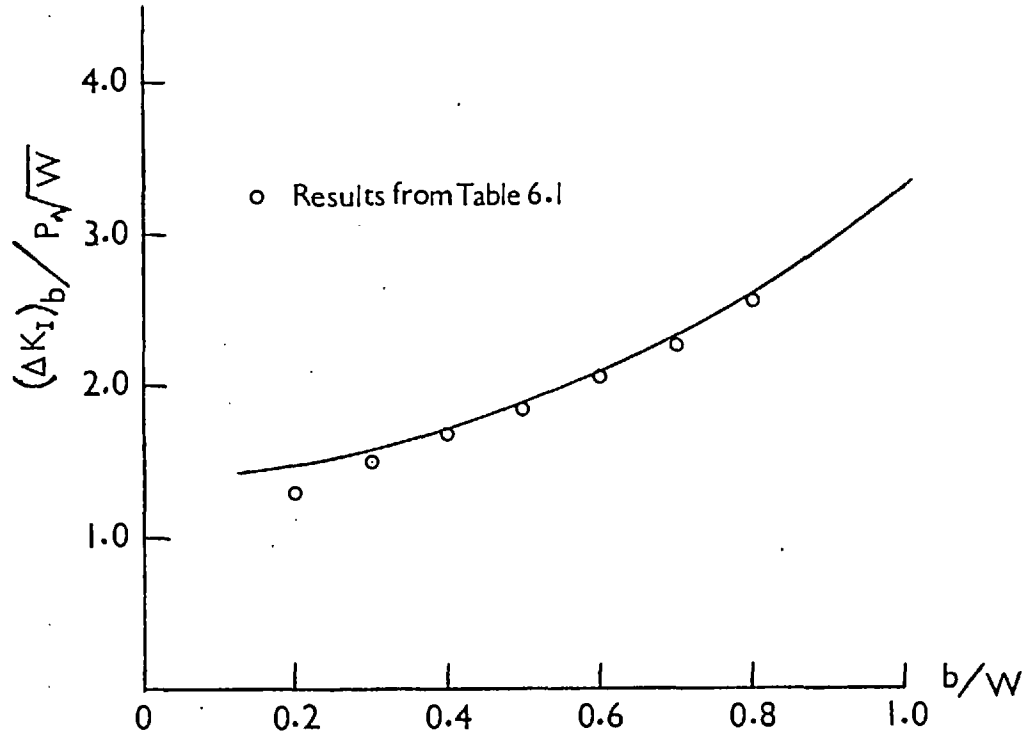



Figure 6.36: Plot of stress intensity factor function (equation (6.12)) for fatigue analysis

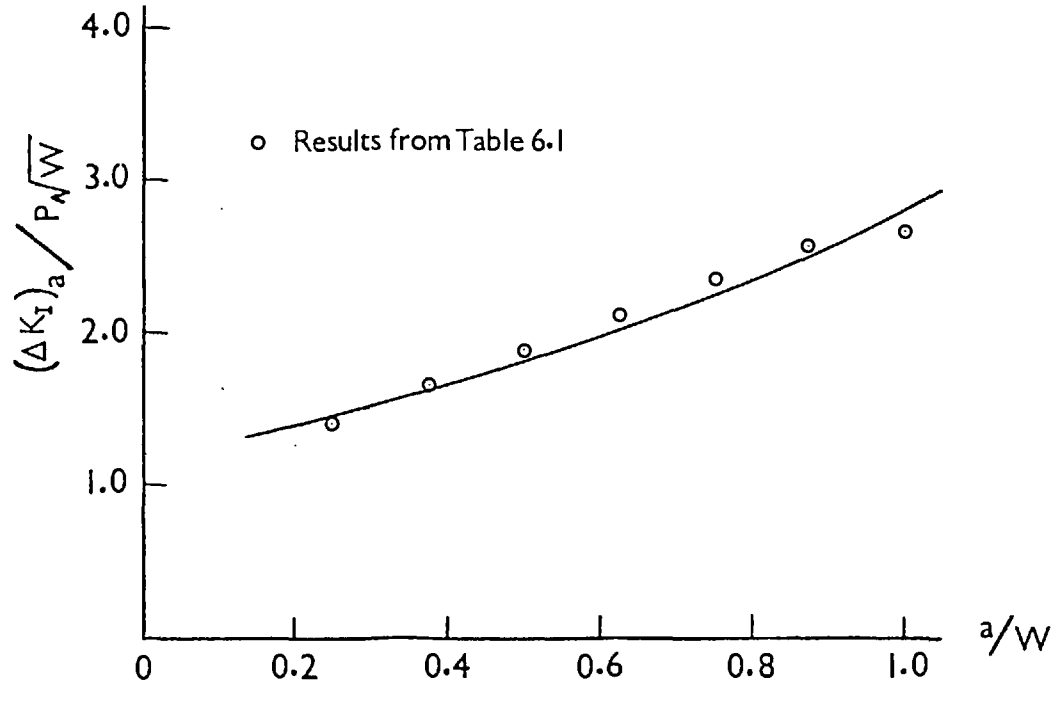



Figure 6.37: Plot of stress intensity factor function (equation (6.13)) for fatigue analysis

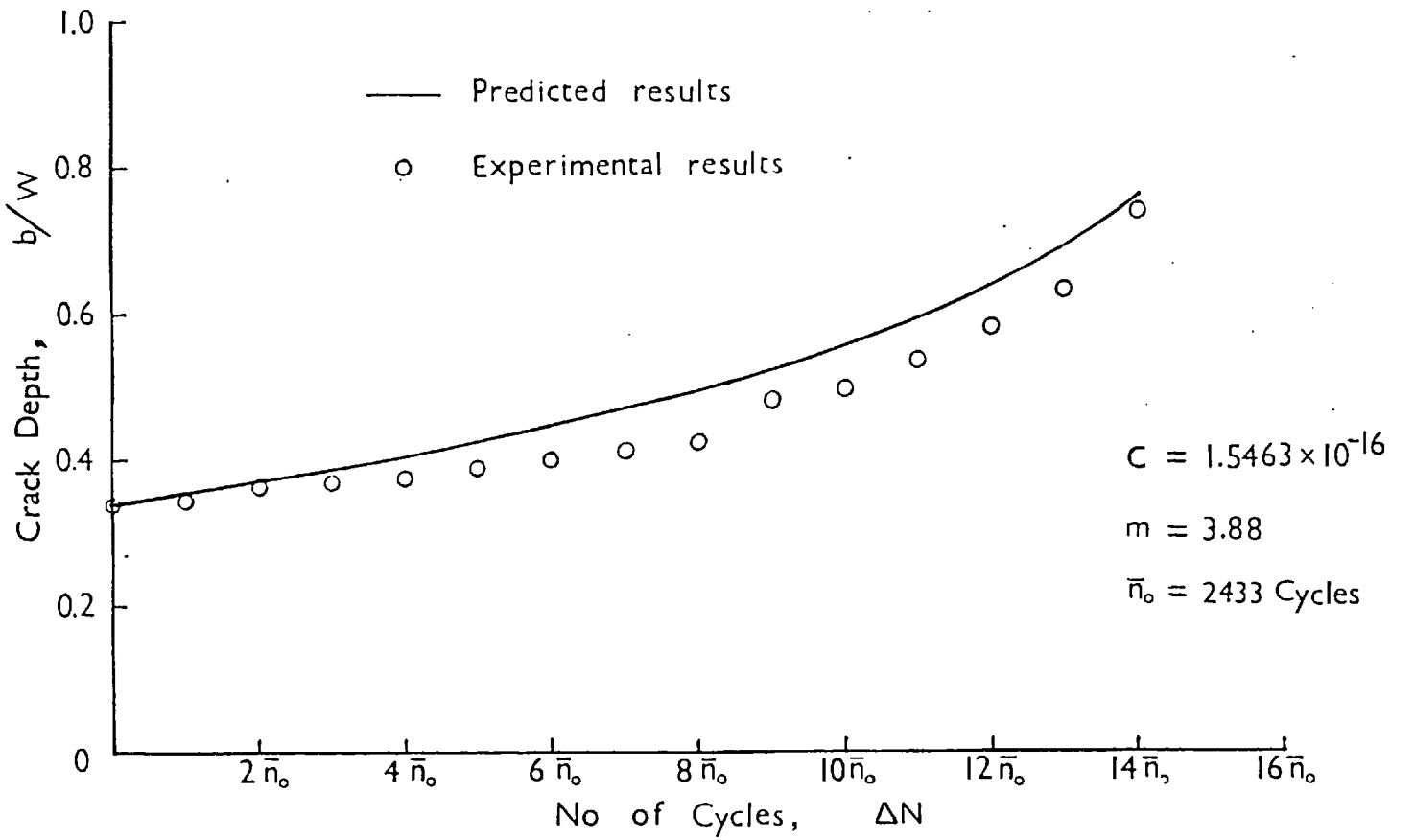



Figure 6.38: Fatigue crack propagation - comparison with experiments

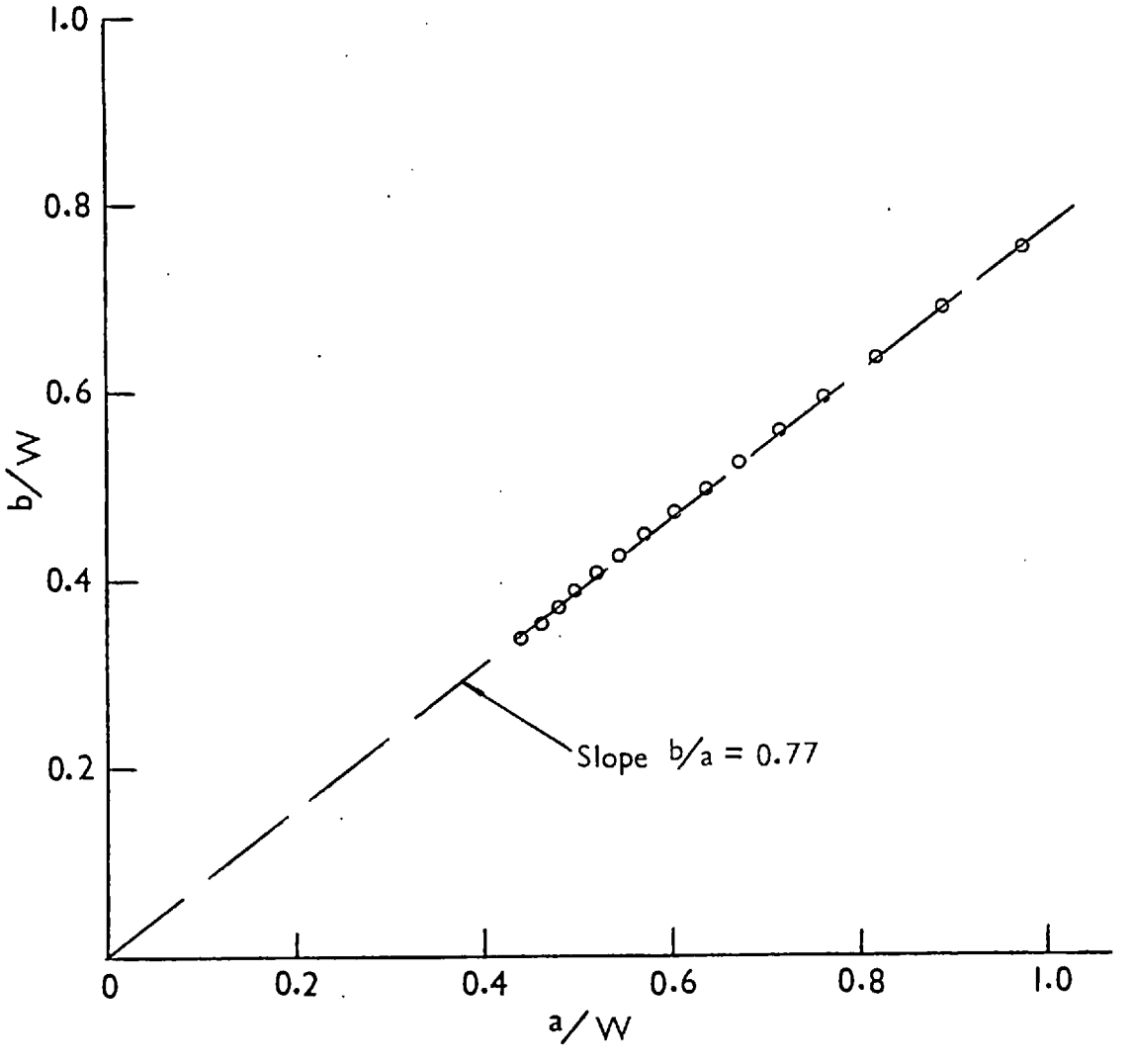



Figure 6.39: Predicted shape of propagating crack

# CHAPTER 7

# ON INTERNALLY PRESSURIZED THICK-WALLED CYLINDERS WITH CROSS-BORES

In the field of high pressure technology, cylindrical vessels or components which are subjected to high internal pressures must often be connected to other parts of a system. It may then be necessary to effect such connections by holes, called cross-bores, which traverse the wall of the vessel in a more or less radial direction. Examples of these situations occur in compressor heads, tee-fittings and pumps, to name just a few. The cross-bore unfortunately introduces stress concentrations in the cylinder at the region of the tee-intersection of the bores. This not only reduces the limit to which the vessel can be pressurized but also provides a source where cracks originate. It is therefore highly desirable to know how great such stress concentrations are and also to what extent the presence of cracks would lower the load carrying capacity of the vessel or component. In this chapter, a numerical stress analysis of the problem will be presented, both with and without the cracks present.

## 7.1 REVIEW OF THE PROBLEM AND SCOPE OF THE PRESENT INVESTIGATION

Before reviewing published work, the physical problem will first be more clearly defined. Figure 7.1 shows a half-section of a cylinder of internal radius $R_1$, external radius $R_2$ and total length $2H$ with a circular cross-bore of radius $R_s$ whose axis coincides with a radial ray from the main cylinder axis at the cross-sectional axial plane which divides the cylinder into two equal halves. Stresses, as will be shown, are greatest at points A in the figure and these are the usual sites of crack initiation. The cracks can grow in either an almost symmetrical or an asymmetrical

fashion about the cross-bore, as shown in Plates 7.1 and 7.2, respectively.

Although a considerable amount of experimental work has been carried out on high pressure components, in particular the fatigue strength of internally pressurized thick-walled cylinders (see, for example, Pugh (1977)), very little is concerned with cylinders with cross-bores. Analytical results, approximate or otherwise, are even more scarce, for, even in the absence of cracks, the cross-bore problem has resisted the efforts of many an applied mathematician to reduce it to analytical tractability in the full three-dimensional sense, let alone the case where cracks are present. One of the first papers on the analysis of stress concentrations in thick-walled cylinders with cross-bores was by Fessler & Lewin (1956), who considered analytically the stress distribution in a tee-junction of thick pipes and compared results with experimental data from a frozen stress photoelastic model. Defining the hoop stress concentration factor, $k_h$, as the ratio of the maximum hoop stress, $(\sigma_h)_{max}$, to the nominal hoop stress $\sigma_h^*$ at the main bore obtained from the Lamé solution (6.1), i.e.

$$k_h = \frac{(\sigma_h)_{max}}{\sigma_h^*} = \frac{(\sigma_h)_{max}}{P\,[\{(R_2/R_1)^2+1\}/\{(R_2/R_1)^2-1\}]} \qquad (7.1)$$

$P$ being the internal pressure, a theoretical value of $k_h$ equal to 3.70 was obtained for $R_2/R_1 = 3$ and $R_1/R_s = 2$. This was 32% greater than the measured value of 2.80. But, although their theory predicted peak stresses which proved to be too large, it did provide the equations from which the limiting values of $k_h$ for cylinders with relatively small cross-bores, i.e. large values of the ratio $R_1/R_s$, could be obtained.

The limiting value of the stress concentration factor when $R_1/R_s$ becomes very large would accordingly be given by:

$$k_h = \frac{4\,(R_2/R_1)^2 + 1}{(R_2/R_1)^2 + 1} \tag{7.2}$$

This equation was derived later by Lake (1956) using a more straightforward approach, and as well by Morrison et al (1959); their analysis is presented in Appendix D. There were still significant deviations between the values of $k_h$ calculated from (7.2) and those experimentally obtained by these authors, but Morrison et al (1959) emphasized the uncertainties in the assumptions which were made in the analysis. An extensive effort, both theoretical and experimental, devoted to the stress concentration problem was also carried out by Faupel & Harris (1957), who predicted a universal value of $k_h = 2.5$ for all closed-ended cylinders with small cross-bores. But, as Morrison et al (1959) pointed out, there was an error in the formers' analysis which, when corrected, yields the same result as (7.2).

All the analytical investigations above, however, did not include the effect of the transverse shear deformation in the cylinder due to the cross-bore. Gerdeen (1972), in a similar but more elaborate analysis, derived an approximate solution for the stress concentration factor at points A in Figure 7.1 which included this transverse shear effect. The length of the cylinder, according to him, would have negligible effects on the value of $k_h$ if $R_2/R_1 > 2$. Although this may be so when the cross-bore is relatively small, it is unlikely that it will hold true when the ratio $R_1/R_s$ gets smaller. The analysis also becomes increasingly inaccurate as this ratio $R_1/R_s$ is decreased towards unity. Nevertheless, it predicts that $k_h$ increases with increasing values of $R_1/R_s$ and the predicted optimum configuration where the stress concentration factor is minimum is the one where $R_s/R_1 = 1$, i.e. a cross-bore of radius equal to

that of the main bore. Figure 7.2 shows the hoop stress concentration factors for a range of radius ratios and for $H/R_2 = 1$, obtained from this approximate analytical solution.

Gerdeen (1972) also compared his calculated values of $k_h$ with those experimentally obtained by the previous authors. They show reasonable agreement, and in some cases it was very good. Experiments were also carried out by Gerdeen & Smith (1972) for low $R_1/R_s$ values approaching and including unity. Their results verified the analytical prediction of the optimum configuration mentioned above. In these two latter papers, the authors emphasized the approximate nature of the analytical solution and suggested that it would be worth checking some of these results by computational means.

To the author's knowledge, no three-dimensional numerical solutions for the cross-bore problem are hitherto available in the literature. Further, a fracture mechanics analysis of the problem when cracks are present seems lacking too, both experimentally and analytically. It is in the light of this background and that the solutions to this problem are of much practical importance that the present numerical investigation was carried out. A complete parametric study of the problem is not very practical in view of the time and computing cost involved, therefore only a limited number of cases were investigated, all of which were for $R_2/R_1 = 2$. Two different ratios of $R_1/R_s$ were considered, namely 8.0 and 4.0, with and without the cracks present.

For the fracture mechanics analyses, the crack fronts were assumed to be circular arcs and two equal quadrant cracks symmetric about the cross-bore were assumed to be present (see Figure 7.3). This is a reasonably good representation of many actual physical situations as shown in Plate 7.1. The quadrants representing the cracks have their origins at points A

as shown, and each is of radius $a$. For each of the two $R_1/R_s$ ratios considered, the elastic responses for three different relative crack depths, $a/W$, where $W = R_2 - R_1$ is the cylinder wall thickness, were analysed. They were $a/W$ = 0.25, 0.5 and 0.75.

The internal pressure acting on the cross-bore was taken to be equal to that acting in the main bore of the cylinder. Where there are cracks, the pressure was assumed to act fully on the crack faces; this would represent the most severe situation for a given crack geometry. In all the cases treated, the total length of the cylinder was taken to be twice its external radius $R_2$. Also, closed-ended boundary conditions were assumed. To simulate this in the numerical models, a uniform tensile stress of magnitude equal to $P/((R_2^2/R_1^2) - 1))$ was applied to the ends of the cylinder in the axial direction. Poisson's ratio was taken to be 0.3 in all cases.

## 7.2 HOOP STRESS DISTRIBUTIONS IN THE ABSENCE OF CRACKS

When cracks are absent, stress concentrations are of primary interest in the stress analysis of cylinders with cross-bores. Since hoop stresses are the largest in magnitude of the stress components in the cylinder, as were also predicted from the computational solutions, only their variations will be discussed here. For the numerical analysis, one quarter of the physical problem was modelled, taking advantage of the two planes of symmetry, namely, the diametrical plane and the axial plane through the axis of the cross-bore. The boundary mesh discretizations for the two $R_1/R_s$ ratios considered, namely, 8 and 4, are shown in Figures 7.4 and 7.5, respectively. In each of these meshes, 90 surface elements with a total of 272 nodal points were used; more elements being employed in the region of the cross-bore to adequately represent the more rapid

variation of the unknowns there.

Figures 7.6 and 7.7 show the variations of the computed hoop stresses, $\sigma_h$, along the internal surface of the cylinder in the radial plane through the axis of the cross-bore. The stresses plotted are normalized with respect to the Lamé solution hoop stress for a plain cylinder, $\sigma_h^*$. Also, $Z$ is the distance from the axis of the cross-bore in the axial direction of the cylinder. It can be seen that in both cases, the computed values of $\sigma_h$ decrease rapidly from the points A towards the Lamé solution value of $\sigma_h^*$ at the ends of the cylinder; the rate of decrease for $R_1/R_s = 8$ being greater than for $R_1/R_s = 4$. For the former ratio, the computed hoop stresses were all within 4% of $\sigma_h^*$ beyond about $Z/H = 0.23$ and were within 2% beyond $Z/H = 0.6$. In the case of $R_1/R_s = 4$, the computed values of were only within 4% of $\sigma_h^*$ at distances greater than $Z/H = 0.6$. These results confirm the adequacy of the mesh configurations to produce results sufficiently accurate for engineering purposes. Further, they also ascertain that the cylinders modelled have been taken sufficiently long so that closed-ended boundary conditions could be simulated by the application of the tensile axial stresses at their ends.

At points A, the computed stress concentration factor, $k_h$, was 2.98 for $R_1/R_s = 8$, while that for $R_1/R_s = 4$ was 2.90. There is thus about a 3% decrease in the computed value of $k_h$ when the cross-bore was increased from the smaller to the larger radius considered. This is consistent with the approximate analytical solution by Gerdeen (1972) which gives stress concentration factor values of 3.44 and 3.32 for $R_1/R_s = 8$ and $R_1/R_s = 4$, respectively, which is about a 3.5% decrease. Using the approximate analysis of Morrison et al (1959), as presented in Appendix D, a value of 3.40 would be obtained. Thus, even for the case where the cross-bore radius was one-eighth of the internal radius of the cylinder,

the computed value of $k_h$ differed from these approximate solutions by about 13%.

Figure 7.8 shows the variations of the computed hoop stresses across the wall thickness of the cylinder along the surface of the cross-bore in the radial plane through A. Also plotted in the figure is the Lamé solution variation of the hoop stress for a plain cylinder. The trends of the curves are qualitatively similar, showing the decreasing magnitude of the hoop stress field across the wall of the cylinder. Nevertheless, the magnitude of the stresses are still significantly higher at all points along A-B, the point B being on the outer surface of the cylinder (Figure 7.6), when there is a cross-bore. It is interesting to note that the computed values of $\sigma_h$ for $R_1/R_s = 4$ become greater than those for $R_1/R_s = 8$ at the same radial distance from the cylinder axis, $r$, along A-B, beyond about $r/R_1 = 1.375$. At B, the computed hoop stress for $R_1/R_s = 8$ was 1.49 $\sigma_h^*$, while that for the bigger cross-bore was 1.62 $\sigma_h^*$. The corresponding Lamé solution value for a plain cylinder is 0.40 $\sigma_h^*$. Using the approach described in Appendix D, the approximate analytical solution for a small cross-bore at B would be 1.60 $\sigma_h^*$.

Although it is of less concern to the designer compared to, say, the peak stresses at A, it is perhaps of interest to examine how the hoop stresses vary around the inner circumference of the cylinder in the cross-sectional axial plane through the axis of the cross-bore. Such a plot for the computed stresses is shown in Figure 7.9 for the two $R_1/R_s$ ratios considered. The circumferential angle $\theta$ is as defined in the figure, the $\theta = 0$ radial plane being that containing the axis of the cross-bore. For both $R_1/R_s = 8$ and $R_1/R_s = 4$, the computed hoop stresses at the interior surface of the cylinder were only compressive in a very small region of the inner circumference near the cross-bore which is subjected to the

internal pressure. The computed values of $\sigma_h$ for $R_1/R_s = 8$ were all within 2% of the Lamé solution value $\sigma_h^*$ beyond $\theta = 45^0$ to about $\theta = 135^0$; between $\theta = 135^0$ and $\theta = 180^0$, the hoop stresses increased marginally, but were still within 4% of $\sigma_h^*$. For the cylinder with the larger cross-bore, $\sigma_h^*$ increased from the value of the applied pressure (compressive) at the cross-bore surface, i.e. - 0.60 $\sigma_h^*$, to a hoop tension of magnitude 1.07 $\sigma_h^*$ at $\theta = 60^0$, thereafter it dropped to a value of 0.98 $\sigma_h^*$ at $\theta = 90^0$ before gradually increasing to a value of 1.11 $\sigma_h^*$ at $\theta = 180^0$.

Finally, to conclude this section, a few remarks. The regions where stresses would be elevated to levels of possible yield due to the presence of a cross-bore in the cylinder have now been discussed. The results provide an overall view of the variations of these stresses in the cylinder rather than just a stress concentration factor for the peak stress; these could be useful in design considerations. Stress concentration factors predicted by the approximate analytical solutions were found to be somewhat higher than those predicted computationally for the two cases analysed. The differences in these predictions should not be too surprising in view of the approximate nature of the analytical solutions, which require that the cross-bore must be "small". Little (1965) in fact suggested that the hole diameter should not exceed about one-tenth of the internal diameter of the cylinder for (7.2) to be used. Finally, it must be said that there are possible ways of reducing the stress elevating effect of a cross-bore in a cylinder, but this is beyond the scope of the present study; a discussion of some of the ways has been presented by Cole (1969).

## 7.3 ANALYSIS OF THE CRACKED COMPONENT

Service cracks almost invariably will nucleate and grow from the region of the tee-intersection of the cross-bore and the main bore of the cylinder (i.e. points A) because stresses are highest there. When cracks are present, the dominant stress fields are no longer at points A but instead are those in the vicinity of the crack front. The primary concern to the stress analyst then is that the stress intensity factor $K_I$ around the crack front should not exceed the value of the fracture toughness of the material, $K_{Ic}$, during service loading.

As in the case of cracks in plain cylinders discussed in the previous chapter, estimates of $K_I$ could be obtained by simplified and approximate methods. For example, if the defects are small they can be treated as cracks under constant magnitude stress fields magnified by a stress concentration factor. When the cracks are not small compared to the hole, an approach would be to consider the cross-bore as part of an "effective" elliptical surface crack in the cylinder. A similar approach was used by Broek (1971) for the solution of corner cracks at holes in plates under tension. But the accuracy of such solutions would be highly dubious. In this respect, experience could perhaps be drawn from the work on reactor vessel nozzles and cylinder tee-junctions where cracks also grow from the corner intersection of the bores. Linear elastic fracture mechanics studies of cracks in these components (see, for example, Hellen & Dowling (1974), Broekhoven & Ruijtenbeek (1975)) show that, for these types of configurations, the use of simplified analytical or semi-analytical solutions to evaluate $K_I$ values may result in considerably inaccurate estimates of the true results. Therefore, a truly three-dimensional solution procedure is necessary to enable accurate values of $K_I$ to be determined for the fracture mechanics analysis of the cross-bore problem.

For the three-dimensional numerical boundary integral equation analysis, only one-quarter of the physical problem was modelled, as previously. Typical boundary mesh idealizations for both the $R_1/R_s$ ratios considered are shown in Figures 7.10 and 7.11, respectively. The element configuration was varied to suit the three different relative crack depths, namely, $a/W$ = 0.25, 0.5 and 0.75, that were analysed. A maximum of 109 surface elements and 329 nodes were used in each case of $R_1/R_s$. The sides of singularity elements with mid-side nodes displaced to quarter point positions were again used to model the crack fronts.

### 7.3.1 Stress Intensity Factors

For each of the three different crack sizes in combination with each of the $R_1/R_s$ ratios considered, the stress intensity factors at points around the crack front of the quarter-circular surface crack were obtained. The values of $K_I$ were calculated by the direct method using the computed crack-face displacement data. Plane strain conditions were assumed to prevail at all points along the crack front, except at the internal surface of the cylinder and at the surface of the cross-bore, which were treated as being under plane stress. The validity of these assumptions is well supported by Figures 7.12 and 7.13 which show the plots of the ratio of computed flow stress to mean stress, $\tau_o/\sigma_m$, at a radial distance of 0.133 $a$ ahead of the crack front when $a/W$ = 0.75, for $R_1/R_s$ = 8 and $R_1/R_s$ = 4, respectively. The trends of this ratio for the smaller crack sizes considered are almost identical in form to those plotted in Figures 7.12 and 7.13, and hence are not presented. As the free surfaces of the cross-bore and the main bore are approached, the ratio $\tau_o/\sigma_m$ can be seen to increase very rapidly to values of unity or greater, reflecting the rapid loss of lateral constraint and increased

tendency to plastic flow there. This feature is typical of surface crack problems and has been discussed in greater detail previously in Chapter 5.

The computed values of the normalized stress intensity factor, $K_I/P\sqrt{\pi a}$, around the crack fronts for $R_1/R_s = 8$ and $R_1/R_s = 4$ are shown in Tables 7.1 and 7.2, respectively. These results are also plotted in Figures 7.14 and 7.15. Position around the crack front is defined by the angle $\phi$, ranging from $\phi = 0$ at the surface of the cross-bore to $\phi = 90^0$ at the internal surface of the cylinder, as illustrated in Figures 7.14 and 7.15.

The qualitative features of the variations of $K_I$ for each of the crack depths and the $R_1/R_s$ ratios are very similar. Moving around the crack front from the point on the surface of the cross-bore, the value of $K_I$ decreases gradually to a minimum and then increases again as the internal surface of the cylinder is approached. In all the cases analysed, this minimum of $K_I$ always occurs between $\phi = 30^0$ and $\phi = 60^0$. In both cases of the $R_1/R_s$ ratios, the value of the normalized stress intensity factor for $a/W = 0.75$ is higher than that for $a/W = 0.5$ at the same angular orientation of the crack front. But the stress intensity factors for $R_1/R_s = 8$ are all significantly lower in value than those for $R_1/R_s = 4$ with the same crack size. This is most probably due to the smaller amount of material constraint in the region of the crack when the cross-bore is larger, therefore for a given size of the crack there is less constraint on the crack faces opening, hence the larger values of $K_I$.

It is interesting to note that, while in the case of $R_1/R_s = 4$, the computed values of $K_I$ are largest at $\phi = 0^0$ for all the three different crack sizes considered, this is not always so in the case of $R_1/R_s = 8$. In the latter case, the value of $K_I$ at the point on the cross-bore surface was found to be larger than that at the point on the

internal surface of the cylinder only for $a/W = 0.25$, by about 11%. For the other two crack sizes, the reverse was found to be true; when $a/W = 0.5$, the value of $K_I$ at $\phi = 90^0$ is about 2% higher than that at $\phi = 0^0$, while it is about 3% higher when $a/W = 0.75$.

No similar solutions are, as far as is known, available in the literature for comparison, therefore not much more can be discussed in this section. Suffice it to say that the complexity of the geometry and the complicated stress system would certainly make the attempt to obtain the stress intensity factors analytically for the fracture problem of the cross-bore in a pressurized cylinder a formidable, if not an impossible, task. Any $K_I$ solutions for this problem in the foreseeable future which are of sufficient accuracy for use in engineering design are most likely to be obtained numerically.

### 7.3.2 Hoop Strains

Whilst it is a relatively easy matter to model the cross-bore problem and obtain $K_I$ and other relevant solutions by computational means, it is, in practice, often a difficult task determining the size and geometry of the service crack in the first place. Radiography offers a solution to this difficulty but it can be a relatively expensive, albeit an often necessary, procedure. A possible practical alternative in which the computational solutions could be used to continuously monitor the crack growth, is perhaps the measurement of hoop strains, $\varepsilon_h$, at points on the outer surface of the cylinder, as was done for the plain cylinder problem in the previous chapter. The measured hoop strains are unlikely to be able to provide information about the actual shapes of the cracks, but they may be a useful guide for estimating their sizes. This can be done by comparing the measured values with the computational solutions

carried out using real crack geometries.

However, there are at least two main difficulties from the practical point of view. First, it is extremely difficult to place a strain gauge for measuring accurately the strains at the edge of the cross-bore due to the fact that it is pressurized as well. Second, the strains vary extremely rapidly in that region, as can be seen in Figure 7.16 which shows the computed variations of the hoop strains around the outer circumference of the cylinder in the axial plane through the axis of the cross-bore, for $R_1/R_s$ = 8 and the different crack depths. The strains are normalized to the Lamé solution hoop strain, $\varepsilon_h^*$, for an uncracked plain cylinder with the same end boundary conditions. Also plotted are the results for the uncracked cylinder with the same cross-bore size obtained from the results of the investigations in Section 7.2. The computed results for $R_1/R_s$ = 4 are qualitatively identical in trends and hence are not presented. It can be seen that the hoop strains vary from a compressive state at the edge of the cross-bore to a tensile state in just a few degrees of the angular orientation, $\theta$; the compressive state being due to the fact that the cross-bore was also subjected to the internal pressure. With such rapid variations of $\varepsilon_h$ in the region of the cross-bore, measured values there would be highly susceptible to error.

On the other hand, the computed results show that the hoop strains at the outer surface of the cylinder in the radial planes remote from the cross-bore do not vary so rapidly, so these quantities could be measured with a greater degree of confidence there. Figures 7.17 and 7.18 show the computed variation of $\varepsilon_h$ with crack size, for $R_1/R_s$ = 8 and $R_1/R_s$ = 4, respectively, at the outer diameter of the cylinder directly opposite the cross-bore along its axis, i.e. at $\theta = 180^o$. The values of $\varepsilon_h$ there in both cases decrease monotonically with the crack sizes analysed

as was also seen previously for the plain cylinder; the rate of decrease is greater for the cylinder with the larger cross-bore. For $R_1/R_s$ = 8, the computed value of $\varepsilon_h$ when there was no crack at the cross-bore, is 0.949 $\varepsilon_h^*$, decreasing to 0.767 $\varepsilon_h^*$ when the quadrant-cracks have grown to a size of $a/W$ = 0.75. The corresponding values for $R_1/R_s$ = 4 are 0.855 $\varepsilon_h^*$ and 0.543 $\varepsilon_h^*$, respectively.

### 7.3.3 Hoop Stress Distributions

The dominant stress fields in a cracked component are characterized by the stress intensity factors around the crack front and these have been discussed for the cross-bore cylinder problem. To the stress analyst, the hoop stresses in regions away from the crack are probably only of secondary interest; nevertheless, for completeness, their variations will now be discussed.

Figures 7.19 and 7.20 show the variations of the computed hoop stress, $\sigma_h$, around the inner circumference of the cylinder in the axial plane through the axis of the cross-bore, for $R_1/R_s$ = 8 and $R_1/R_s$ = 4, respectively. The results presented are normalized to the Lamé solution hoop stress for a plain uncracked cylinder, $\sigma_h^*$. Also shown for comparison in each figure are the results for an uncracked plain cylinder with the corresponding cross-bore size from Figure 7.9. Both sets of results are qualitatively similar to each other and it is interesting to note that for the deeper cracks, $a/W$ = 0.75, the computed hoop stresses in the small region away from the cross-bore are significantly more compressive in state than that at the edge of the hole. But the compressive hoop stress then decreases in magnitude and becomes tensile at about $\theta = 40^o$, increasing further in magnitude in the tensile state with $\theta$. Also, in both cases of the $R_1/R_s$ ratios considered, the computed hoop stresses at

$\theta = 90^0$ for all crack depths were all within 4% of the Lamé solution value for an uncracked plain cylinder, $\sigma_h^*$. Beyond $\theta = 90^0$, the hoop stresses are higher, the larger the crack size.

Figure 7.21 shows the variations of $\sigma_h$ with distance away from the axis of the cross-bore at the inner surface of the cylinder at $\theta = 90^0$ for $R_1/R_s = 8$. The corresponding variations for $R_1/R_s = 4$ is shown in Figure 7.22. The qualitative features in these figures are again very similar to each other; of interest, perhaps, is that the hoop stresses are all within 4% of the Lamé solution value, $\sigma_h^*$, at $Z/H = 0$, but they decrease with increasing $Z/H$ to a minimum value at about $Z/H = 0.7$ before increasing marginally in magnitude as the ends of the cylinder are approached. For both $R_1/R_s$ ratios, the rate of decrease is greater the larger the crack size; and for the same crack size, the drop in magnitude of $\sigma_h$ is, in turn, greater in the case of the cylinder with the larger cross-bore. At $a/W = 0.75$, for example, the computed hoop stress at $Z/H = 0.8$ is 0.85 $\sigma_h^*$ for $R_1/R_s = 8$, the corresponding value for $R_1/R_s = 4$ is 0.79 $\sigma_h^*$.

While the features of the stress variations discussed so far have been rather similar between the two $R_1/R_s$ ratios considered, this is not so at the internal surface of the cylinder in the radial plane diametrically opposite that containing the cracks. Figure 7.23 shows the variations of $\sigma_h$ with $Z/H$ in this $\theta = 180^0$ plane for $R_1/R_s = 8$, while in Figure 7.24 are the corresponding results for $R_1/R_s = 4$. Also shown for comparison in these figures are the results obtained in the investigations in Section 7.2 for the cases without cracks. When there are no cracks, $\sigma_h$ increases from about 1.03 $\sigma_h^*$ at $Z/H = 0$ to 1.05 $\sigma_h^*$ at the ends of the cylinder, for $R_1/R_s = 8$. With $a/W = 0.25$, the computed hoop stresses are almost constant at 1.04 $\sigma_h^*$ throughout the length of the cylinder in this

radial plane. With the deeper cracks, $a/W$ = 0.5 and 0.75, the values of $\sigma_h$ are higher than the Lame solution value at $Z/H$ = 0 by 10% and 20%, respectively, but they decrease in magnitude as the ends of the cylinder are approached, to values of 1.07 $\sigma_h^*$ and 1.13 $\sigma_h^*$, respectively, there.

On the other hand, all the results for $R_1/R_s$ = 4 in this $\theta = 180^0$ plane show that the hoop stresses at the inner surface of the cylinder tend to increase with distance from the axis of the cross-bore towards the ends of the cylinder. Even for the cylinder without the cracks at the cross-bore, the computed value of $\sigma_h$ is 11% higher than $\sigma_h^*$ at $Z/H$ = 0, increasing to the value of 1.16 $\sigma_h^*$ at $Z/H$ = 1. The increase of $\sigma_h$ with $Z/H$ when $a/W$ = 0.25 is the most dramatic and what is perhaps most interesting here is that at $Z/H$ = 1, the value of $\sigma_h$ is almost equal to that when $a/W$ = 0.5. The hoop stresses, when $a/W$ = 0.5, tend to remain fairly constant at about 1.28 $\sigma_h^*$ from about $Z/H$ = 0.8; but when $a/W$ = 0.75, $\sigma_h$ increases from a value of 1.33 $\sigma_h^*$ at $Z/H$ = 0 to a maximum value of 1.40 $\sigma_h^*$ at $Z/H$ = 0.8 before decreasing marginally to 1.38 $\sigma_h^*$.

It is probably of significance to note that, while the hoop stresses at the $\theta = 90^0$ radial plane are generally lower than the Lame solution value, those at the $\theta = 180^0$ plane are generally higher. Not much more can perhaps be said about these features, except to conclude that the stresses in the cylinder in the presence of the defects and a cross-bore have re-distributed in such a way as to sustain the static equilibrium of the component.

TABLE 7.1

Normalized Stress Intensity Factors, $K_I/P\sqrt{\pi a}$, for Internal Surface Quadrant Cracks at the Cross-Bore of Cylinder Subjected to Internal Pressure, $R_2/R_1 = 2$, $R_1/R_s = 8$

| $a/W$ | $\phi$ (see Figure 7.15) | | | | | | |
|---|---|---|---|---|---|---|---|
| | 0° | 15° | 30° | 45° | 60° | 75° | 90° |
| 0.25 | 2.165 | 1.963 | 1.818 | 1.753 | 1.787 | 1.859 | 1.953 |
| 0.50 | 1.795 | 1.653 | 1.570 | 1.550 | 1.607 | 1.712 | 1.836 |
| 0.75 | 1.843 | 1.672 | 1.590 | 1.568 | 1.630 | 1.738 | 1.899 |

TABLE 7.2

Normalized Stress Intensity Factors, $K_I/P\sqrt{\pi a}$, for Internal Surface Quadrant Cracks at the Cross-Bore of Cylinder Subjected to Internal Pressure, $R_2/R_1 = 2$, $R_1/R_s = 4$

| $a/W$ | $\phi$ (see Figure 7.14) | | | | | | |
|---|---|---|---|---|---|---|---|
| | 0° | 15° | 30° | 45° | 60° | 75° | 90° |
| 0.25 | 2.545 | 2.313 | 2.124 | 2.016 | 2.023 | 2.111 | 2.198 |
| 0.50 | 2.223 | 2.000 | 1.822 | 1.785 | 1.793 | 1.829 | 1.986 |
| 0.75 | 2.346 | 2.046 | 1.848 | 1.789 | 1.794 | 1.887 | 2.033 |

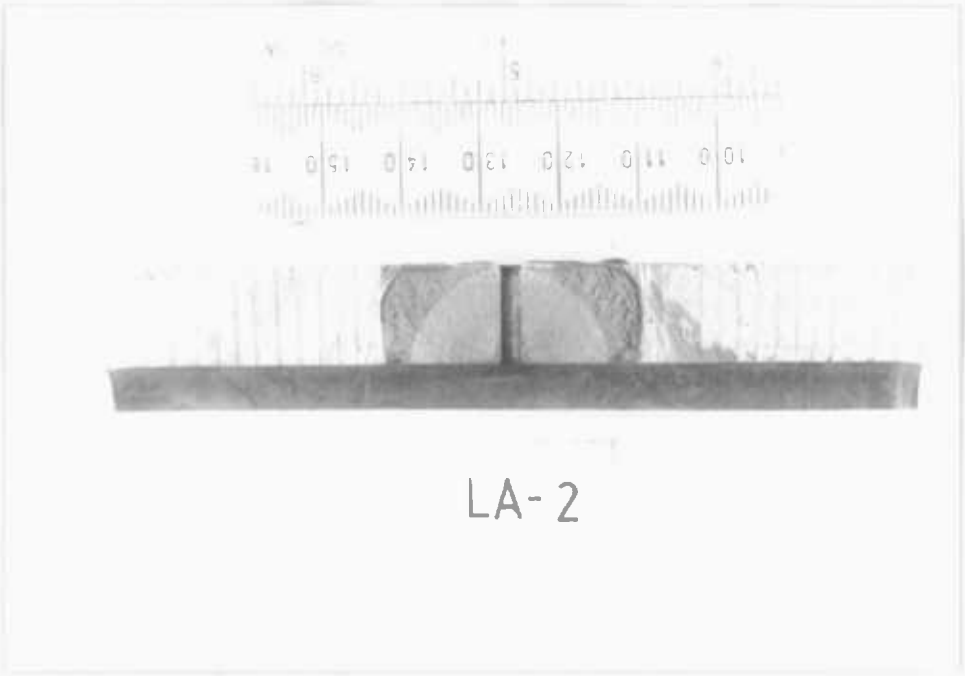



Plate 7.1

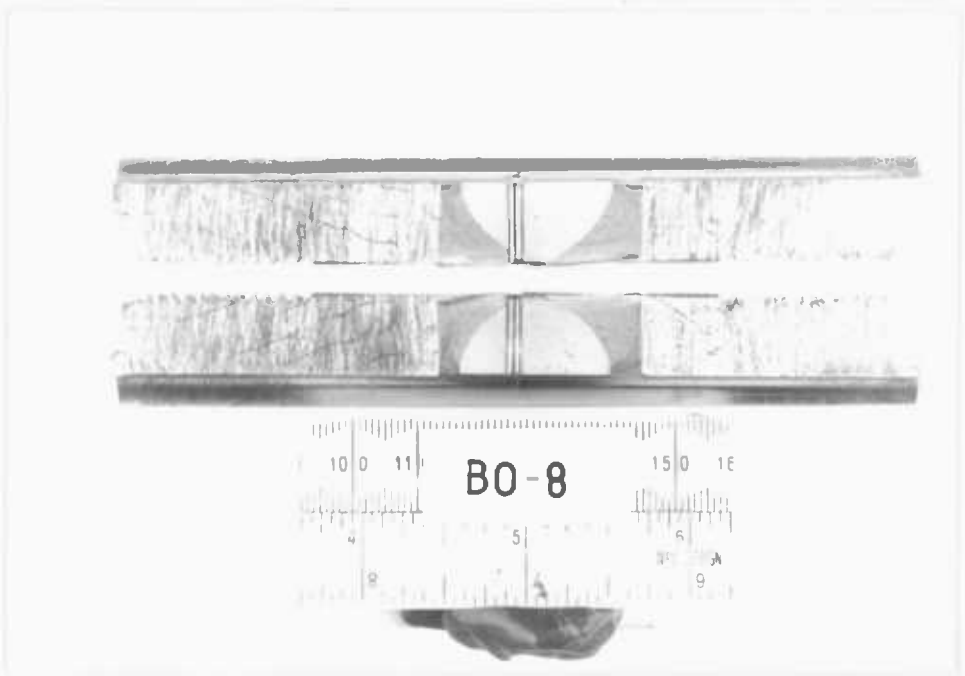



Plate 7.2

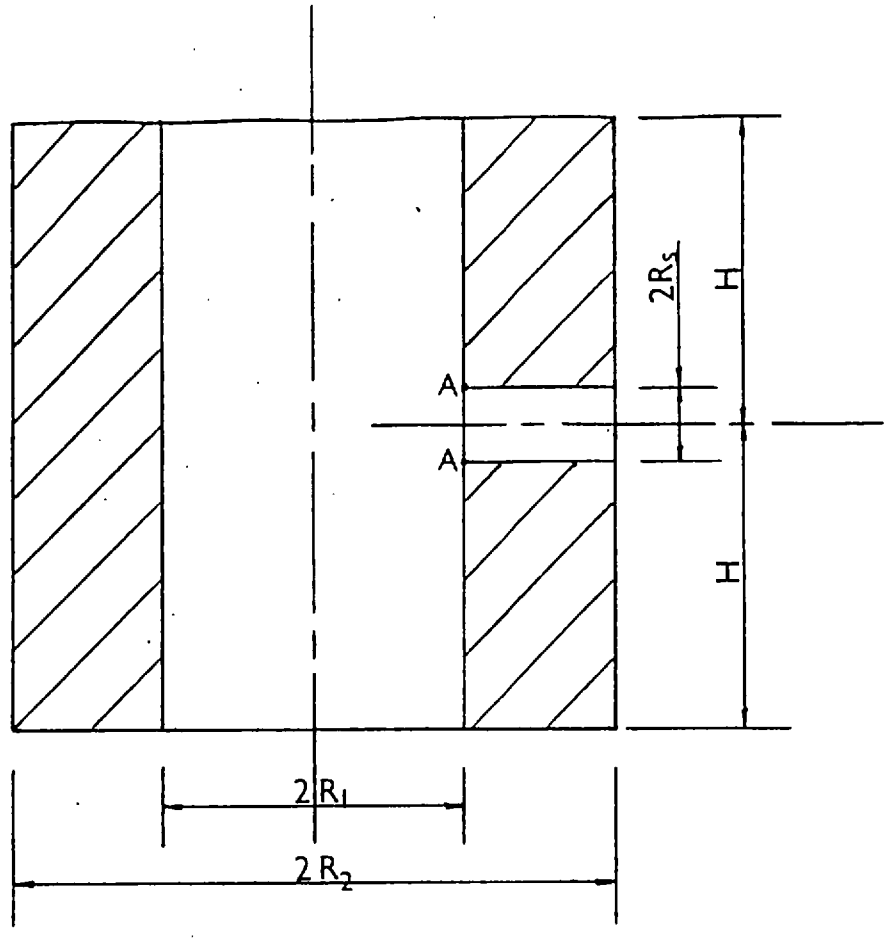



Figure 7.1: Thick-walled cylinder with a circular cross-bore

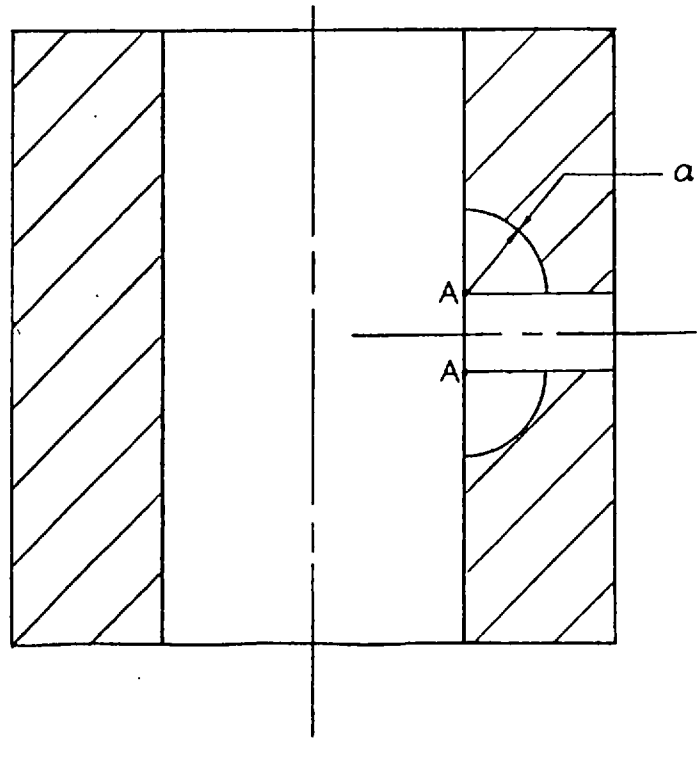



Figure 7.3: Symmetrical quadrant cracks at cross-bore of pressurized cylinder

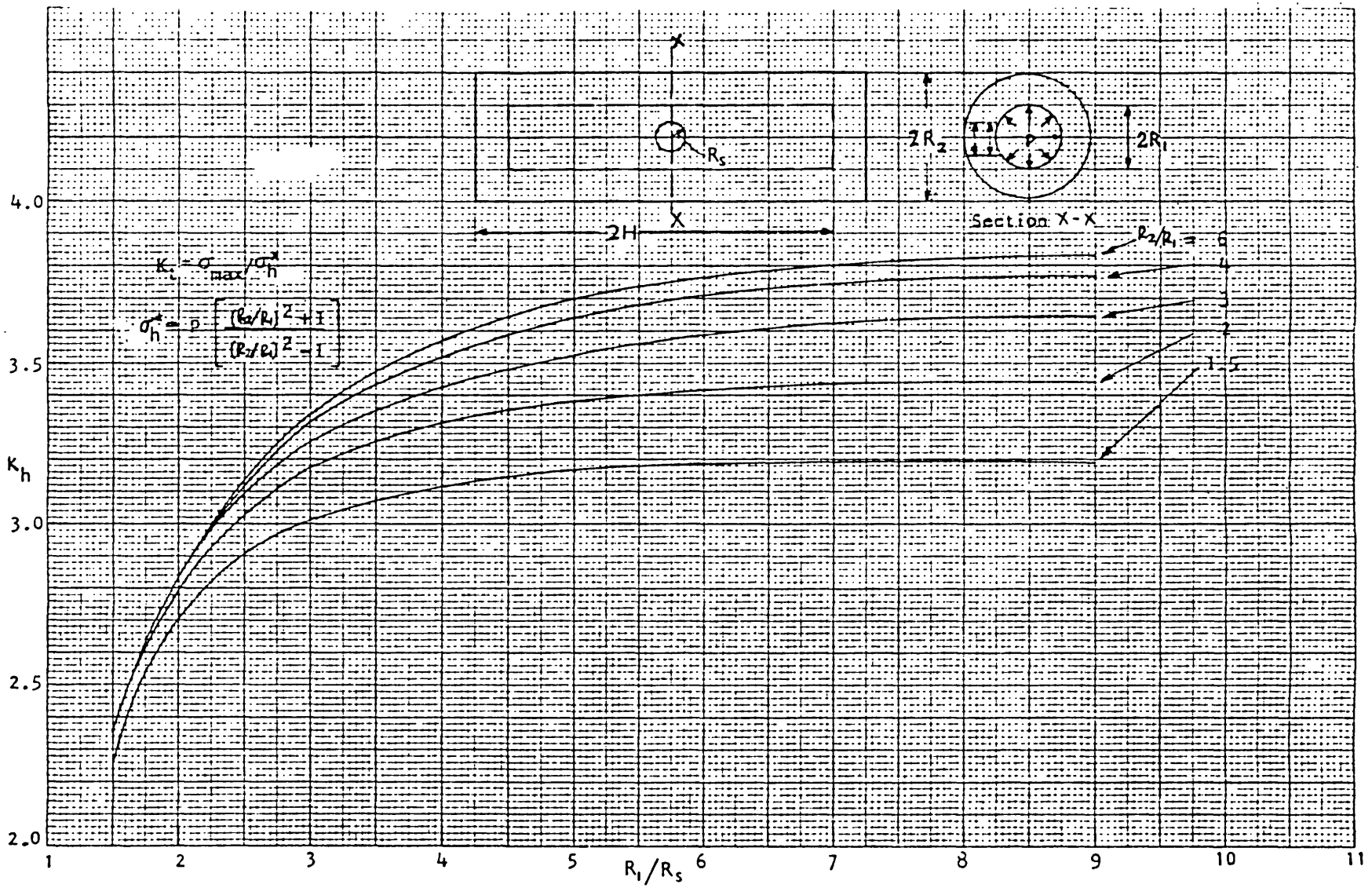



Figure 7.2: Hoop stress concentration factor, $k_h$, for a pressurized cylinder with a cross-bore (Gerdeen (1972))

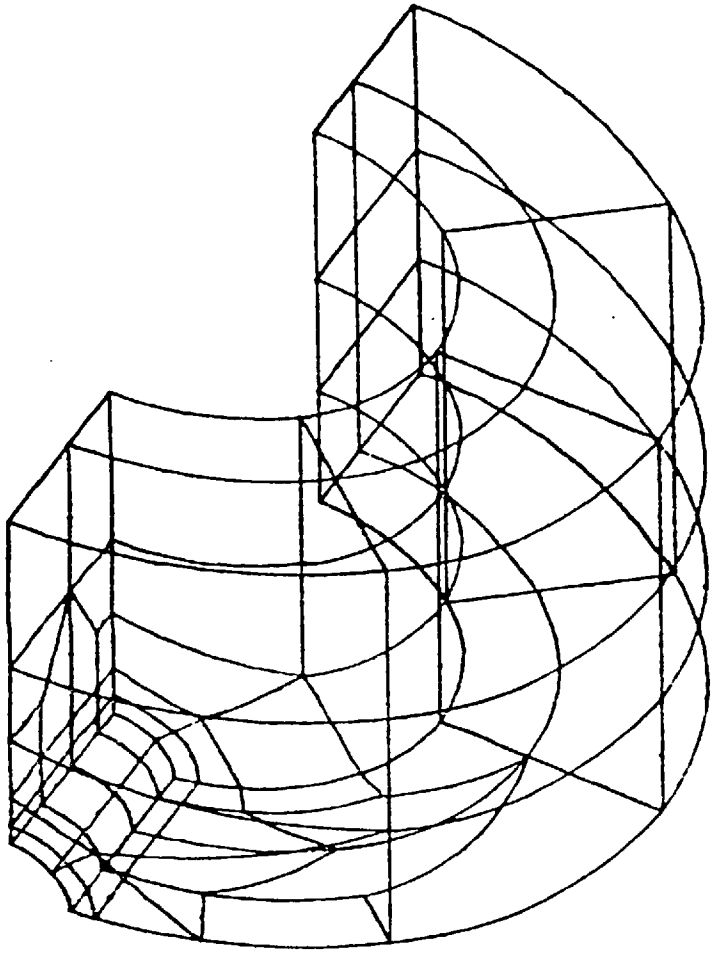


Figure 7.5: Boundary mesh for $R_2/R_1 = 2$, $R_1/R_s = 4$, $H/R_2 = 1$

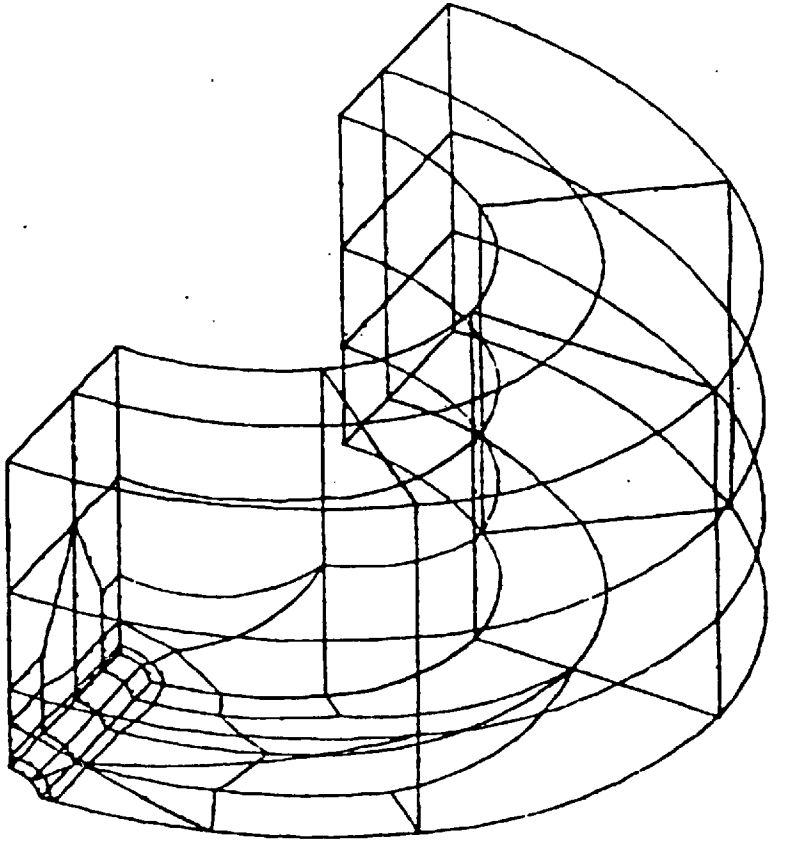


Figure 7.4: Boundary mesh for $R_2/R_1 = 2$, $R_1/R_s = 8$, $H/R_2 = 1$

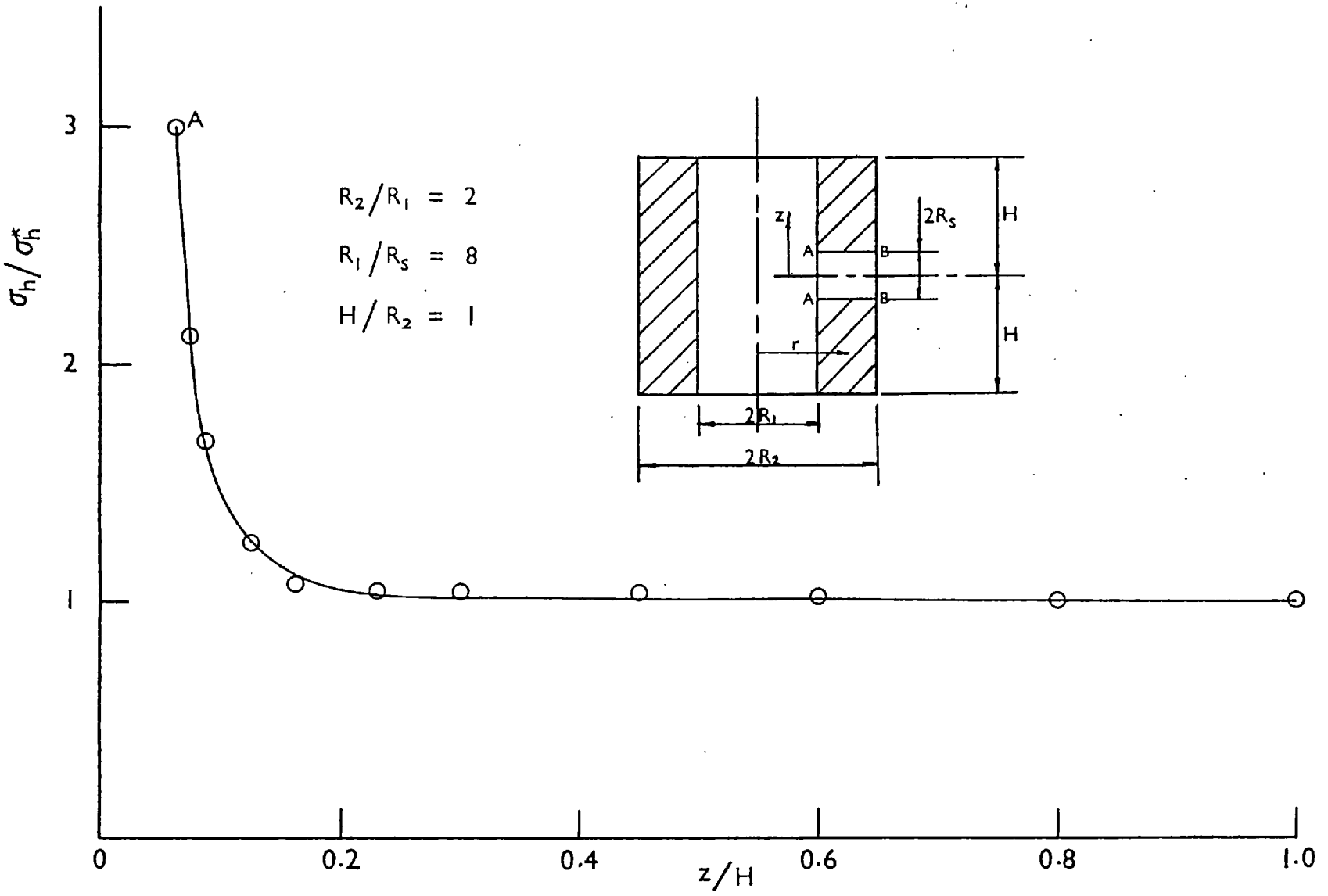



Figure 7.6: Variation of hoop stress along the internal surface of the cylinder at $\theta = 0°$ radial plane, $R_1/R_s = 8$

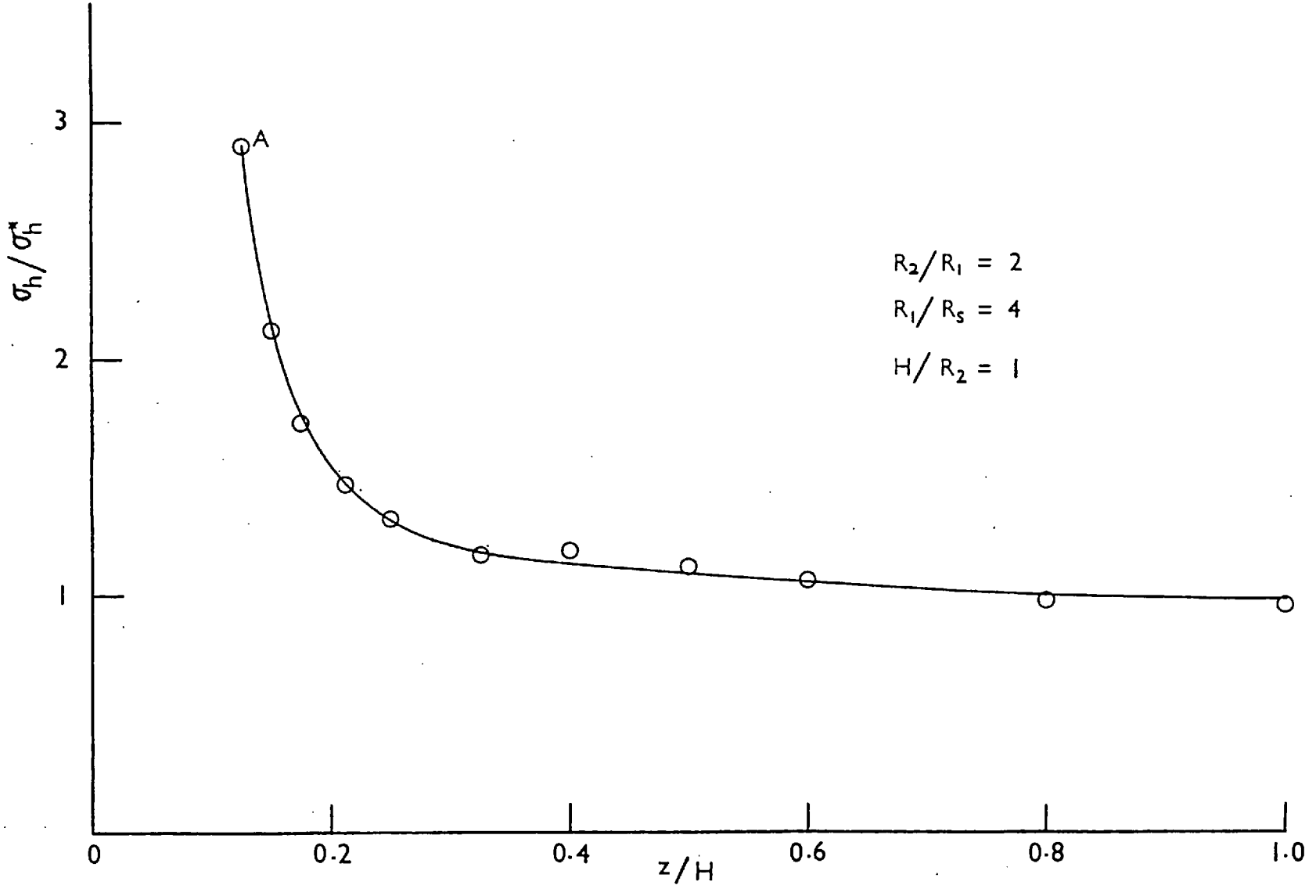



Figure 7.7: Variation of hoop stress along the internal surface of the cylinder at θ = 0° radial plane, $R_1/R_s = 4$

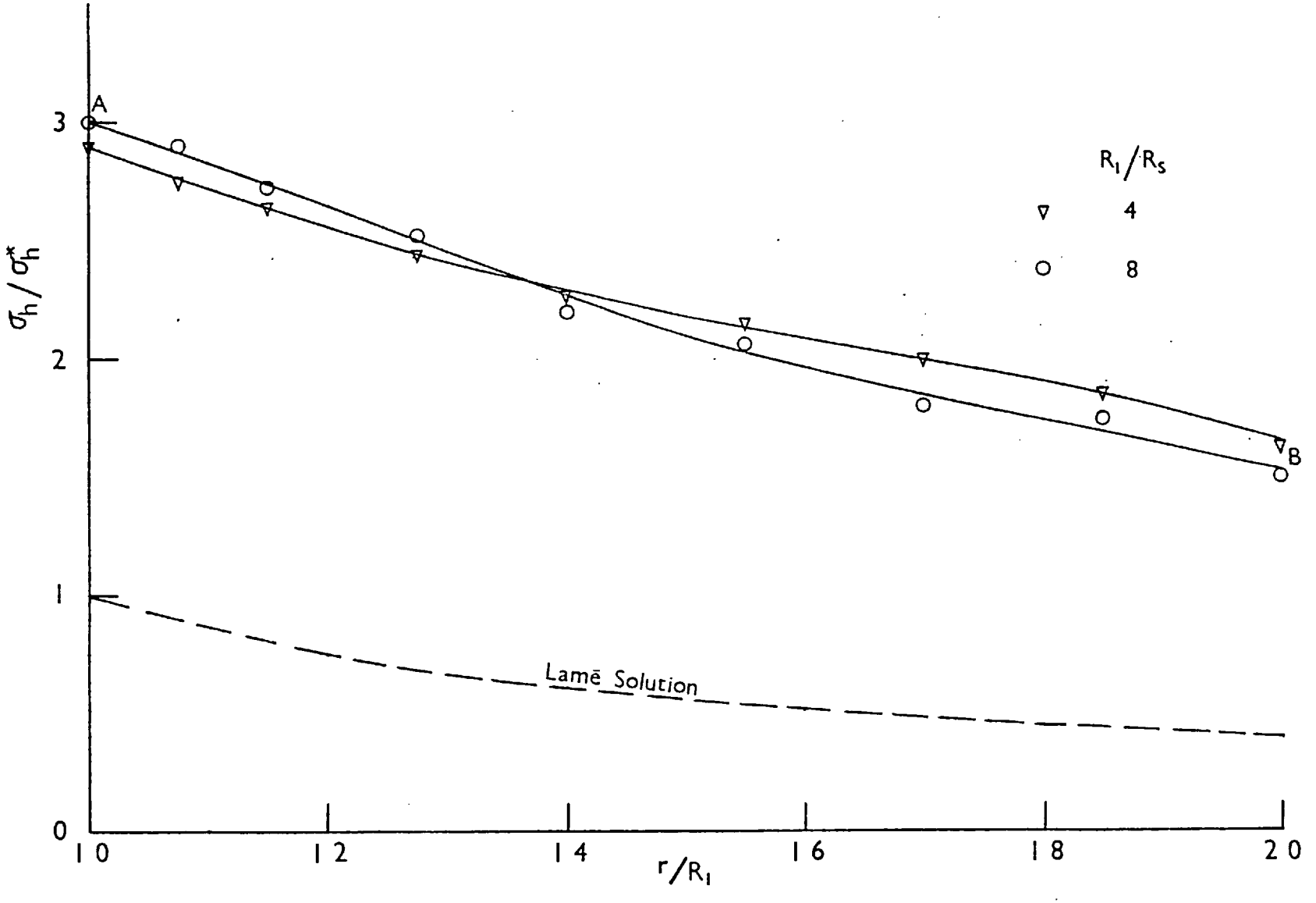



Figure 7.8: Variation of hoop stress with radius along the surface of the cross-bore, A-B

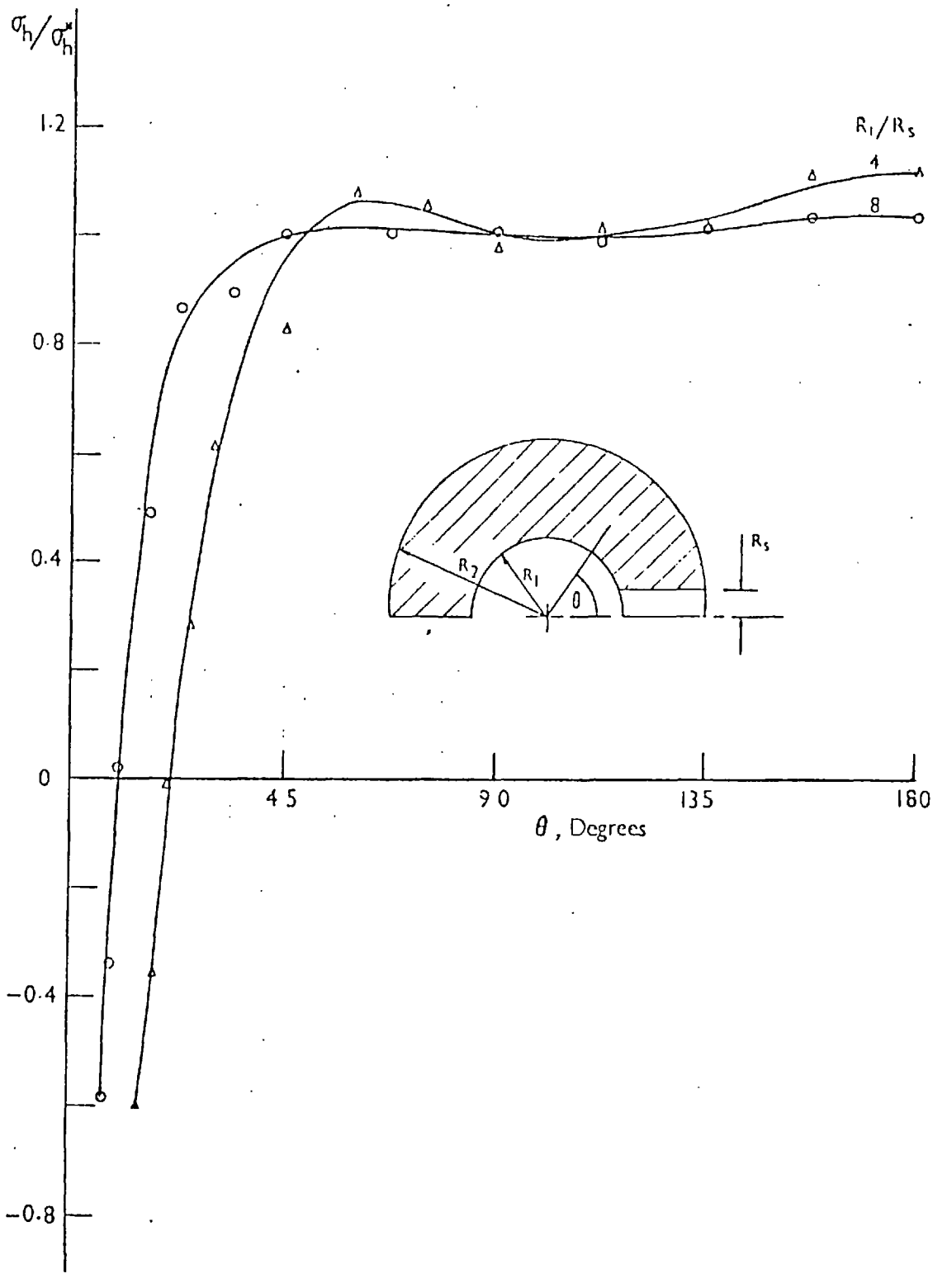



Figure 7.9: Variation of hoop stress along inner circumference of cylinder at $Z/H$ = 0 axial plane

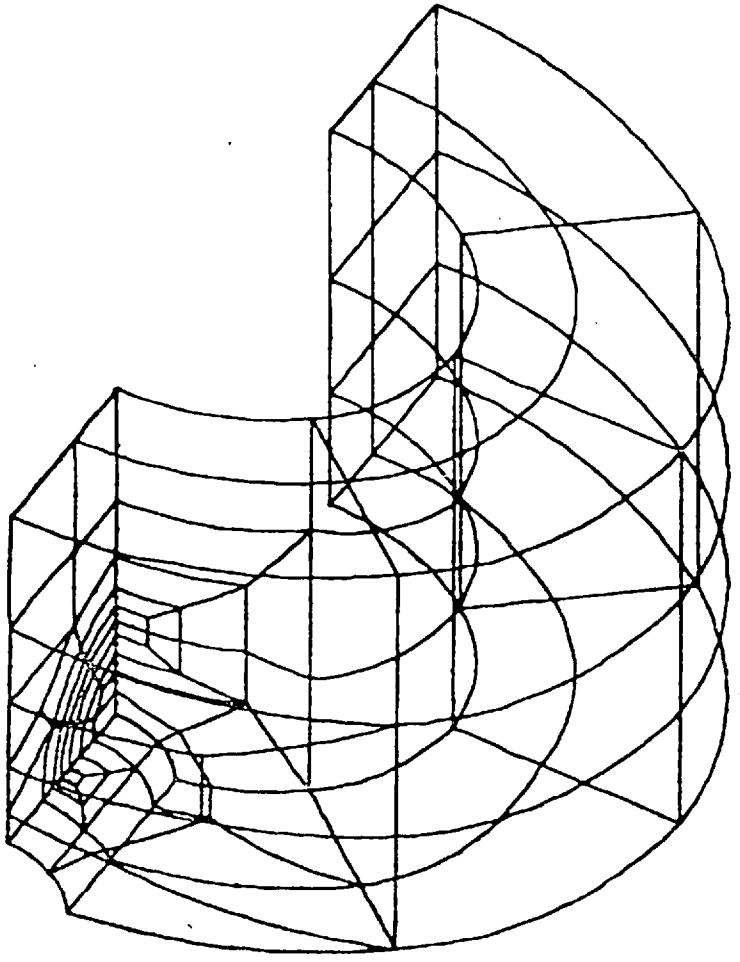


Figure 7.11: Boundary mesh for $R_2/R_1$ = 2, $R_1/R_s$ = 4, $a/W$ = 0.5

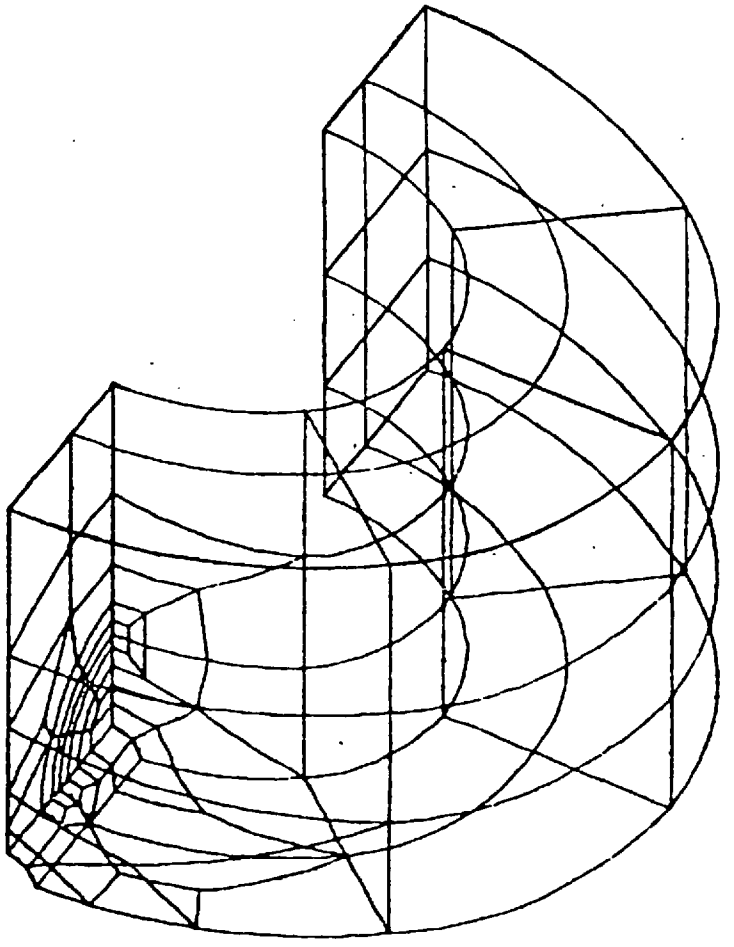


Figure 7.10: Boundary mesh for $R_2/R_1$ = 2, $R_1/R_s$ = 8, $a/W$ = 0.5

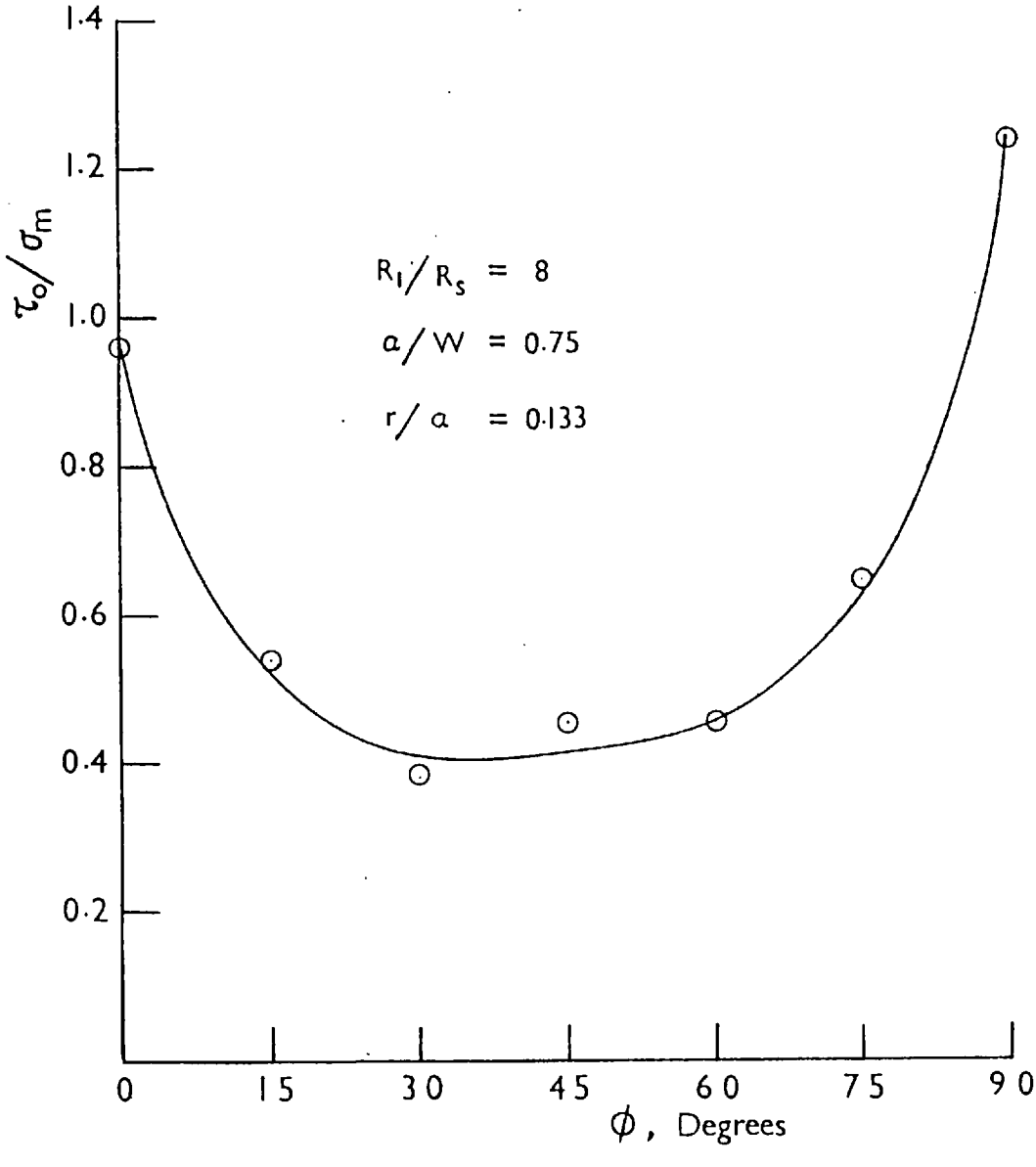



Figure 7.12: Plot of flow stress to mean stress ratio, $\tau_o/\sigma_m$

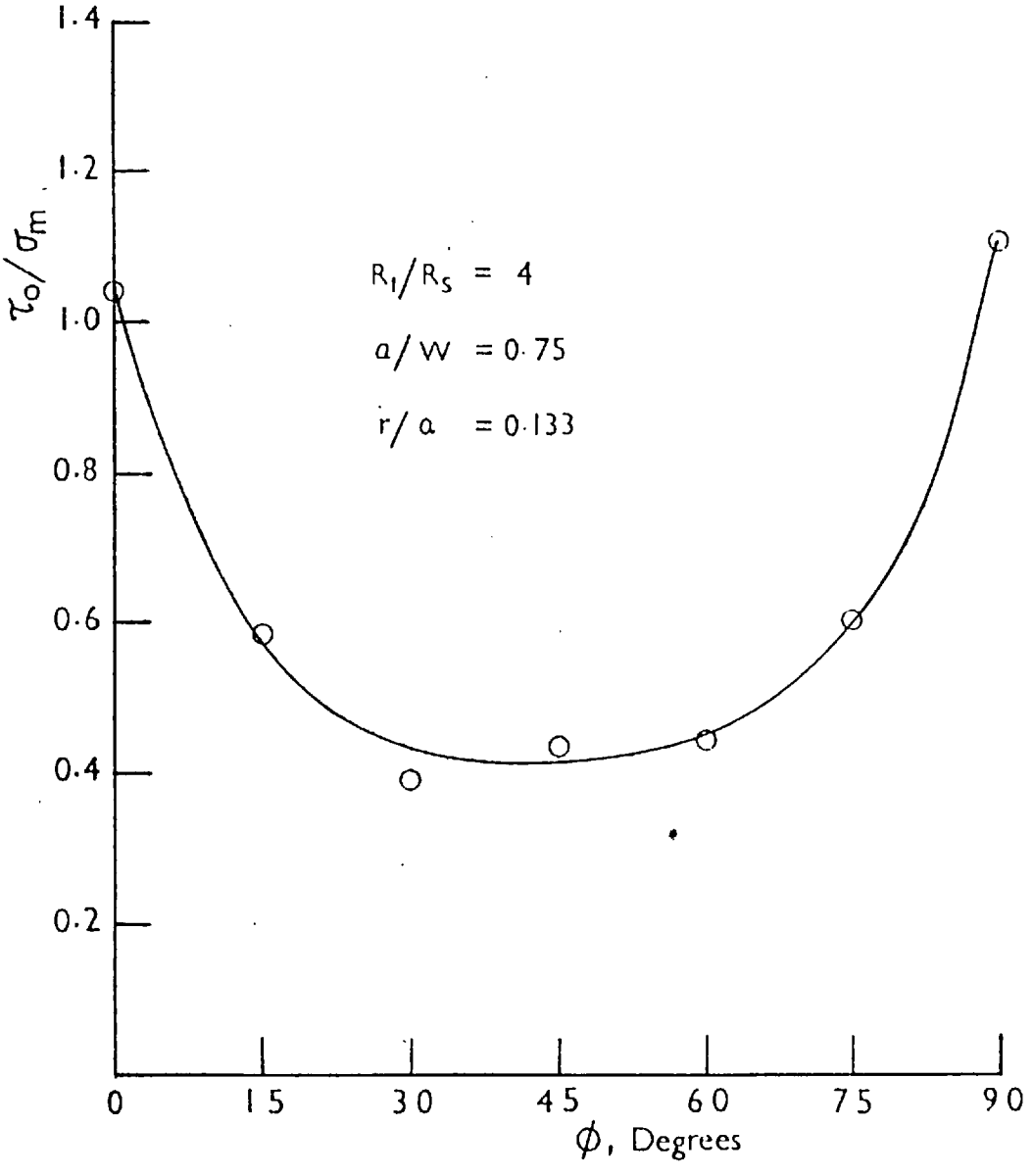



Figure 7.13: Plot of flow stress to mean stress ratio, $\tau_o/\sigma_m$

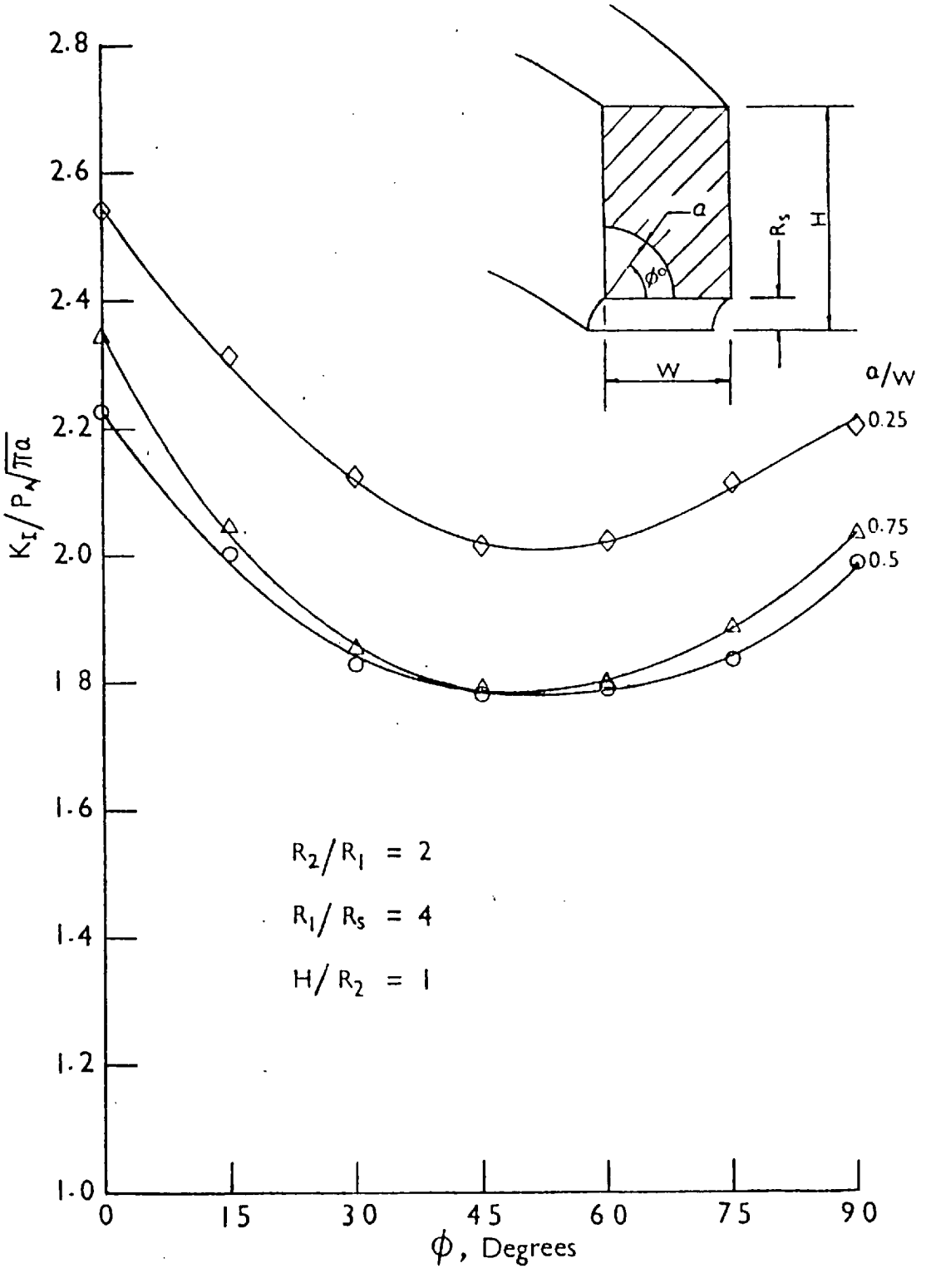



Figure 7.14: Stress intensity factors for quadrant cracks at cross-bore of thick-walled cylinder under internal pressure

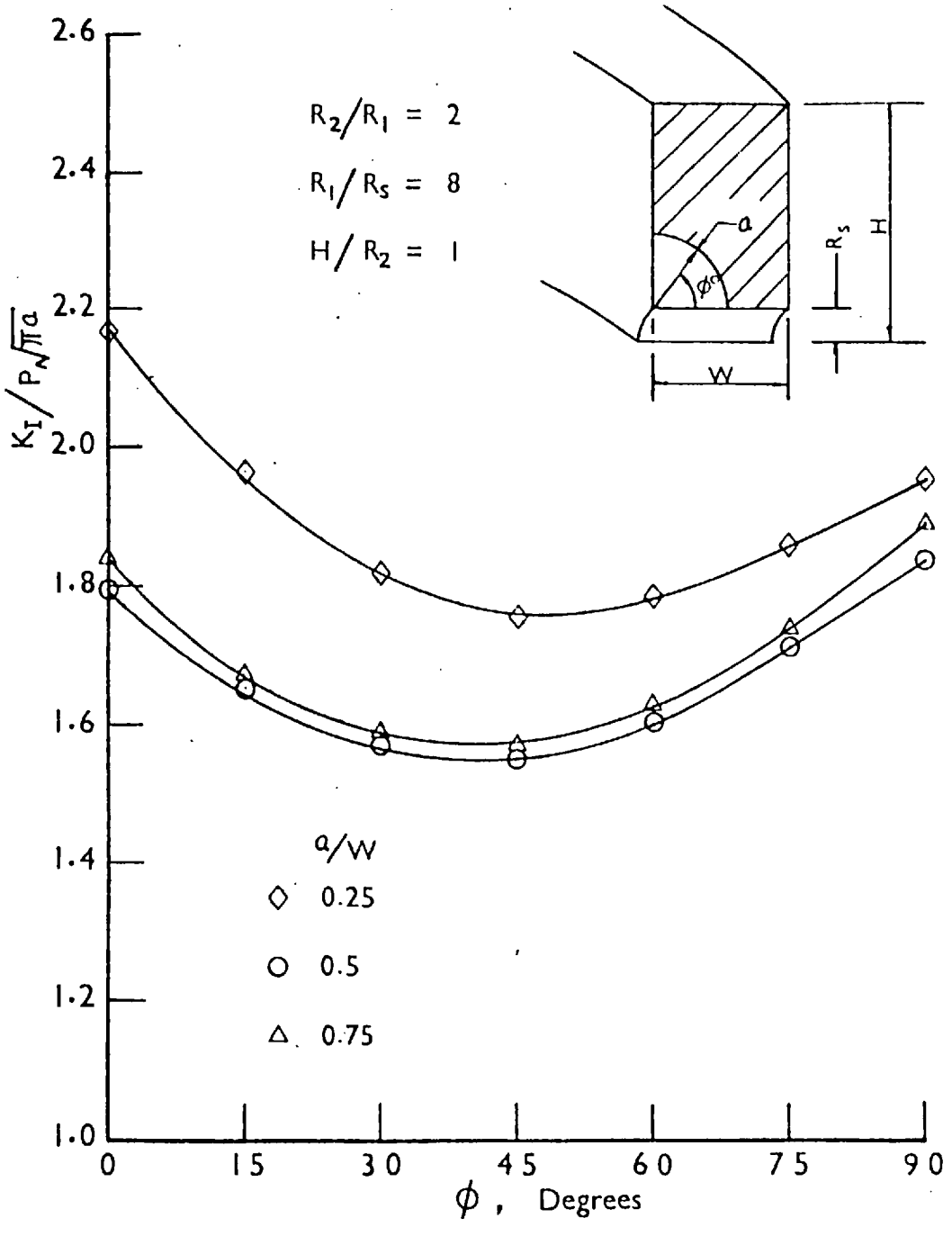



Figure 7.15: Stress intensity factors for quadrant cracks at cross-bore of thick-walled cylinder under internal pressure

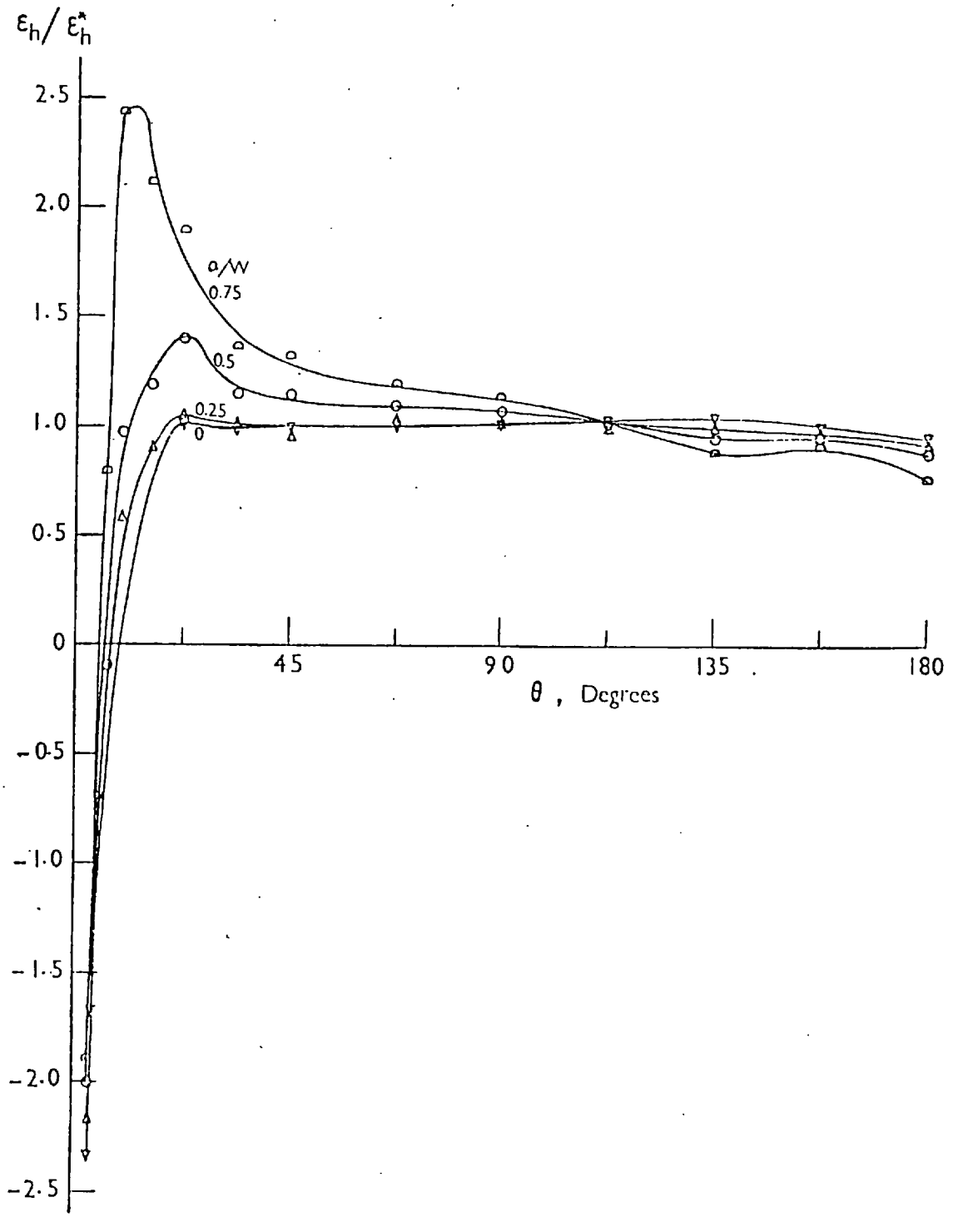



Figure 7.16: Variation of hoop strain along the inner circumference of cylinder at $Z/H$ = 0 axial plane, $R_1/R_s$ = 8

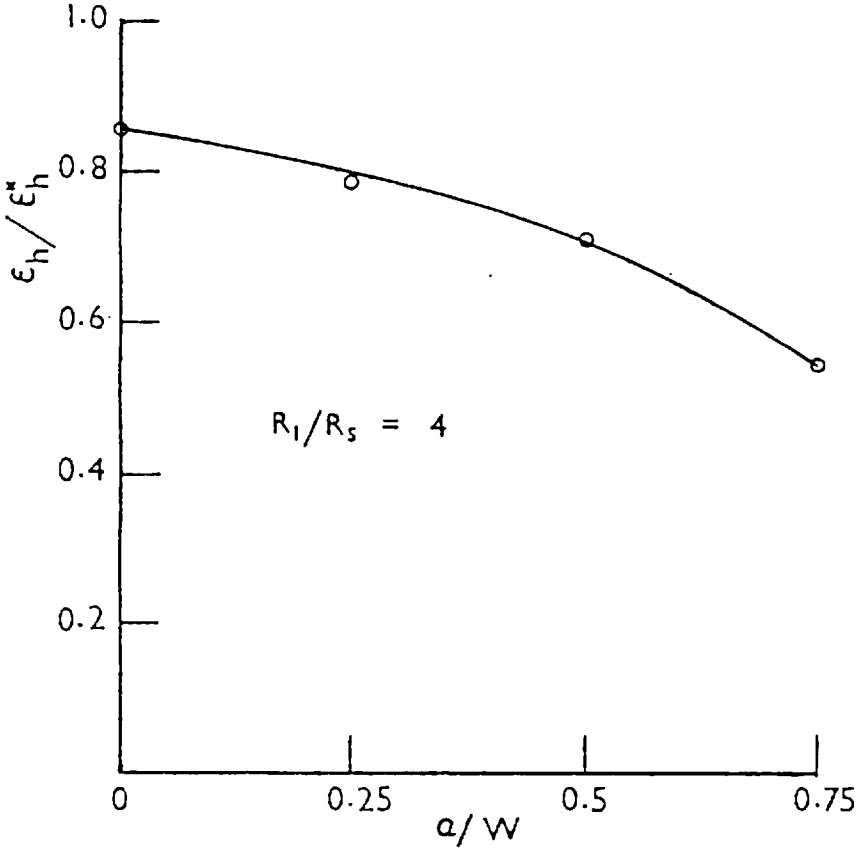



Figure 7.18: Variation of hoop strain with crack size at $Z/H$ = 0, $\theta$ = 180°

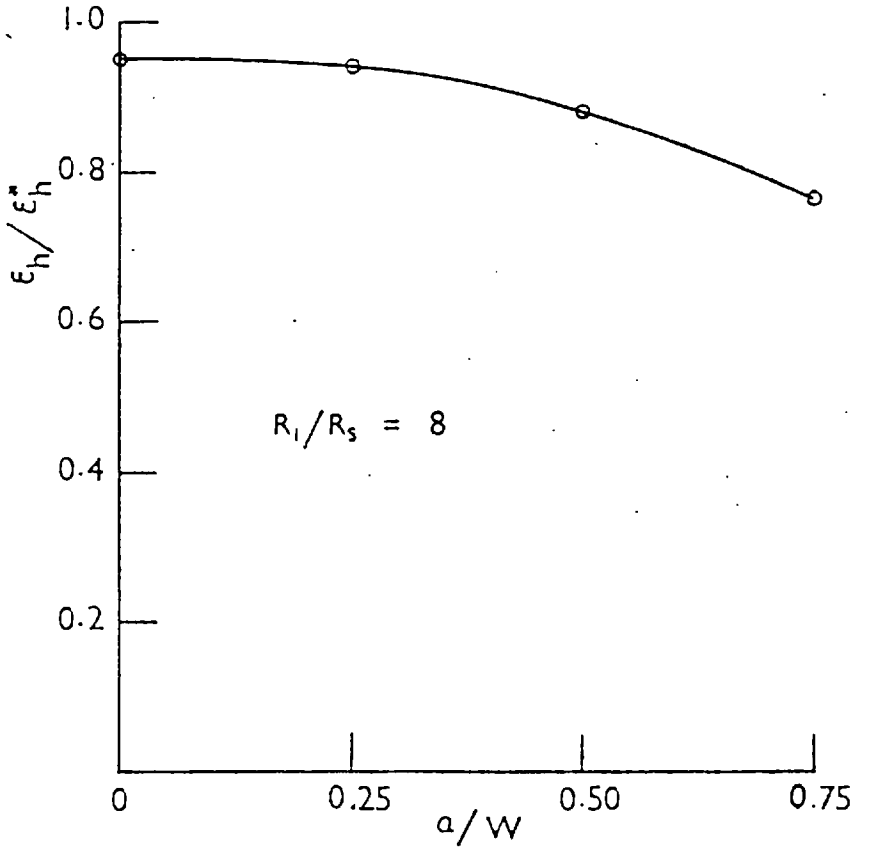



Figure 7.17: Variation of hoop strain with crack size at $Z/H$ = 0, $\theta$ = 180°

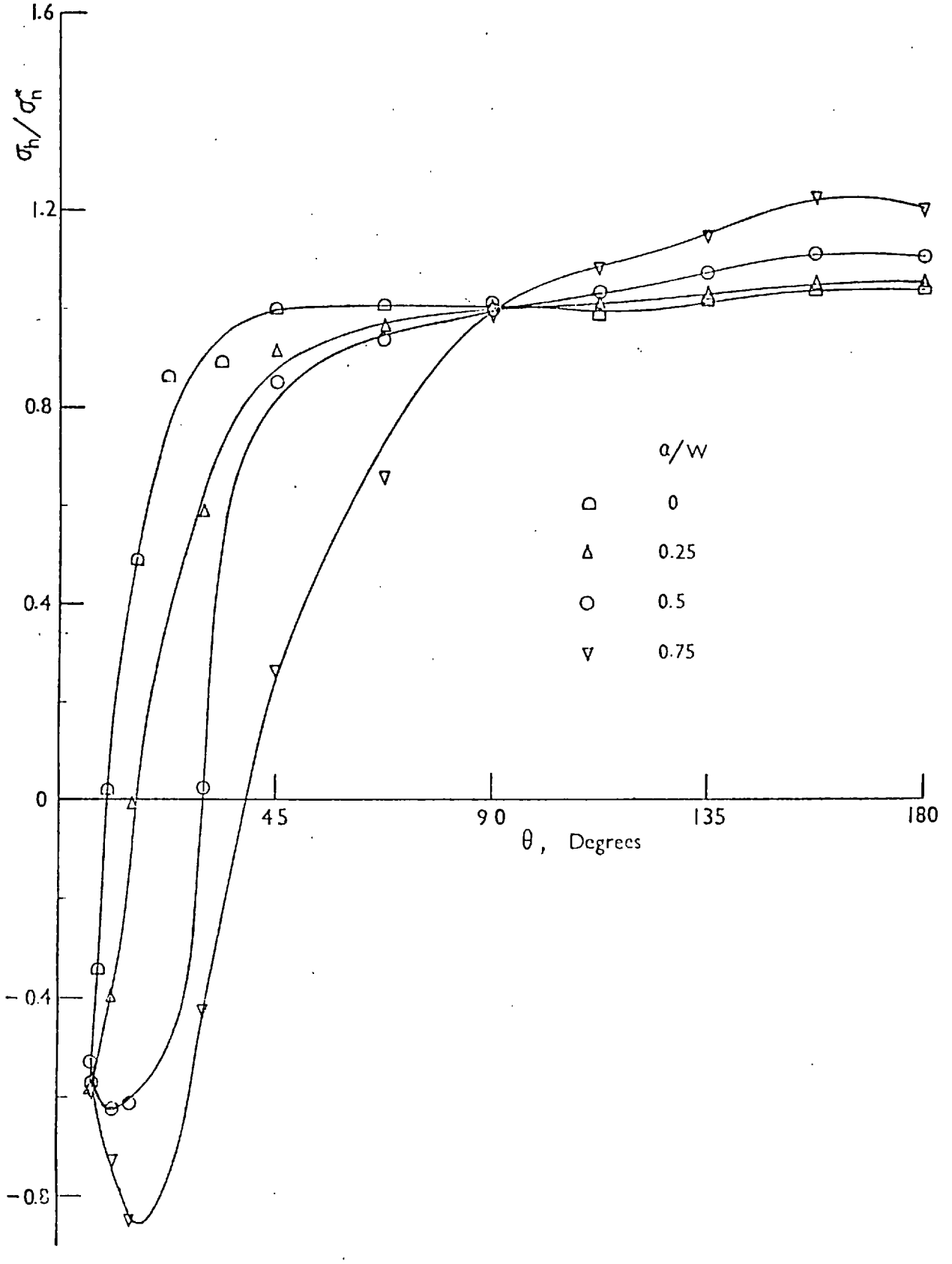



Figure 7.19: Variation of hoop stress along the inner circumference of cylinder at $Z/H$ = 0 axial plane, $R_1/R_s$ = 8

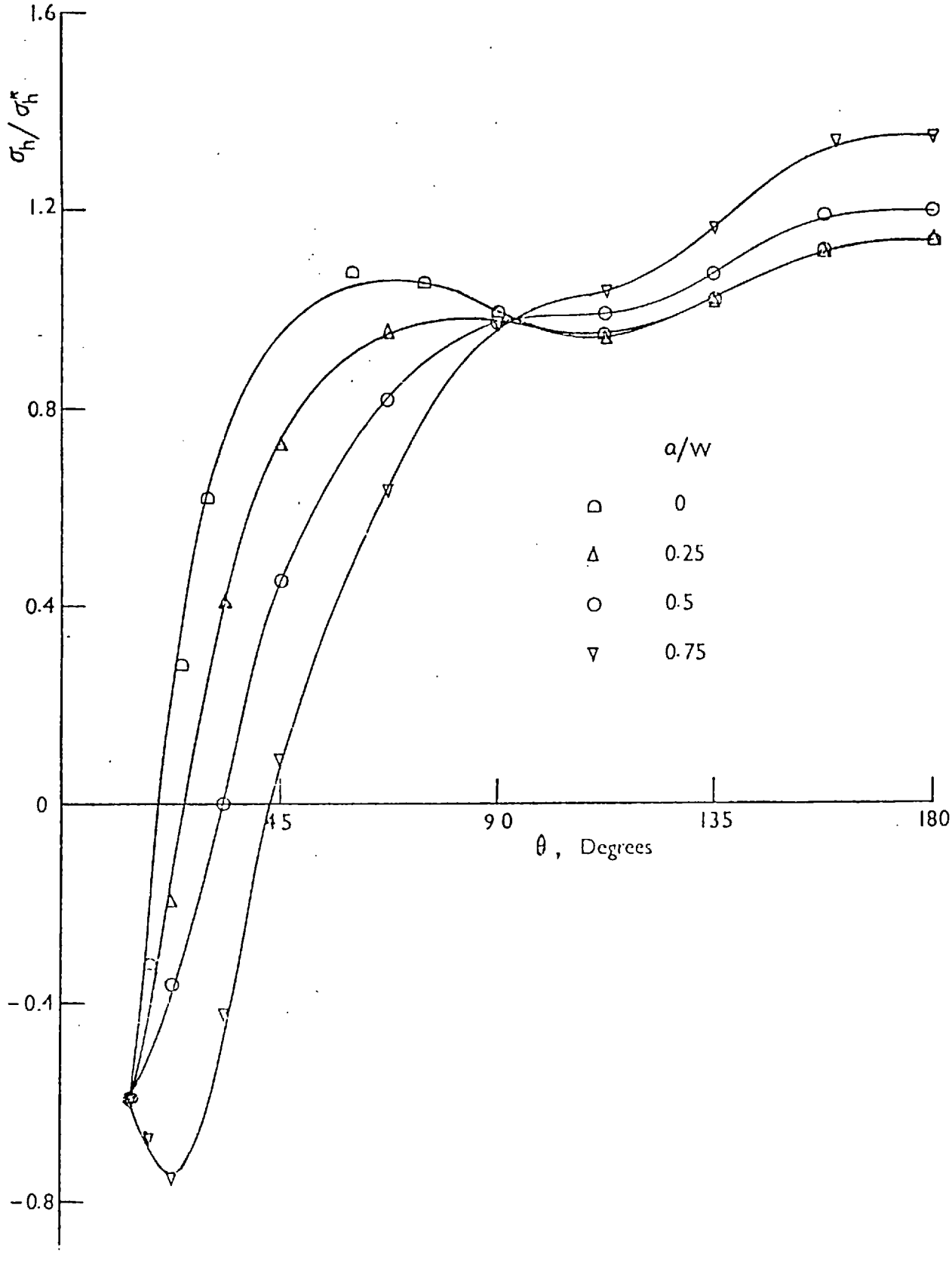



Figure 7.20: Variation of hoop stress along the inner circumference of cylinder at $Z/H$ = 0 axial plane, $R_1/R_s$ = 4

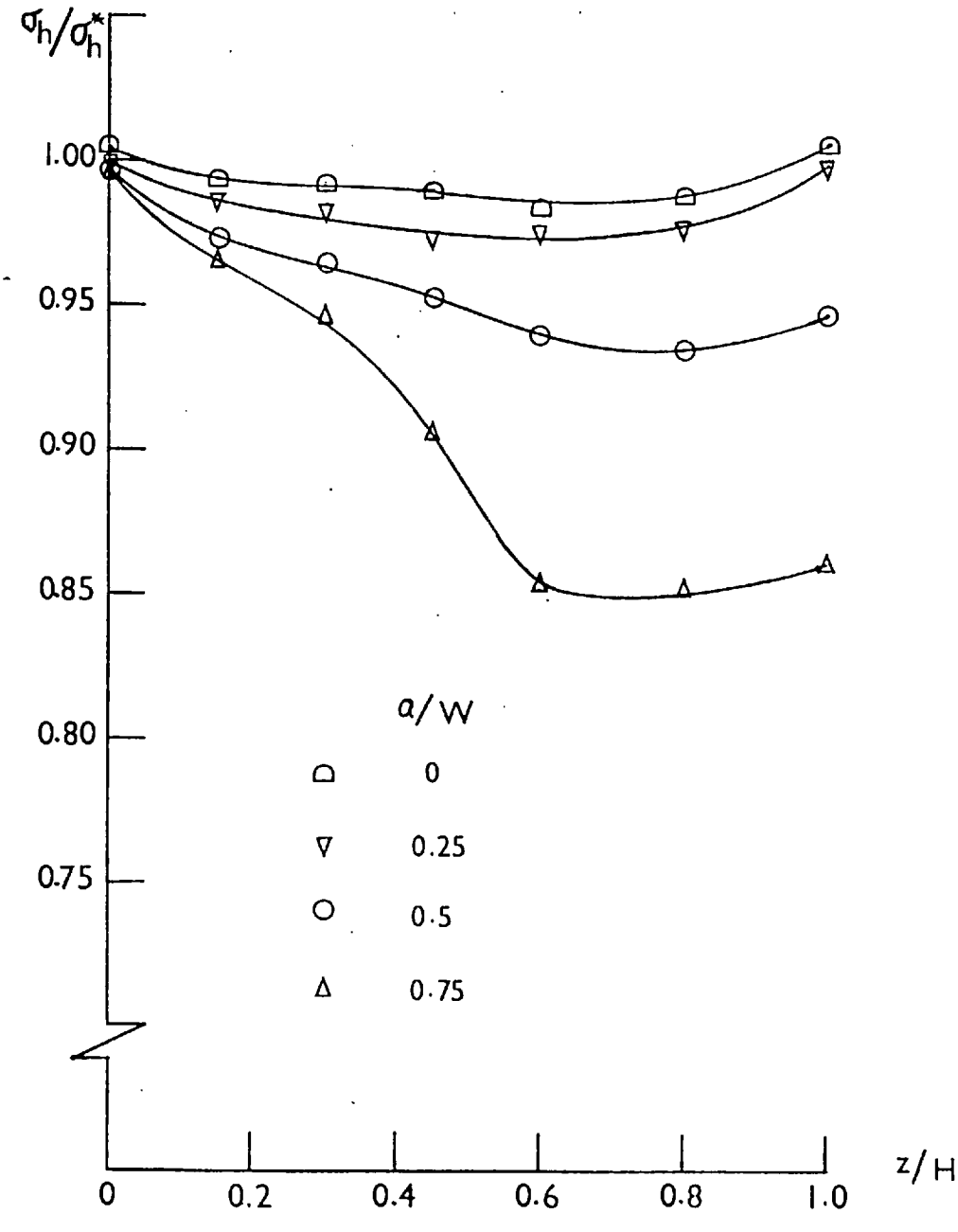



Figure 7.21: Variation of hoop stress along the internal surface of cylinder at $\theta = 90°$ radial plane, $R_1/R_s = 8$

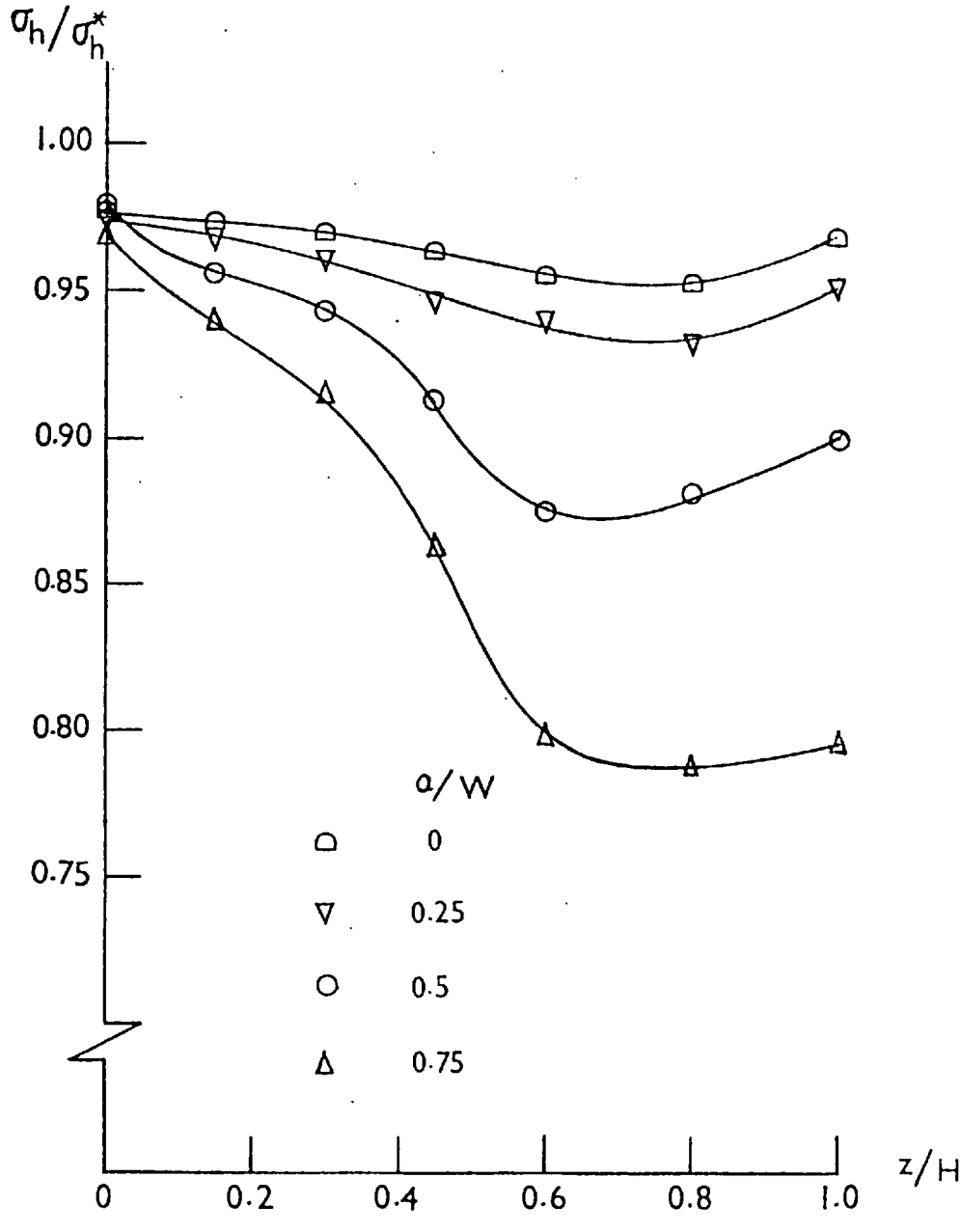



Figure 7.22: Variation of hoop stress along the internal surface of cylinder at $\theta$ = 90° radial plane, $R_1/R_s$ = 4

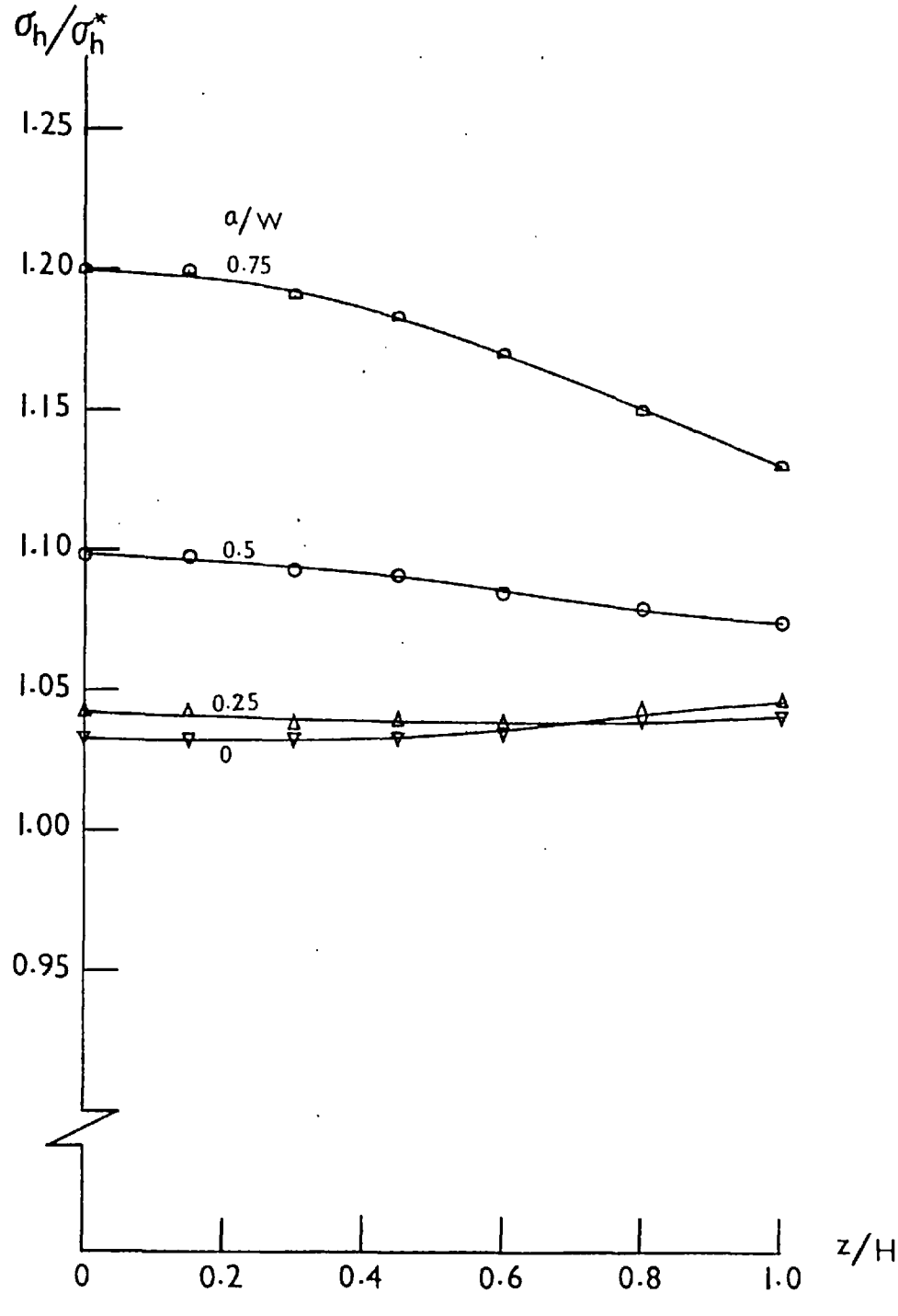



Figure 7.23: Variation of hoop stress along the internal surface of cylinder at $\theta = 180°$ radial plane, $R_1/R_s = 8$

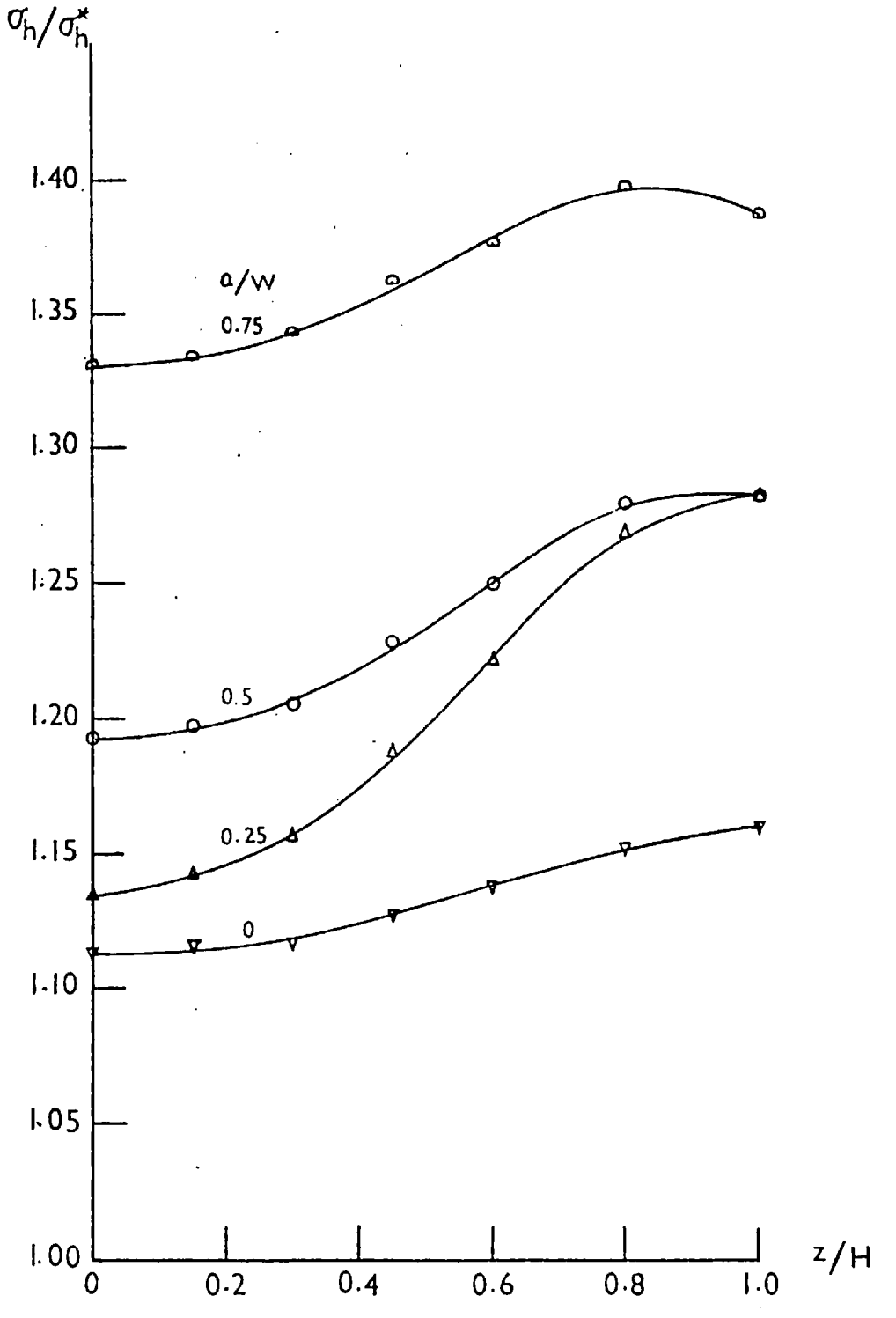



Figure 7.24: Variation of hoop stress along the internal surface of cylinder at $\theta$ = 180° radial plane, $R_1/R_s$ = 4

# CHAPTER 8

# CONCLUSIONS

The basic principles of the theory of linear elastic fracture mechanics have been presented, with the limitations also discussed. Design methods using the concepts of this discipline allow the continued use of a cracked component, provided the crack has not grown to the critical size to cause fracture. This has no counterparts in traditional design procedures.

The most useful parameter for characterizing cracks under linear elastic conditions is the stress intensity factor which describes the $r^{-\frac{1}{2}}$ singularity of stress (strain) near the crack tip or front. For loading normal to the plane of the crack (Mode I), fracture occurs when the stress intensity factor, $K_I$, at the crack front becomes equal in value to the fracture toughness of the material, $K_{Ic}$, which is a material property. Elastic fracture mechanics analysis is thus concerned with modelling the cracked component to determine the value of the crack front stress intensity factors which could then be used to predict the residual static strength for brittle fracture or the fatigue life of the component.

For most practical three-dimensional problems, numerical methods using high speed digital computers have to be employed to obtain the stress intensity factor solutions. To this end, the boundary integral equation method has been shown to be a powerful tool for stress analysis, through the numerical solution of a set of constraint equations relating boundary tractions and boundary displacements. No approximation is imposed on the solution at the interior points of the elastic body. As a result, computer storage requirements, program execution times and the amount of data preparation required are all reduced relative to other numerical

methods, while solution accuracy can be increased.

The mathematical basis of the boundary integral equatiom method has been presented and the numerical implementation of the technique for three-dimensional elastostatics was described. The latter involves using isoparametric surface elements where both functions and geometry are defined by quadratic shape functions. A computer program based on this numerical formulation, BIESIF, was developed for use in this study. A plotting program, DRAW, was also developed, using off-line graphic facilities at ICCC, whereby the various mesh discretization data could be visually checked in terms of the element topology and nodal coordinates before they are used with BIESIF. Using DRAW, an isometric view of the mesh, from any direction specified, could be generated.

For the crack problems investigated, attention was confined to the opening mode of fracture and various methods of obtaining stress intensity factors by the BIE method were discussed. A comparative study of the accuracy and cost of these approaches was carried out on a number of three-dimensional test problems. Of the schemes, the direct displacement method which utilizes the crack face displacement data offers a quick, easy and accurate means of obtaining $K_I$ at the crack front. But if stress intensity factors are required from a large number of computer runs of the same problem with different crack sizes, as in fatigue analysis, the indirect energy method could be relatively cheaper. Also, the use of singularity elements around the crack front, in which mid-side nodes nearest the front are shifted to quarter-point positions, was found to significantly enhance the accuracy of the $K_I$ solution obtained, hence they were employed throughout the course of this study for crack problems.

Doubts were expressed over the meaning of numerical values of $K_I$ obtained for the points where the front of a crack intersects a free

surface and previous investigations on this issue were reviewed. At these points, the stress (strain) singularity may no longer be of the inverse square root form, but the strength of this singularity, as far as is known, had not been elucidated by direct numerical means previously. An attempt to do this by the BIE method was presented for two problems with different crack front geometries. It was found that the stress (strain) singularity at the intersection was generally one of a lower order than $\frac{1}{2}$, and it varied with the value of Poisson's ratio. Comparison of the BIE results with those obtained semi-analytically by the eigenfunction-expansion method which are available in the literature, showed some differences between the two sets of results, although the trends were similar with the latter solutions predicting a greater reduction in the order of singularity with increasing values of $\nu$.

The BIE method of numerical stress analysis was successfully applied to the problem of an internally pressurized thick-walled cylinder with a semi-elliptical surface crack. Two different cylinder radius ratios and a wide range of different relative crack depths were considered. Stress intensity factor solutions were obtained and presented, as were other results of the stress analysis. Predicted hoop strains at the outer surface of the cylinder at various crack depths were compared with experimentally measured values and there was reasonably good agreement. Further suggestions were made whereby the computed results could be used to monitor the growth of the crack in the cylinder. The fracture mechanics analysis of the problem also included the numerical fatigue crack growth prediction of the semi-elliptical surface crack. The technique was based on the strain energy release rate approach for calculating the stress intensity factor, and, in principle, can be applied to cracks of arbitrary shapes in general three-dimensional components or

structures. Comparison of the predicted crack growth rate and propagating crack shape with those obtained experimentally again showed very encouraging agreement with each other.

The BIE method was also applied to the problem of an internally pressurized thick-walled cylinder with a radial cross-bore. Two different cross-bore to cylinder-bore diameter ratios were considered. For the uncracked component, the hoop stresses, as expected, were found to be greatest in magnitude at the intersection of the bores but the computed stress concentration factors were significantly lower than those approximate analytical solutions available in the literature. For the cases where cracks were present at the cross-bore, elastic fracture mechanics analyses were also successfully carried out.

The results presented for these two latter practical problems concerning thick-walled cylinders should be of considerable practical importance, particularly in high pressure technology. It is not very surprising that few direct three-dimensional solutions for these problems have been obtained previously in view of the numerical problem size involved. But no difficulty was encountered as far as computer central memory requirements were concerned, when solving them by the BIE method.

As a matter of interest, for all the problems analysed in the course of this study, the computer core memory required by BIESIF was less than 48000 words. This figure was chosen for convenience of usage in the computing system available at Imperial College, but it could be reduced further, say, to 35000 words, if desired, without much difficulty. The computing cost of running BIESIF was found to be approximately proportional to the square of the number of surface elements used. To give an idea of the absolute cost with a fourth-order Gaussian quadrature rule for integration over the elements, BIESIF used about 52 composite units on the

CDC 6600 computer to obtain the solutions for a cracked-cylinder problem in Chapter 6 which was modelled by 82 surface elements and 248 nodal points. Commercially, the rate per composite unit in 1979 is about £8 in monetary terms. Despite the fact that the charging formula for the composite unit at ICCC does take into account the different performance of the various computers in use, it was found that variations of between 20% to 40% in the units charged for problems of the same numerical size could occur depending on which machine was used.

Although many of the numerical modelling concepts are similar to those involved with the finite element method, it is worth noting that the boundary element mesh used for the BIE analysis is not simply a finite element mesh with the internal nodes removed. Such a mesh would be inefficient because a BIE mesh can be much coarser than a finite element one in regions of the boundary where the dependent variables of the problem do not vary rapidly. It is also worth noting that in all the problems treated in this study, stresses or displacements at points within the body were not required from the analysis. It is for such problems, which are very common in practice, that the BIE method, in the current form, is best suited. When predictions for many interior points are required, the computing time advantage over, say, the finite element method, is not so clear. Also, the problems considered in this study have moderate surface area-to-volume ratios. It is probable that for problems involving relatively thin structural components, particularly in the absence of localized regions of rapid stress variations, this form of the BIE approach will be less advantageous.

## APPENDIX A

## DERIVATION OF $U_{ij}(p,q)$ AND $T_{ij}(p,q)$

The steps for obtaining the tensors $U_{ij}(p,q)$ and $T_{ij}(p,q)$ have been outlined in the main text (Chapter 3). What is being presented here are the detailed algebraic manipulations from the governing equations and relevant identities to the final forms of the tensors that were shown.

(i) $U_{ij}(p,q)$

Recall that the governing equations of elasticity (3.5) are satisfied when:

$$2\,\mu\,u_i = 2\,(1-\nu)\,G_{i,jj} - G_{j,ji} \tag{A.1}$$

and:
$$G_i = \frac{1}{8\,\pi\,(1-\nu)}\,r(p,q)\,e_i \tag{A.2}$$

where:
$$r(p,q) = [(\bar{x}_i - \zeta_i)(\bar{x}_i - \zeta_i)]^{\frac{1}{2}} \tag{A.3}$$

Also:
$$r_{,i} = \frac{\partial r}{\partial \bar{x}_i} = -\frac{\partial r}{\partial \zeta_i} = \frac{1}{r}\,(\bar{x}_i - \zeta_i) \tag{A.4}$$

Thus:
$$G_{i,j} = \frac{1}{8\,\pi\,(1-\nu)}\left[\frac{\partial r}{\partial \bar{x}_i}\right] e_i$$

i.e.
$$G_{i,j} = \frac{1}{8\,\pi\,(1-\nu)}\left[\frac{1}{r}\,(\bar{x}_j - \zeta_j)\,\delta_{ij}\right] e_j \tag{A.5}$$

$$G_{j,j} = \frac{1}{8\,\pi\,(1-\nu)}\left[\frac{1}{r}\,(\bar{x}_j - \zeta_j)\right] e_j \tag{A.6}$$

$$G_{j,ji} = \frac{1}{8\,\pi\,(1-\nu)}\left[\frac{1}{r}\,\delta_{ij} + (\bar{x}_j - \zeta_j)\left(-\frac{1}{r^2}\right)(r_{,i})\right] e_j \tag{A.7a}$$

i.e.
$$G_{j,ji} = \frac{1}{8\,\pi\,(1-\nu)}\left[\frac{1}{r}\,\delta_{ij} - \frac{1}{r}\,r_{,i}\,r_{,j}\right] e_j \tag{A.7b}$$

$$G_{i,jj} = \frac{1}{8\pi(1-\nu)}\left[\frac{3}{r}\delta_{ij} + \left(-\frac{1}{r^2}\right)\delta_{ij}\left(\frac{r^2}{r}\right)\right] e_j$$

i.e. $$G_{i,jj} = \frac{1}{8\pi(1-\nu)}\left(\frac{2}{r}\delta_{ij}\right) e_j \qquad (A.8)$$

Putting (A.7) and (A.8) into (A.1):

$$2\mu u_i = \frac{1}{8\pi(1-\nu)}\left(\frac{1}{r}\right)\{4(1-\nu)\delta_{ij} - \delta_{ij} + r_{,i}\, r_{,j}\} e_j$$

i.e. $$2\mu u_i = \frac{1}{8\pi(1-\nu)}\left(\frac{1}{r}\right)\{(3-4\nu)\delta_{ij} + r_{,i}\, r_{,j}\} e_j \qquad (A.9)$$

Since: $$u_i = U_{ij} e_j \qquad (A.10)$$

therefore:

$$U_{ij} = \frac{1}{16\pi\mu(1-\nu)}\left(\frac{1}{r}\right)\{(3-4\nu)\delta_{ij} + r_{,i}\, r_{,j}\} \qquad (A.11)$$

(ii) $\underline{T_{ij}(p,q)}$

The tractions at point $p(x)$ can be obtained by differentiation at $p(x)$ of the displacement solution using (3.8), i.e.

$$t_i(p,q) = \left[\frac{2\mu\nu}{1-2\nu} u_{k,k}\,\delta_{ij} + \mu(u_{i,j} + u_{j,i})\right] n_j \qquad (A.12)$$

Since: $u_i = U_{ij} e_j$ and $t_i = T_{ij} e_j$ (A.13)

therefore:

$$T_{ij}(p,q) = \frac{2\mu\nu}{1-2\nu} U_{kj,k}\, n_i + \mu\,(U_{ij,k} + U_{kj,i})\, n_k \qquad (A.14)$$

From (A.11):

$$U_{ij,k} = \frac{1}{16\pi\mu(1-\nu)} \left\{ \frac{1}{r} (r_{,i}\, r_{,j})_{,k} + \left(-\frac{1}{r^2}\right)(r_{,k}) \left[(3-4\nu)\,\delta_{ij} + r_{,i}\, r_{,j}\right] \right\} \qquad (A.15)$$

But:

$$(r_{,i}\, r_{,j})_{,k} = -\frac{2}{r} r_{,i}\, r_{,j}\, r_{,k} + \frac{1}{r}\left(\delta_{ik}\, r_{,j} + \delta_{jk}\, r_{,i}\right) \qquad (A.16)$$

Therefore:

$$U_{ij,k} = -\frac{1}{16\pi\mu(1-\nu)} \left(\frac{1}{r^2}\right) \left\{ (3-4\nu)\,\delta_{ij}\, r_{,k} - \delta_{jk}\, r_{,i} - \delta_{ik}\, r_{,j} + 3\, r_{,i}\, r_{,j}\, r_{,k} \right\} \qquad (A.17)$$

and:
$$U_{kj,k} = -\frac{(1-2\nu)}{8\pi(1-\nu)\mu} \left(\frac{1}{r^2}\right)(r_{,j}) \qquad (A.18)$$

Thus:

$$\frac{2\mu\nu}{(1-2\nu)} U_{kj,k}\, n_i = -\frac{2\mu\nu}{(1-2\nu)} \frac{(1-2\nu)}{8\pi\mu(1-\nu)} \left(\frac{1}{r^2}\right) n_i\, r_{,j}$$

i.e.
$$\frac{2\mu\nu}{1-2\nu} U_{kj,k}\, n_i = -\frac{2}{8\pi(1-\nu)} \left(\frac{1}{r^2}\right) n_i\, r_{,j} \qquad (A.19)$$

$$\mu\,(U_{ij,k})\, n_k = -\frac{1}{16\pi(1-\nu)} \left(\frac{1}{r^2}\right) \left\{ 2\, r_{,i}\, r_{,j} \frac{\partial r}{\partial n} - n_i\, r_{,j} - n_j\, r_{,i} + (3-4\nu)\,\delta_{ij} \frac{\partial r}{\partial n} + r_{,i}\, r_{,j} \frac{\partial r}{\partial n} \right\}$$

i.e.

$$\mu\,(U_{ij,k})\,n_k = -\frac{1}{16\,\pi\,(1-\nu)}\,(\frac{1}{r^2})\,\{\frac{\partial r}{\partial n}\,[(3-4\nu)\,\delta_{ij} + 3\,r_{,i}\,r_{,j}] - n_i\,r_{,j} - n_j\,r_{,i}\} \tag{A.20}$$

In (A.20): $$\frac{\partial r}{\partial n} = \frac{\partial r}{\partial \bar{x}_i}\,n_i = \frac{1}{r}\,(\bar{x}_i - \zeta_i)\,n_i \tag{A.21}$$

Also:

$$\mu\,(U_{kj,i})\,n_k = -\frac{1}{16\,\pi\,(1-\nu)}\,(\frac{1}{r^2})\,\{(3-4\nu)\,n_j\,r_{,i} - \delta_{ij}\,\frac{\partial r}{\partial n} - n_i\,r_{,j} + 3\,r_{,i}\,r_{,j}\,\frac{\partial r}{\partial n}\}$$

i.e.

$$\mu\,(U_{kj,i})\,n_k = -\frac{1}{16\,\pi\,(1-\nu)}\,(\frac{1}{r^2})\,\{\frac{\partial r}{\partial n}\,[3\,r_{,i}\,r_{,j} - \delta_{ij}] + (3-4\nu)\,n_j\,r_{,i} - n_i\,r_{,j}\} \tag{A.22}$$

Adding (A.19), (A.20) and (A.22) as in (A.14):

$$T_{ij}(p,q) = -\frac{1}{8\,\pi\,(1-\nu)}\,(\frac{1}{r^2})\,\{\frac{\partial r}{\partial n}\,[(1-2\nu)\,\delta_{ij} + 3\,r_{,i}\,r_{,j}] - (1-2\nu)(n_j\,r_{,i} - n_i\,r_{,j})\} \tag{A.23}$$

# APPENDIX B

## THE VALUE OF $C_{ij}(P)$ WHEN THE TANGENT PLANE AT $P(\underset{\sim}{x})$ IS SMOOTH

Consider the case where $P(\underset{\sim}{x})$ lies on a smooth surface of $R$ and take $R_\varepsilon$ as the part of $R$ with surface $S_\varepsilon$ contained within a sphere with centre at $P(\underset{\sim}{x})$ and radius $\varepsilon$ (see Figure 3.4). Recall the identity (3.56):

$$C_{ij}(P) = \lim_{\varepsilon \to 0} \int_{S'_\varepsilon - S_\varepsilon} T_{ij}(P,Q)\, dS(Q) \qquad \text{(B.1)}$$

For convenience, a spherical system of coordinates as defined in Figure B.1 is used.

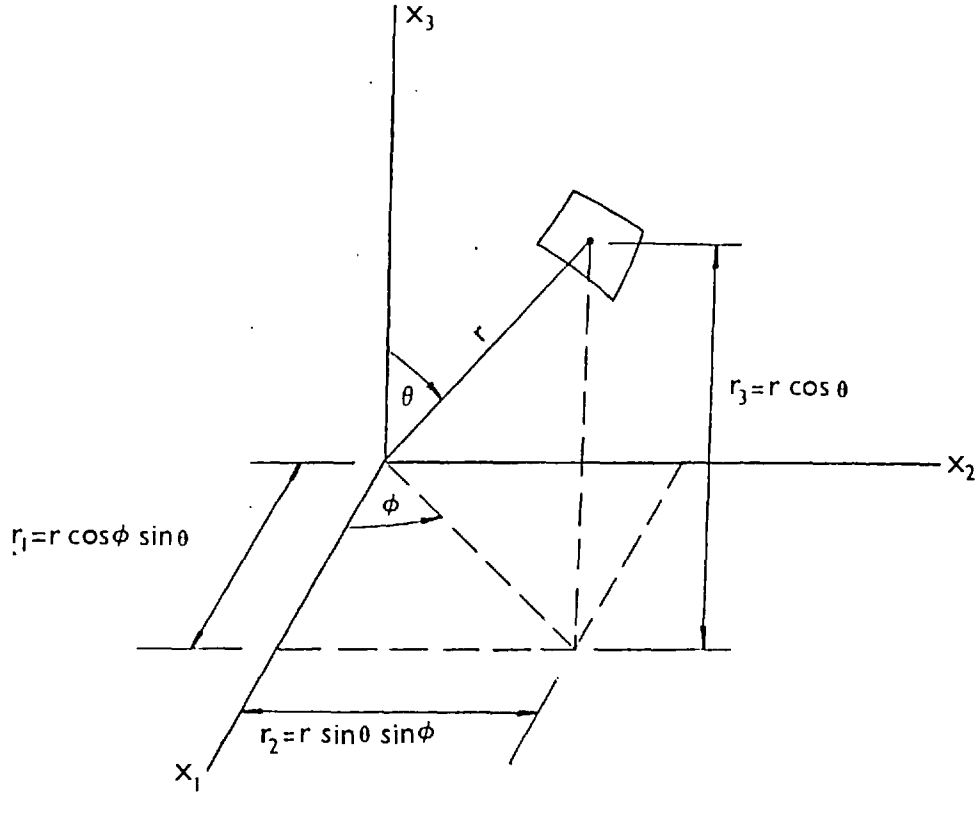



Figure B.1: Spherical coordinate system

Now:

$$dS = r^2 \sin\theta \, d\theta \, d\phi \tag{B.2}$$

and:

$$\frac{\partial r}{\partial n} = -1 \tag{B.3}$$

since the outward normal is towards $P(x)$ on the surface $S_\varepsilon'$ and $S_\varepsilon$ (in the limit as $\varepsilon \to 0$).

Further:

$$n_i = \frac{\partial r}{\partial x_i} = \frac{r_i}{r} \tag{B.4}$$

As an example, let $i = j = 1$. Thus:

$$C_{11}(P) = \lim_{\varepsilon \to 0} \int_{S_\varepsilon' - S_\varepsilon} -\frac{1}{8\pi(1-\nu)} \left(\frac{1}{r^2}\right) \left\{\frac{\partial r}{\partial n}\left[(1-2\nu) + 3\left(\frac{\partial r}{\partial x_1}\right)^2\right]\right\} dS \tag{B.5a}$$

$$= \int_0^{2\pi} \int_0^{\pi/2} \left[(1-2\nu) + 3\sin^2\theta\cos^2\phi\right] \frac{\sin\theta \, d\theta \, d\phi}{8\pi(1-\nu)} \tag{B.5b}$$

$$= \frac{1}{8\pi(1-\nu)} \left[(1-2\nu)\,2\pi + 2\pi\right] = \tfrac{1}{2}$$

Similarly, it can be shown that $C_{22}(P) = C_{33}(P) = \frac{1}{2}$.

Consider now the case when $i \neq j$. In the limit as $\varepsilon \to 0$:

$$C_{12}(P) = \int_0^{2\pi} \int_0^{\pi/2} \left[3\sin^2\theta\cos\phi\sin\phi\right] \frac{\sin\theta \, d\theta \, d\phi}{8\pi(1-\nu)}$$

$$= \int_0^{2\pi} \frac{1}{8\pi(1-\nu)} \left[2\cos\phi\sin\phi\right] d\phi = 0 \tag{B.6}$$

$$C_{13}(P) = \int_0^{2\pi} \int_0^{\pi/2} \left[3\sin\theta\cos\theta\cos\phi\right] \frac{\sin\theta \, d\theta \, d\phi}{8\pi(1-\nu)}$$

$$= 0 \tag{B.7}$$

$$C_{23}(P) = \int_0^{2\pi} \int_0^{\pi/2} [3 \sin\theta \sin\phi \cos\theta] \frac{\sin\theta \, d\theta \, d\phi}{8\pi(1-\nu)}$$

$$= 0 \tag{B.8}$$

Since $T_{ij}(P,Q) = T_{ji}(P,Q)$, when $i \neq j$, $C_{ij}(P) = 0$. Thus, the complete set of results for the case when the normal direction at $P(x)$ is continuous may be summarized:

$$C_{ij}(P) = \tfrac{1}{2} \delta_{ij} \tag{B.9}$$

## APPENDIX C

## TANGENTIAL STRAINS AT THE SURFACE IN THE LOCAL ORTHOGONAL COORDINATE SYSTEM OF ELEMENTS

Referring to Figure 4.7, the local orthogonal coordinates in the surface tangential directions, $\mu_{1j}$ and $\mu_{2j}$, are related to the intrinsic coordinates, $\xi_1$ and $\xi_2$, as follows:

$$\mu_{1j} = m_{1j} = |s_{i2}|\ \xi_2 \cos\theta + |s_{i1}|\ \xi_1 \tag{C.1}$$

$$\mu_{2j} = m_{2j} \sin\theta = |s_{i2}|\ \xi_2 \sin\theta \tag{C.2}$$

Therefore:
$$\mu_{1j} = \{\mu_{2j} \frac{\cos\theta}{\sin\theta}\} + |s_{i1}|\ \xi_1 \tag{C.3}$$

thus:
$$\xi_1 = \frac{1}{|s_{i1}|} \{\mu_{1j} - \frac{\cos\theta}{\sin\theta} \mu_{2j}\} \tag{C.4}$$

$$\xi_2 = \frac{1}{|s_{i2}|} \frac{1}{\sin\theta} \mu_{2j} \tag{C.5}$$

Differentiating $\xi_1$ and $\xi_2$ with respect to $\mu_{1j}$ and $\mu_{2j}$:

$$\frac{\partial \xi_1}{\partial \mu_{1j}} = \frac{1}{|s_{i1}|} \quad ; \quad \frac{\partial \xi_2}{\partial \mu_{1j}} = 0 \tag{C.6}$$

$$\frac{\partial \xi_1}{\partial \mu_{2j}} = -\frac{1}{|s_{i1}|} \frac{\cos\theta}{\sin\theta} \quad ; \quad \frac{\partial \xi_2}{\partial \mu_{2j}} = \frac{1}{|s_{i2}|} \frac{1}{\sin\theta} \tag{C.7}$$

The displacements in the orthogonal tangential directions are given by (4.19):

$$\bar{u}_\alpha(\xi) = N^c(\xi)\ u_j^c\ \mu_{\alpha j} \tag{C.8}$$

Therefore:

$$\frac{\partial \bar{u}_\alpha}{\partial \mu_{1j}} = \frac{\partial \bar{u}_\alpha(\xi)}{\partial \xi_1}\frac{\partial \xi_1}{\partial \mu_{1j}} + \frac{\partial \bar{u}_\alpha(\xi)}{\partial \xi_2}\frac{\partial \xi_2}{\partial \mu_{1j}} \quad , \quad \alpha = 1,2$$

$$= \frac{\partial N^c(\xi)}{\partial \xi_1}\frac{u_j^c \mu_{\alpha j}}{|s_{\alpha 1}|} + 0 \tag{C.8a}$$

i.e. $$\frac{\partial \bar{u}_\alpha}{\partial \mu_{1j}} = \frac{\partial N^c(\xi)}{\partial \xi_1} u_j^c \frac{\mu_{\alpha j}}{|s_{\alpha 1}|} \tag{C8.b}$$

Similarly: $$\frac{\partial \bar{u}_\alpha}{\partial \mu_{2j}} = \frac{\partial \bar{u}_\alpha(\xi)}{\partial \xi_1}\frac{\partial \xi_1}{\partial \mu_{2j}} + \frac{\partial \bar{u}_\alpha(\xi)}{\partial \xi_2}\frac{\partial \xi_2}{\partial \mu_{2j}} \tag{C.9a}$$

i.e.

$$\frac{\partial \bar{u}_\alpha}{\partial \mu_{2j}} = -\frac{\partial N^c(\xi)}{\partial \xi_1} u_j^c \frac{\mu_{\alpha j}\cos\theta}{|s_{\alpha 1}|\sin\theta} + \frac{\partial N^c(\xi)}{\partial \xi_2} u_j^c \frac{\mu_{\alpha j}}{|s_{\alpha 2}|\sin\theta} \tag{C.9b}$$

From (C.8) and (C.9), the tangential strains in the local coordinate system defined in Figure 4.7 are thus:

$$\bar{e}_{11} = \frac{\partial \bar{u}_1}{\partial \mu_{1j}} \tag{C.10a}$$

$$\bar{e}_{22} = \frac{\partial \bar{u}_2}{\partial \mu_{2j}} \tag{C.10b}$$

$$\bar{e}_{21} = \bar{e}_{12} = \left(\frac{\partial \bar{u}_1}{\partial \mu_{2j}} + \frac{\partial \bar{u}_2}{\partial \mu_{1j}}\right) \tag{C.10c}$$

## APPENDIX D

## APPROXIMATE SOLUTION FOR THE STRESS CONCENTRATION FACTOR FOR A PRESSURIZED CYLINDER WITH A SMALL CIRCULAR CROSS-BORE (MORRISON ET AL (1959))

The main assumption made in the following analysis is that the radius of the cross-bore, $R_s$, is small compared with the bore radius of the cylinder, $R_1$. Figure D.1 shows the cross-sectional plane of the cylinder normal to the axis of the cross-bore and Figure D.2 shows the enlarged view of the region around the hole.

For a plain circular cylinder, the maximum stress is the hoop stress at its inner surface. In the presence of the hole, the maximum stress must therefore be at points A, the ends of the diameter of the cross-bore parallel to the axis of the cylinder at the inner surface of the cylinder.

The stresses at A can be obtained from two considerations as follows:

(1) The small cross-bore can be regarded as the bore of a cylinder with very large radius ratio, $R_e/R_s$, where $R_e$ is the "equivalent" external radius of this equivalent cylinder itself subjected to the internal pressure, $P$. The nominal stresses at A in the cylindrical coordinates centred on the axis of the hole are then:

Hoop stress , $\sigma'_h = P\dfrac{(R_e/R_s)^2 + 1}{(R_e/R_s)^2 - 1} \simeq P$ , (which, relative to the main cylinder, is also a hoop stress)

Radial stress , $\sigma'_r = -P$ , (which, relative to the main cylinder, is an axial stress)

Axial stress , $\sigma'_z = 0$ , since the hole is "open-ended" , (which, relative to the main cylinder, is in the radial direction)

(2) Now consider the stresses in the cylindrical coordinate system centred on the axis of the main cylinder. If the hole is absent, the stresses at A would be:

Hoop stress , $\sigma_h^* = P \dfrac{(R_2/R_1)^2 + 1}{(R_2/R_1)^2 - 1}$

Radial stress , $\sigma_r^* = - P$

Axial stress , $\sigma_z^* = \dfrac{P}{(R_2/R_1)^2 - 1}$

The presence of the hole does not change the value of $\sigma_r^*$. Since the hole is relatively small, it can be regarded as existing in the two-dimensional stress field $\sigma_h^*$, $\sigma_z^*$, and the well-known stress concentration factors at a hole in a "plate" subjected to uniaxial tension can be applied. The hoop stress component at A due to $\sigma_h^*$ would be $3\,\sigma_h^*$ and that due to $\sigma_z^*$ would be $-\sigma_z^*$.

The stresses at A from consideration (1) and (2) may now be added together:

| | | Consideration (1) | | Consideration (2) | | Total |
|---|---|---|---|---|---|---|
| Hoop stress at A : | $\sigma_h$ = | $\sigma_h'$ | + | $3\,\sigma_h^* - \sigma_z^*$ | = | $\dfrac{4(R_2/R_1)^2 + 1}{(R_2/R_1)^2 - 1} P$ |
| Radial stress at A: | $\sigma_r$ = | $\sigma_z'$ | + | $\sigma_r^*$ | = | $- P$ |
| Axial stress at A : | $\sigma_z$ = | $\sigma_r'$ | + | $0$ | = | $- P$ |

The last two of these results are exact since the surfaces are subjected to

a pressure $P$. The approximate hoop stress concentration factor at A is thus:

$$k_h = \frac{4\,(R_2/R_1)^2 + 1}{(R_2/R_1)^2 - 1} P \div \frac{(R_2/R_1)^2 + 1}{(R_2/R_1)^2 - 1} P$$

i.e.

$$k_h = \frac{4\,(R_2/R_1)^2 + 1}{(R_2/R_1)^2 + 1}$$

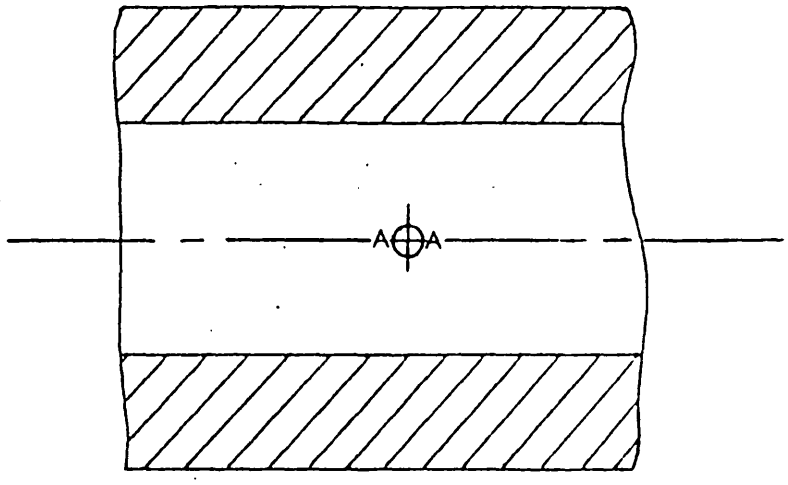



Figure D.1: Cross-section of thick-walled cylinder with cross-bore

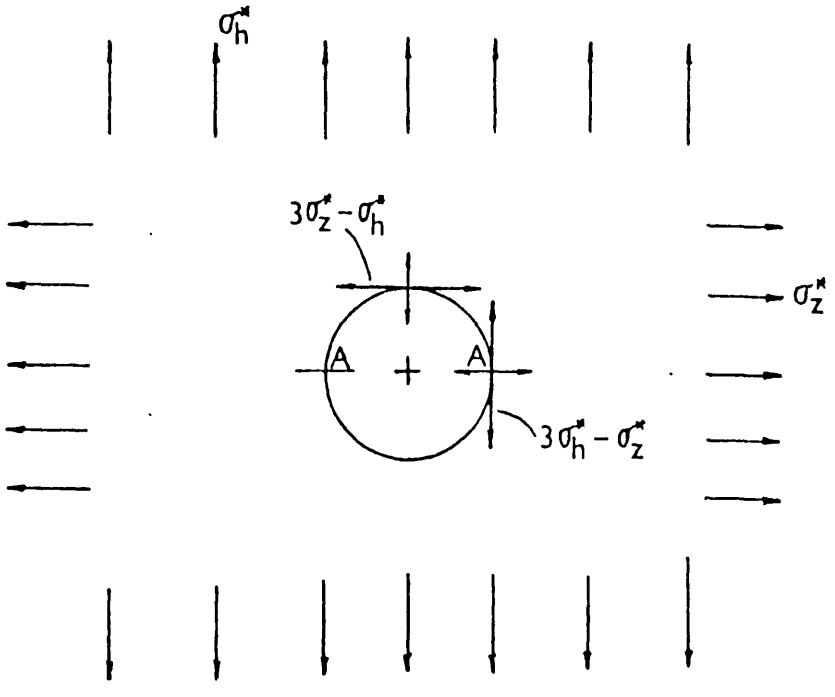



Figure D.2: Enlarged view of cross-bore

## REFERENCES

ALTIERO, N.J., & SIKARSKIE, D.L. (1975)

"An Integral Equation Method Applied to Penetration Problems in Rock Mechanics",

in Boundary Integral Equation Method: Computational Applications in Applied Mechanics, (eds. T.A. Cruse & F.J. Rizzo), ASME Proc. AMD-11, New York, pp. 119-141.

ASTM DESIGNATION E399-74 (1974)

"Method of Test for Plane-Strain Fracture Toughness of Metallic Materials",

pp. 471-490.

ATLURI, S.N., & KATHIRESAN, K. (1979)

"3D Analysis of Surface Flaws in Thick-Walled Reactor Pressure Vessels Using Displacement-Hybrid Finite Element Method",

*Nucl. Eng. & Des.*, 51, pp. 163-176.

BARNERJEE, P.K. (1976)

"Integral Equation Methods for the Analysis of Piece-Wise Non-Homogeneous Three-Dimensional Elastic Solids of Arbitrary Shape",

*Int. J. Mech. Sci.*, 18, pp. 293-303.

BARR, B.I.G., EVANS, W.T., WATKINS, J., & ROUHI, M.R. (1978)

"Fracture Path Prediction Using Numerical and Experimental Technique",

Proc. 1st Int. Conf. Numerical Methods in Fracture Mechanics, Swansea, (eds. A.R. Luxmoore & D.R.J. Owen), pp. 193-206.

BARSOUM, R.S. (1976)

"On the Use of Isoparametric Finite Elements in Linear Elastic Fracture Mechanics",

*Int. J. Num. Methods Eng.*, 10, pp. 25-37.

BAZANT, Z.P., & ESTENSSORO, L.F. (1977)

"General Numerical Method for Three-Dimensional Singularities in Cracked or Notched Elastic Solids",

in Fracture 1977, Proc. 4th Int. Conf. on Fracture, University of Waterloo, Canada, (ed. D.M.R. Taplin), 3, pp. 371-385.

BAZANT, Z.P., & ESTENSSORO, L.F. (1979)

"Surface Singularity and Crack Propagation",

*Int. J. Solids Struct.*, 15, pp. 405-426.

BENTHEM, J.P. (1975)

"Three-Dimensional State of Stress at the Vertex of a Quarter-Infinite Crack in a Half-Space",

Delft University of Technology, Report No. 563, Delft, The Netherlands.

BERGAN, P.G., & AAMODT, B. (1974)

"Finite Element Analysis of Crack Propagation in Three-Dimensional Solids Under Cyclic Loading",

*Nucl. Eng. & Des.*, 29, pp. 180-188.

BESUNER, P.M. (1977)

"The Influence Function Method for Fracture Mechanics and Residual Fatigue Life Analysis of Cracked Components Under Complex Stress Fields",

*Nucl. Eng. & Des.*, 43, pp. 115-154.

BLACKBURN, W.S., & HELLEN, T.K. (1974)

"Calculation of Stress Intensity Factors for Elliptical and Semi-Elliptical Cracks in Blocks and Cylinders",

CEGB Report No. RD/B/N3103.

BLACKBURN, W.S., & HELLEN, T.K. (1977)

"Calculation of Stress Intensity Factors in Three-Dimensions by Finite Element Method",

*Int. J. Num. Methods Eng.*, 11, pp. 211-229.

BOWIE, O.L. (1956)

"Analysis of an Infinite Plate Containing Radial Cracks Originating at the Boundary of an Internal Circular Hole",

*J. Math. Phys.*, 35, pp. 60-71.

BOWIE, O.L. (1973)

"Solutions of Plane Crack Problems by Mapping Techniques",

in Mechanics of Fracture, (ed. G.C. Sih), Noordhoff, 1, pp. 1-55.

BOWIE, O.L., & FREESE, C.E. (1972)

"Elastic Analysis for a Radial Crack in a Circular Ring",

*Eng. Fract. Mech.*, 4, pp. 315-321.

BOWIE, O.L., & NEAL, D.M. (1969)

"A Modified Mapping Collocation Technique for Accurate Calculation of Stress Intensity Factors",

AMMRC TR 69-28.

BOYD, G.M. (1970)

Brittle Fracture in Steel Structures,

Butterworth, London.

BRANCO, M.C.A. (1976)

"A Fracture Mechanics Approach to Environmental and Elastic-Plastic Fatigue Crack Propagation",

Ph.D. Thesis, Imperial College, University of London.

BREBBIA, C.A. (1978a)

The Boundary Element Method for Engineers,

Pentech Press, London.

BREBBIA, C.A. (1978b) (ed.)

Recent Advances in Boundary Element Methods,

Conference Proceedings, University of Southampton.

BROEK, D. (1971)

"Applicability of Fracture Toughness Data to Surface Flaws and to Corner Cracks at Holes",

National Aerospace Institute, Amsterdam, Report TR 71033.

BROEK, D., & SCHIJVE, J. (1963)

"The Influence of the Mean Stress on the Propagation of Fatigue Cracks in Aluminium Alloy Sheets",

National Aerospace Institute, Amsterdam, Report TR-M-2111.

BROEKHOVEN, M.J.G., & RUIJTENBEEK, M.G. (1975)

"Fatigue Crack Extension in Nozzle Junctions: Comparison of Analytical Approximations with Experimental Data",

in Proc. 3rd Int. Conf. on Structural Mechanics in Nuclear Reactor Technology, London, G4/7.

BUTTERFIELD, R., & TOMLIN, G.R. (1972)

"Integral Techniques for Solving Zoned Anisotropic Continuum Problems",

in Proc. Int. Conf. on Variational Methods in Engineering,

University of Southampton, 2, pp. 9/31-9/51.

CARTWRIGHT, D.J., & ROOKE, D.P. (1975)

"Evaluation of Stress Intensity Factor",

*J. Strain Anal.*, 10-4, pp. 217-224.

CHAN, S.K., TUBA, I.S., & WILSON, W.K. (1970)

"On the Finite Element Method in Linear Fracture Mechanics",

*Eng. Fract. Mech.*, 2, pp. 1-17.

COLE, B.N. (1969)

"Strategy for Cross-Bores in High Pressure Containers",

*J. Mech. Eng. Sci.*, 11, pp. 151-161.

CROFTON, P.S.J. (1977)

Unpublished results,

Imperial College, University of London.

CRUSE, T.A. (1969)

"Numerical Solutions in Three-Dimensional Elastostatics",

*Int. J. Solids Struct.*, 5, pp. 1259-1274.

CRUSE, T.A. (1972)

"Numerical Evaluation of Elastic Stress Intensity Factors by the Boundary Integral Equation Method",

in The Surface Crack: Physical Problems and Computational Solution, (ed. J.L. Swedlow), ASME, New York, pp. 153-170.

CRUSE, T.A. (1973)

"Application of the Boundary Integral Equation Method to Three-Dimensional Stress Analysis",

*Comp. & Struct.*, 3, pp. 509-527.

CRUSE, T.A. (1974)

"An Improved Boundary Integral Equation Method for Three-Dimensional Elastic Stress Analysis",

*Comp. & Struct.*, 4, pp. 741-754.

CRUSE, T.A. (1975)

"Boundary Integral Equation Method for Three-Dimensional Elastic Fracture Mechanics Analysis",

Air Force Office of Scientific Research TR-75-0813.

CRUSE, T.A. (1977)

"Mathematical Foundations of the Boundary Integral Equation Method in Solid Mechanics",

Pratt & Whitney Aircraft Group Report No. AFOSR-TR-77-1002.

CRUSE, T.A., & BESUNER, P.M. (1975)

"Residual Life Prediction for Surface Cracks in Complex Structural Details",

*J. Aircraft*, 12-4, pp. 369-375.

CRUSE, T.A., & MEYERS, G.J. (1977)

"Three-Dimensional Fracture Mechanics Analysis",

*J. Struct. Div.*, ASCE, 103-ST2, pp. 309-320.

CRUSE, T.A., MEYERS, G.J., & WILSON, R.B. (1977)

"Fatigue Growth of Surface Cracks",

ASTM, STP 631, pp. 174-189.

CRUSE, T.A., & RIZZO, F.J. (1975) (eds.)

Boundary Integral Equation Method: Computational Application in Applied Mechanics,

ASME Proc. AMD, 11, New York.

CRUSE, T.A., & VAN BUREN, W. (1971)

"Three-Dimensional Elastic Stress Analysis of a Fracture Specimen with an Edge Crack",

*Int. J. Fract. Mech.*, 7, pp. 1-15.

CRUSE, T.A., & WILSON, R.B. (1978)

"Advanced Application of Boundary Integral Equation Methods",

*Nucl. Eng. & Des.*, 46, pp. 223-234.

DAS, P.C. (1978)

"A Disc Based Block Elimination Technique Used for the Solution of Non-Symmetrical Fully Populated Matrix Systems Encountered in the Boundary Element Method",

in Recent Advances in Boundary Element Methods, (ed. C.A. Brebbia), Southampton, pp. 391-404.

DUGDALE, D.S. (1960)

"Yielding of Steel Sheets Containing Slits",

*J. Mech. Phys. Solids*, 8, pp. 100-108.

DUGGAN, T.V. (1977)

"A Theory of Fatigue Crack Propagation",

*Eng. Fract. Mech.*, 9, pp. 735-747.

ELBER, W. (1971)

"The Significance of Fatigue Crack Closure",

ASTM, STP 486, pp. 230-242.

ERDOGAN, F. (1967)

"Crack Propagation Theories",

NASA-CR-901.

FAUPEL, J.H., & HARRIS, D.B. (1957)

"Stress Concentration in Heavy-Walled Cylindrical Pressure Vessels",

*J. Ind. Chem.*, 49, pp. 1979-1986.

FESSLER, H., & LEWIN, B.H. (1956)

"Stress Distribution in a Tee Junction of Thick Pipes",

*Br. J. Appl. Phys.*, 7, pp. 76-79.

FOLIAS, E.S. (1975)

"On the Three-Dimensional Theory of Cracked Plates",

Trans. ASME, Series E, *J. Appl. Mech.*, 42-3, pp. 663-674.

FORMAN, R.G., KEARNEY, V.E., & ENGLE, R.M. (1967)

"Numerical Analysis of Crack Propagation in a Cyclic-Loaded Structure",

*J. Basic Eng.*, Trans. ASME, 89D, pp. 459-464.

GALLAGHER, G.H. (1978)

"A Review of Finite Element Techniques in Fracture Mechanics",

in Proc. 1st Int. Conf. on Numerical Methods in Fracture Mechanics,

Swansea, (eds. A.R. Luxmoore & D.R.J. Owen), pp. 1-25.

GERDEEN, J.C. (1972)

"Analysis of Stress Concentrations in Thick Cylinders with Sideholes and Crossbores",

*J. Eng. Ind.*, Trans. ASME, 94-3, pp. 815-824.

GERDEEN, J.C., & SMITH, R.E. (1972)

"Experimental Determination of Stress Concentration Factors in Thick-Walled Cylinders with Crossholes and Sideholes",

*Exp. Mech.*, pp. 530-536.

GRIFFITH, A.A. (1921)

"The Phenomena of Rupture and Flow in Solids",

*Phil. Trans. R. Soc. Lond.*, A221, pp. 163-197.

GRIFFITH, A.A. (1924)

"The Theory of Rupture",

in Proc. 1st Int. Congress on Applied Mechanics, Delft, pp. 55-63.

HARTRANFT, R.J., & SIH, G.C. (1970)

"Approximate Three-Dimensional Theory of Plates with Applications to Crack Problems",

*Int. J. Eng. Sci.*, 8, pp. 711-729.

HARTRANFT, R.J., & SIH, G.C. (1973)

"Alternating Method Applied to Edge and Surface Crack Problems",

in Mechanics of Fracture, (ed. G.C. Sih), Noordhoff, 1, pp. 179-229.

HARTRANFT, R.J., & SIH, G.C. (1977)

"Stress Singularity for a Crack with an Arbitrary Curved Crack Front",

*Eng. Fract. Mech.*, 9, pp. 705-718.

HELIOT, J. LABBENS, R.C., & PELLISSIER-TANON, A. (1978)

"Semi-Elliptical Cracks in the Meridianal Plane of a Cylinder Subjected to Stress Gradients. Calculation of Stress Intensity Factors by the Boundary Integral Equation Method",

ASTM 11th National Symp. on Fracture Mechanics, 12-14 June, Blacksburg, Virginia, USA.

HELLEN, T.K., & DOWLING, A.R. (1974)

"Three-Dimensional Crack Analysis Applied to an LWR Nozzle-Cylinder Intersection",

CEGB Report RD/B/N3042.

HENSHELL, R.D., & SHAW, K.G. (1975)

"Crack Tip Elements are Unnecessary",

*Int. J. Num. Methods Eng.*, 9, pp. 495-509.

HIBBITT, H.D. (1977)

"Some Properties of Singular Isoparametric Elements",

*Int. J. Num. Methods Eng.*, 11, pp. 180-184.

INGLIS, C.E. (1913)

"Stresses in a Plate Due to the Presence of Cracks and Sharp Corners",

*Trans. Inst. Nav. Archit.*, 55, pp. 219-241.

IRWIN, G.R. (1948)

"Fracture Dynamics",

in Fracturing of Metals, ASM Publishers, pp. 147-166.

IRWIN, G.R. (1957a)

"Relation of Stresses Near a Crack to the Crack Extension Force",

in Proc. 9th Int. Congress on Applied Mechanics, Brussels, pp. 245-251.

IRWIN, G.R. (1957b)

"Analysis of Stresses and Strains Near the End of a Crack Traversing a Plate",

*J. Appl. Mech.*, 24, pp. 361-364.

IRWIN, G.R. (1958)

"Fracture",

in Encyclopaedia of Physics, Springer, Heidelberg, VI, pp. 551-590.

IRWIN, G.R. (1960)

"Plastic Zone Near a Crack and Fracture Toughness",

in Proc. 7th Sagamore Conf., pp. IV-63.

JASWON, M.A. (1963)

"Integral Equation Methods in Potential Theory I",

*Proc. R. Soc. Lond.*, A275, pp. 23-32.

JASWON, M.A., & SYMM, G.T. (1977)

Integral Equation Methods in Potential Theory and Elastostatics,

Academic Press, London.

KLESNIL, M., & LUKAS, P. (1972)

"Influence of Strength and Stress History on Growth and Stabilisation of Fatigue Cracks",

*Eng. Fract. Mech.*, 4, pp. 77-92.

KNOTT, J.F. (1973)

Fundamentals of Fracture Mechanics,

Butterworth, London.

KOBAYASHI, A.S., EMERY, A., POLVANICH, N., & LOVE, W.J. (1977)

"Surface Flaw in a Pressurized and Thermally Shocked Hollow Cylinder",

*Int. J. Pres. Ves. & Piping*, 5, pp. 103-122.

KOBAYASHI, A.S., POLVANICH, N., EMERY, A., & LOVE, W.J. (1975)

"Stress Intensity Factor of a Surface Crack in a Pressurized Cylinder",

in Computational Fracture Mechanics, (eds. E. Rybicki & S. Benzley),

ASME Special Publication, pp. 121-132.

KUPRADZE, V.D. (1963)

"Dynamical Problems in Elasticity",

in Progress in Solid Mechanics, (eds. I.N. Sneddon & R. Hill), III,

Wiley.

LACHAT, J.C. (1975)

"A Further Development of the Boundary Integral Technique for Elastostatics",

Ph.D. Thesis, University of Southampton.

LACHAT, J.C., & WATSON, J.O. (1975)

"A Second Generation Boundary Integral Equation Program for Three-Dimensional Elastic Analysis",

in Boundary Integral Equation Method: Computational Applications in Applied Mechanics, (eds. T.A. Cruse & F.J. Rizzo), ASME Proc. AMD, 11, New York, pp. 85-100.

LACHAT, J.C., & WATSON, J.O. (1976)

"Effective Numerical Treatment of Boundary Integral Equation: A Formulation for Three-Dimensional Elastostatics",

*Int. J. Num. Methods Eng.*, 10, pp. 991-1005.

LACHAT, J.C., & WATSON, J.O. (1977)

"Progress in the Use of the Boundary Integral Equation Illustrated by Examples",

*Comp. Methods Appl. Mech. Eng.*, 10, pp. 273-289.

LAKE, G.F. (1956)

in Proc. Int. Conf. on Fatigue of Metals, Inst. Mech. Engrs., p. 743.

LANCASTER, J.F. (1973)

"Failures of Boilers and Pressure Vessels: Their Causes and Prevention",

*Int. J. Pres. Ves. & Piping*, 1, pp. 155-170.

LITTLE, R.E. (1965)

"Stress Concentrations for Holes in Cylinders",

*Mach. Des.*, 23 December, pp. 133-135.

LOVE, A.E.H. (1944)

A Treatise on the Mathematical Theory of Elasticity,

Dover.

LUXMOORE, A.R., & OWEN D.R.J. (1978) (eds.)

Proc. 1st Int. Conf. on Numerical Methods in Fracture Mechanics,

Swansea.

MARCAL, P.V. (1972)

"Three-Dimensional Finite Element Analysis for Fracture Mechanics", in The Surface Crack: Physical Problems and Computational Solutions, (ed. J.L. Swedlow), ASME, New York, pp. 187-202.

McCARTNEY, L.N., & COOPER, P.M. (1977)

"A Numerical Method of Processing Fatigue Crack Propagation Data", *Eng. Fract. Mech.*, 9, pp. 265-272.

McGOWAN, J.J., & RAYMUND, M. (1978)

"Stress Intensity Factor Solutions for Internal Longitudinal Semi-Elliptical Surface Flaws in a Cylinder Under Arbitrary Loadings", ASTM 11th National Symp. on Fracture Mechanics, 12-14 June, Blacksburg, Virginia, USA.

MENDELSON, A. (1973)

"Boundary Integral Methods in Elasticity and Plasticity", NASA TND 7418.

MIKHLIN, S.G. (1965)

Multidimensional Singular Integrals and Integral Equations, Pergamon Press, London.

MONTULLI, L.M. (1975)

"The Development and Solution of Boundary Integral Equations for Crack Problems in Fracture Mechanics", Ph.D. Dissertation, Air Force Institute of Technology, Dayton, Ohio, USA.

MORRISON, J.L.M., CROSSLAND, B., & PARRY, J.S.C. (1959)

"Fatigue Strength of Cylinders with Cross-Bores", *J. Mech. Eng. Sci.*, 1-3, pp. 207-210.

NEWMAN, J.C., Jr. (1974)

"Stress Analysis of the Compact Specimen Including the Effects of Pin Loading", ASTM, STP 560, pp. 105-121.

NISHIOKA, K., & HIRAWAKA, K. (1975)

"Effect of Internal Surface Flaw on the Fatigue Strength of a Thick-Walled Cylinder Under Cyclic Internal Pressure",

in Proc. 2nd Int. Conf. on High Pressure Engineering, University of Sussex, (ed. H.Ll. Pugh), Inst. Mech. Engrs. Publication (1977).

OROWAN, E. (1949)

"Fracture ans Strength of Solids",

*Rep. Prog. Phys.*, 12, pp. 185-232.

OROWAN, E. (1955)

"Energy Criteria of Fracture",

*Weld. J. Res. Suppl.*, 34, pp. 157s-160s.

PARIS, P.C., & ERDOGAN, F. (1963)

"A Critical Analysis of Crack Propagation Laws",

*J. Basic Eng.*, Trans. ASME, 85, pp. 528-534.

PARIS, P.C., GOMEZ, H.P., & ANDERSON, W.E. (1961)

"A Rational Analytic Theory of Fatigue",

*The Trend in Engineering*, 13-9, pp. 9-14.

PARIS, P.C., & SIH, G.C. (1965)

"Stress Analysis of Cracks",

ASTM, STP 381, pp. 30-83.

PEARSON, C.E. (1959)

Theoretical Elasticity,

Harvard University Press.

PEREIRA, M.F.S. (1977)

"Three-Dimensional Linear-Elastic Fracture Mechanics Analysis of Thick-Walled Pressure Vessel Components",

Ph.D. Thesis, Imperial College, University of London.

PRIDDLE, E.K. (1976)

"High Cycle Fatigue Crack Propagation Under Random and Constant Amplitude Loadings",

*Int. J. Pres. Ves. & Piping*, 4, p. 89.

PUGH, H.Ll.D. (1977) (ed.)

Proc. 2nd Int. Conf. on High Pressure Engineering, University of Sussex, July 1975, Inst. Mech. Engrs. Publication.

RAJU, I.S., & NEWMAN, J.C., Jr. (1977)

"Three-Dimensional Finite Element Analysis of Finite-Thickness Fracture Specimens",

NASA TND-8414.

RAJU, I.S., & NEWMAN, J.C., Jr. (1979)

"Stress Intensity Factors for a Wide Range of Semi-Elliptical Surface Cracks in Finite-Thickness Plates",

*Eng. Fract. Mech.*, 11, pp. 817-829.

RICARDELLA, P.C. (1973)

"An Implementation of the Boundary Integral Technique for Planar Problems on Elasticity and Elasto-Plasticity",

Report SM 73-10, Mechanical Engineering Department, Carnegie-Mellon University, Pittsburgh, Pennsylvania, USA.

RICE, J.R., & LEVY, N. (1970)

"The Part-Through Surface Crack in an Elastic Plate",

NASA NGL 40-002-080/3.

RICH, T.P., & CARTWRIGHT, D.J. (1977) (eds.)

Case Studies in Fracture Mechanics,

AMMRC MS 77-5.

RIZZO, F.J. (1967)

"An Integral Equation Approach to Boundary Value Problems of Classical Elastostatics",

*Q. Appl. Math.*, 25, pp. 83-95.

RIZZO, F.J., & SHIPPY, D.J. (1977)

"An Advanced Boundary Integral Equation Method for Three-Dimensional Thermo-Elasticity",

*Int. J. Num. Methods Eng.*, 11, pp. 1753-1768.

SHAH, R.C., & KOBAYASHI, A.S. (1973)

"Effect of Poisson's Ratio on Stress Intensity Magnification Factor",

*Int. J. Fract.*, 9, pp. 360-362.

SHANK, M.E. (1954)

A Critical Survey of Brittle Fracture in Carbon Plate Steel Structures Other than Ships,

Welding Research Council Engineering Foundation Publication.

SHANNON, R.W.E. (1974)

"Stress Intensity Factors for Thick-Walled Cylinders",

*Int. J. Pres. Ves. & Piping*, 2, p. 19.

SHANNON, R.W.E., & AUSTIN, B.A. (1971)

"The Application of Fracture Mechanics to Failure of Thick-Walled Cylinders",

in Proc. Conf. on Practical Applications of Fracture Mechanics to Pressure Technology, Inst. Mech. Engrs., London, C32/71, pp. 109-118.

SIH, G.C. (1973)

"A Special Theory of Crack Propagation",

in Mechanics of Fracture, (ed. G.C. Sih), Noordhoff, 1, pp. XXI-XLV.

SIH, G.C. (1975)

"A Three-Dimensional Strain Energy Density Theory of Crack Propagation",

in Mechanics of Fracture, (ed. G.C. Sih), Noordhoff, 2, pp. XV-LIII.

SIH, G.C. (1978)

"Mechanics of Fracture: Linear Response",

in Proc. 1st Int. Conf. on Numerical Methods in Fracture Mechanics,

Swansea, (eds. A.R. Luxmoore & D.R.J. Owen), pp. 155-192.

SMITH, F.W., & ALAVI, M.J. (1971)

"Stress Intensity Factors for a Penny-Shaped Crack in Halfspace",

*Eng. Fract. Mech.*, 3, pp. 241-254.

SNEDDON, I.N. (1946)

"The Distribution of Stress in the Neighbourhood of a Crack in an Elastic Solid",

*Proc. R. Soc. Lond.*, A187, pp. 229-260.

SNYDER, M.D., & CRUSE, T.A. (1975)

"Boundary-Integral Equation Analysis of Cracked Anisotropic Plates",

*Int. J. Fract.*, 11-2, pp. 315-328.

SOKOLNIKOFF, I.S. (1956)

Mathematical Theory of Elasticity,

McGraw-Hill.

SRAWLEY, J.E., & GROSS, B. (1972)

"Stress Intensity Factors for Bend and Compact Specimens",

*Eng. Fract. Mech.*, 4, pp. 587-589.

STROUD, A.H., & SECREST, D. (1966)

Gaussian Quadrature Formulas,

Prentice-Hall, New York.

SWEDLOW, J.L. (1972) (ed.)

The Surface Crack: Physical Problems and Computational Solutions,

ASME, New York.

SYMM, G.T. (1963)

"Integral Equation Methods in Potential Theory II",

*Proc. R. Soc. Lond.*, A275, pp. 33-46.

TAN, C.L., & CROFTON, P.S.J. (1977)

Unpublished results,

Imperial College, University of London.

TAN, C.L., & FENNER, R.T. (1978)

"Three-Dimensional Stress Analysis by the Boundary Integral Equation Method",

*J. Strain Anal.*, 13-4, pp. 213-219.

TAN, C.L., & FENNER, R.T. (1979a)

"Stress Intensity Factor for Semi-Elliptical Surface Cracks in Pressurized Cylinders Using the Boundary Integral Equation Method",

*Int. J. Fract.*, to be published.

TAN, C.L., & FENNER, R.T. (1979b)

"Elastic Fracture Mechanics Analysis by the Boundary Integral Equation Method",

*Proc. R. Soc. Lond.*, to be published.

TRACEY, D.M. (1973)

"3-D Elastic Singularity Element for Evaluation of $K$ Along an Arbitrary Crack Front",

*Int. J. Fract.*, 9, pp. 340-343.

UNDERWOOD, J.H. (1972)

"Stress Intensity Factors for Internally Pressurized Thick-Walled Cylinders",

ASTM, STP 513, pp. 59-70.

VOGEL, S.M., & RIZZO, F.J. (1973)

"An Integral Equation Formulation of Three-Dimensional Anisotropic Elastostatic Boundary Value Problems",

*J. Elas.*, 3, pp. 203-216.

WALKER, E.K. (1970)

"Effects of Environment and Complex Load History on Fatigue Life", ASTM, STP 462, pp. 1-14.

WATSON, J.O. (1978)

"The Solution of Boundary Integral Equations of Three-Dimensional Elastostatics for Infinite Regions", in Recent Advances in Boundary Element Methods, (ed. C.A. Brebbia), Southampton.

WATSON, J.O. (1979)

Private communication.

WEAVER, J. (1977)

"Three-Dimensional Crack Analysis", *Int. J. Solids Struct.*, 13, pp. 321-330.

WILLIAMS, P.W. (1972)

Numerical Computation, Nelson, London.

WILSON, R.B., & CRUSE, T.A. (1978)

"Efficient Implementation of Anisotropic Three-Dimensional Boundary Integral Equation Stress Analysis", *Int. J. Num. Methods Eng.*, 12, pp. 1383-1397.

ZIENKIEWICZ, O.C. (1977)

The Finite Element Method, McGraw-Hill, London.